CARBON-NEUTRAL SYNTHETIC FUEL PRODUCTION VIA CO_2 METHANATION OVER SUPPORTED Ni CATALYSTS

by

OSAZE OMOREGBE



A thesis submitted to the University of Birmingham for the degree of

DOCTOR OF PHILOSOPHY

School of Chemical Engineering

College of Engineering and Physical Sciences

University of Birmingham

October 2023

UNIVERSITY OF
BIRMINGHAM

University of Birmingham Research Archive

e-theses repository

This unpublished thesis/dissertation is copyright of the author and/or third parties. The intellectual property rights of the author or third parties in respect of this work are as defined by The Copyright Designs and Patents Act 1988 or as modified by any successor legislation.

Any use made of information contained in this thesis/dissertation must be in accordance with that legislation and must be properly acknowledged. Further distribution or reproduction in any format is prohibited without the permission of the copyright holder.

Abstract

The innovative Power-to-Gas concept is a promising solution for converting surplus energy into synthetic natural gas (SNG). Through catalytic CO_2 methanation, renewable H_2 and captured CO_2 are converted to methane (CH_4) or SNG, thereby offering a potent energy storage medium characterised by its elevated heating value. Intrinsic to the global push towards sustainable energy solutions, CO_2 methanation stands as a mature reaction, perpetually demanding high-performing catalyst design and synthesis to enhance industrial process efficiency.

The main thesis goals come together along three crucial trajectories. First, it involves the synthesis of high-performance Ni-based catalysts, including YSZ, CeO_2, Al_2O_3, and SBA-15, followed by their performance evaluation for CO_2 methanation. Second, the investigation of the influence of distinct reactor conditions, encompassing temperature, H_2/CO_2 ratio, catalyst positioning, CH_4 presence in feed, gas hourly space velocity (GHSV), pressure, and the effect of La-promoter on the yield and selectivity of the optimal catalyst. Finally, the third trajectory delves into the design and modification of monolithic and split reactors for CO_2 methanation. This chapter encompasses an investigation into dual catalyst beds and the dynamic interplay of catalyst ratios within reactor subsections.

The thesis started with a background on the recent trend in energy demand, the impact of high fossil fuel dependency on climate change, and the transition from fossil fuel to renewable energy. The discussion also covered an overview of carbon capture technologies and the potential of CO_2 methanation as a strategy for CO_2 mitigation. The thermodynamics, reactor considerations, and intricate reaction mechanisms of CO_2 methanation are discussed.

The catalysts were synthesised using the wetness impregnation technique, followed by comprehensive characterisation, including BET surface measurements, thermogravimetric analysis, scanning electron microscopy, and Raman spectroscopy, for the understanding of their physicochemical properties. The performance of the synthesised catalysts was studied in a continuous flow quartz tube fixed-bed reactor with an internal diameter of 5.5 mm and wall thickness of 2 mm at a temperature range of 473

to 823 K and pressure range of 0.5 to 3 bar depending on the test setup. The gaseous feed stream employed contains N_2 (60 mL min^{-1}), H_2 (60 mL min^{-1}) and CO_2 (15 mL min^{-1}) in the ratio of 4:4:1. Mears' and Weisz-Prater criteria obtained indicated negligible transport limitations.

Activity tests revealed Ni/YSZ as the optimal catalyst with a CO_2 conversion rate of approximately 83%. The superior performance of Ni/YSZ is attributed to its distinctive properties, including high oxygen vacancies, augmented basic sites, and an intrinsic resilience to metal sintering, underscored by a low activation energy. The optimum temperature was between 633 and 643 K beyond which the catalyst activity declined. While an increase in the H_2:CO_2 ratio favoured both the CH_4 yield and CO_2 conversion, CH_4 yield was found to decline at an H_2:CO_2 ratio beyond 4.

For the investigation of the effect of La-promoter on the performance of Ni/YSZ, a slight stability enhancement was observed, but the catalytic activity was largely unaltered. Notably, there was a structural change in Ni/YSZ as observed from the characterisation results upon La-promoter addition indicating its potential to positively influence catalyst performance in other reforming reactions.

For the reactor design, three distinctive configurations—the single reactor with one catalyst bed, the single reactor with dual catalyst beds, and a two-reactor series, were considered. In the latter configuration, the catalyst ratio within the reactors was varied from 20 to 80%. The outcome revealed that the series-connected two-reactor system with an installed water-removing device and catalyst of ratio of 30%:70% is the best, providing a CO_2 conversion of approximately 99%.

In a broader perspective, the findings from this work can help in advancing the research on the seamless and efficient integration of a methanation reactor with a solid oxide electrolyser, considering that the best performance was achieved at reaction conditions such as relatively elevated temperatures and low pressures, which are similar to the operating conditions of a solid oxide electrolyser.

Acknowledgements

I extend my heartfelt gratitude to Professor Robert Steinberger-Wilckens, my dedicated supervisor, whose unwavering guidance, and support have been a cornerstone of my PhD journey. His patience and encouragement propelled me through challenges, igniting my perseverance. Professor Steinberger-Wilckens' passion for research profoundly influenced my determination to pursue a career in this field. Additionally, I sincerely appreciate his guidance in helping me to secure organised funding for the final stages of my work.

Special thanks also go to both Dr Ahmad El-Kharouf and Dr Artur Majewski, my second supervisors, for their invaluable insights and practical assistance with experiments. Their invaluable proved instrumental in navigating the complexities of thesis writing.

I am incredibly grateful to the entire team at the Hydrogen and Fuel Cell Research Centre. Their warm welcome and unwavering support made my transition to a new country much smoother. Their camaraderie and willingness to help enriched my research journey and brought a sense of joy to my new life. This positive environment undoubtedly played a vital role in the success of this work.

My gratitude extends to Jie Chen and colleagues from the Centre for Energy Storage for sharing expertise on BET surface area and FT-IR spectroscopy. Ludwig Schneider from the Electron Microscopy Centre offered invaluable training on microscopy techniques. Amy Newell and Mark Duffield provided essential assistance with XRD and Raman spectroscopy, respectively.

I am sincerely thankful for the financial support from the Petroleum Technology Development Fund (PTDF), GilChrist Educational Trust, Student Support Fund (University of Birmingham), and The Institution of Chemical Engineers (IChemE) that facilitated the completion of my PhD.

Lastly, my deepest gratitude goes to my incredible family: my wife, Ngozi Blessing Omoregbe, my siblings, David Osakue and Joshua O. Omoregbe, and my parents, Emmanuel and Mabel Omoregbe. In my darkest moments, their encouragement became my anchor, guiding me through challenges and inspiring my resilience. I cherish their unwavering presence and support.

Table of Contents

Abstract ..... **ii**
Acknowledgements ..... **iv**
Table of Contents ..... **v**
List of Figures ..... **ix**
List of Tables ..... **xvi**
List of Definition/ Nomenclature ..... **xviii**
ROMAN SYMBOLS XVIII
GREEK SYMBOLS XIX
ABBREVIATIONS XIX
List of Publications and Conferences ..... **xx**
LIST OF PUBLICATIONS XX
LIST OF CONFERENCES XX
CHAPTER 1 Introduction **1**
1.1 BACKGROUND 1
1.2 OVERVIEW OF CO_2 CAPTURE TECHNOLOGIES 6
1.2.1 Pre-combustion carbon capture technology *6*
1.2.2 Post-combustion carbon capture technology *7*
1.2.3 Oxy-fuel combustion technology *7*
1.3 OVERVIEW OF CO_2 METHANATION REACTION 8
1.3.1 Thermodynamic Considerations of CO_2 methanation *8*
1.3.2 Reactor consideration *9*
1.3.3 Mechanism of CO_2 methanation *11*
1.4 AIMS AND OBJECTIVES 17
CHAPTER 2 Literature Review **19**
2.1 DEVELOPMENT OF CO_2 METHANATION CATALYSTS 19
2.3.1 Active Metal Component for CO_2 methanation Catalysts *20*
2.3.2 Noble Metal *20*
2.3.2.1 Ruthenium 20
2.3.2.2 Rhodium 26
2.3.2.3 Palladium 30
2.3.3 Non-noble Metal: Nickel-based catalysts *33*
2.3.4 Catalyst Promoters *36*
2.3.4.1 Alkali and alkaline metals 37
2.3.4.2 Lanthanide promoters 40
2.3.5 Catalyst supports *46*
2.3.5.1 Ceria 47

2.3.5.1.1 Cerium oxide 48
2.3.5.1.2 Application of ceria in heterogenous catalytic reactions 50
2.3.5.2 Alumina 55
2.3.5.3 Yttria-stabilized zirconia 59
2.3.5.4 Santa Barbara Amorphous 15 60
2.3.5.4.1 Synthesis of SBA-15 61
2.3.5.4.2 Applications of SBA-15 62
2.2 DEACTIVATION MECHANISM OF CO_2 METHANATION CATALYSTS 64
2.4.1 Fouling *64*
2.4.1.1 Adsorbed atomic carbon 65
2.4.1.2 Amorphous carbon 66
2.4.1.3 Whisker carbon 67
2.4.1.4 Graphitic carbon 68
2.4.2 Poisoning *69*
2.4.3 Thermal deactivation *70*
2.4.4 Structural changes *71*
2.3 CONCLUDING REMARK 72
CHAPTER 3 Research Methodology 75
3.1 INTRODUCTION 75
3.2 MATERIALS AND EQUIPMENT 75
3.2 CATALYSTS PREPARATION 79
3.3 CATALYST CHARACTERISATION 81
3.4.1 Textural Analysis *81*
3.4.2 X-ray diffraction measurement *84*
3.4.3 Thermogravimetric analysis *86*
3.4.3.1 Temperature-programmed calcination TPC 86
3.4.3.2 Temperature-programmed oxidation 88
3.4.3.3 H_2 temperature-programmed reduction 89
3.4.4 Scanning electron microscopy *91*
3.4.5 Raman spectroscopy *91*
3.5 CATALYTIC ACTIVITY TEST 92
CHAPTER 4 Characterisation results and discussion 96
4.1 TEXTURAL ANALYSIS 96
4.1.1 Textural properties of Ni-based YSZ catalysts *96*
4.1.2 Textural properties of Ni-based Al_2O_3, CeO_2 and SBA-15 catalysts *100*
4.2 X-RAY DIFFRACTION MEASUREMENT 103
4.2.1 XRD of Ni-based YSZ catalysts *104*
4.2.2 XRD of Ni-based Al_2O_3, CeO_2 and SBA-15 catalysts *108*
4.3 THERMOGRAVIMETRIC ANALYSIS 112

4.3.1 Temperature-programmed calcination (TPC) *112*
4.3.2 H_2 temperature-programmed reduction *114*
4.3.2.1 H_2-TPR profiles for YSZ catalysts 114
4.3.2.2 H2-TPR profiles of 10%Ni/SBA-15, 10%Ni/CeO_2, 10%Ni/Al_2O_3 catalysts 116
4.4 SEM ANALYSIS 118
4.4.1 SEM images of Ni/YSZ catalysts *118*
4.4.2 SEM images of 10%Ni/SBA-15, 10%Ni/CeO_2, 10%Ni/Al_2O_3 catalysts *122*
CHAPTER 5 Determination of transport limitations 126
5.1 BLANK TEST 126
5.2 MASS & HEAT TRANSPORT LIMITATIONS 126
5.3 EXTERNAL MASS TRANSFER 128
5.4 INTERNAL MASS TRANSFER (PORE DIFFUSION) 129
5.5 EXTERNAL HEAT TRANSFER 130
5.6 INTRAPARTICLE HEAT TRANSFER 131
5.7 WALL AND RADIAL HEAT DISPERSION EFFECTS 132
CHAPTER 6 Catalyst activity 134
6.1 EFFECT OF CATALYST SUPPORT 134
6.1.1 Temperature dependency of the catalyst activity *134*
6.1.2 Arrhenius coefficient and energy of activation *137*
6.1.3 Stability test *141*
6.2 THE ROLE OF CATALYST POSITION IN THE REACTOR 143
6.3 EFFECT OF VARYING NI LOADING 144
6.4 EFFECT OF H_2/CO_2 RATIO 150
6.5 EFFECT OF GAS HOURLY SPACE VELOCITY (GHSV) 151
6.6 EFFECT OF ADDING CH_4 TO THE REACTANTS 152
6.7 EFFECT OF PRESSURE 153
6.8 EFFECT OF LA-PROMOTER 154
6.9 EFFECT OF REACTOR CONFIGURATION 157
6.9.1 A single fixed-bed quartz reactor containing two catalyst beds *157*
6.9.2 Two fixed-bed quartz reactors arranged in series *159*
CHAPTER 7 Post-reaction Characterisation results and discussion 165
7.1 XRD MEASUREMENT 165
7.2 RAMAN SPECTROSCOPY 167
7.3 SCANNING ELECTRON MICROSCOPY (SEM) 168
7.4 TEMPERATURE-PROGRAMMED OXIDATION (TPO) 169
CHAPTER 8 Conclusions and future work 174
8.1 CONCLUSIONS 174
8.2 FUTURE WORK 175

8.2.1 Synthesis of SBA-15 ..... *175*
8.2.2 Water effect at high pressure *176*
8.2.3 In-depth study on the Ni-YSZ Interaction *176*
8.2.4 Reactor configuration *176*
8.2.5 Integration of methanation and co-electrolysis *177*
8.2.6 Scale-up and techno-economic analysis *177*
References **178**
Appendix A Calculations for catalyst preparation **230**
Appendix B Crystallite size calculation from XRD data **234**
Appendix C TPO calculations for mass of carbon deposited **236**
Appendix D Activation energy calculation **238**
Appendix E Determination of transport resistances **241**
E.1 EXTERNAL MASS TRANSFER RESISTANCE 241
E.1.1 Calculation of mass transfer coefficient *241*
Superficial gas velocity 242
Colburn's J-factor for mass transfer 243
Schmidt number (S_c) 247
E.2 INTERNAL (INTRAPARTICLE) MASS TRANSFER RESISTANCE 250
E.3 EXTERNAL HEAT TRANSFER RESISTANCE 251
E.3.1 Estimation of the heat of reaction (ΔH_r) *252*
E.3.2 Estimation of the heat transfer coefficient, h *253*
Estimation of Prandtl number 254
E.4 INTERNAL HEAT TRANSFER RESISTANCE 257
E.5 WALL AND RADIAL HEAT DISPERSION EFFECTS 258

List of Figures

Figure 1.1 Annual global CO_2 emissions from energy combustion and industrial processes from 1900-2022. Adapted from ref (IEA, 2023). 2

Figure 1.2 Cumulative emissions of CO_2 and future non-CO_2 radiative forcing in determining the probability of limiting warming to 1.5℃ (Masson-Delmotte et al., 2018). 3

Figure 1.3 The capture and utilisation of CO_2 for SNG production via the methanation reaction. 5

Figure 1.4 Product compositions for CO (a) and CO_2 (b) methanation at equilibrium (0.1 MPa). Adapted from ref (Gao et al., 2015). 9

Figure 1.5 Fixed-bed reactor configuration (a) single tubular reactor (b) multi-tubular reactor configuration. Figure 2.2 (b) was adapted and modified from (Zhu et al., 2020). 10

Figure 2.1 Plot of temperature versus maximum conversion attained during CO_2 methanation, where C1 = Al_2O_3 supported Ru catalyst, C2 = CeO_2 supported Ru catalyst and C3 = CeO_2-Al_2O_3 supported Ru catalyst. Adapted from ref (Rynkowski et al., 2000).....21

Figure 2.2 Amount of methane produced (μmole of methane by gram of catalyst/minute) as a function of the CO_2/O_2 ratio over Rh(1%)/γ-Al_2O_3 at 398 K. The line plot represents the theoretical values. Adapted from (Beuls et al., 2012). 27

Figure 2.3 Catalytic performance of Ni-based catalysts at different temperatures (a) CO_2 conversion and (b) CH_4 selectivity. Adapted from (Ma et al., 2019). 34

Figure 2.4 Activity test profiles of Ni-based NSZ catalysts at different temperatures (a) CO_2 conversion and (b) CH_4 selectivity; reaction conditions: H_2/CO_2 = 4, GHSV = 12000 mL g^{-1} h^{-1}, 1 atm. Adapted from (Yang et al., 2020a). 39

Figure 2.5 Lab-scale 50 h long-term stability tests over different catalysts: (a) CO_2 conversion and (b) CH_4 selectivity; reaction conditions: H_2/CO_2 = 4, GHSV = 12000 mL g^{-1} h^{-1}, 400 °C, 1 atm. Adapted from (Yang et al., 2020a). 39

Figure 2.6 Activity profile showing (a) CH_4 and (b) CO_2 conversions with respect to time-on-stream during DRM conducted at 973 K. Adapted from ref (Cao et al., 2022b). 41

Figure 2.7 Activity profile showing the influence of varying Ce-promoter loading on the product yields and H_2/CO ratio for DRM runs at 973 K. Adapted from ref (Cao et al., 2022b). 43

Figure 2.8 TPO profiles of the selected spent Ce-promoted 10%Co/Al_2O_3 catalysts. Adapted from ref (Cao et al., 2022b). 43

Figure 2.9 Crystallographic unit cells of (a) CeO_2 in the fluorite structure, (b) A-type Ce_2O_3 and (c) C-type Ce_2O_3 bulk structures. In the figures, red balls are oxygen and grey balls are cerium. Adapted from ref (Du et al., 2018)...49

Figure 2.10 Schematic of the phase transformation pathways of aluminium hydroxides and oxides after heat treatment. Adapted from ref (Busca, 2019). 55

Figure 2.11 Effect of Ni content on CO_2 conversion in CO_2 methanation conducted at GHSV = 9000 mL g^{-1}_{cat} h^{-1}, H_2/CO_2 molar ratio = 3.5....58

Figure 2.12 Structure of SBA-15 formed from the hydrolysis of Pluronic 123 and tetraethyl orthosilicate. Modified from ref (Chaudhary and Sharma, 2017). 61

Figure 2.13 Activity profile showing (a) CO_2 conversion and (b) CH_4 selectivity during CO_2 methanation over Ni-based SBA-15 catalysts at atmospheric pressure, GHSV of 30,000 mL g^{-1} h^{-1}, H_2/CO_2 ratio of 4 and operating temperature within the range of 473 – 673 K. Ref (Hongmanorom et al., 2021). 63

Figure 3.1 Flowchart for the preparation of SBA-15 support. 80

Figure 3.2 Flowchart for catalyst synthesis using the wetness impregnation method. 80

Figure 3.3 Micromeritics® TriStar II Plus analyser with degasser. 81

Figure 3.4 A typical N_2 adsorption–desorption isotherm profile from a Micromeritics® TriStar II Plus analyser. 82

Figure 3.5 Diagrams (a) and (b) represent the principle of X-rays diffraction as proposed by Bragg's Law, and (c) shows the inner chamber of a Proto Benchtop AXRD equipment during a typical XRD analysis. 85

Figure 3.6 NETZSCH Analysing & Testing instrument for Temperature-programmed calcination. 87

Figure 3.7 Representation of a typical temperature and weight change profile from a TPC analysis conducted with the NETZSCH Analysing & Testing instrument in Figure 3.6. 88

Figure 3.8 TPO profile showing CO_2 signal as a function of the oxidation temperature. 89

Figure 3.9 H_2-TPR profile showing H_2 consumption as a function of temperature. The reduction peaks P1 and P2 are signals indicating the consumption of hydrogen at the lower and higher temperatures, respectively. 90

Figure 3.10 Diagrams representing the Tabletop Scanning Electron Microscope Hitachi TM3030. 91

Figure 3.11 inVia^{TM} Qontor confocal Raman microscope (M&M 2A04).....92
Figure 3.12 Scheme of (a) a single fixed-bed quartz reactor containing one catalyst bed, (b) a single fixed-bed quartz reactor containing two catalyst beds, and (c) two fixed-bed quartz reactors arranged in series with a water trap placed between them for the CO_2 methanation reaction. 95
Figure 4.1 N_2-adsorption/desorption isotherms of the YSZ support and the calcined Ni/YSZ catalysts with various Ni-loading before the reaction. 97
Figure 4.2 Nitrogen adsorption/desorption isotherms of YSZ support, 10%Ni/YSZ and La-promoted Ni/YSZ catalysts before reduction in H_2. 99
Figure 4.3 Nitrogen adsorption/desorption isotherms of SBA-15 and 10%Ni/SBA-15 before reduction in H_2. 101
Figure 4.4 Nitrogen adsorption/desorption isotherms of Al_2O_3 and 10%Ni/Al_2O_3 before reduction in H_2. 102
Figure 4.5 Nitrogen adsorption/desorption isotherms of CeO_2 and 10%Ni/CeO_2 before reduction in H_2. 103
Figure 4.6 XRD patterns of (a) fresh and (b) reduced Ni/YSZ catalysts with different Ni-loading. 104
Figure 4.7 XRD patterns of (a) fresh and (b) reduced La-promoted Ni/YSZ catalysts. 107
Figure 4.8 XRD patterns of (a) SBA-15, (b) unreduced 10%Ni/SBA-15 and (c) reduced 10%Ni/SBA-15 catalysts. 109
Figure 4.9 XRD patterns of (a) Al_2O_3, (b) unreduced 10%Ni/Al_2O_3 and (c) reduced 10%Ni/Al_2O_3 catalysts. 111
Figure 4.10 XRD patterns of (a) CeO_2 (b) unreduced 10%Ni/CeO_2 and (c) reduced 10%Ni/CeO_2 catalysts. 112
Figure 4.11 Temperature-programmed calcination profile of uncalcined SBA-15 at heating rate of 10 K min^{-1} under N_2 atmosphere. Equipment model: NETZSCH - TG 209 F1. 113
Figure 4.12 TPC profile of 10%Ni/YSZ, 10%Ni/Al_2O_3, 10%Ni/SBA-15 and 10%Ni/CeO_2 catalysts at heating rate of 10 K min^{-1} under N_2 atmosphere. Equipment model: NETZSCH - TG 209 F1.....113
Figure 4.13 H_2-TPR profiles of 5%Ni/YSZ, 10%Ni/YSZ, 20%Ni/YSZ, 30%Ni/YSZ, 40%Ni/YSZ, 50%Ni/YSZ and 75%Ni/YSZ calcined catalysts before the reaction. 115
Figure 4.14 H_2-TPR profiles of 10%Ni/YSZ and La-promoted Ni/YSZ catalysts. .116
Figure 4.15 H_2-TPR profiles and peak deconvolution of (a) 10%Ni/SBA-15, (b) 10%Ni/CeO_2, (c) 10%Ni/Al_2O_3, and (d) 10%Ni/YSZ catalysts. 117
Figure 4.16 SEM images of (a) YSZ, (b) 5%Ni/YSZ, (c) 10%Ni/YSZ, (d) 20%Ni/YSZ, (e) 30%Ni/YSZ, (f) 40%Ni/YSZ, (g) 50%Ni/YSZ and (h)

75%Ni/YSZ calcined catalysts before the reaction. Note: Images were taken in Zeiss Evo10. 119

Figure 4.17 SEM-EDS images of (a) YSZ, (b) 5%Ni/YSZ, (c) 10%Ni/YSZ, (d) 20%Ni/YSZ, (e) 30%Ni/YSZ, (f) 40%Ni/YSZ, (g) 50%Ni/YSZ and (h) 75%Ni/YSZ calcined catalysts after reduction. 120

Figure 4.18 SEM-EDS images of (a) YSZ, (b) 10%Ni/YSZ, (c) 2%La-10%Ni/YSZ, (d) 3%La-10%Ni/YSZ, (e) 4%La-10%Ni/YSZ, (f) 5%La-10%Ni/YSZ, catalysts after reduction. 121

Figure 4.19 SEM-EDS images of (a) SBA-15, (b) 10%Ni/SBA-15, (c) reduced 10%Ni/SBA-15 and (d) EDX mapping of reduced 10%Ni/SBA-15. ... 122

Figure 4.20 SEM-EDS images of (a) CeO_2, (b) 10%Ni/ CeO_2, (c) reduced 10%Ni/ CeO_2 and (d) EDX mapping of reduced 10%Ni/ CeO_2. 123

Figure 4.21 SEM-EDS images of (a) Al_2O_3, (b) 10%Ni/Al_2O_3, (c) reduced 10%Ni/Al_2O_3 and (d) EDX mapping of reduced 10%Ni/Al_2O_3. 124

Figure 6.1 Activity profiles of various supported Ni catalysts showing (a) CO_2 conversion and (b) CH_4 yield in a CO_2 methanation conducted within the temperature range of 473 to 713K at a pressure of 1 bar, GHSV 20250 mL h^{-1} g^{-1}_{cat} and H_2:CO_2:N_2 ratio of 4:1:4. 135

Figure 6.2 Activity profiles of various supported Ni catalysts showing CH_4 and CO selectivity in a CO_2 methanation conducted within the temperature range of 473 to 713K at a pressure of 1 bar, GHSV 20250 mL h^{-1} g^{-1}_{cat} and H_2:CO_2:N_2 ratio of 4:1:4. 136

Figure 6.3 Activation energies for CO_2 conversion during methanation over various supported catalysts estimated within the temperature range of 473 – 713 K. Other reaction conditions: pressure of 1 bar, GHSV 20250 mL h^{-1} g^{-1}_{cat} and H_2:CO_2:N_2 ratio of 4:1:4. 138

Figure 6.4 Longevity test profile for 10%Ni/SBA-15 and 10%Ni/YSZ catalysts in CO_2 methanation conducted under atmospheric pressure, temperature of 643 K, GHSV 20250 mL h^{-1} g^{-1}_{cat} and 72 hr-on-stream. 142

Figure 6.5 Effect of catalyst position in the reactor on CO_2 conversion and CH_4 selectivity in CO_2 methanation over 10%Ni/YSZ catalyst at 643K, 1 bar, GHSV 20250 mL h^{-1} g^{-1}_{cat} and reactor length of 30 cm. The colours were used to show the variation in temperature along the reactor: The light and dark colours represent the low and high temperature regions, respectively. 144

Figure 6.6 Activity test profile showing (a) CO_2 conversion and (b) CH_4 yield during CO_2 methanation over Ni/YSZ catalysts. Reaction conditions: Total flow = 135 mL min^{-1}, H_2:CO_2 ratio = 4, pressure = 1 bar, temperature = 473 – 703 K, GHSV 40,500 mL h^{-1} g^{-1}_{cat}. 146

Figure 6.7 Activity profile showing the influence of temperature and pressure on CO_2 equilibrium conversion and selectivity for CO_2 methanation conducted at a H_2:CO_2 ratio of 4. These results were achieved by minimising the Gibbs energy based on the NASA database. Adapted with permission from ref (Mebrahtu et al., 2019). Copyright 2019 Elsevier B.V. 147

Figure 6.8 Activity test profile showing the selectivity to CH_4 and CO formation during CO_2 methanation at 643 K over a Ni/YSZ catalysts. Reaction conditions: Total flow = 135 mL min^{-1}, H_2:CO_2 ratio = 4, pressure = 1 bar, GHSV 40,500 mL h^{-1} g^{-1}_{cat}. 149

Figure 6.9 Activity test profile showing the effect of varying the H_2/CO_2 ratio on CO_2 conversion and CH_4 yield during CO_2 methanation over a 10%Ni/YSZ catalyst. Reaction conditions: Total flow = 135 mL min^{-1}, H_2:CO_2 ratio = 4, pressure = 1 bar, temperature = 643 K, GHSV 20,250 mL h^{-1} g^{-1}_{cat}. 150

Figure 6.10 Influence of varying the GHSV on CO_2 conversion, CH_4 yield and selectivity during CO_2 methanation conducted over the 10%Ni/YSZ catalyst at 643 K and 1 bar. 152

Figure 6.11 Effect of adding CH_4 to the feed on CO_2 conversion and CH_4 and CO selectivity during CO_2 methanation conducted over 10%Ni/YSZ catalyst at 643 K, 1 bar and GHSV 20250 mL h^{-1} g^{-1}_{cat}. 153

Figure 6.12 Effect of pressure on the performance of 10%Ni/YSZ catalyst in CO_2 methanation conducted over at 573 K and GHSV 20250 mL h^{-1} g^{-1}_{cat}. . 154

Figure 6.13 Performance of 10%Ni/YSZ with the variation in the La-content in CO_2 methanation conducted under atmospheric pressure at 643 K and GHSV 40500 mL h^{-1} g^{-1}_{cat}. 156

Figure 6.14 Longevity test profiles showing the stability of 10%Ni/YSZ and 3%La-10%Ni/YSZ catalysts in CO_2 methanation conducted under atmospheric pressure at 643 K, GHSV 20250 mL h^{-1} g^{-1}_{cat} and 48hr on-stream. 156

Figure 6.15 Effect of varying the catalyst ratio in a single fixed-bed quartz reactor containing two catalyst beds on (a) CO_2 conversion and CH_4, and (b) CH_4 and CO selectivities during CO_2 methanation conducted at total feed flow = 135 mL min^{-1}, N_2:H_2:CO_2 ratio = 4:4:1, pressure = 1 bar, temperature = 643 K, GHSV 13,500 mL h^{-1} g^{-1}_{cat}. 158

Figure 6.16 Pictorial view of the two-reactors in series configuration without water-trap. 160

Figure 6.17 Pictorial view for two-reactors in series configuration with a water-trap. 161

Figure 6.18 CH_4 yield during longevity test over 10%Ni/YSZ catalysts in a single and two reactor configurations with a water-removing device at 643 K, 1 bar and 48 hr on-stream. 162

Figure 6.19 Effect of varying the catalyst ratio in the two fixed-bed quartz reactors setup arranged in series with a water trap on (a) CO_2 conversion and CH_4, and (b) CH_4 and CO selectivities during CO_2 methanation conducted at total feed flow = 135 mL min^{-1}, N_2:H_2:CO_2 ratio = 4:4:1, pressure = 1 bar, temperature = 643 K, GHSV 13,500 mL h^{-1} g^{-1}_{cat}. ... 164

Figure 7.1 XRD patterns of (a) SBA-15 supported, and (b) YSZ supported catalysts before and after 48hr on-stream longevity tests under the following CO_2 methanation conditions: Total feed flow = 135 mL min^{-1}, N_2:H_2:CO_2 ratio = 4:4:1, pressure = 1 bar, temperature = 643 K, GHSV 13,500 mL h^{-1} g^{-1}_{cat}. 166

Figure 7.2 Raman spectra of spent SBA-15 supported, and YSZ supported catalysts after 48hr on-stream longevity tests under the following CO_2 methanation conditions: Total feed flow = 135 mL min^{-1}, N_2:H_2:CO_2 ratio = 4:4:1, pressure = 1 bar, temperature = 643 K, GHSV 13,500 mL h^{-1} g^{-1}_{cat}. 167

Figure 7.3 SEM micrographs of spent (a) 10%Ni/SBA-15, (b) 10%Ni/YSZ and (c) 3%La-10%Ni/YSZ catalysts after 48hr on-stream longevity tests under the following CO_2 methanation conditions: Total feed flow = 135 mL min^{-1}, N_2:H_2:CO_2 ratio = 4:4:1, pressure = 1 bar, temperature = 643 K, GHSV 13,500 mL h^{-1} g^{-1}_{cat}. 168

Figure 7.4 TPO profiles showing the weight loss of graphite and spent catalysts after 48hr on-stream longevity tests under the following CO_2 methanation conditions: Total feed flow = 135 mL min^{-1}, N_2:H_2:CO_2 ratio = 4:4:1, pressure = 1 bar, temperature = 643 K, GHSV 13,500 mL h^{-1} g^{-1}_{cat}. 169

Figure 7.5 TPO profiles showing the CO_2 signals from carbon oxidation of spent (a) 10%Ni/YSZ, (b) 10%Ni/SBA-15 and (c) 3%La-10%Ni/YSZ catalysts after 48hr on-stream longevity tests under the following CO_2 methanation conditions: Total feed flow = 135 mL min^{-1}, N_2:H_2:CO_2 ratio = 4:4:1, pressure = 1 bar, temperature = 643 K, GHSV 13,500 mL h^{-1} g^{-1}_{cat}. 171

Figure A.1 Pictorial view of the synthesis stages for SBA-15 (a) dissolution of P123, (b) introduction of TEOS into the dissolved P123, (c) washing and filtration and (d) Teflon-lined autoclave for hydrothermal treatment of as-synthesised SBA-15. 233

Figure A.2 Pictorial view showing the effect of washing the as-synthesised SBA-15 before calcination (a) calcined washed SBA-15 and (d) calcined unwashed SBA-15.....233

Figure B.1 XRD pattern of reduced Ni-based catalyst showing the FWHM as obtained from OriginPro software. 235

Figure C.1 Profile of (a) CO2 signals for each mass of carbon black burnt, and (b) calibration curve showing the relationship between the mass of carbon and the total area under the curve of the CO2 signals during TPO.....237

Figure D.1 Arrhenius plot demonstrating the relationship between activation energy and the slope.....240

List of Tables

Table 1.1 Proposed reaction steps over the catalyst's surface during CO_2 methanation through the CO intermediate route (Weatherbee and Bartholomew, 1982). 12

Table 1.2 Proposed reaction steps over the catalyst's surface during CO_2 methanation via the formation of CH_xO_y complex or complexes (Bian et al., 2018). 13

Table 1.3 Proposed reaction steps over Ru/TiO_2 catalyst during CO_2 methanation via the RWGS + CO hydrogenation pathway with their activation energy barriers (Ea) and reaction energies (ΔE) (Yang et al., 2020). 14

Table 2.1 Summary of various of Ru catalysts for CO_2 methanation. 23

Table 2.2 Literature showing the application of Rh-based catalysts for CO_2 methanation. 28

Table 2.3 Recent studies on the catalytic activities of Pd catalysts for CO_2 methanation. 31

Table 2.4 Application of ceria as catalyst support in CO_2 methanation conducted under atmospheric pressure. 52

Table 2.5 Crystal data of stable and metastable aluminas. Adapted from ref (Shackelford and Doremus, 2008; Busca, 2019). 56

Table 2.6 Physical properties of the most common transitional aluminas at different calcination temperatures. Adapted from ref Bartholomew & Farrauto (2011). 56

Table 2.7 The possible forms of carbon deposits by decomposition of CO on nickel (Bartholomew, 2001). 65

Table 3.1 List of equipment used for catalyst preparation. 76

Table 3.2 List of main materials used for sample preparation and testing. 78

Table 4.1 Physicochemical properties of the YSZ support and the calcined Ni/YSZ catalysts before reduction in H_2. 98

Table 4.2 Physicochemical properties of the YSZ support, 10%Ni/YSZ and La-promoted Ni/YSZ catalysts before reduction in H_2. 99

Table 4.3 Textural properties of SBA-15, CeO_2, Al_2O_3 and YSZ supports and their Ni-based catalysts before reduction in H_2. 102

Table 4.4 Crystallite size of Ni and NiO in both fresh and reduced Ni/YSZ catalysts. Estimation from Scherrer equation with the (2 0 0) reflection for NiO phase in the unreduced Ni/YSZ catalysts and (1 1 1) for Ni phase in the reduced Ni/YSZ catalysts in the XRD data. 105

Table 4.5 Crystallite size of Ni and NiO in both fresh and reduced 10%Ni/YSZ and La-promoted Ni/YSZ catalysts. Estimation from Scherrer Equation with the (2 0 0) reflection for NiO phase in the unreduced Ni/YSZ catalysts and (1 1 1) for Ni phase in the reduced Ni/YSZ catalysts in the XRD data 107

Table 4.6 Crystallite size of Ni and NiO in both fresh and reduced 10%Ni/YSZ, 10%Ni/Al_2O_3, 10%Ni/SBA-15 and 10%Ni/CeO_2 catalysts.....110

Table 4.7 Reduction peak temperatures during the H2-TPR of calcined Ni/YSZ catalysts. 115

Table 5.1 Parameters for the estimation of transport limitations. 127

Table 6.1 Range of activation energies for CO_2 conversion during methanation over different catalysts reported in the literature. 139

Table 7.1 Crystallite size of Ni in the reduced catalysts before (d_{Ni}) and after (d_{Ni}^*) CO_2 methanation reaction. 165

Table 7.2 Estimated weight gain/loss percent for the Ni^0 and carbon oxidation zones during the TPO of catalysts used in a 48 h on-stream longevity test for CO_2 methanation at 643 K.....170

Table 7.3 Total mass of carbon deposited during a 48 h on-stream longevity test for CO_2 methanation at 643 K estimated from TPO of the spent catalysts in a mass spectrometer. 172

Table 7.4 Results of carbon balance and carbon deposition rates obtained from the GC data during a 48 h on-stream longevity test for CO_2 methanation at 643 K.....173

Table E. 1 Composition of feed gas and their molecular weights. 244

Table E. 2 Vapor viscosity of the components of the feed gas (kg m^{-1} s^{-1}). Adapted from ref (Perry and Green, 2008).....245

List of Definition/ Nomenclature

Roman symbols

A_t	Area of the tubular reactor **(**m^2**)**
B_{iw}	Biot number of the tube wall (-)
d_t	Reactor's tubular diameter (m)
d_p	Average particle diameter (m)
C_{Ab}	Concentration of reactant A (CO_2) in the bulk gas phase (mol m^{-3})
C_{AS}	Concentration of reactant A (CO_2) at the catalyst external surface (mol m^{-3})
C_p	Specific heat capacity for each component gas (J kg^{-1} K^{-1})
C_{pg}	Specific heat capacity of feed gas mixture at constant pressure (J kg^{-1} K^{-1})
D_g	Diffusivity of CO_2 in the gas mixture (m^2 s^{-1})
D_{eff}	Effective diffusivity of CO_2 in a mixture N_2 and H_2 (m^2 s^{-1})
E_A	Activation energy for CO_2 conversion (J mol^{-1})
h	heat transfer coefficient (W m^{-2} K^{-1} *or* J m^{-2} s^{-1} K^{-1})
h_w	heat transfer coefficient of reactor tube wall (W m^{-2} K^{-1} *or* J m^{-2} s^{-1} K^{-1})
ΔH_r	Heat of reaction (J mol^{-1})
j_D	Colburn's J-factor for mass transfer (-)
k_c	Mass transfer coefficient (m s^{-1})
M_g	Molar mass of gas mixture (kg mol^{-1})
y_i	Mole fraction of component *i* in a gas mixture (-)
P	Pressure (Pa or atm)
R	Gas constant (m^3 Pa K^{-1} mol^{-1})
Re	Reynold number (-)
R_p	Catalyst pellet radius (m)
$-r_{exp}$	Reaction rate (mol kg_{cat}^{-1} s^{-1})
Pr	Prandtl number (-)
S_c	Schmidt number (-)
S	Sutherland constant (K)
T	Reaction temperature (K or °C)
T_1	Reference temperature (K or °C)
T_2	Set temperature (K or °C)
T_w	Reactor's wall temperature (K)
t	Time (sec)
U	Superficial gas velocity (m s^{-1})

Greek symbols

ρ_b	Catalyst bulk density (kg m^{-3})
ρ_g	Density of the gas mixture (kg m^{-3})
μ_g	Viscosity of the gas mixture (kg m^{-1} s^{-1})
$\dot{v}$	Volumetric gas flow rate (m^3 s^{-1})
ε	Pellet porosity (-)
λ_p	Thermal conductivity of the catalyst pellet (W m^{-1} K^{-1} or J s^{-1} m^{-1} K^{-1})
λ_g	Thermal conductivity of the gas mixture (W m^{-1} K^{-1} or J s^{-1} m^{-1} K^{-1})
τ	Tortuosity parameter (-)

Abbreviations

BET	Brunauer-Emmett-Teller
CCS	CO_2 capture and storage
CCU	CO_2 capture and utilisation
DRM	Dry reforming of methane
EPA	Environmental Protection Agency
FESEM	Field-emission scanning electron microscope
FWHM	Full width at half maximum
FTS	Fischer-Tropsch synthesis
GHG	Greenhouse gas
GHSV	Gas hourly space velocity
Gt	Gigatonne (1 Gt = 1 billion tonnes)
I.D.	Inner diameter
MDR	Methane dry reforming
OSC	Oxygen storage capacity
ppm	Parts per million
RWGS	Reverse water–gas shift
SEM	Scanning electron microscopy
SNG	Synthetic natural gas
TEM	Transmission electron microscopy
TGA	Thermogravimetric analysis
TPC	Temperature-programmed calcination
TPD	Temperature-programmed desorption
TPO	Temperature-programmed oxidation
TPR	Temperature-programmed reduction
XRD	X-ray diffraction

List of Publications and Conferences

List of publications

1. **Omoregbe O.**, Majewski A.J., Steinberger-Wilckens R., El-kharouf A. (2023). Investigating the effect of Ni loading on the performance of yttria-stabilised zirconia supported Ni catalyst during CO_2 methanation. J. Methane 2(1) 86-102.
2. **Omoregbe O.**, Abarasi H. (2022). Global Trends in Heavy Oil and Bitumen Recovery and In-situ Upgrading: A Bibliometric Analysis during 1900 to 2020 and Future Outlook. J. Energy Resour. Technol. 144(12), 123007.
3. Aimiuwu G., Osagie E., **Omoregbe O.** (2022). Process simulation for the production of methanol via CO_2 reforming of methane route. J. Chemical Product and Process Modelling 17(1) 69-79.
4. **Omoregbe O.**, Mustapha N.A., Steinberger-Wilckens R., El-Kharouf A., Onyeaka H. (2020). Carbon capture technologies for climate change mitigation: A bibliometric analysis of the scientific discourse during 1998–2018. Energy Report, 6, 1200-1212.

List of conferences

1. CO_2 Methanation over a Ni/YSZ catalyst: Impact of altering the catalyst bed ratio in two reactors in series (Poster presentation). 243rd ECS Meeting with the 18th International Symposium on Solid Oxide Fuel Cells (SOFC-XVIII), May 28 – June 2, 2023, Boston, MA, U.S.A.
2. The influence of reactor configuration on the performance of yttria-stabilized zirconia-Ni catalyst during CO_2 hydrogenation (Poster presentation). Catalysis Fundamentals and Practice Summer School, July 18 – 22 2022 University of Liverpool, U.K.
3. CO_2 methanation over Ni/YSZ catalysts: Effect of La-promoter (Poster presentation). 15th European SOFC & SOE Forum (EFCF 2022), July 6 – 7, 2022, Lucerne, Switzerland.
4. The impacts of collaborations in the development of solid oxide fuel cell technologies from 2000 to 2019: A bibliometric analysis (Poster presentation). 14th European SOFC & SOE Forum (EFCF 2020), September 20 – 23, 2020, Lucerne, Switzerland.

CHAPTER 1

Introduction

1.1 Background

The acceleration in population and economic growth is responsible for the rising energy demand which is a major climate change driver (Shah et al., 2023). Among the various sources of energy, fossil fuels account for the majority of the global energy consumption owing to their availability and low market cost (Barreto, 2018). In 2022, energy from fossil fuels constituted about 82% of the global energy supply (Energy Institute, 2023; Ambrose, 2023). This high consumption of fossil fuels for energy generation comes with its own challenges, amongst which the emission of CO_2 is a major one.

Since the industrial revolution, energy generation via the combustion of fossil fuels has resulted in a rapid rise in the amount of annual net CO_2 emissions from near zero to approximately 36.8 $GtCO_2$ in 2022 (see Figure 1.1). The amount of CO_2 in the atmosphere has continued to increase with a record of about 402.3 ppm on global average in 2016 (Edenhofer et al. 2015), 405.5 ± 0.1 ppm in 2017 (World Meteorological Organization WMO, 2018) and about 417.06 ppm in 2022 (Lindsey, 2023). The high concentration of atmospheric greenhouse gas (GHG) is evident in the rising global temperature which is already causing severe environmental stress such as an increase in global average sea level, occurrence of severe storms, alterations in rainfall patterns resulting in droughts and floods which affect food production, as well as higher incidences of heat waves, human disease and mortality (IPCC, 2023).

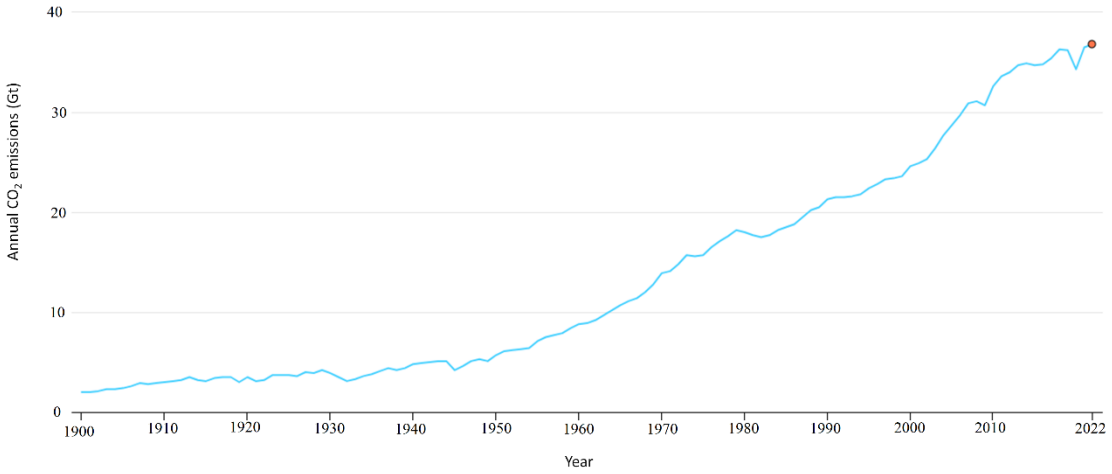


Figure 1.1 Annual global CO_2 emissions from energy combustion and industrial processes from 1900-2022. Adapted from ref (IEA, 2023).

According to a special report released by the Intergovernmental Panel on Climate Change (IPCC) in 2018, if the rise in CO_2 concentration is allowed to continue, it will result in an increase in the global average temperature exceeding 1.5℃ (see Figure 1.2) (Masson-Delmotte et al., 2018). As of 2022, the global average land and ocean surface temperature had surpassed the 20th-century average by 0.86℃ and by 1.06℃ above the pre-industrial period (1880-1900) (Lindsey, 2023; NOAA, 2023). In July 2023, the global average surface temperature rose above 17 ˚C marking it as the highest temperature recorded since 2016 (Hausfather, 2023). This prompted the UN chief to declare that 'the era of global boiling has arrived' (UN News, 2023).

If this is allowed to happen, we should expect even worse environmental stress and irreversible impacts on human and other lives. Therefore, swift action is imperative to restrict the global temperature increase to 1.5℃. In the 2023 IPCC report, it is recommended that global carbon emissions would need to be halved by 2030 and reach net zero by 2050 to ensure that the global temperature is kept within the 1.5℃ target (IPCC, 2023). There have also been various agreements on climate change mitigation in the past. The most famous among these treaties are the 1997 Kyoto Protocol (Breidenich et al., 1998) and the 2015 Paris climate agreement (Horowitz, 2016). In the Kyoto treaty, 37 industrialised nations committed to drastically reducing their emissions of GHGs by an average of 5 % below the 1990 levels over a period of five years (2008 to 2012).

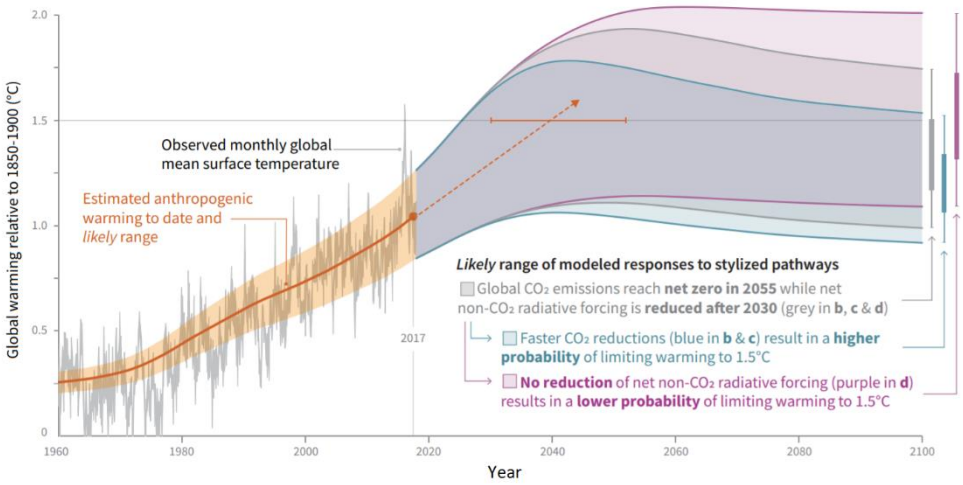


Figure 1.2 Cumulative emissions of CO_2 and future non-CO_2 radiative forcing in determining the probability of limiting warming to 1.5℃ (Masson-Delmotte et al., 2018).

In line with this commitment of 5 % average reduction of GHG emissions, different countries had set their targets. A target of 8 % cut below 1990 levels was set by the 15 countries in the European Union at the time, together with some eastern European countries and Switzerland. A 7% reduction was set by the United States and 6 % cut by Japan, along with Canada, Hungary, and Poland. This Kyoto agreement did not mandate emerging economies such as China and India to set targets because the basis of the agreement was that most of the global greenhouse gas emissions since the 1800s stemmed from the developed countries. Consequently, some countries like the United States who feel the deal is unfair in exempting the emerging economies, have been having wavering commitment towards the deal. This lack of total commitment by some of these developed countries was a major setback to the Kyoto Protocol.

Notwithstanding, there has been increasing attention towards the use of alternative energy such as solar energy, wind energy, and bioenergy to curb GHGs emissions. However, various challenges including the issue of storage of excess energy generated have been some of the factors preventing the use of alternative energy sources such as solar and wind energy from reaching their full potential (Karakoyun et al., 2023; Jlidi et al., 2023). Considering the wide availability, high energy density, ease of use and storage, existing infrastructure, and most importantly, low cost of fossil fuels, it might take some years for a complete shift from the use of fossil fuels to alternative energy sources to be achieved. Thus, the reduction of CO_2 emissions from the combustion of fossil fuels has been a subject of research over the past decades.

Accordingly, research has focussed on CO_2 capture and storage (CCS) (Raza et al., 2019; Jung et al., 2019; Zhang et al., 2023) and CO_2 capture and utilisation (CCU) (Mebrahtu et al., 2019; Jang et al., 2019; Lv et al., 2023) as options for mitigation of climate change. For economic reasons, the conversion of CO_2 into synthetic fuel appears to be one of the most promising approaches to climate change mitigation in comparison with its utilisation for other chemicals. This is because the amount of CO_2 emitted annually from energy combustion and industrial processes has been consistently above 30 Gt since 2010 compare to about 0.5 Gt/yr CO_2 required by the chemical industries that utilise CO_2 for the production of the top 100 chemicals globally (Kocs, 2017; IEA, 2023). Thus, this work will focus on the recycling of carbon through the conversion of CO_2 to synthetic natural gas (SNG) by a hydrogenation reaction.

The production of SNG by the hydrogenation of CO or CO_2 (see Eqs. **(**1.1) and **(**1.2)) was first reported by Paul Sabatier in 1902 (Sabatier and Senderens, 1902). This reaction is known as CO or CO_2 methanation or Sabatier reaction. Meanwhile Beuls et al. (2012) reported that the major difference between the mechanism of CO and CO_2 methanation reactions is in the dissociation step of CO_2.

$$CO + 3H_2 \rightleftharpoons CH_4 + H_2O \qquad \Delta H_{298K} = -206 kJmol^{-1} \tag{1.1}$$

$$CO_2 + 4H_2 \rightleftharpoons CH_4 + 2H_2O \qquad \Delta H_{298K} = -164 kJmol^{-1} \tag{1.2}$$

Considering the fluctuating nature of renewable energy, the Sabatier process is recognised as a feasible way of storing the excess energy generated from renewable sources. In this case, excess energy may be used to power an electrolyser to produce hydrogen required in the methanation reaction (see Figure 1.3). CO_2 can be captured from various industrial processes including oil refineries, power plants, biogas facilities, biomass combustion and gasification, and cement kilns. Methanation technology is a form of power-to-gas technology employed in overcoming the mismatch between energy generation and immediate demand (Lindorfer et al., 2019; Tichler and Bauer, 2016; Thema et al., 2019). Moreover, this reaction is a practical way of utilising hydrogen

produced from renewable sources as an energy vector, and therefore overcoming the challenge of transportation resulting from its low volumetric energy density and the challenge of suitable, modifiable, and well controlled storage systems (Abdalla et al., 2018).

Lastly, investment in SNG is economically viable because its global market is expected to grow as the demand for energy increases. In this regard, the Business Research Company projected the global methane market size to grow from $97.06 billion in 2022 to $152.33 billion in 2027 at a compound annual growth rate (CAGR) of 9.3% while the Market Research Future has estimated the methane market to grow to $153.2 billion in 2032 at CAGR of 6.1% using forecast period of 2023-2032 (The Business Research Company, 2023; Market Research Future, 2023).

However, the estimated market size of SNG from these reports includes all the sources of methane. To estimate the potential market size for methane produced specifically through CO_2 methanation, it is important to consider factors such as the efficiency of the carbon capture and methanation processes, the cost of capture and conversion into methane, and the price of the methane produced through methanation in the market. Therefore, a more detailed analysis is required to determine the market size of methane produced from captured carbon.

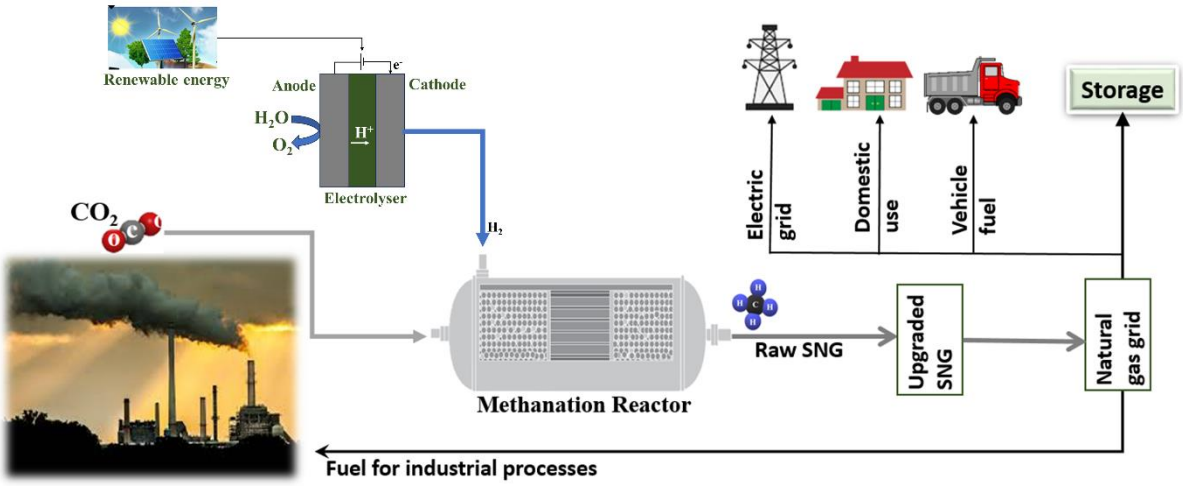


Figure 1.3 The capture and utilisation of CO_2 for SNG production via the methanation reaction.

Notwithstanding the promising potential of CO_2 methanation as a tool for climate change mitigation, certain drawbacks such as heat management and catalyst deactivation are

associated with the process. Although CO_x (CO or CO_2) methanation is thermodynamically favoured at low temperatures (Beuls et al., 2012), the temperature in the reactor is likely to increase above the starting temperature since the reaction is highly exothermic (see Eqs. **(**1.1) and **(**1.2)). Consequently, reactor overheating can lead to hot spot formation causing catalyst deactivation through agglomeration and carbon deposition (Gao et al., 2015). Interestingly, the heat released in the exothermic CO_2 methanation reaction can provide the energy required for the adsorbed CO_2 on a dispersed adsorbent to spillover to the catalyst active sites where they are further converted (Duyar et al., 2015b). Therefore, appropriate heat management is essential in the methanation system for effective utilisation/removal of the heat and to prevent or minimise catalyst deactivation and sintering. It is also important to develop thermally stable catalysts with high activity and exceptional resistance to carbon deposition and sintering at the CO_x methanation reaction conditions.

1.2 Overview of CO_2 capture technologies

Carbon capture and utilisation are being investigated to simultaneously combat climate change while producing sustainable, synthetic fuels, therefore triggering renewed interest in these technologies. To synthesise methane as a low or re-used carbon fuel, which is the core topic of this thesis, carbon needs to be introduced to the reactions and, also, be captured from fossil or renewable sources. The commonly considered carbon capture technologies (CCT) are pre-combustion, post-combustion, and oxy-fuel combustion.

1.2.1 Pre-combustion carbon capture technology

This involves the capture of carbon from the fuel before combustion is completed. Basically, the fuel undergoes a pre-treatment stage, such as biomass and coal gasification and steam reforming of natural gas before the actual combustion stage. Syngas (the mixture of H_2 and CO) is formed during this pretreatment stage. Thereafter, CO in the syngas is reacted with steam via the water gas shift (WGS) reaction to produce additional H_2 and CO_2. The latter can then easily be separated out and processed (Sheikh et al., 2018). After the elimination of the CO_2 component, the H_2 gas can be employed as a gaseous fuel in fuel cells, engines, gas turbines or gas turbine combined-cycle plants

(Olajire, 2010). This technology can also be used in Integrated Gasification Combined Cycle (IGCC) power plants with biomass or coal as fuel (Leung et al., 2014). Nevertheless, the WGS reaction and the pre-combustion capture systems imply efficiency penalties (Gibbins & Chalmers, 2008). Moreover, H_2-combustion engines and gas turbines have lower efficiencies compared to natural gas turbines owing to the lower viscosity of H_2 gas and the increased blow-by (Gibbins & Chalmers, 2008).

1.2.2 post-combustion carbon capture technology

In this type of CCT, the carbonaceous fuel first undergoes combustion before CO_2 in the flue gas is separated out. The flue gas needs to be pre-treated to ensure that impurities including particulates, sulphur dioxide, nitrogen oxides, and corrosive substances (Cl, F etc.) are removed. Since the temperature of flue gas from the combustion units is likely to be high (in the range of 120 to 180 °C) (Spigarelli and Kawatra, 2013), energy-intensive cooling systems are required before pre-treatment. Likewise, large equipment sizes are required due to the high volume of flue gases and the low partial pressure of CO_2 (between 3 and 20%, depending on the type of combustion and fuel). Both aspects considerably increase the cost of capture (Jiang et al., 2019; Leung et al., 2014; Spigarelli and Kawatra, 2013).

1.2.3 Oxy-fuel combustion technology

This involves the combustion of carbonaceous fuel in a stream of pure oxygen instead of air. Since the oxidant (O_2) is free of major air components such as nitrogen, the CO_2 concentration in the flue gas will be very high, whilst the water vapour content can be easily removed (Stanger et al., 2015). Therefore, separation/capture is far simpler. However, impurities such as sulphur oxide, nitrous oxides, and particulates will be present and pretreatment is again required before CO_2 processing (Gibbins & Chalmers, 2008). Additionally, the high cost of supplying oxygen for oxy-fuel combustion may be a limiting factor in commercialisation. Other challenges associated with oxy-fuel combustion, such as high temperatures of combustion, have been extensively discussed in the literature (Zheng et al., 2015a; Seddighi et al., 2018; Jordal et al., 2005).

Following this brief overview of the three types of CCT, it is clear that none of the systems is without challenges. Sanders et al. (2013) identified technological, market and political risk as the major barrier towards assessing private funds for carbon capture and storage research from investors. Recent studies have suggested that the availability of economical and affordable facilities is crucial for the advancement of CCS technology on a large scale. The second factor pointed out which is in agreement with the findings in a different study (Durmaz, 2018) was the creation and implementation of regulatory and policy framework to ensure financial stability which will help in building investors' confidence in participating in CCS projects. Interest in carbon capture and storage during a transition phase to a decarbonised energy supply system will continue to increase until fossil fuels can be fully substituted by renewable energy sources.

1.3 Overview of CO_2 Methanation Reaction

The methanation of CO_2 involves the reaction between CO_2 and H_2 over a suitable catalyst to produce synthetic methane also called synthetic natural gas (SNG). CO_2 methanation is considered to be a green process because the H_2 required in the system can be obtained from the electrolysis of water powered by renewable sources such as solar energy, and the CO_2 can be captured from various industrial operations including fossil fuels, biogas and biomass combustion/gasification in power plants, oil refineries, and cement kilns (Frontera et al., 2017). CO_2 methanation can be categorised under the power-to-gas processes since SNG (gas) is produced by utilising excess energy from renewable sources and/or the national electric grid in powering both the electrolyser and the methanation reactor. As an energy carrier, the inherent advantages of SNG such as easy handling and storage compared with pure H_2 make methanation of CO_2 a promising process (Mota and Kim, 2019). Moreover, SNG can seamlessly be transported through the existing natural gas pipelines (Aziz et al., 2015).

1.3.1 Thermodynamic Considerations of CO_2 methanation

CO_2 methanation is a highly exothermic reaction which is thermodynamically feasible at low temperatures. Applying the Le Châtelier's Principle, CO_2 methanation can occur at high pressures and low temperatures (Chang, 2008). However, the reaction is slow at low

temperatures since the reactants lack sufficient energy for chemical reaction to take place, and this makes CO_2 methanation kinetically unfavourable at low temperatures. Although an increase in temperature will result in increased rates of reaction, the problem with this is that a rise in the reaction temperature beyond the optimum point will result in declining SNG production. Moreover, the exothermic nature of the CO_2 methanation reaction and the likelihood of hot-spot formation makes it difficult to control the heat in the reactor. Razzaq et al. (2013) reported that instead of the yield of SNG increasing, CO formation via reverse water-gas shift (RWGS) reaction was favoured at temperatures above 673 K. Similarly, Panagiotopoulou et al. (2009) observed that at reaction temperatures greater than 633 K, the formation rate of CO through RWGS was greater than the rate at which CO was consumed in the methanation reaction which led to the decrease in CO conversion. Figure 1.4**Error! Reference source not found.** represents one of the results of an extensive investigation of the thermodynamics of methanation reactions carried out by Gao et al. (2015). As seen, the primary products in the CO_2 methanation at low temperatures (473-523 K) are CH_4 and H_2O. An increase in the reaction temperature above 723 K led to a decrease in CH_4 yield whilst side reactions such as RWGS were favoured alongside the increase in unreacted CO_2 and H_2.

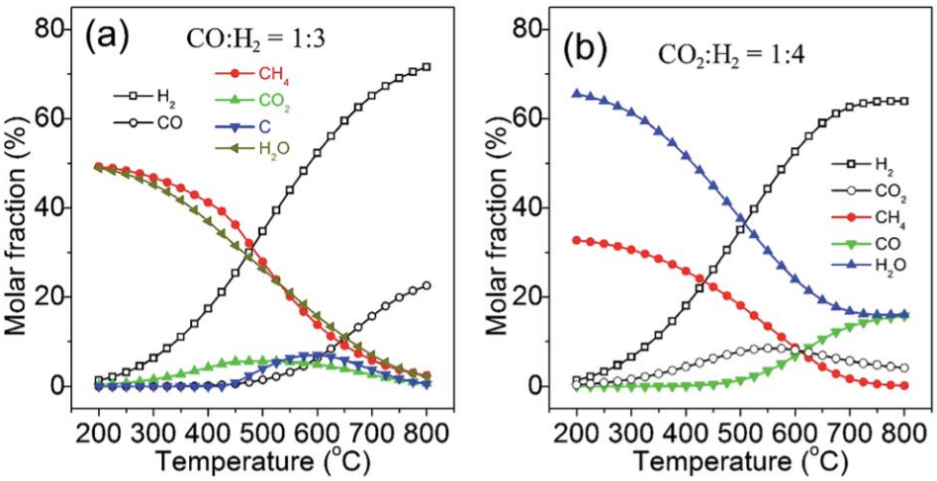


Figure 1.4 Product compositions for CO (a) and CO_2 (b) methanation at equilibrium (0.1 MPa). Adapted from ref (Gao et al., 2015).

1.3.2 Reactor consideration

Considering the exothermic nature of the CO_2 methanation reaction, one major challenge is how to efficiently manage the heat in the system to ensure optimum yield of CH_4.

Moreover, the overheating of a reactor can result in a rapid catalyst deactivation through sintering and excess carbon deposition. Therefore, a good reactor design and configuration are crucial for an efficient methanation process. The two commonly employed reactors for CO_2 methanation are the fixed-bed (Kiewidt and Thöming, 2015; Willauer et al., 2013) and fluidised bed (Nam et al., 2021; Martin-del-Campo and Kopyscinski, 2020) reactors, while a detailed study on the identification of flow behaviours and reaction kinetics along the reactor length in both reactors can be found in (Ngo et al., 2020).

A fixed bed catalytic reactors are usually tubular in form with packed catalyst pellets that enhances the reaction between reactants passing through the bed to form the products. Fixed bed reactors can be classified based on energy exchange as either adiabatic or non-adiabatic (Worstell, 2014). The common configurations for fixed bed reactors are the single large bed, and the multi-tubular fixed bed reactors. The multi-tubular configuration can be multiple beds in their own shells, many packed tubes in parallel or several horizontal beds.

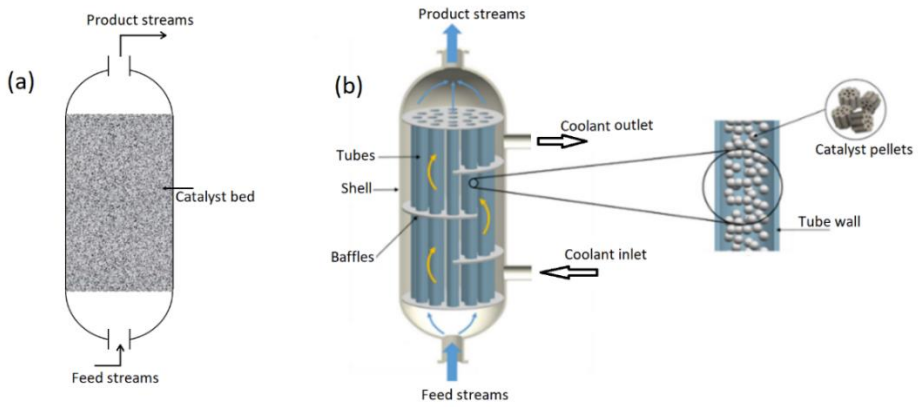


Figure 1.5 Fixed-bed reactor configuration (a) single tubular reactor (b) multi-tubular reactor configuration. Figure 2.2 (b) was adapted and modified from (Zhu et al., 2020).

The heat management efficiency of the multi-tubular reactors can be enhanced by employing tubes with smaller diameters since this will help to increase the heat transfer area per volume of catalyst. In addition, the linear flowrate of the feed streams will be enhanced and gives an excellent well-mixed conditions that increase the heat transport rate (Onsan and Avci, 2016). The higher flowrates can also be a challenge since they encourage the loss of mechanical energy of the reacting species due to frictional loss, causing a pressure drop, and thus requiring more compression and incurring additional

costs. Therefore, extensive work is still ongoing on the modifications of fixed-bed reactors for effective performance. One suggestion on compensating the difference between the effect of heat transfer rates and pressure drop is to employ catalyst pellets with varying size, shape, and material types (Eigenberger et al., 2008). Fixed bed reactors in both cross-flow and parallel form can achieve isothermal states by obtaining adequate heat transfer in a moderately endothermic or exothermic reactions (Eigenberger et al., 2008). Studies have also linked the overall efficiency and performance of the reactor with the catalyst structure.

While fixed bed reactors are generally employed in reforming and methanation reactions, the use of fluidised bed reactor is beginning to gain recognition due to its ability to achieve a highly uniform temperature in the reactor (Rönsch et al., 2016). Other forms of reactors that are gaining recognition include the honeycomb monolith reactors which are structured forms of fixed bed reactors (Huynh and Yu, 2020), microchannel reactors (Shen et al., 2021), flat bed reactors (Lopez et al., 2012), membrane reactors (Lu and Xie, 2016; Gallucci et al., 2006), and three-phase slurry reactors (Lefebvre et al., 2018; Eilers et al., 2016).

There have been a lot of discussion about which of the reactor configurations is best suited for CO_2 methanation. For example, Schlereth et al. (2015) compared the heat transfer efficiency of honeycomb monolith reactors with fixed-bed reactors through reactor modelling studies and found that the honeycomb monolith reactors have superior performance compared to other fixed-bed reactors at certain operating parameters for CO_2 methanation. Pérez et al. (2019) reported a modified fixed-bed reactor which is effective for Sabatier and other exothermic reactions. This reactor which is designed at Tecnalia R&I Spain is a multichannel minireactor with an internal diameter in the range of 1.75 to 2 mm is configured to adequately regulate the heat produced during the methanation reaction.

1.3.3 Mechanism of CO_2 methanation

The mechanism of CO_2 methanation still remains a subject of research since there is yet to be a generally acceptable consensus on the reaction routes from the reacting stage to the production of SNG. Furthermore, the main debate on the behaviour of the intermediate compounds in the rate determining steps and the SNG formation has been whether the CO_2 methanation follows a CO intermediate formation pathway or not. In

this regard, the nature of intermediates formed are mainly studied either for the sake of enhancing proper design of catalysts or the design of the process by an in situ investigations via different spectroscopic techniques together with computational modelling of the basic steps (Miao et al., 2016). Moreover, the operating conditions such as CO_2/H_2 ratio, temperature and pressure, and the nature of catalyst employed also affect the reaction pathways for the production of SNG during CO_2 methanation (Muroyama et al., 2016; Mota and Kim, 2019). Accordingly, there are three commonly proposed mechanisms, namely, the CO intermediate route which involves the formation and cleavage of a CO intermediate (Koschany et al., 2016; Ho and Harriott, 1980), the formate/formyl route which involves the formation of a CH_xO_y complex or complexes (formyl, formates, bicarbonate species, etc) (Mota & Kim, 2019; Solymosi, Erdöhelyi, & Kocsis, 1981; Wang et al., 2016), and the reverse water gas shift (RWGS) (Champon et al., 2019; Hernandez Lalinde et al., 2020) pathway for SNG production during CO_2 methanation.

Table 1.1 Proposed reaction steps over the catalyst's surface during CO_2 methanation through the CO intermediate route (Weatherbee and Bartholomew, 1982).

Reaction Type	Reaction Number
$CO_{2(g)} + 2 * \rightleftharpoons CO^* + O^*$	A-1
$CO^* \rightleftharpoons CO_{(g)} + *$	A-2
$H_2 + 2 * \rightleftharpoons 2H^* + *$	A-3
$CO^* + * \rightleftharpoons C^* + O^*$	A-4
$C^* + H^* \rightleftharpoons CH^* + *$	A-5
$O^* + H^* \rightleftharpoons OH^* + *$	A-6
$OH^* + H^* \rightleftharpoons H_2O^* + *$	A-7
$H_2O^* \rightleftharpoons H_2O_{(g)} + *$	A-8
$CH^* + H^* \rightleftharpoons CH_2{}^* + *$	A-9
$CH_2{}^* + H^* \rightleftharpoons CH_3{}^* + *$	A-10
$CH_3{}^* + H^* \rightleftharpoons CH_4{}^* + *$	A-11
$CH_4{}^* \rightleftharpoons CH_{4(g)} + *$	A-12

* Vacant site(s) while the attached asterisks, for instance, O^* and H^*, are adsorbed atoms.

For the CO intermediate route, Weatherbee & Bartholomew (1982) assumed that CO_2 and H_2 are dissociatively adsorbed on the catalyst's surface (see Table 1.1**Error! Reference source not found.**). The CO_2 dissociates into adsorbed carbon monoxide (CO_{ads}) and adsorbed oxygen (O_{ads}), and H_2 dissociates into adsorbed hydrogen atoms (H_{ads}). The CO_{ads} is further dissociated into surface carbon (C_{ads}) and O_{ads}. Other steps include the hydrogenation of C_{ads} into carbenes intermediates which are further hydrogenated into methane while O_{ads} is hydrogenated into water. For the formate pathway, Bian et al., 2018 reported that the formation of CH_4 via this route is influenced by the presence of oxygen vacancies on the catalyst surface or the active sites (see Table 1.2**Error! Reference source not found.**). This kind of mechanism (formate intermediate routes promoted by oxygen-vacancy) has also been reported in other studies (Mota and Kim, 2019; Ye et al., 2013).

Table 1.2 Proposed reaction steps over the catalyst's surface during CO_2 methanation via the formation of CH_xO_y complex or complexes (Bian et al., 2018).

Reaction Type	Reaction number
$H_2 + 2* \rightleftharpoons 2H^* + *$	B-1
$H^* + O^* \rightleftharpoons OH^* + *$	B-2
$CO_{2(g)} + O^* \rightleftharpoons OCO_2{}^*$	B-3
$OCO_2{}^* + OH^* \rightleftharpoons \mathrm{OCOOH}^* + O^*$	B-4
$\mathrm{OCOOH}^* + H_2 \rightleftharpoons \mathrm{OCOH}^* + H_2O$	B-5
$\mathrm{OCOH}^* + H_2 \rightleftharpoons \mathrm{OC}H_2\mathrm{OH}^*$	B-6
$\mathrm{OC}H_2\mathrm{OH}^* + H_2 \rightleftharpoons OCH_3^* + H_2O$	B-7
$OCH_3^* + H_2 \rightleftharpoons CH_4 + OH$	B-8
$OCO_2{}^* + H_2 \rightleftharpoons OCO^* + H_2O$	B-9
$\mathrm{OCOH}^* + OCO_2{}^* \rightleftharpoons \mathrm{OCO}^* + OCOOH^*$	B-10
$\mathrm{OCOH}^* + O^* \rightleftharpoons \mathrm{OCO}^* + OH^*$	B-11
$\mathrm{OCOOH}^* + \mathrm{OH}^* \rightleftharpoons OCO^* + H_2O$	B-12
$OCO^* \rightleftharpoons \mathrm{CO} + O^*$	B-13

* Vacant site(s) while the attached asterisks, for instance, O^* and H^*, are adsorbed atoms.

Yang et al., 2020 studied the reaction mechanism of CO_2 methanation over a Rh/TiO_2 catalyst and provided the activation energies and reaction energies of the various elementary reactions leading to the formation of CH_4 via the three proposed pathways: viz. direct C–O bond cleavage, formate, and RWGS + CO hydrogenation. The formation of CH_4 through the RWGS + CO hydrogenation route was proposed to occur through any of the intermediate pathways namely, HCO* formation pathway via the CH* intermediate, HCO* formation pathway via the H_2CO* intermediate or, COH* formation pathway via the H_2COH* intermediate (see Table 1.3). The RWGS + CO hydrogenation route through the COH* intermediate was reported to be a more thermodynamically and kinetically favourable pathway than the direct C–O bond cleavage and the formate routes for the formation of CH_4 during CO_2 methanation over $RuTiO_2$ catalyst owing to the lower activation energy barrier in the former compared to the latter pathways. It was also revealed that the metal-support interface is an important part of the catalyst since it contains bulk of electrons required for the activation and reduction of the adsorbed CO_2 leading to the formation of CH_4.

Table 1.3 Proposed reaction steps over Ru/TiO_2 catalyst during CO_2 methanation via the RWGS + CO hydrogenation pathway with their activation energy barriers (Ea) and reaction energies (ΔE) (Yang et al., 2020).

Reaction Type	E_a (kJ/mol)	ΔE ((kJ/mol)	Reaction number
$CO_2^* + H_2 \rightarrow CO_2^* + H_2^*$	-	-94.32	C-1
$CO_2^* + H_2^* \rightarrow COOH^* + H^*$	151.75	38.05	C-2
$COOH^* + H^* \rightarrow CO^* + H_2O^*$	228.90	29.82	C-3
$CO^* + H_2O^* \rightleftharpoons CO^* + H_2O \uparrow$	-	64.46	C-4
$CO^* + H_2 \rightleftharpoons CO^* + H_2^*$	-	-97.59	C-5

Table continues on next page

HCO* formation pathway via the CH* intermediate

$CO^* + H_2^* \rightarrow HCO^* + H^*$	110.43	-51.28	C-6
$HCO^* + H^* \rightarrow CH^* + OH^*$	210.01	54.83	C-7
$CH^* + OH^* + H_2 \rightarrow CH^* + OH^* + H_2^*$	-	-105.68	C-8
$CH^* + OH^* + H_2^* \rightarrow CH^* + H_2O^* + H^*$	172..3	100.04	C-9
$CH^* + H_2O^* + H^* \rightarrow CH^* + H^* + H_2O \uparrow$	-	24.79	C-10
$CH^* + H^* \rightarrow CH_2^*$	237.15	65.85	C-11
$CH_2^* + H_2 \rightarrow CH_2^* + H_2^*$	-	-140.39	C-12
$CH_2^* + H_2^* \rightarrow CH_3^* + H^*$	101.97	-77.99	C-13
$CH_3^* + H^* \rightarrow CH_4^*$	70.26	17.84	C-14

Table 1.3 Proposed reaction steps over Ru/TiO_2 catalyst during CO_2 methanation via the RWGS + CO hydrogenation pathway with their activation energy barriers (Ea) and reaction energies (ΔE) (Yang et al., 2020) (Continuation).

HCO* formation pathway via the H_2CO^* intermediate.

$HCO^* + H^* \rightarrow H^* + H_2CO^*$	36.06	-97.32	C-15
$H_2CO^* + H_2 \rightarrow H_2CO^* + H_2^*$	-	-100.62	C-16
$H_2CO^* + H_2^* \rightarrow H_3CO^* + H^*$	97.81	4.68	C-17
$H_3CO^* + H^* \rightarrow CH_3^* + OH^*$	368.32	173.77	C-18
$CH_3^* + OH^* + H_2 \rightarrow CH_3^* + OH^* + H_2^*$	-	-146.45	C-19
$CH_3^* + OH^* + H_2^* \rightarrow CH_3^* + H_2O^* + H^*$	51.21	22.58	C-20
$CH_3^* + H_2O^* + H^* \rightarrow CH_3^* + H^* + H_2O \uparrow$	-	64.81	C-21
$CH_3^* + H^* \rightarrow CH_4^*$	70.26	17.84	C-22

Table continues on next page

COH* formation pathway via the CH* intermediate			
$CO^* + H_2^* \rightarrow COH^* + H^*$	153.96	141.51	C-23
$COH^* + H^* \rightarrow HCOH^*$	196.62	-20.79	C-24
$HCOH^* \rightarrow CH^* + OH^*$	196.24	-45.02	C-25
$CH^* + OH^* + H_2 \rightarrow CH^* + OH^* + H_2^*$	-	-48.18	C-26
$CH^* + OH^* + H_2^* \rightarrow CH_2^* + H_2O^*$	243.43	7.46	C-27
$CH_2^* + H_2O^* \rightarrow CH_2^* + H_2O \uparrow$	-	53.57	C-28
$CH_2^* + H_2 \rightarrow CH_2^* + H_2^*$	-	-140.39	C-29
$CH_2^* + H_2^* \rightarrow CH_3^* + H^*$	101.97	-77.99	C-30
$CH_3^* + H^* \rightarrow CH_4^*$	70.26	17.84	C-31

Table 1.3 Proposed reaction steps over Ru/TiO_2 catalyst during CO_2 methanation via the RWGS + CO hydrogenation pathway with their activation energy barriers (Ea) and reaction energies (ΔE) (Yang et al., 2020) (Continued).

COH* formation pathway via the H_2COH^* intermediate			
$HCOH^* + H_2 \rightarrow HCOH^* + H_2^*$	-	-123.28	C-32
$HCOH^* + H_2^* \rightarrow H_2COH^* + H^*$	145.86	-47.08	C-33
$H_2COH^* + H^* \rightarrow CH_3^* + OH^*$	99.76	-21.13	C-34
$CH_3^* + OH^* + H_2 \rightarrow CH_3^* + OH^* + H_2^*$	-	-146.45	C-35
$CH_3^* + OH^* + H_2^* \rightarrow CH_3^* + H_2O^* + H^*$	51.21	22.58	C-36
$CH_3^* + H_2O^* + H^* \rightarrow CH_3^* + H^* + H_2O \uparrow$	-	64.81	C-37
$CH_3^* + H^* \rightarrow CH_4^*$	70.26	17.84	C-38

*Refers to vacant site(s) while the attached asterisks, for instance, O^* and H^*, are adsorbed atoms; $H_2O\uparrow$ is desorbed or released water from the catalytic sites.

It can be deduced that the different pathways described for the formation of CH_4 during CO_2 methanation are influenced by the nature of catalyst used. Therefore, the kinetic expressions which are determined by the rate-determining step(s) will also depend on the type of catalyst employed.

In this work, Al_2O_3, CeO_2, YSZ and SBA-15 supported Ni catalysts will be synthesised, characterised, and tested for their CO_2 methanation performance to determine the optimum catalyst. Thereafter, the effect of operating conditions, including Ni loading, temperature, and pressure is studied for the optimum catalyst. To the best of our knowledge, there is no reported work on the influence of reactor configuration with variation in catalyst ratio in CO_2 methanation, which is the main novelty of this research. The comparative study of Ni based yttria-stabilized zirconia (YSZ), alumina (Al_2O_3), ceria (CeO_2) and Santa Barbara Amorphous 15 (SBA-15) supported catalysts in CO_2 methanation will also be conducted. The above supports were chosen because of reports on their roles in high selectivity towards CO_2 methanation. The properties of these catalyst components that made them suitable for CO_2 methanation will be critically reviewed in the following section.

1.4 Aims and Objectives

This work is aimed at developing efficient methanation catalysts with high selectivity towards CH_4 production and determining the optimum conditions for maximum CH_4 yield during CO_2 methanation. In particular, the main objectives of this PhD work are:

1. to synthesise Ni/YSZ, Ni/CeO_2, Ni/Al_2O_3 and Ni/SBA-15 catalysts and characterise them using various characterisation techniques to examine their physicochemical properties. Thereafter, conduct a comparative study on the performance of the synthesised catalysts for the CO_2 methanation.

2. to investigate the influence of varying reaction conditions including temperature, H_2/CO_2 ratio, catalyst position in the reactor, CH_4 in feed, gas hourly space velocity (GHSV), pressure, and La-promoter on the yield and selectivity of the optimum catalyst.

3. to design and fabricate/modify a monolithic and a split reactor for CO_2 methanation: investigate the effect of the multiple reactor configurations—the single reactor with

one catalyst bed, the single reactor with dual catalyst beds, and two reactors in series. Then, examine the effect of the catalyst ratio distribution in the reactor sub-sections.

The rationale for the selection of the four supports is that their distinct physicochemical properties, which are extensively discussed in chapter two (Literature review), can affect the performance of their Ni-based catalysts in CO_2 methanation. For example, CeO_2 is a metal oxide support with a high oxygen storage capacity (Wang et al., 2015). This can be beneficial for CO_2 methanation, as it can help to maintain a high H_2/CO_2 ratio in the reaction zone. CeO_2 can also promote the formation of Ni/CeO_2 interfaces, which are active for CO_2 methanation. Al_2O_3 is a versatile support that is widely used in catalysis because it is relatively inexpensive and has good thermal stability. However, its moderate to high Lewis acidity can lead to the deactivation of the catalyst (Feng et al., 2014). YSZ is a ceramic support with high thermal stability and oxygen storage capacity material (Hofer et al., 2019; Cousland et al., 2014). This makes it a good candidate for CO_2 methanation, which is a high-temperature process. YSZ can also help to disperse the Ni catalyst nanoparticles, which can improve the catalytic activity. SBA-15 is a mesoporous silica support with a high surface area and pore volume which encourages the distribution and dispersion of active metals (Lin et al., 2023). This makes it a good candidate for CO_2 methanation, as it can provide many active sites for the reaction. SBA-15 is also relatively inert, which can help to reduce the deactivation of the Ni catalyst.

In particular, the performance of the Ni catalysts of these selected supports will be investigated in connection with their distinctive pore structure and surface area which can influence the dispersion of the active metal particles, the degree of reduction in hydrogen and the thermal stability properties.

For the reactor configuration, the CO_2 methanation process would be conducted in continuous fixed-bed reactors in a 'hybrid' mode, namely, the monolithic reactor containing a single catalyst bed, a split reactor containing two catalyst beds and two reactors in series. The monolithic reactor. While the monolith reactors would be employed in the investigation of most of the experiments including the influence of the supports, and the effect of reaction parameters such as temperature, pressure, and gas hourly space velocity on the performance of the catalyst, the split and the multiple reactors would be used to investigate the effect of water interference and catalyst ratio distribution on the optimisation of the overall performance of the process.

CHAPTER 2

Literature Review

2.1 Development of CO_2 methanation catalysts

The synthesis of suitable catalysts with high selectivity towards SNG production via CO_2 methanation has been a subject of research over the past three decades owing to their significance in ensuring maximum SNG production. Although CO_2 methanation is thermodynamically feasible, the yield of SNG from the process is not economical without the use of a catalyst.

Catalysis is the science of altering the rates or pathways of chemical reactions by the introduction of a functional material known as a catalyst (Robertson and Thnard, 1975). Jöns Jakob Berzelius was the first researcher to suggest the term catalysis where he defined it as "the property of exerting on other bodies an action which is very different from chemical affinity. By this action, they produce decomposition in bodies, and form new compounds into the composition of which they do not enter" (Berzelius, 1835). In recent times, the advent and rapid growth in the production of various chemicals can be attributed to the birth of this concept. The various methods of catalyst preparation have been described extensively in the literature (Perego and Villa, 1997; Schwarz et al., 1995; Deraz, 2018b, 2018a). Although there are two main categories of catalysts, viz., homogeneous, and heterogeneous catalysts, only the latter will be discussed in this study.

Heterogeneous catalysts are a diverse group of catalysts, typically composed of two main components: active metal particles and (sometimes) a support surface. While not all heterogeneous catalysts require support surfaces, supported catalysts, comprising both active metal and support, represent a prevalent category within heterogeneous catalysis. Heterogeneous catalysts can also be defined as functional materials that are introduced into a system to alter the rate of a chemical reaction by continually creating active sites

for the reactants while the thermodynamic equilibrium between the materials remain unchanged at the end of the reaction (Schlögl, 2015). Among other factors, the nature of the active metal and support, the synthesis method, and the operating conditions for the reaction can influence the activity of a heterogeneous catalyst.

2.3.1 Active Metal Component for CO_2 methanation Catalysts

Over the past decade, several metals have been employed in heterogeneous catalysts for SNG production via the methanation reaction, among which most of the metals in group VIII of the periodic table have been reported to catalyse the reaction (Solis-Garcia and Fierro-Gonzalez, 2019; Sreedhar et al., 2019; Kirchner et al., 2020). These active metals are classified into noble metals and earth-abundant transition metals. The common noble metals used in methanation catalysts are iridium (Ir), osmium (Os), palladium (Pd), platinum (Pt), ruthenium (Ru), and rhodium (Rh), while nickel (Ni), iron (Fe), cobalt (Co) and copper (Cu) are the most used earth-abundant transition metals. The noble metals are generally more active and stable as catalysts than the non-noble metals. However, they are not readily available and are expensive. Therefore, the subsequent subsections are reviews of how some of these noble metals and non-noble metals have been employed for the development of methanation catalysts.

2.3.2 Noble Metal

2.3.2.1 Ruthenium

Ru is the most used noble metal for methanation catalysts owing to its high activity, high CH_4 selectivity, and high resistance to oxidising atmospheres (Ghaib et al., 2016). However, the catalytic activity and selectivity of Ru towards CH_4 strongly depend on the metal dispersion, which is influenced by factors such as the type of support employed and the incorporation of promoters (Frontera et al., 2017). Ru metal catalysts have been designed using various types of supports including Al_2O_3, SiO_2, CeO_2, TiO_2 and ZrO_2. Rynkowski et al. (2000) conducted a study on the influence of mixing supports on the activity of Ru catalysts. In their investigation, CeO_2 and Al_2O_3 supports were mixed to

support the active phase of Ru for CO_2 methanation. Results showed that not only does the mixed supported catalyst exhibits the best performance but also influenced the reaction temperature required to attain maximum CO_2 conversion. The maximum CO_2 conversions obtained are 72%, 74.5% and 76% for the Al_2O_3, CeO_2 and CeO_2-Al_2O_3 supported Ru catalysts, respectively, and the temperatures at which these were obtained are shown in Figure 2.1.

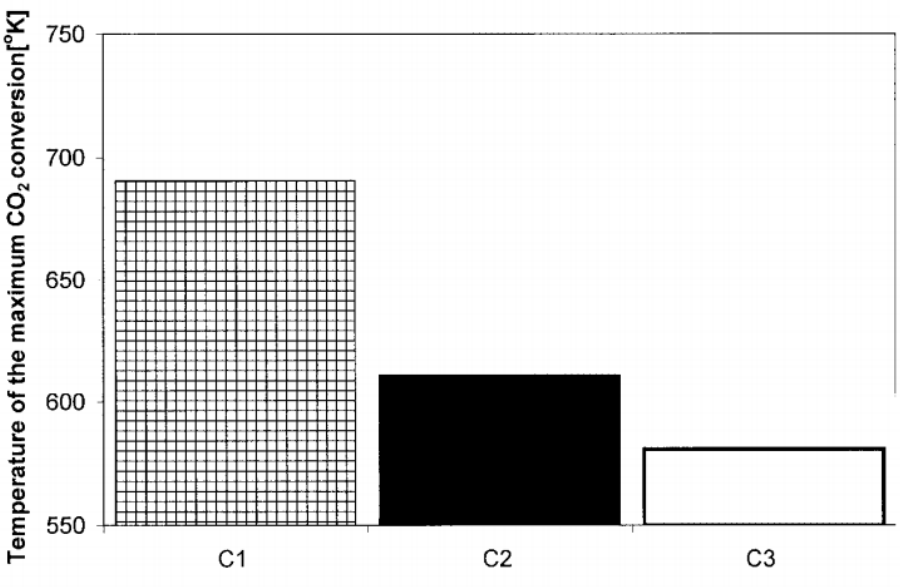


Figure 2.1 Plot of temperature versus maximum conversion attained during CO_2 methanation, where C1 = Al_2O_3 supported Ru catalyst, C2 = CeO_2 supported Ru catalyst and C3 = CeO_2-Al_2O_3 supported Ru catalyst. Adapted from ref (Rynkowski et al., 2000).

The higher activity of the mixed supported Ru catalyst was attributed to the promoting effect of the ceria component which most likely helps in creating more active sites and improving Ru dispersion. In addition, the stabilisation effect of the Ce(III) ion in $CeAlO_3$ was suggested to be a driving force that influences the activation of CO_2. This stabilisation effect of ceria on catalysts physicochemical properties has also been reported elsewhere (Damyanova et al., 2009). In a recent study, Kim et al. (2018) investigated the effect of mixing supports on the activity of Ru catalysts for CO_2 methanation. In this study, two forms of TiO_2 supports with different crystallinity (anatase and rutile) were used. The rutile TiO_2, anatase TiO_2 and mixed (anatase and rutile TiO_2) supported RuO_2 catalysts were tested in CO_2 methanation. The results revealed that rutile TiO_2 supported RuO_2 catalyst as more active than the anatase TiO_2 supported RuO_2 catalyst. Depending

on the method of preparation, the mixing of both the anatase and rutile TiO_2 as support for RuO_2 did not significantly change the catalytic activity towards CO_2 methanation in comparison with the performance of the rutile TiO_2 supported RuO_2 catalyst. Nevertheless, the major advantage of mixed support was the high resistance to active metal sintering during the methanation reaction. In the case of support sintering, the authors reported that mixing of supports can help in hindering the active metal phase from being trapped in the bulk of the sintered support. This study showed that the type of support for methanation catalysts depends on the properties desired; high activity, stability, or both. Other studies on the use of Ru catalysts for CO_2 methanation is summarised in Table 2.1.

Table 2.1 Summary of various of Ru catalysts for CO_2 methanation.

Catalyst	Preparation method	Investigation	operating conditions				Activity		Ref
			Feed gases	T (K)	P (atm)	GHSV ($mL.g^{-1}.h^{-1}$)	X_{CO2} (%)	S_{CH4} (%)	
Ni−Ru/CeO_2	Wet impregnation	Influence of Ru	$4H_2$:CO_2 and N_2	498	1	36,000	~72	~100	(Pan et al., 2023)
Ni/CeO2							~70	~100	
Ru/CeO_2							0	~2	
Ru@MIL-101	Electrospinning, dip-coating and sol gel	Synthesis method and morphologies	$4H_2$:CO_2 and He	573	-	10,435	~90	~99	(Loccufier et al., 2023)
Ru_1Ni/CeO_2	One-pot synthesis and sol gel	Synergy between Ru and Ni	$4H_2$:CO_2 and He	598	1	30,000	~90	~98	(Zhang et al., 2023b)
Ni/CeO_2							~85	~98	
Ru_1/CeO_2							~12	~31	
Ru/CeO_2	Wet impregnation	Influence of oxygen vacancies and basic sites	$4H_2$:CO_2	623	1	3,600	~85	~100	(Wang et al., 2023a)
Ru/SiO_2							~75	~98	
Ru/MgO							~32	~82	
Ru_1/γ-Al_2O_3							~14	~92	
Ru/CeO_2 (0°)	Wet impregnation and special method reported in this study	Effect of twist angle in spiral-type Ru/CeO_2 catalysts	$5H_2$:CO_2:$3.5N_2$:$0.5O_2$	473	1	120,000	~47	~100	(Hossain et al., 2023)
Ru/CeO_2 (90°)							~56	~100	
Ru/CeO_2 (180°)							~78	~100	
Ru/CeO_2 (360°)							~81	~100	
Ru/CeO_2 (540°)							~84	~100	
Ru/CeO_2 (720°)							~84	~100	

Table 2.1 Summary of various of Ru catalysts for CO_2 methanation (Continuation).

$Ru/7\%CrO_x/Al_2O_3$	Wet impregnation and co-impregnation	Influence of modifying Al_2O_3 support with Cr	$4H_2:CO_2$	623	1	36,000	~78	~100	(Zhang et al., 2023c)
Ru/Al_2O_3							~20	~100	
PT-Ru/TiO_2	Incipient wetness impregnation	Influence of TiO_2 under light illumination	$4H_2:CO_2$ and N_2	573	1	11,000	~80	~85	(Li et al., 2022a)
T-Ru/TiO_2							~72	~85	
4Ru-TiO_2/palygorskite	Strong electrostatic adsorption (SEA) and wet impregnation	Effect of TiO_2/palygorskite as support and preparation method	$4H_2:CO_2:5N_2$	598	~1	30,000	88.7	~100	(Liang et al., 2022a)
IM-Ru-TiO_2/palygorskite							~14	~85	
4Ru-TiO_2							88.7	~99	
Ru/Na-ZrO_2	Wet impregnation	Promotional effect of Li, Na and K	$3H_2:CO_2$	473	-	-	~21	~100	(Gao et al., 2022)
Ru/K-ZrO_2							~15	~100	
Ru/Li-ZrO_2							~11	~100	
Ru/ZrO_2							~1.75	~100	
3%Ru/Al	Incipient wetness impregnation	Promotional effect of K, Na and Ba	$4H_2:CO_2:7Ar$	~703	-	19,000a	~83	~100	(García-Bordejé et al., 2022)
3%Ru-10%Ba/Al							~69	~94	
3%Ru-10%K/Al							~48	~46	
3%Ru-10%Na/Al							~48	~56	
RuHNS	Wet impregnation	Morphology effect of MnO_x support	$4H_2:CO_2:5N_2$	673	-	12,000	~67.5	~92	(Tang et al., 2021b)
RuONS							~48	~76	
1%Ru/CeO_2	Wet impregnation	Effect of Ru loading	$4H_2:CO_2$ and He	623	1	60,000	~74	-	(López-Rodríguez et al., 2021)
2%Ru/CeO_2							~82		
3%Ru/CeO_2							~91		
5%Ru/CeO_2							~88		
Li-Ru/Al_2O_3	Incipient wetness impregnation	Influence of alkali promoters (Li, Na, K)	$4H_2:CO_2:5N_2$	648	1	25,000	~72	~100	(Cimino et al., 2020)
Na-Ru/Al_2O_3							~18	~30	
K-Ru/Al_2O_3							~10	~5	

Table 2.1 Summary of various of Ru catalysts for CO_2 methanation (Continuation).

3.54 %Ru/500C12A7:OH^- 1.76 %Ru/500C12A7:OH^- 1.76 %Ru/400C12A7:OH^- 1.90%Ru/γ-Al_2O_3	Wet impregnation	Effect of encaged anions on catalytic mechanism	$4H_2$:CO_2:Ar	648	1	72,000	~82 ~66 ~60 ~50	-	(Wu et al., 2020)
Ru/CeO_2 Ru/SiO_2-CeO_2 Ru/TiO_2-CeO_2	Precipitation-deposition method	Effect of support mixing: SiO_2-CeO_2 and TiO_2-CeO_2 on resistance to catalyst sintering	$4H_2$:CO_2:15Ar	573	-	12,000	-	~81[b] ~83[b] ~76[b]	(Nguyen et al., 2019)
Mn-Al_2O_3 60Cu/Mn-Al_2O_3 3Ru60Cu/Mn-Al_2O_3 5Ru60Cu/Mn-Al_2O_3	Incipient Wet Impregnation method	Promotional influence of Ru, effect of reactor configuration,	$4H_2$:CO_2	573	1	1000	5.1 54.7 78.8 80.1	-	(Zamani et al., 2019)
Ru/pBN-1.76%F	Sonication and Vacuum filtration process	Influence of using porous hexagonal boron nitride (pBN) as support		673	9.87	18000	81.1	98.8	(Fan et al., 2019)
Ru/TiO_2	One-pot synthesis via Solvothermal method	Effect of support structure	$4H_2$:CO_2 and N_2	623	1	6000	~85	100	(Chai et al., 2019)
Ru/UiO-66	One-pot synthesis via Solvothermal method	Effect of synthesis method for UiO-66		200	-	6000			(Xu, Dong, Di, & Zhang, 2019)

[a] = GHSV in h^{-1}, [b] = CH_4 yield (%), X_{CO2} = CO_2 conversion, S_{CH4} = CH_4 selectivity, T = operating temperature, P = operating pressure

2.3.2.2 Rhodium

Rh is a noble metal that has received considerable attention for the synthesis of methane owing to its properties of enhancing catalyst performance. For instance, its oxidation state allows the easy adsorption and reduction of CO_2 which is an essential stage in methanation reaction (Frontera et al., 2017). In an earlier work, Beuls et al. (2012) showed that the oxidation state of Rh and the presence of oxygen can greatly influence the catalyst performance in CO_2 methanation. The oxidation state of Rh, which determines the type of species that are adsorbed, favoured the formation of gem-dicarbonyl $Rh(CO)_2$ species. Gem-dicarbonyl $Rh(CO)_2$ species are chemical complexes comprising of a rhodium (Rh) metal center coordinated to two carbonyl (CO) ligands, where the two carbonyl groups are connected to the same carbon atom of a ligand or molecule. These complexes are generally represented as follows $[Rh(CO)_2]$-L, where Rh represents the rhodium atom, CO represents the carbonyl ligands, and L denotes the ligand to which the rhodium complex is coordinated. The ligand L can be a wide range of molecules or coordination groups. Gem-dicarbonyl $Rh(CO)_2$ species, which are formed by the dissociative adsorption of CO_2 to form CO (ads) and O (ads)), are reportedly more reactive than the Rh-CO linear species (Jacquemin et al., 2010). In contrast, earlier research suggested that the linear bound Rh is more reactive than CO bound to dispersed, dicarbonyl bound CO ($Rh(CO)_2$) or bridge bound CO (Chuang and Pien, 1992; McClure et al., 2011). This means that further research is required to understand the mechanism of adsorption of species on Rh catalysts during reactions such as CO_2 methanation.

The presence of oxygen could either enhance or decrease the activity of Rh catalysts during CO_2 methanation. The effect of oxygen availability on the activity of reduced Rh (1 wt.%)/γ-Al_2O_3 catalyst in CO_2 methanation conducted at 398 K is represented in Figure 2.2 (Beuls et al., 2012). As seen in the Figure, there was improvement in CH_4 production when oxygen is present in low percentages. The enhanced reactivity towards CH_4 production was attributed to the formation of reactive species such as gem-dicarbonyl on the catalyst surface owing to the presence of oxygen which encouraged oxidation.

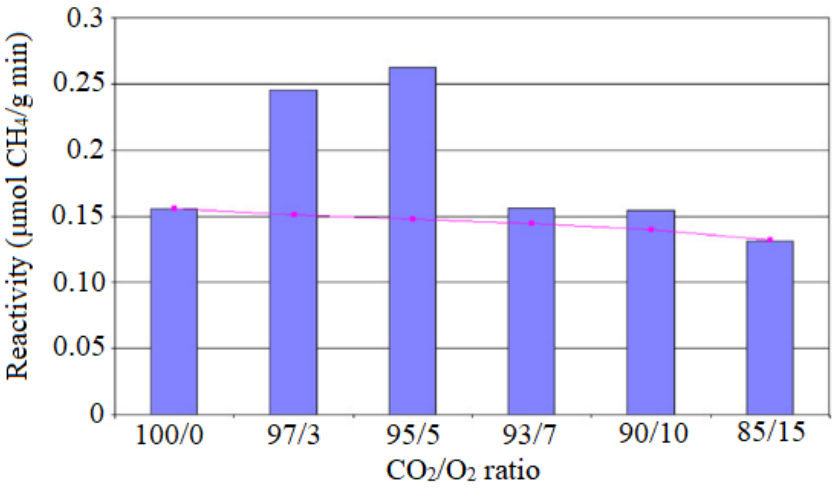


Figure 2.2 Amount of methane produced (µmole of methane by gram of catalyst/minute) as a function of the CO_2/O_2 ratio over Rh(1%)/γ-Al_2O_3 at 398 K. The line plot represents the theoretical values. Adapted from (Beuls et al., 2012).

However, there was a decline in the catalyst activity when the proportion of oxygen became higher than the optimum value: when the CO_2/O_2 ratio exceeded 95/5. The authors proposed that a high fraction of oxygen caused an unfavourable competition with other species for adsorption sites which most likely resulted in the deactivation of the Rh catalyst. It was also suggested that the high percentage of oxygen likely caused the complete oxidation of Rh which rendered the catalyst less active. The most recent review on the application of various supported Rh catalysts also reported the influence of the presence of oxygen in the catalyst activity (Erdőhelyi, 2020).

Another factor that has been reported to influence the performance of Rh catalysts is the amount of Rh loading and Rh particle size in analogy to catalysts with larger Ru particle sizes showing a superior activity than the ones with smaller sizes (Frontera et al., 2017; Karelovic and Ruiz, 2012). Others have reported the effect of temperature both at calcination and reaction stage on the activity of Rh catalysts (Jacquemin et al., 2010). A summary of the applications of Rh-based catalysts as reported in the literature for CO_2 methanation is given in Table 2.2.

Table 2.2 Literature showing the application of Rh-based catalysts for CO_2 methanation.

Catalyst	Preparation method	Investigation	operating conditions				Activity		Ref
			Feed gases	T (K)	P (atm)	GHSV ($mL.g^{-1}.h^{-1}$)	X_{CO2} (%)	S_{CH4} (%)	
xNa-Rh_1/ZrO_2	Incipient-wetness impregnation	Tuning both Rh_1 atoms and ZrO_2 support with alkali ions	$3H_2$:CO_2:18Ar	673	1	18,000	~58	~99	(Li et al., 2023a)
Rh_1/ZrO_2							~39	~99	
75Rh25Pt/ZrO_2	Precipitation and wet impregnation	Effect of Pt addition	$4H_2$:CO_2	573	1	22660[a]	12.9	-	(Mendoza-Núñez et al., 2022)
100Rh/ZrO_2							9.3		
100Pt/ZrO_2							0		
1.5%Rh/FSA	Microwave-assisted microemulsion and incipient wetness impregnation	Effect of Rh loading	$4H_2$:CO_2	773	1	15,000	~72	-	(Siang et al., 2021)
1%Rh/FSA							~83		
0.5%Rh/FSA							~36		
(Rh-Ni)/αβ-Mo_XC	Wet impregnation and co-impregnation precipitation method	The roles of bimetallic Rh-Ni	$4H_2$:CO_2 and N_2	873	1	6000	~70	~81	(Lin et al., 2021)
Rh/αβ-Mo_XC							~63	~72	
Ni/αβ-Mo_XC							~65	~79	
Rh/Al	Electric explosion of Al wires and ethylene glycol reduction method	Solar-Driven CO_2 Methanation	-	473	-	-	-	~99	(Fu et al., 2021)
1%Rh/TiO_2	Wet impregnation	Effect TiO_2, Al_2O_3, and ZnO supports	$4H_2$:CO_2	643	19.74	120,000	-	~96	(Jiang et al., 2020)
1%Rh/Al_2O_3								~87	
1%Rh/ZnO								~8	

Table 2.2 Literature showing the application of Rh-based catalysts for CO_2 methanation (Continuation).

Rh/CeO_2	Incipient wetness impregnation	Infrared modulation excitation spectroscopy measurements	-	-	-	-	-	-	(Hemmingsson et al., 2020)
$Rh/\gamma\text{-}Al_2O_3$ $Rh/CeO_2\text{-}ZrO_2$ $Rh/\gamma\text{-}Al_2O_3\text{-}CeO_2\text{-}ZrO_2$	Wet impregnation	Effect of support oxygen storage capacity and Rh particle size	$4H_2;CO_2:15Ar$	623	1	-	~27 ~15 ~40	~100 ~39 ~100	(Botzolaki et al., 2020)
Rh(111)	Floating zone method	Mechanism of CO_2 dissociation over Rh catalyst	-	-	-	-	-	-	(Kim et al., 2020)
Rh(100)		Rh-catalysed rate-determining step and the associated hydrogen assisted dissociation steps	-	-	-	-	-	-	(Vanzan et al., 2021)
Rh/CeO_2 Ni/CeO_2	Incipient wetness impregnation	Structure-function relationship for the two catalysts in CO_2 methanation	$14H_2;CO_2$	515 - 625	0.2[b]				(Martin et al., 2019)
Rh/TiO_2	Polyol and wet impregnation	Effect of illumination in plasmon-enhanced CO_2 methanation	-	-		-	-	-	(Li, Everitt, & Liu, 2019)
3DOM LNAO Rh/3DOM LAO Rh-Ni/3DOM LAO	Exsolution, sol-gel and wet impregnation methods	Effect preparation method and morphology	$4H_2;CO_2:15N_2$	~603	1	48,000	~65 ~90 100	-	(Arandiyan et al., 2018)

2.3.2.3 Palladium

Palladium is a noble metal that has found application in various catalytic reactions including hydrogen production via methanol steam reforming (Xu et al., 2017b; Lorenz et al., 2013), steam reforming of methane (Didenko et al., 2019b, 2019a) and dry reforming of methane (Köpfle et al., 2018; Yue et al., 2018) as the active metal component owing to its high catalytic performance. Moreover, Pd-based catalysts have been found to be very active in the CO_2 methanation reaction. The high catalytic performance of Pd-based catalysts for the aforementioned reactions can be ascribed to the ability of Pd to absorb significant amounts of protons following the dissociative adsorption of hydrogen molecules (Albers et al., 2001; Borodziński and Bond, 2006). Likewise, other studies have also shown that operating parameters such as catalyst preparation methods (Martins et al., 2015) and nature of support used (Kikuzono et al., 1981; Erdöhelyi et al., 1986) have great influence on the activity of Pd-based catalysts. Despite their ability to enhance catalytic reactions, Pd-based catalysts have not been extensively used for CO_2 the methanation reaction. Very few studies have been reported on the use of Pd as a CO_2 methanation catalyst in recent times. A summary of some of the work on the applications of Pd-based catalysts as reported in the literature for CO_2 methanation is given in Table 2.3.

Table 2.3 Recent studies on the catalytic activities of Pd catalysts for CO_2 methanation.

Catalyst	Preparation method	Investigation	operating conditions				Activity		Ref
			T (K)	P (atm)	Feed gases	GHSV ($mL.g^{-1}.h^{-1}$)	X_{CO2} (%)	S_{CH4} (%)	
4%Pd/UiO-66 6%Pd/UiO-66	Solvent-thermal and supercritical fluid deposition methods	Synthesis method and effect of Pd loading	603	~39.48	$4H_2$:CO_2 and N_2	1,350[a]	~53 ~41	~94 ~96	(Jiang et al., 2021)
NiO_TPd-T	Sequential chemisorption and impregnation method described in the study	Pathway for CO_2 thermal methanation	323 – 573	1	$3H_2$:CO_2	-	-	-	(Yan et al., 2020)
PdFe	Seeded growth and a method described in the study	Efficiency of PdFe intermetallic nanocrystals catalyst	373 – 473	1	$4H_2$:CO_2	-	-	-	(Luo et al., 2020)
75%Ni-25%Pd/SBA-15 Pd/SBA-15 Ni/SBA-15	One-pot synthesis and impregnation method	Effect of metal loading	703	1	$4H_2$:CO_2	6000	~95 ~58 ~69	-	(Li et al., 2019)
Ni/Al_2O_3 Ni-Pd/ Ni/Al_2O_3 Ni-Pt/ Ni/Al_2O_3 Ni-Rh/ Ni/Al_2O_3	Wet and Co-impregnation	Promotional effect of Pt, Pd and Rh	513	1	$4H_2$:CO_2 and Ar	5700[a]	~40 ~64 ~60 ~28	~92 ~98 ~97 ~89	(Mihet and Lazar, 2018)
SiO_2, Al_2O_3, CeO_2, ZSM-5 and MCM-41 supported Pd, Rh and Ni catalysts	Incipient wetness impregnation and ion-exchange methods	Effect of support type	423 – 723	1	$5H_2$:CO_2	60,000	-	-	(Martin et al., 2017)

Table 2.3 Recent studies on the catalytic activities of Pd catalysts for CO_2 methanation (Continuation).

Pd/Ce-TiO_2	Sol-gel and impregnation	Performance of Pd in Photocatalytic CO_2 methanation	-	24.67	$4H_2$:CO_2	-	-	-	(Li et al., 2017)
5%Ru/35%Mn/60Cu–Al_2O_3 5%Pd/35%Mn/60Cu–Al_2O_3 5%Rh/35%Mn/60Cu–Al_2O_3	Incipient wetness impregnation method	Optimisation of CO_2 methanation reaction	573	1	$4H_2$:CO_2	-	100 ~93 ~63	-	(Zamani et al., 2015)
Pd-MgO/SiO_2	Impregnation and simple mechanical mixing	Effect of Pd addition	723	1	$4H_2$:CO_2 and Ar	6120	~59	~95	(Park and McFarland, 2009)

[a] = GHSV in h^{-1}, X_{CO2} = CO_2 conversion, S_{CH4} = CH_4 selectivity, T = operating temperature, P = operating pressure

2.3.3 Non-noble Metal: Nickel-based catalysts

Although the use of noble metals as catalysts in heterogeneous reactions such as steam reforming of hydrocarbons and CO_2 methanation has been proven in various studies to greatly enhance the overall catalyst performance, their high cost remains a major limitation. Accordingly, the use of non-noble metals such as the ones in the first-row transition series (Mn, Fe, Co, Ni, and Cu) as alternative active metal component has become a subject of research since studies have shown that these metals can also improve catalyst activity (Daroughegi et al., 2020; Mutschler et al., 2018; Burger et al., 2018; Qin et al., 2019; Qiu et al., 2019). In particular, there has been increasing attention in the use of Ni for methanation catalysts in recent times owing to its appreciable activity and relatively low cost (Huynh and Yu, 2020).

Among other factors, the catalytic properties of Ni have been connected to its ability of inducing the C-C, C-H and C-O bond scission in reactions involving carbon conversion (Gamliel, Wilcox, & Valla, 2017; Lechkar et al., 2018; Omoregbe et al., 2017). Chen et al. (2004) stated from their observation that the presence of the Ni metal phase can promote the cleavage of the C–H bond to form CH_x groups, which is a crucial stage in both CO_2 reforming of methane and CO_2 methanation reactions. Despite the numerous benefits of using Ni metal for methanation catalysts, its limitations include vulnerability to (i) oxidation in oxidising atmospheres, (ii) sintering of Ni particles, (iii) low resistance to carbon deposition and (iv) the tendency to form mobile nickel carbonyls (Ghaib et al., 2016; Su et al., 2016). The activity and stability of Ni-based catalysts for CO_2 methanation strongly depends on the nature of support, preparation conditions, promoter addition, and the use of optimum reaction conditions (Huynh and Yu, 2020).

In a recent study, Ma et al. (2019) investigated the influence of the catalyst support on the performance of Ni-based catalysts in CO_2 methanation. In their study, four supports, namely Al_2O_3, CeO_2, ZrO_2 and TiO_2, were employed. The Ni catalysts were synthesised using deposition precipitation and tested in the CO_2 methanation reaction in the temperature range of 250 to 550℃ under atmospheric pressure and a space velocity of 120,000 mL/g/h.

Prior to the reaction, the catalysts were reduced under atmospheric pressure at 600°C for 4 h by passing a 10 vol% H_2/N_2 stream (50 mL/min). At the end of reduction, N_2 (50 mL/min) was sent in to purge the system while cooling down to reaction temperature. The results are summarised in Figure 2.3.

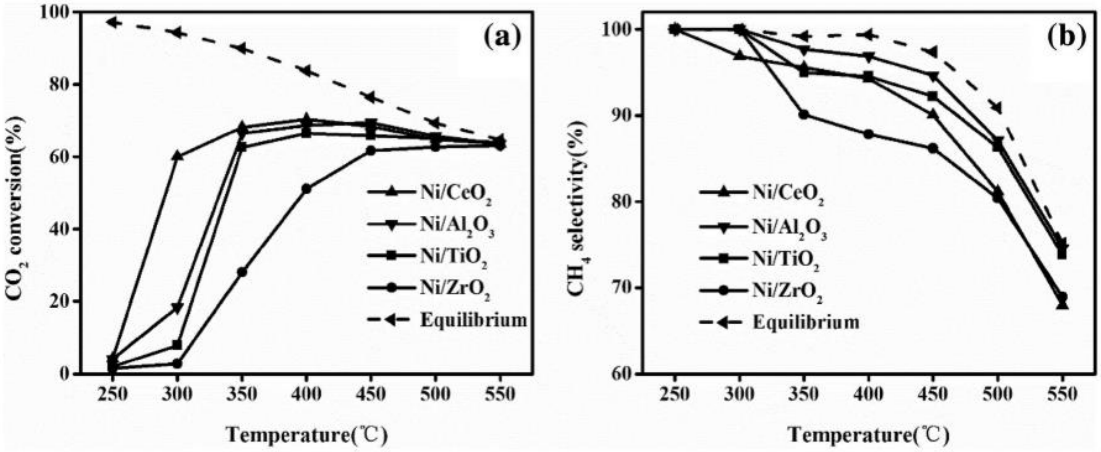


Figure 2.3 Catalytic performance of Ni-based catalysts at different temperatures (a) CO_2 conversion and (b) CH_4 selectivity. Adapted from (Ma et al., 2019).

As seen in Figure 2.3(a), CO_2 conversion for all the catalysts increased with rising temperature with the Ni/CeO_2 catalyst showing the highest conversion. However, CO_2 conversion over Ni/CeO_2 started declining beyond 400°C. Similarly, CH_4 selectivity over Ni/CeO_2 was relatively stable for temperatures below 400°C while there was a steady decrease in CH_4 selectivity for other catalysts within the temperature range. The superior activity of the Ni/CeO_2 catalyst at low temperatures was attributed to the strong synergy between the active centers, the Ni nanoparticles, and the support basic sites. The CeO_2 support, which exhibited remarkable weak basic sites, can adsorb CO_2 to form bridged bidentate carbonate species which can reduce the activation energy for formate formation. The Ni active center helps to adsorb and activate H_2.

Subsequently, the adsorbed H increases the chances of hydrogenation of the bridged bidentate carbonates species to CH_4. A high synergy was also observed between Ni and Al_2O_3 support in Ni/Al_2O_3 catalysts which improved the H_2 uptake. Nevertheless, its performance at low temperatures was inferior to that of the Ni/CeO_2 catalyst owing to the presence of significant strong basic sites that encouraged CO_2 adsorption at high temperatures. The Ni/ZrO_2 catalyst showed the least performance, probably due to the

poor capacity of the ZrO_2 support for CO_2 adsorption as revealed in the chemisorption results. In summary, the decreasing order of catalyst performance at temperatures below 400℃ was given as $Ni/CeO_2 > Ni/Al_2O_3 > Ni/TiO_2 > Ni/ZrO_2$. This result is in agreement with a previous study (Le et al., 2017).

Kesavan et al. (2018) investigated the influence of Ni particle size on the performance for CO_2 methanation. During the study, five Ni/YSZ catalysts were prepared by using five different methods, namely Wetness Impregnation (WI) with $Ni(NO_3)_2{\cdot}6H_2O$, Wetness Impregnation (WI) with a $Ni[EDTA]^{-2}$ complex, Electroless Ni Plating (EP), and mechanical mixing of NiO and YSZ at different conditions. Results showed that the Ni/YSZ(EDTA) had the best performance for CO_2 methanation of all the Ni catalysts. The superior activity of the Ni/YSZ(EDTA) catalyst was attributed to the high Ni^0 dispersion which was enabled by the small Ni^0 particle size (19 nm) in comparison with its size in other catalysts. Smaller Ni particles promoted the formation of CO instead of CH_4 owing to the reaction pathway where a m-HCOO− intermediate is decomposed into CO (Marconi et al., 2019). Although this pathway may lead to the formation of CH_4 after successive pathways, the amount of CH_4 formed will be less since more H_2 will be required for the successive hydrogenation reactions (low H_2 coverage).

A similar result was obtained in a different study by Wu et al. (2015). The authors investigated the influence of particle size on selectivity and reaction pathway in methanation of CO_2 and reverse water gas shift reactions over Ni/SiO_2 catalysts prepared by employing 0.5 wt% and 10 wt% Ni loadings. It was found that the 10%Ni catalyst exhibited a better performance than the 0.5%Ni catalyst. This was ascribed to the presence of large Ni particle size (9 nm) which provided wide coverage for H_2 adsorption and activation. Although Ni crystallite size has been shown to influence the catalyst activity towards CO_2 methanation, the Ni size should not be too small nor too big. For instance, Meerten et al. (1983) reported 4.4 nm as the optimum Ni crystallite size during the CO methanation reaction. Therefore, the optimum Ni particle size for various supports remains a subject of research since different studies have reported different optimum values. The tables of various literature where Ni-based catalysts have been employed for CO_2 methanation are given in the next section, discussing supports for CO_2

methanation. This is to avoid repetition since Ni is the most used active metal, applied to various supports.

2.3.4 Catalyst Promoters

Promoters are mostly metals or metal oxides which are usually not effective when employed as standalone catalysts due to limited catalytic activity, but can enhance a catalyst's physicochemical properties such as the dispersion of the active metal in the support's pores or the metal-support interaction (Babakouhi et al., 2023) and basic site strengths (Liu et al., 2022b) when introduced into the catalyst's structure. These promoters can be grouped in terms of their structural arrangement or capacity for electron transfer. In terms of structural arrangement, there are two main classes of promoters, namely, textural and chemical promoters. Textural promoters are promoters that have the capacity of improving the textural properties of a catalyst such as surface area and degree of dispersion which are crucial for inhibiting or supressing the sintering of active species (Jang et al., 2019). Some of the examples of the generally used textural promoters include TiO_2 (Lázaro et al., 2008), La_2O_3 (Wachs et al., 2013), Al_2O_3 (Moeini and Meshkani, 2023) , Y_2O_3 and ZrO_2 (Wang et al., 2023b) and silica (Ermakova et al., 1999). In some cases, most textural promoters can act as catalyst supports depending on the type of reaction involved. For example, Al_2O_3, ZrO_2 and SiO_2 are widely employed as catalyst supports in reactions such as methane dry reforming (Pizzolato et al., 2023) and CO and CO_2 methanation reactions (Hou et al., 2023).

Chemical promoters are promoters that are introduced into a catalyst system to reduce or improve its surface acidity. While textural promoters mainly help to improve the textural properties, chemical promoters are used to enhance catalytic performance such as the activity and selectivity of the catalytic phase (Bartholomew and Farrauto, 2011; Stanke and Kampars, 2022). Chemical promoters can further be classified as acidic (Liu et al., 2021; Cai et al., 2013) and basic promoters (Al-Fatesh, 2015; Oemar et al., 2016) depending on how they influence the transfer of electrons. In this study, attention is given to only the basic promoters. Acid promoters are not suitable for methanation or reforming reactions because they are not able to act as surface stabilisers since efficient CO_2

adsorption requires a basic surface or a surface with low acidity. The oxides/compounds of alkali and earth alkaline metals (Ahmad et al., 2021; Previtali et al., 2020), and the lanthanides (Daza et al., 2010; Foo et al., 2011a; Liu et al., 2008; Natesakhawat et al., 2005a) are the most common examples of basic promoters used in heterogeneous catalytic reactions.

2.3.4.1 Alkali and alkaline metals

Alkali and alkaline earth metals are often used as promoters for heterogeneous catalysts due to their unique properties and ability to enhance the catalytic activity of the catalyst. The following are some of the reasons alkali and alkaline earth metals are employed as promoters: (1) Increase in surface area (Li et al., 2013): Alkali and alkaline earth metals are highly reactive and can readily form oxides or hydroxides on the surface of the catalyst, which can increase the surface area of the catalyst. This increased surface area provides more active sites for the reactants to adsorb and react, leading to higher catalytic activity; (2) Enhanced CO and CO_2 adsorption (Panagiotopoulou, 2018; Iruretagoyena et al., 2015): Alkali and alkaline earth metals can modify the electronic properties of the catalyst surface and prove its basicity, making it more favourable for reactant adsorption. This can increase the concentration of reactants at the catalyst surface and promote their interaction, leading to improved catalytic activity; (3) Modified reaction pathways (Siakavelas et al., 2022): Alkali and alkaline earth metals can alter the reaction pathways of catalytic reactions. For example, they can facilitate the formation of intermediates or promote certain reaction steps, leading to modified reaction pathways that may be more favourable or selective for the desired product; (4) Improved catalyst stability: Alkali and alkaline earth metals can also enhance the stability of the catalyst by reducing catalyst deactivation due to poisoning or sintering. For example, the addition of Ca can prevent the adsorption of carbon species on the surface of Ni/Al_2O_3 catalyst during CO_2 methanation, and this enhances its stability (Cho et al., 2022). Alkali or alkaline earth metals can form stable compounds or alloys with the catalyst material, preventing the loss of active sites and maintaining high catalytic activity over extended periods of time.

Gao et al. (2022) investigated the influence of alkali promoters (Li, Na and K) on the catalytic performance of Ru/ZrO_2 in CO_2 methanation. The outcome of the study revealed that the incorporation of alkali elements did not only improve the catalyst's adsorption strengths for CO_2 and CO but also enhanced the charge density of the metal-support interfacial phase. Onrubia-Calvo et al. (2023) developed $La_{1-x}Ca_xNiO_3/CeO_2$ dual function materials and investigated the effect of introducing Ca on the catalysts' performances in CO_2 capture and hydrogenation to methane. Characterisation results reviewed that the Ca^{2+} addition promoted the sample reducibility by substituting La^{3+} within the perovskite structure. More importantly, Ca doping enhanced the surface basicity which was measured in terms of medium and strong basic sites. Finally, the authors suggested that the presence of Ca was also essential in partially suppressing the competitive adsorption of H_2O on CO_2 storage sites which further boosted the CO_2 adsorption.

Yang et al., (2020a) fabricated a highly dispersed Ni catalyst by incipient wetness impregnation using an amine functionalised nanosponge zeolite (represented as AF-NSZ) as the support. The catalyst was then modified by the introduction of La_2O_3 and MgO to give Ni-La/AF-NSZ and Ni-Mg/AF-NSZ, respectively. From the XRD results, the amine functionalised NSZ supported (AF-NSZ) catalysts displayed lower metallic Ni peak intensities than the non-functionalised catalyst. This indicates that the functionalisation of the NSZ support with amine helped to improve the degree of metallic Ni dispersion. Hydrogen temperature-programmed reduction (H_2-TPR) results also revealed that the amine functionalised NSZ supported (AF-NSZ) catalysts possessed stronger metal-support interaction between Ni and the AF-NSZ support than the non-functionalised catalyst. Finally, the temperature-programmed desorption (CO_2-TPD) revealed that the promotion of the catalysts with La_2O_3 and MgO improved the surface basicity substantially. All the catalysts were tested in CO_2 methanation, and the results of the activity tests are represented in Figure 2.4.

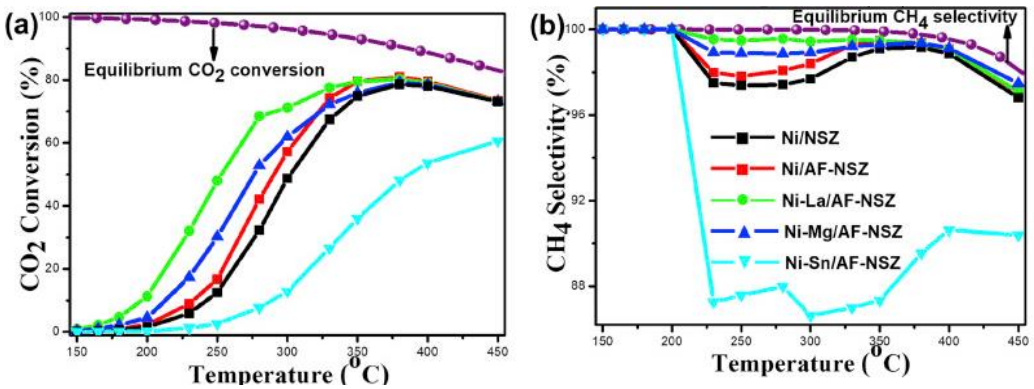


Figure 2.4 Activity test profiles of Ni-based NSZ catalysts at different temperatures (a) CO_2 conversion and (b) CH_4 selectivity; reaction conditions: H_2/CO_2 = 4, GHSV = 12000 mL g^{-1} h^{-1}, 1 atm. Adapted from (Yang et al., 2020a).

As seen in the figure, the La and Mg-promoted catalysts showed superior performances compared to the unpromoted catalysts. According to the authors, the enhanced surface basicity via the La and Mg promoters resulted in improved CO_2 adsorption and activation. In addition, the apparent activation energies of CO_2 methanation, and the low-temperature activities were greatly improved.

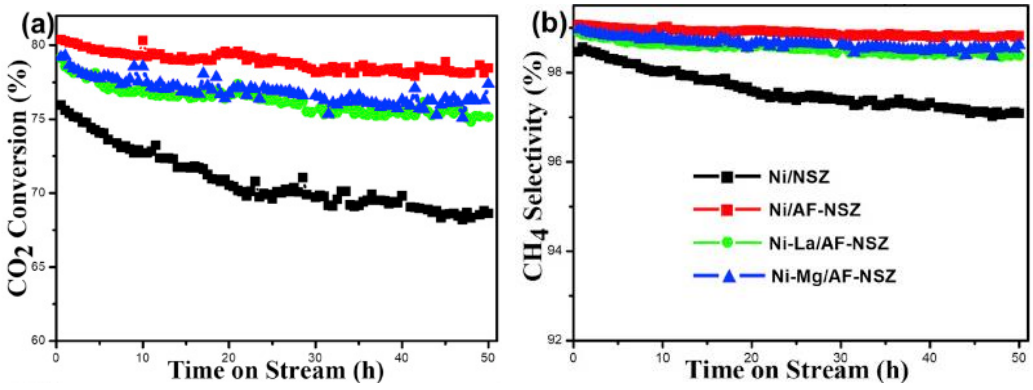


Figure 2.5 Lab-scale 50 h long-term stability tests over different catalysts: (a) CO_2 conversion and (b) CH_4 selectivity; reaction conditions: H_2/CO_2 = 4, GHSV = 12000 mL g^{-1} h^{-1}, 400 °C, 1 atm. Adapted from (Yang et al., 2020a).

Finally, the 50 h on-stream longevity test results presented in Figure 2.5 revealed that the amine functionalised catalysts (promoted and unpromoted) are more stable than the non-functionalised NSZ supported catalyst. The improved stability was attributed to the high dispersion exhibited by the catalysts. The confinement of the active species helped in

supressing the occurrence of thermal sintering, and this translated into improved catalytic stabilities toward CO_2 methanation.

Overall, the use of alkali and alkaline earth metals as promoters in heterogeneous catalysts offers several advantages, including increased catalytic activity, improved stability, modified reaction pathways, and tailored selectivity. However, the specific mechanism and effectiveness of these promoters depend on the catalyst system and the reaction being catalysed, and careful selection and optimisation of the promoter are necessary to achieve the desired catalytic performance. Therefore, it is important to thoroughly understand the specific catalyst system and reaction conditions before using alkali and alkaline earth metals as promoters in heterogeneous catalysis.

2.3.4.2 Lanthanide promoters

Lanthanides (Ln) are the rare earth elements found in the f-block of period six in the periodic table with members starting from lanthanum (atomic number 57) through cerium (atomic number 58) to lutetium (atomic number 71). The use of lanthanides in promoting the performances of heterogeneous catalysts has attracted increasing attention of researchers due to their unique properties such as high oxygen storage capacity which makes them favourable for redox reactions involving carbon or carbon-based species (Cheng et al., 1996; Wang & Lu, 1998). The addition of Lanthanides as promoters can enhance the capacity to prevent carbon deposition, metal dispersion, and reducibility, which are crucial for high catalytic performance (Natesakhawat et al., 2005b; Wang & Lu, 1998).

Cao et al. (2022) investigated the effect of a Ce-promoter on the activity of Co/Al_2O_3 catalysts in dry reforming of methane (DRM). In the study, the amount of Ce-promoter was varied from 0.1 to 2wt% while Co was fixed at 10 wt%. Characterisation results revealed that the promotion of the Co/Al_2O_3 catalyst with Ce helped to improve the Co metal dispersion. However, the Co particles sintering was favoured at cerium content above 0.5 wt%. It was also revealed that the addition of Ce-promoter resulted in the modification of the Co_3O_4 crystal structure and the metal-support interaction.

The activity test results of the catalysts in DRM are presented in Figure 2.6 (a) and (b).

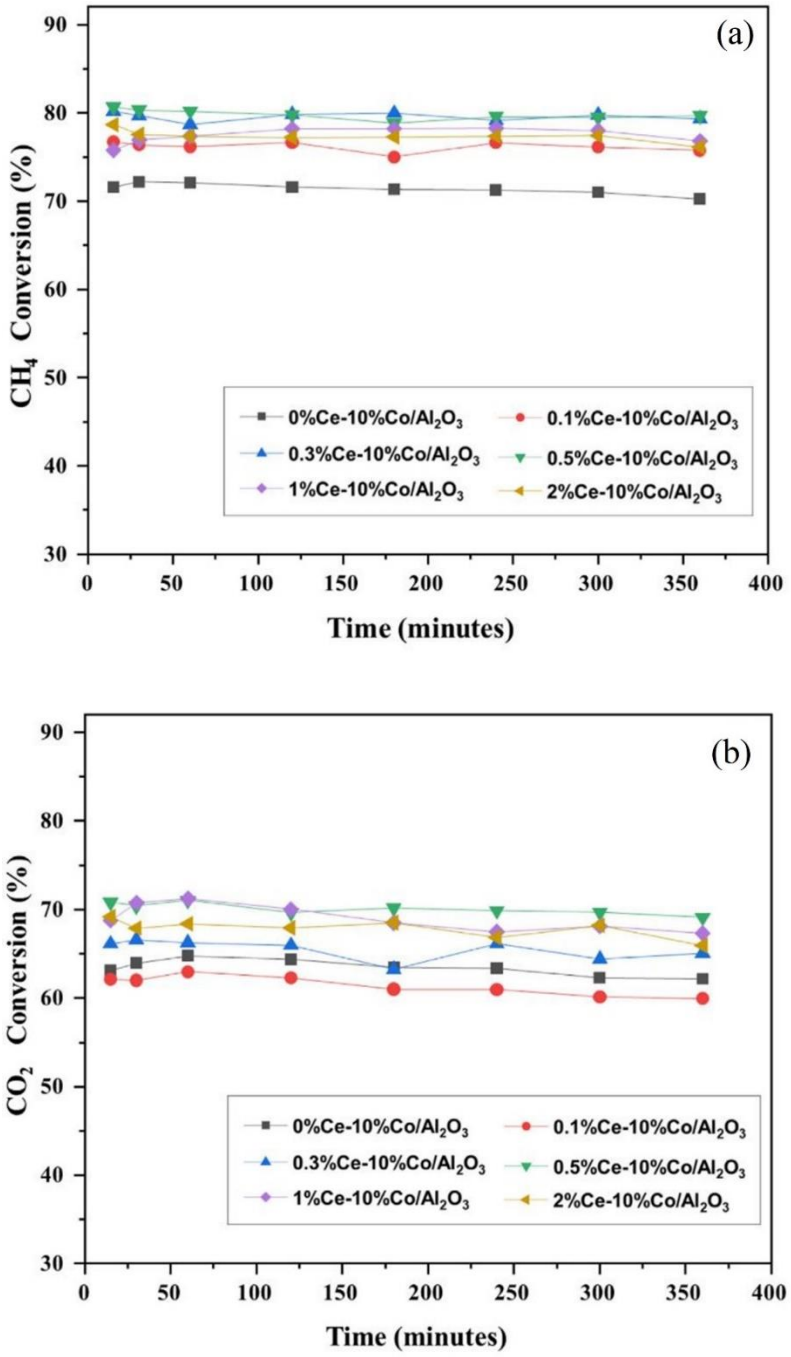


Figure 2.6 Activity profile showing (a) CH_4 and (b) CO_2 conversions with respect to time-on-stream during DRM conducted at 973 K. Adapted from ref (Cao et al., 2022b).

As seen in Figure 2.6 (a), CH_4 conversion over all the catalysts was relatively stable with the time on stream considered. In terms of performance, all the Ce-promoted catalysts were more active than the unpromoted catalyst. It can also be seen that the catalyst activity improved with the increase in the amount of Ce-promoter up to 0.5 wt% Ce where the maximum CH_4 conversion of 80% was achieved. The observed improvement in the catalyst performance with the increase in amount of Ce-promoter until 0.5 wt% was ascribed to the increase in basic site concentration, which favoured the adsorption of CO_2 on the catalyst surface. The adsorbed CO_2 is crucial for the gasification of the surface C_xH_y species obtained from the dissociation of CH_4 to form the products (H_2 and CO). The author also mentioned the role of oxygen storage capacity (OSC) of the Ce-promoter in enhancing the catalyst performance.

Figure 2.7 indicates the product yields and H_2/CO ratio from the DRM conducted at 973 K. As in CH_4 and CO_2 conversions, the H_2 and CO yields were favoured with the increase in Ce loading up to 0.5 wt%Ce. Beyond this optimum Ce loading, the catalyst activity started declining. This decrease in the catalyst performance at higher Ce loading was attributed to favoured clustering of cobalt particles and the blockage of the cobalt active sites by the excess cerium. Temperature programmed oxidation (TPO) analysis shown Figure 2.8 revealed the presence of low-temperature carbidic carbon (amorphous carbon) and high-temperature graphitic carbon on the unpromoted 10%Co/Al_2O_3 catalyst while only the amorphous carbon was found on the Ce-promoted catalysts. Low temperature carbonaceous species are generally reactive and are easily oxidised. Hence, this type of carbon does not readily influence catalyst deactivation. On the other hand, graphitic carbon can be low-temperature reactive such as filamentous carbon (Pechimuthu et al., 2007) or high-temperature non-reactive carbon (Kress and Tielens, 2001; Ahn et al., 1996). Therefore, the great performance of the Ce-promoted catalyst was also ascribed to its ability to suppress the formation of the non-reactive carbon whose buildup on the active sites leads to the deactivation of the catalyst.

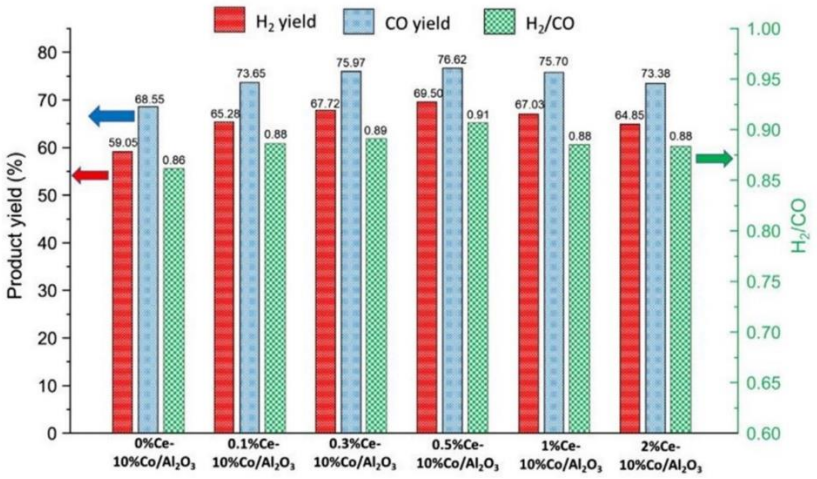


Figure 2.7 Activity profile showing the influence of varying Ce-promoter loading on the product yields and H_2/CO ratio for DRM runs at 973 K. Adapted from ref (Cao et al., 2022b).

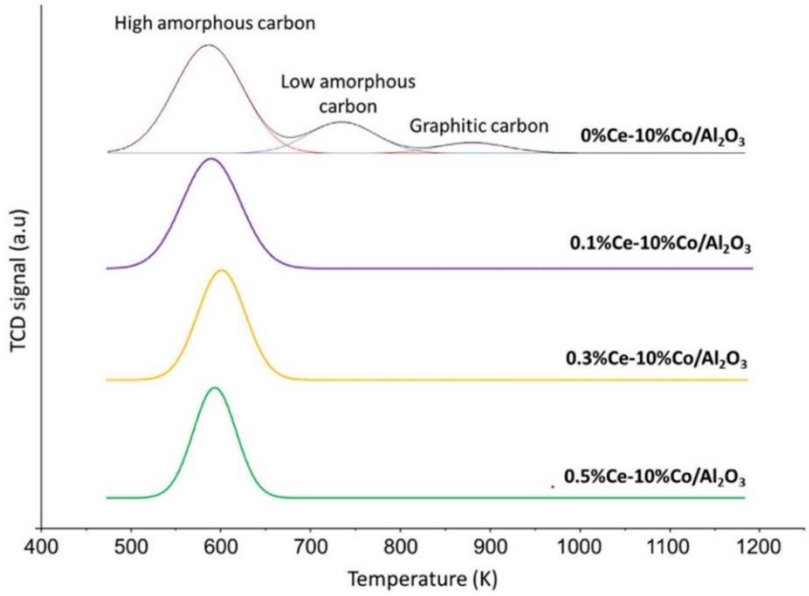


Figure 2.8 TPO profiles of the selected spent Ce-promoted 10%Co/Al_2O_3 catalysts. Adapted from ref (Cao et al., 2022b).

In another study, Fakeeha et al. (2021) reported that the incorporation of Ce on yttria modified zirconia (YSZ) supported Ni-based catalysts in DRM reaction encouraged carbon deposition instead of suppressing it. Consequently, the unpromoted Ni-YSZ catalyst was found to be more stable than the Ce-promoted Ni-YSZ catalyst. the

observation from this study is in sharp contrast to what was observed in the work mentioned earlier (Cao et al., 2022b) where the Ce-promoter exhibited the property of supressing the formation of non-reactive carbon, thereby improving the catalyst's stability. The discrepancies between these two studies may arise from the nature of the active metal used (Co and Ni) or even the support (Al_2O_3 and YZ).

Lanthanum oxide (La_2O_3), also known as lanthana, is widely employed as a promoter in processes such as dry reforming and CO_2 methanation due to its unique properties including high basicity, which is important in promoting CO_2 adsorption and activation (Boukha et al., 2022). Liang et al. (2022b) synthesised a series of Lanthanide-modified cobalt-palygorskite composites (palygorskite is a type of clay comprising mainly magnesium aluminium phyllosilicate) and tested them in the CO_2 methanation reaction under atmospheric pressure. The authors revealed from their investigation that the addition of lanthanide helped to improve the active Co metal-support interaction resulting in the enhancement of the anti-carbon deposition and anti-sintering ability of the catalyst. There was an increase in the active reaction sites with enhanced Co particle dispersion. The presence of the lanthanides also improved the adsorption of CO_2, and slightly improved reducibility of the catalyst via the promotion of the electron transfer between the metal and the palygorskite matrix.

Similar behaviours were reported by Liang et al. (2023) in a study on the effect of doping a Co/Al_2O_3 catalyst with different lanthanides for dry reforming of methane. From the investigation, it was stated that the addition of a La-promoter to Co/Al_2O_3 catalyst can; (1) influence the dispersion of the active metal Co on the catalyst surface through a particle size reduction effect; (2) enhance the redox performance of the catalyst by encouraging the electron transfer of Co species, generating more active. This increase in the number of active sites favoured the adsorption and activation of species such as CH_4 on the catalyst surface; (3) provide sufficient oxygen vacancies and enhanced basic sites which are crucial for suppressing the carbon deposition and improving the CO_2 adsorption and activation capacity of the catalyst.

Zhang et al. (2019) also verified the influence of a La-promoter during a study on CO methanation over a Ni/Al_2O_3 catalyst prepared by the deposition-precipitation and co-impregnation method. It was found that the catalyst performance was greatly improved

while the sintering of Ni particles and coke formation were significantly inhibited by the addition of La-promoter. Characterisation results revealed that the incorporation of the La-promoter improved the reducibility of Ni particles and decreased the size of the Ni crystallites resulting in high dispersion on the alumina support. Finally, it was also noticed that the preparation method affected the catalyst performances, where the catalyst prepared by the modified deposition-precipitation method showed a superior activity than the catalyst prepared by the co-impregnation method.

Mihet et al. (2021) investigated how the addition of MgO, CeO_2, La_2O_3 into a Ni/SiO_2 catalyst affected its catalytic performance in CO_2 methanation. The incorporation of MgO and La_2O_3 into the catalyst structure resulted in improved dispersion of Ni particles on the catalyst surface, an increase in the number of active sites for the adsorption and activation of H_2. In terms of basicity, the La- and Ce-modified catalysts displayed superior basic site strength to the Mg-modified catalyst, which is crucial for the adsorption and activation of CO_2. The activity test results indicated that the La-modified catalyst exhibited the best performance in a relatively low-temperature range. This was attributed to the enhanced capacity of the La-modified catalyst for H_2 and CO_2 adsorption and activation, improved anti-sintering capacity, the combined effect of Ni nanoparticle stabilisation inside the medium sized mesopores, and the facilitated access of reagents to active centers due to the large mesopores.

Interestingly, La-promoter has been reported to improve catalyst resistance to sulfur poisoning by inhibiting the chemisorption of gaseous H_2S on the catalyst surface in a study by Dou et al. (2021). From the preceding paragraphs, it is apparent that the addition of alkali and alkaline metals and lanthanides into the framework of heterogeneous catalysts can positively influence their activity. It should also be noted that the nature of the support employed can also affect the overall properties of promoted catalysts. Therefore, the next section will be discussing some of the commonly used catalyst supports for CO_2 methanation.

2.3.5 Catalyst supports

In heterogeneous catalysis, supports are materials with high surface area and pore volume, which alone have little or no activity, but can provide a medium for the dispersion of active constituents or metals, resulting in an overall active material (catalyst) for the desired reaction (Ribeiro et al., 2014). Apart from serving as a medium for active metal dispersion, a catalyst support can also help to stabilise and enhance the active sites, or even form part of the active sites (Bartholomew and Farrauto, 2011). Catalysts support for most heterogeneous catalytic reactions are usually in the form of metallic oxides with very few non-metallic oxides.

Examples of metallic oxide supports that are commonly employed for the development of reforming and methanation catalysts include lanthana (La_2O_3) (Xin et al., 2023; Xiao et al., 2023), ceria (CeO_2), alumina (γ-Al_2O_3 or α-Al_2O_3), zirconia (ZrO_2) , titania (TiO_2) (Yuan et al., 2023; Krishnan J N et al., 2023), and perovskites (Blanco et al., 2022; Du et al., 2023). Porous silica or silicon dioxide (SiO_2) are the most common example of non-metallic oxide supports. Porous silica can be nanoporous, microporous, or mesoporous, depending on the method of preparation or the forms it exists in. Porous silica can exist as amorphous silica (SiO_2) or modified silica such as the Mobil Composition of Matter (MCM) and Santa Barbara Amorphous 15 (SBA-15) (Santos et al., 2019; Bacariza et al., 2018). Siliceous based materials such as zeolite have been widely employed as support in methanation reactions (Cui et al., 2023; Goodarzi et al., 2018). Non oxide porous materials such as activated carbon, are also employed as support.

The choice of support to be used for any catalyst depends on the nature of the reaction to be catalysed. Apart from the structure such as high surface and pore volume of a support, the chemical properties including the acid site strength greatly influence the overall performance. Some reactions require a mild or low acid site strength while others require a high acid site strength. For example, it was reported that a high acid site strength is crucial in achieving a high level of pentenes conversion during a study on the cracking of pentenes to C_2–C_4 light olefins (Bortnovsky et al., 2005). Meanwhile, acidic supports with strong acid sites strength favour the deposition of carbonaceous species during reforming or methanation reactions due to their weak dissociative adsorption capacity of CO_2, which make them inefficient in preventing the accumulation of highly

dehydrogenated carbon deposits. Some of these carbonaceous species further undergo ageing and graphitisation on the surface as the reaction proceeds and causes the deactivation of the catalyst (Horváth et al., 2011; Naeem et al., 2014).

2.3.5.1 Ceria

Cerium is the most abundant rare-earth element with approximately 0.0046 wt% composition of the Earth's crust (Montini et al., 2016). Cerium (Ce) with electron configuration of $4f^2 5d^0 6s^2$ is a rare-earth metal with a partially filled f orbital, and a member of the lanthanide series of the periodic table. It can either exist in Ce^{3+} or in the stable Ce^{4+} state. Ce exists naturally in four isotopic forms namely ^{136}Ce (0.19%), ^{138}Ce (0.25%), ^{140}Ce (88.45%), and ^{142}Ce (11.11%) where the ^{140}Ce isotope is the most abundant (Shao et al., 2020). Bastnaesite and monazite are its main ores. One of the unique properties of Ce is its ability to undergo γ-α isostructural transition during which the volume of its unit cell abruptly collapses at a critical pressure while retaining its face-centered cubic configuration (Skorodumova et al., 2002). This γ-α isostructural transition in Ce can be induced at temperatures below the critical temperature Tc of about 600 K and under pressure (Lanatà et al., 2013).

Although the description of this isostructural transition phenomenon in Ce remains a subject of debate, the Kondo volume collapse (KVC) and the orbital-selective Mott transition within the Hubbard model are the two most common models that have been proposed to explain it. According to the KVC model proposed in 1982 (Allen and Martin, 1982; Lavagna et al., 1982), the γ-α isostructural transition of Ce is caused by a sudden alteration in the degree of hybridisation between the *f* electrons and the *spd* conduction bands, and hence, of the Kondo temperature (Lanatà et al., 2014). According to the Mott transition model proposed by Johansson (1974), the delocalisation of the 4f electron under pressure is responsible for the abrupt change in volume at the γ-α isostructural transition point.

This suggests that while the 4f electron in the γ phase is strongly localised on the Ce atom, the 4f states are part of the valence band in the α phase of Ce (Skorodumova et al., 2002). Consequently, the α phase has four valence electrons that participate in the

metallic bonding, while the γ phase has only three valence electrons. The difference in the number of valance electrons is what causes the huge volume change between the two phases during transition. These exceptional electronic structures of Ce make it suitable for production of various materials including alloys, phosphors, magnetics, cells for fuel cells and catalysts.

2.3.5.1.1 Cerium oxide

Cerium can form various oxides with varying proportion with oxygen in the range CeO_2 to Ce_2O_3 due to its unique properties of easily releasing or taking up oxygen. CeO_2, also known as ceria or Cerium (IV) oxide, is a yellowish white powder. Under certain reduction environments at an elevated temperature, CeO_2 can easily release oxygen to form oxygen-deficient cerium oxide (see Eq **(**2.1)) while preserving its fluorite lattice structure.

$$CeO_2 \leftrightarrow CeO_{2-x} + \frac{x}{2}O_2 \qquad \textbf{(}2.1\textbf{)}$$

From Eq **(**2.1), the extent of reduction determined by x is a function of both the temperature, surface termination and the oxygen partial pressure (Bulfin et al., 2013; Ghillanyova and Galusek, 2011). Ce_2O_3 (with oxidation state Ce^{3+}) is the most common oxide of cerium formed when CeO_2 (with oxidation state Ce^{4+}) is reduced under conditions of limited oxygen with the formation of oxygen vacancies during the lattice oxygen released process (Xiao et al., 2003). While CeO_2 and Ce_2O_3 are the main forms of cerium oxide, the key difference between both oxides lies in their structures. CeO_2 usually takes the form of a fluorite cubic-crystal structure with the $Fm\bar{3}m$ space group (Sun et al., 2012), and the Ce atoms are in a tetravalent valence state (Ce^{4+}) with empty Ce *4f* orbitals (Sun et al., 2019). The Ce_2O_3 mainly exhibits the hexagonal A-type structure (Bärnighausen and Schiller, 1985), and sometimes displays the C-type structure (Skorodumova et al., 2002) depending on conditions such as temperature and pressure. The A-type Ce_2O_3 has an hexagonal structure with space group $P\bar{3}m1$ (Qi et al., 2013) in

which all the Ce atoms exist in the Ce^{3+} state while each Ce^{3+} contains one localised *4f* electron (Sun et al., 2019). A typical representation of the crystallographic structure of unit cells of CeO_2 and Ce_2O_3 is given in Figure 2.9. Apart from different crystal structures, the physical properties of CeO_2 and Ce_2O_3 are at variance. Therefore, it is crucial to fully understand the theories behind the structures of these oxides of cerium and how they can be tuned or modified to enable their effective application in various processes.

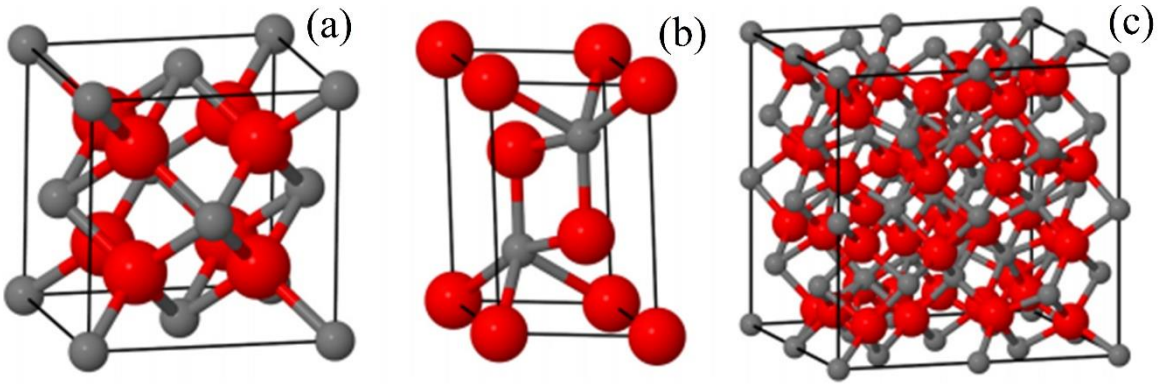


Figure 2.9 Crystallographic unit cells of (a) CeO_2 in the fluorite structure, (b) A-type Ce_2O_3 and (c) C-type Ce_2O_3 bulk structures. In the figures, red balls are oxygen and grey balls are cerium. Adapted from ref (Du et al., 2018).

Notwithstanding the limited knowledge about γ-α isostructural transition in Ce and the changes in the atomic electronic structure of CeO_2 after reduction, the unique redox property of CeO_2 together with its mechanical strength and high oxygen storage capacity (OSC) have been utilised in a wide range of applications including biomedical (Sathyaseelan et al., 2022; Li et al., 2020; Hu et al., 2023), agricultural (Wang et al., 2020; Mary Isabella Sonali et al., 2022; Pansambal et al., 2022), wastewater treatment (Apostolescu et al., 2023; Borgohain et al., 2022), and other catalytic processes (Yang et al., 2021; Montini et al., 2016). In this study, discussion on the applications of CeO_2 will be limited to reforming and methanation catalysis.

2.3.5.1.2 Application of ceria in heterogenous catalytic reactions

CeO_2 has been described as a material with exceptional redox property and high OSC, which are both crucial in minimising carbon deposition during carbon conversion processes such as methane dry reforming and CO or CO_2 methanation. However, it is less active in most heterogeneous catalytic processes when solely used as a catalyst. Therefore, the inherent properties of CeO_2 are activated either by employing it as a support where noble or transition metals are incorporated into its framework via impregnation, or by employing it as a catalyst promoter (Hatta et al., 2023).

For instance, Wang et al. (2015) fabricated a series of Ru/CeO_2 catalysts with tunable CeO_2 morphology/facet as a support and Ru as the active metal and tested the catalyst performances in CO_2 methanation. In this study, the authors stated that the oxygen vacancies in ceria behaved as the active sites where a high availability of the oxygen vacancies favoured the activation and conversion of carbon oxides. After the activation and adsorption, these oxygen vacancies also helped in breaking the C-O bond in the adsorbed carbon oxides. The C-O bond breaking results in the release of oxygen which fills the vacancies while the carbon undergoes hydrogenation to CH_4.

Li et al. (2022) synthesised CeO_2 with three different structures, namely, the honeycomb-lantern-like (CeO_2-H), spherical (CeO_2-S) and bulk particle (CeO_2-P) structures and impregnated them with nickel to produce various Ni/CeO_2 catalysts. These catalysts were then tested in dry reforming of methane (DRM). The author observed that the Ni/CeO_2-H catalyst exhibited the best activity towards DRM with 83.94% and 82.81% conversions of CO_2 and CH_4, respectively, and superior stability. This exceptional catalytic performance of the Ni/CeO_2-H catalyst was attributed to the surface spatial confinement effect of its outstanding honeycomb-lantern-like morphology.

Hou et al. (2015) investigated the catalytic performance of CeO_2 supported Ir catalyst in syngas production from ethanol dry reforming. According to the study, ethanol was completely converted at 973 K where the products mainly comprised hydrogen and carbon monoxide. In addition, the Ir/CeO_2 catalyst also displayed excellent stability after a 70h longevity test. The authors attributed the exceptional performance of Ir/CeO_2 catalyst to a strong interaction between iridium and ceria which was important for the

activation of ethanol and CO_2. It was also stated that this interaction helped to improve the catalyst's resistance Ir to sintering and coke formation.

Lian et al. (2020) employed first-principles DFT calculations to study the reaction mechanism and the stability of a Ni/CeO_2 catalyst in DRM. In this study, the authors investigated the activities of five different sites which included the Ni metal **(m)**, CeO_2 support **(s)**, metal–support interface **(ms)**, oxygen vacancy on support **(ovs)**, and oxygen vacancy at metal-support interface **(ovms)**. The results obtained from their investigation of the reaction pathway of CH_4 and CO_2 activation during DRM indicated that the m, ms and ovms sites were the most active sites for the activation of CH_4 while CO_2 activation was most favoured at the ovs and ovms sites. Notwithstanding, the activation of both CH_4 and CO_2 at the interface site was said to be balanced. It was also stated that the Ni/CeO_2 catalyst exhibited am exceptional stability which was attributed to the influence of the interfacial oxygen in the regeneration of active sites, and the prevention of coke formation. Some of the recent studies on CO_2 methanation using ceria as a catalyst support are given in Table 2.4.

Table 2.4 Application of ceria as catalyst support in CO_2 methanation conducted under atmospheric pressure.

Catalyst	Synthesis method	Investigation	Operating conditions			Activity		Refs
			Reaction gases	GHSV (mL g^{-1} h^{-1})	T (K)	X_{CO2} (%)	S_{CH4} (%)	
$Ni/Ce_{1-x}Pr_xO_{2-\delta}$	Citrate sol-gel and wet impregnation Reaction	Influence of Pr	$4H_2$:CO_2 and Ar	25,000	673	72	98	(Tsiotsias et al., 2022)
Ni/La-Pr-CeO_2 Ni/La-Sm-CeO_2 Ni/La-Mg-CeO_2	Wet impregnation	CeO_2 support modified with La, Pr, Sm, Mg	$4H_2$:CO_2 and Ar	25,000	673	~58 ~58 ~55	~100 ~100 ~100	(Siakavelas et al., 2021)
Ni-Co/CeO_2-ZrO_2 Ni-Mn/CeO_2-ZrO_2	Wet impregnation	Effect of CH_4 concentration	$4H_2$:CO_2	12,000	623	72 ~66	~99 ~87	(Pastor-Pérez et al., 2020)
Ni/CeO_2	Incipient wetness impregnation	Effect of morphologies	$4H_2$:CO_2	12,000	623	~84	~99	(Bian et al., 2023)
Ni/CeO_2-NZP	Wet impregnation	Effect of morphologies, effect of operating parameters	$4H_2$:CO_2 and N_2	8,200[b]	573	~78	~100	(Varvoutis et al., 2023)
Ni/CeO_2	Wet impregnation	Effect modifying CeO_2	$4H_2$:CO_2 and N_2	60,000	623	~82	~100	(He et al., 2022b)

Table 2.4 Application of ceria as catalyst support in CO_2 methanation conducted under atmospheric pressure (Continuation).

Ni/CeO_2	Wet impregnation	Effect of morphologies	$4H_2$:CO_2 and He	21,000	623	~58	~100	(Jomjaree et al., 2021)
Ni/CeO_2	Sol-gel	Synthesis method	$4H_2$:CO_2 and N_2	40,000	523	82.5	94.8	(Ye et al., 2020)
Ni/CeO_2	One-pot	Synthesis method	$4H_2$:CO_2	45,000	598	~79	~100	(Tang et al., 2021a)
Ru/CeO_2	Wet impregnation	Effect of morphologies	$4H_2$:CO_2 and N_2	72,000	598	~79	99	(Sakpal and Lefferts, 2018)
Ni/CeO_2	Electrospinning	Synthesis method	$4H_2$:CO_2	36,000	598	82.3	~99	(Hu et al., 2022)
$Ru/Ce_{0.9}Cr_{0.1}O_x$	Wet impregnation	Roles of surface oxygen vacancies and hydroxyl groups	$4H_2$:CO_2	36,000	598	~82	~99	(Xu et al., 2021b)
12Ni3Co/M-Ce80Zr20	Incipient wetness impregnation	Influence of Mn, Co, Fe, and Cu	$4H_2$:CO_2	12,000	623	~80	~99	(Xu et al., 2021a)
12Ni3Mn/M-Ce80Zr20						~76	~98	
12Ni3Fe/M-Ce80Zr20						~76	~98	
12Ni3Cu/M-Ce80Zr20						~30	~81	

Table 2.4 Application of ceria as catalyst support in CO_2 methanation conducted under atmospheric pressure (Continuation).

9Ni/CeEu Ni/CeO_2 Ni/Eu_2O_3	Co-precipitation	Influence of Eu	$4H_2$:CO_2 and N_2	30,300	473	~99 ~75 ~24	-	(Zhang et al., 2022)
1%Co-15%Ni/CeO_2	wet impregnation	Influence of Co, reactor system	$4H_2$:CO_2	52,000[b]	573	82	98	(Hasrack et al., 2022)

2.3.5.2 Alumina

Aluminium oxide, also known as alumina, is an important ceramic material which is used in a wide range of industrial processes such as in the production of adsorbents for wastewater treatment and water purification (Baran Aydın et al., 2022; Wang et al., 2022), refractory materials (Liu et al., 2022a), abrasives (Nadolny, 2014), biomedicine (Gudkov et al., 2022; Pourmadadi et al., 2022) and catalyst development for heterogeneous reactions. Alumina can be produced from Bauxite which is the principal ore of aluminium. Meanwhile, Bauxite mainly comprises of a mixture of aluminium hydroxides namely boehmite (γ-AlO(OH)), diaspore (α-AlO(OH)) and gibbsite ($Al(OH)_3$). Depending on the temperature and other operating conditions, these aluminium hydroxides can be transformed into various crystalline polymorphic phases including the metastable aluminas (γ-Al_2O_3, δ-Al_2O_3, and θ-Al_2O_3) which can further undergo a series of phase transitions to form the most stable form of alumina (α-Al_2O_3) as shown in Figure 2.10.

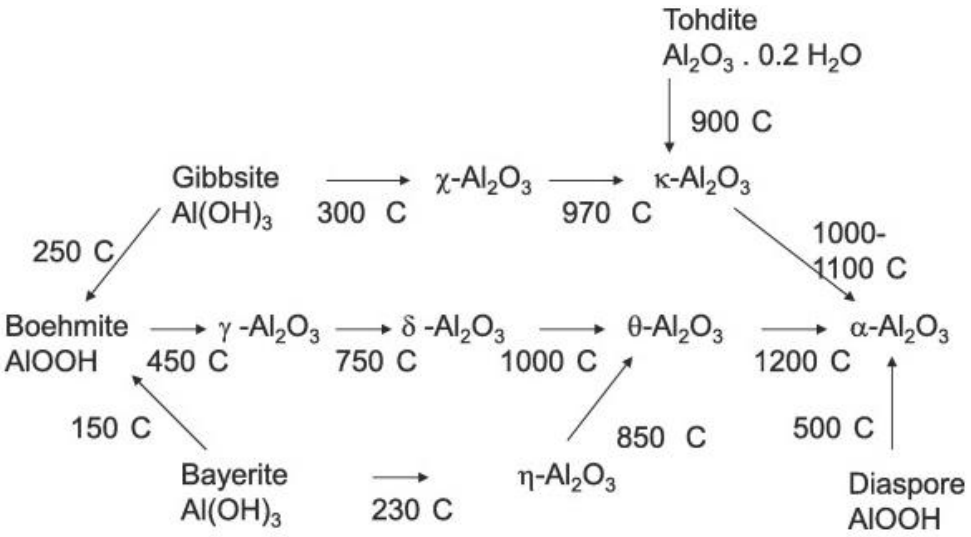


Figure 2.10 Schematic of the phase transformation pathways of aluminium hydroxides and oxides after heat treatment. Adapted from ref (Busca, 2019).

Apart from the phases of alumina described in Figure 2.10, other intermediate phases exist. An example is the amorphous (non-crystalline) and metastable hydratable alumina (ρ-Al_2O_3) phase which can be obtained from gibbsite by flash calcination within a temperature range of 575 of 700 K in a vacuum (Wefers and Misra, 1987; Salomão et al., 2017). The crystal data of

some of the metastable and stable aluminas are given in Table 2.5 while the physical properties of the most common transitional aluminas formed at various at their various calcination temperatures are shown in Table 2.6.

Table 2.5 Crystal data of stable and metastable aluminas. Adapted from ref (Shackelford and Doremus, 2008; Busca, 2019).

Alumina phase	Crystal structure	Space group	Lattice parameters, (Å)		
			A	B	c
γ-Al_2O_3	Tetragonal	$Fd\bar{3}m$	7.95	–	7.79
η-Al_2O_3	Cubic (spinel)	$Fd\bar{3}m$	7.90	–	–
θ-Al_2O_3	Monoclinic	C2/m	5.63	2.95	11.86
α-Al_2O_3	Hexagonal (rhombohedral)	$R\bar{3}c$	4.758	–	12.991
δ-Al_2O_3	Tetragonal	$P\bar{4}m2$	7.97	–	23.47
κ-Al_2O_3	Orthorhombic	Pna21	8.49	12.73	13.39

Table 2.6 Physical properties of the most common transitional aluminas at different calcination temperatures. Adapted from ref Bartholomew & Farrauto (2011).

$T_{calcination}$ (^0C)	Phase	Surface area ($m^2\ g^{-1}$)	V_{pore} ($cm^3\ g^{-1}$)	D_{pore} (nm)
250	Pseudoboehmite	390	0.50	5.2
450	γ-Al_2O_3	335	0.53	6.4
650	–	226	0.55	9.8
850	–	167	0.58	14
950	δ-Al_2O_3	120	0.50	16.6
1050	θ-Al_2O_3	50	0.50	28
1200	α-Al_2O_3	1 to 5	–	–

Amongst the alumina phases, the gamma alumina (γ-Al_2O_3) is the most extensively employed in catalysis as a support because it is relatively economical to prepare, possesses exceptional mechanical strength, and is easily tunable to give high surface area. Moreover, the presence of weak and moderate acid strength on the surface of alumina makes it suitable as a support or even as a standalone catalyst in some processes. For instance, studies have shown that the ordered mesoporous γ-Al_2O_3 can be employed as a standalone catalyst for the synthesis of dimethyl ether due to its high activity and selectivity (Keshavarz et al., 2010; Luan et al., 2015). In some cases, γ-Al_2O_3 is functionalised to improve its Brönsted acid sites strength for other reactions such as fluid catalytic cracking (FCC) since the traditional material is considered to have moderate to high Lewis acidity which encourages severe coke formation as a result of excessive hydrogen transfer reactions (Feng et al., 2014).

However, the use of alumina as a standalone catalyst for CO_2 methanation is limited and not feasible because while the CO_2 can be adsorbed and activated on the surface, alumina lacks the main sites required for the activation of the H_2 reactant. Therefore, alumina serves as a support for the impregnation of active metals such as Ni, Ru, Rh and Pd which provide the medium for the activation of the H_2 reactant, thereby improving the overall catalyst performance and selectivity towards CH_4. Meanwhile, the performance of these metal based Al_2O_3 catalysts depends on various factors including the preparation method and the reaction operation conditions.

For instance, Rahmani et al. (2014) prepared Ni/Al_2O_3 catalysts by varying the amount of Ni from 10 to 25 wt.% using the wet impregnation method. Then, the effect of Ni content on the performance of Ni/Al_2O_3 catalysts in CO_2 methanation was investigated. The results as represented by Figure 2.11 revealed that all the catalyst performances generally improved as the operating temperature increased from 473 K and attained an optimum at 623 K. The optimum Ni content was found to be 20 wt.%. The decline in the activity of the catalyst at higher Ni content (25 wt.%) was attributed to the favoured formation of bigger crystallite size and lower surface area of the catalyst, resulting in a decrease in CO_2 conversion.

Daroughegi et al. (2017) also conducted similar studies on the effect of Ni content on the performance of Ni/Al_2O_3 catalysts in CO_2 methanation but the Ni/Al_2O_3 catalysts were synthesised by the ultrasound-assisted co-precipitated method. The results indicated that the optimum temperature in this study was also at 623 K, but the optimum Ni content was 25 wt.%.

The small discrepancy between the results of this study and Rahmani et al. (2014) may be ascribed to other factors such as the synthesis method and the synthesis operating conditions, the reactor's setting, the reaction operating conditions, and finally, measurement error. In any case, it is crucial to always consider these factors while testing for the performance of a catalyst in CO_2 methanation.

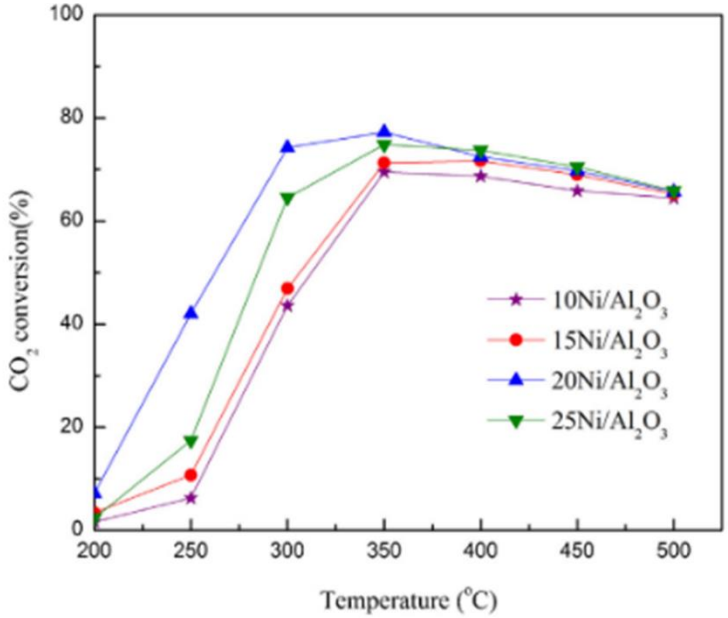


Figure 2.11 Effect of Ni content on CO_2 conversion in CO_2 methanation conducted at GHSV = 9000 mL g^{-1}_{cat} h^{-1}, H_2/CO_2 molar ratio = 3.5.

In some cases, a promoter is introduced into the Al_2O_3 supported catalyst to improve properties such as carbon formation resistance and the overall stability of the catalyst. For instance, Hu et al. (2012) reported that the addition of MgO as a promoter into Ni/Al_2O_3 improved the catalyst's stability by suppressing the formation of carbon deposition during CO methanation. Shafiee et al. (2022) reported that the addition of Fe, Mn, La, Ce, and Ba promoters into the bimetallic $15Ni\text{-}12.5Co/Al_2O_3$ catalyst resulted in the improvement of the catalyst's performance by reducing the average crystallite size and enhancing the adsorption and activation capacity of CO_2 on the catalyst.

2.3.5.3 Yttria-stabilized zirconia

Zirconia, also known as zirconium dioxide (ZrO_2) has shown to be an exceptional catalyst support for the CO_2 hydrogenation owing to its high thermal and chemical stability, high mechanical strength, and strong resistance to carbon deposition. These superior properties of ZrO_2 can be attributed to its physicochemical properties which include the presence of defect sites (e.g. oxygen vacancies), Lewis acid sites (Zr^{3+}, Zr^{4+}), adsorbed O^{2-} and OH groups (basic sites), and Zr^{4+}-O^{2-} acid-base pairs (Jia et al., 2019; Alves et al., 2021). These properties also make the tuning and doping of ZrO_2 more feasible for various catalytic processes. Moreover, the Lewis basic oxygen vacancies on ZrO_2 are crucial for the adsorption and activation of CO_2 (Ilsemann et al., 2021) which is one of the major steps in the mechanism of CH_4 formation during the CO_2 hydrogenation.

Generally, pure zirconia exists in three different crystal configurations at atmospheric pressure and different temperatures: monoclinic (m-ZrO_2), tetragonal (t-ZrO_2) and cubic (c-ZrO_2) (Kouva et al., 2015; Fan et al., 2021; Najafi et al., 2021; Kalita et al., 2021; Comba et al., 2021). Notwithstanding the great properties displayed by ZrO_2, its redox activity is low due to the difficulty of its surfaces in discharging lattice oxygen atoms to form vacancies (de Souza and Appel, 2021). This challenge is overcome by doping the ZrO_2 with metals with a lower valency than Zr (less than +4) such as Ni, La, Co, Ca, and Ti. The introduction of these dopants helps in lowering the energy required for the formation of oxygen vacancies through the substitution of some of the Zr^{4+} ions and the cleavage of the local symmetry of the lattice structure (de Souza and Appel, 2021). The introduction of lower valence dopants also results in the alteration of the electronic arrangement of ZrO_2, which affects the catalytic properties. It is worth noting that two unpaired electrons are left behind when oxygen vacancies are formed. These unpaired electrons can influence the catalytic cycle by enhancing the catalyst's surface activity (de Souza and Appel, 2021).

At low temperatures, the alteration in the crystal structure of ZrO_2 can cause instability, which limits its use in industry (Ricca et al., 2015; Chevalier et al., 2009). This is why the cubic and tetragonal forms are generally stabilised at room temperature by doping with various metal oxides such as CeO_2, MgO, CaO and Y_2O_3 (Chevalier et al., 2009). Consequently, Y_2O_3 is mostly employed in stabilising ZrO_2 owing to the improved stability effect it provides (Fan et al., 2021). Another reason for the high preference in stabilising ZrO_2 by Y_2O_3 is its influence

in creating an oxygen vacancy in the anionic sub-lattice when two Zr^{4+} ions are replaced by two Y^{3+} ions, and this assists in the migration of oxygen ions through the yttria-stabilised zirconia (YSZ) material (Hofer et al., 2019; Cousland et al., 2014).

The use of ZrO_2 as a support for CO_2 methanation catalysts has been reported by many researchers. Gac et al. (2020) studied the effect of Ni loading on Al_2O_3, ZrO_2 and CeO_2 supports. The authors reported that the increase in Ni loading from 10% to 40% on the ZrO_2 resulted in a gradual decrease in the Ni crystallite size. The CeO_2-supported catalysts showed the best performance followed by the ZrO_2-supported catalysts in terms of CO_2 conversion at 553K. While an increase in Ni loading was favoured for the CeO_2 support, the performance of the ZrO_2-supported catalyst was found to decrease beyond 20%Ni loading. In another study by Traitangwong et al. (2020), Ni loading was varied from 15% to 45% over a Ni-modified ceria-zirconia support (e.g., $Ni_{0.05}Ce_{0.20}Zr_{0.75}O_2$) and the catalysts were tested for CO_2 methanation. The catalyst with 45% Ni loading exhibited the best performance. The authors stated that increasing the Ni loading favoured the number of H_2 molecules that were activated, which translated into higher catalytic performance.

Kosaka et al. (2020) investigated the influence of Ni content on the performance of a Ni/YSZ catalyst by varying the Ni loading from 25% to 75%. The authors found that the catalyst performance was favoured with the increase in Ni content where the 75%Ni/YSZ catalyst displayed the best activity. Kesavan et al. (2018) investigated the influence of Ni particle size on the performances of Ni-based YSZ-supported catalysts during CO_2 methanation. The variation in Ni^0 particle sizes for the Ni/YSZ catalysts was achieved by employing different preparation steps, namely wetness impregnation, electroless plating and mechanical mixing. The study revealed that the size of Ni^0 and its morphology influenced the Ni/YSZ catalysts, where the catalyst with a smaller Ni^0 particle size exhibited the best performance. It should be noted that Ni^0 (reduced nickel) is obtained when nickel oxide (NiO) is reduced in a hydrogen environment at the reduction temperature corresponding to the catalyst structure.

2.3.5.4 Santa Barbara Amorphous 15

Santa Barbara Amorphous 15 (see Figure 2.12), also known as SBA-15, is a mesoporous silica comprising of uniform hexagonally ordered cylindrical mesopores in one dimension with a

narrow pore-size distribution and a tunable pore diameter within the range of 5 and 30 nm (Zhao et al., 1998a). The mesopores in SBA-15 are usually connected by a microporous network known as the corona (Imperor-Clerc et al., 2000; Ryoo et al., 2000). This connection of the mesopores with each other was stated to be responsible for the high surface area of SBA-15. Ryoo et al. (2000) were the first to identify the existence of a microporous network within the framework of SBA-15 during an investigation into the imaging of inverse platinum replica of ordered mesoporous structures. The presence of interconnection of mesopores through the network of nanorods was observed, and these rods were later referred to as micropores.



Figure 2.12 Structure of SBA-15 formed from the hydrolysis of Pluronic 123 and tetraethyl orthosilicate. Modified from ref (Chaudhary and Sharma, 2017).

Fulvio et al. (2005) suggested that the hexagonal configuration of the nanorods is preserved by the network between the mesopores and micropores even after silica removal in its inverse replicas, and this benefits the diffusion of species inside the entire porous structure. Other unique properties such as easily tunable pore structure, large pore size, and high hydrothermal and mechanical stability have made SBA-15 very attractive and extensively studied silica material (Rahmat et al., 2010; Ryoo et al., 2000).

2.3.5.4.1 Synthesis of SBA-15

SBA-15 can be synthesised by acid hydrolysis (pH ≤ 2) of an amphiphilic triblock copolymer surfactant of the type poly(ethylene oxide)–poly(propylene oxide)–poly(ethylene oxide) or Pluronic P-123 as structure directing agent with a silica precursor as reported in the literature

(Zhao et al., 1998a, 1998b). Typically, a triblock copolymer known as Pluronic P-123 is dissolved in an aqueous solution of HCl whose pH is regulated between 1 and 2 under thorough stirring. After the complete dissolution of the surfactant, tetraethyl orthosilicate (TEOS) is added in drops as the silica precursor and the mixture is stirred continuously for about 24 h. The SBA-15 formed is then filtered off while rinsing with deionised water until the pH is neutral or about 7. This sample is dried in an oven and then calcined to remove residual organic template.

2.3.5.4.2 Applications of SBA-15

The unique properties of SBA-15 include high surface area, large pore size and volume and hydrothermal stability and make it a promising material for many applications. In some cases, mesoporous SBA-15 is modified or functionalised to make it more suitable for applications such as in the drug delivery system (Ulagesan et al., 2022), wastewater treatment (Hassanzadeh-Afruzi et al., 2022; Ezzeddine et al., 2023) and sensing materials (Saha et al., 2023; Mohammadi Ziarani et al., 2023). In heterogeneous catalysis, SBA-15 is extensively employed as support in catalyst synthesis since active metals can be evenly distributed and dispersed on the surface (Lin et al., 2023). In a dry reforming of methane experiment, Song et al. (2023) synthesised Ni/SBA-15 and Ni/SiO_2 catalysts using the ammonia evaporation method. The results revealed that the Ni/SBA-15 catalyst was superior to the microporous silica supported Ni catalyst (Ni/SiO_2). This excellent catalytic activity of Ni/SBA-15 was attributed to the high dispersion of Ni in the framework of SBA-15, and consequently caused a significant resistance to Ni sintering and carbon deposition. Meanwhile, the Ni particles were not well dispersed in the Ni/SiO_2 due to smaller pore size, and this encouraged relatively more intensive Ni sintering and carbon deposition.

Hongmanorom et al. (2021) prepared a series of Ni/SBA-15 catalysts by using ammonia evaporation (Ni/SBA-15-AE and Ni-Mg/SBA-15-AE) and wet impregnation (Ni/SBA-15-WI) methods and tested the catalysts in CO_2 methanation. The results of this investigation are presented in Figure 2.13 (a) and (b). As seen in Figure 2.13 (a), the increase in temperature from 473 to 673 K favoured CO_2 conversion for all the catalysts.

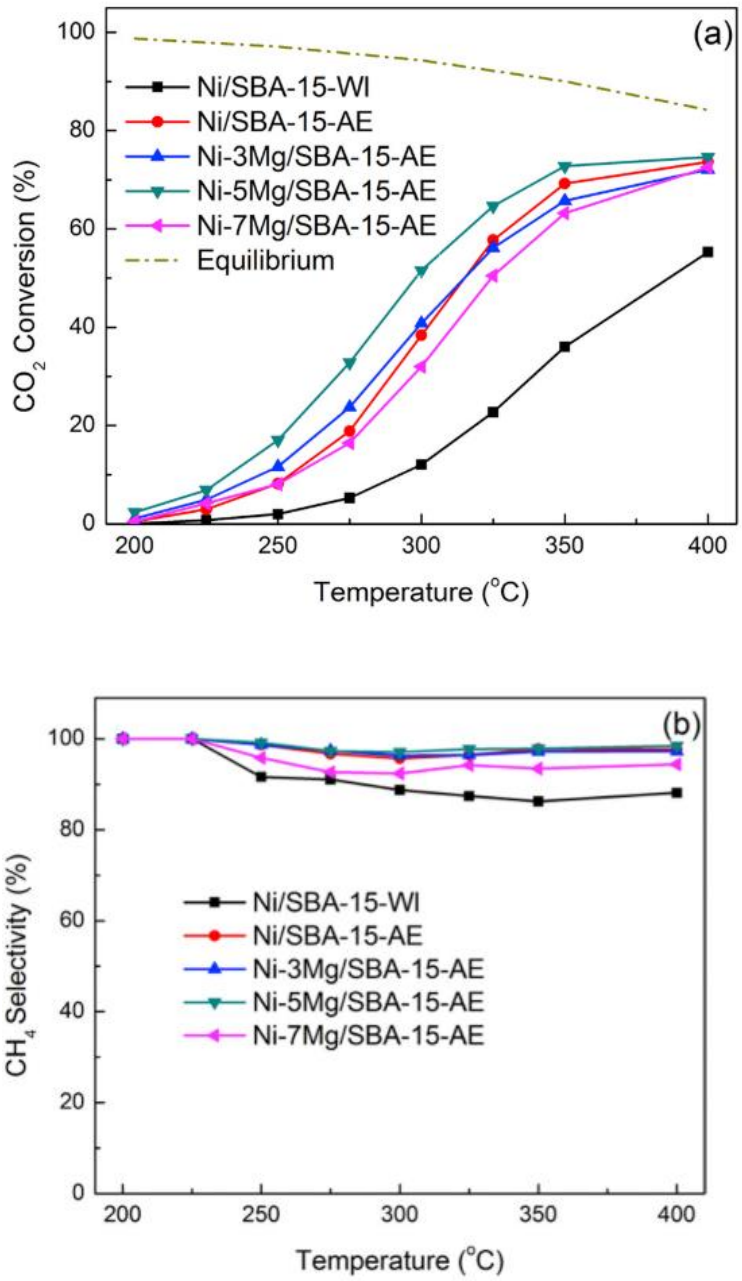


Figure 2.13 Activity profile showing (a) CO_2 conversion and (b) CH_4 selectivity during CO_2 methanation over Ni-based SBA-15 catalysts at atmospheric pressure, GHSV of 30,000 mL g^{-1} h^{-1}, H_2/CO_2 ratio of 4 and operating temperature within the range of 473 – 673 K. Ref (Hongmanorom et al., 2021).

However, the reverse was the case for CH_4 selectivity as shown in Figure 2.13 (b). The decrease in CH_4 selectivity with increasing temperature was attributed to the occurrence of side reactions such as the reverse water gas shift (RWGS) reaction which are encouraged at higher reaction temperatures. In terms of the preparation method, the Ni/SBA-15 catalyst prepared by the ammonia evaporation showed a superior activity to the one prepared by wet impregnation.

Overall, the Ni-5%Mg/SBA-15-AE catalyst showed the best performance. The authors stated that the introduction of 5 wt.%Mg into Ni/SBA-15 caused an increase in the medium basic sites, and this favoured the activation of CO_2 with an overall improvement in the activity. In terms of stability, both Ni/SBA-15-AE and Ni-5Mg/SBA-15-AE were stable for a 50 h on-stream longevity test conducted at 623 K while the Ni/SBA-15-WI catalyst showed a steady decline. This study clearly revealed that the type of synthesis method employed, and the operating conditions greatly influence the activity of SBA-15 supported catalysts.

2.2 Deactivation mechanism of CO_2 methanation catalysts

Catalyst deactivation refers to the loss of catalytic activity over time due to various factors such as poisoning, fouling, thermal deactivation, or structural changes. The tolerance of a catalyst to deactivation depends on its physicochemical properties which may be influenced by synthesis methods or reaction operating conditions. A deactivation study is crucial to understand how long a catalyst can last on stream before completely losing its catalytic properties. In industry, where large quantities of catalysts are employed, a highly stable catalyst is more economical than the less stable since the number of catalyst replacement in the reactor bed is greatly reduced. Moreover, deactivation studies can help to draw a connection between catalyst deactivation, the synthesis method, and the design of the process employed. In this section, the various causes of catalyst deactivation will be discussed.

2.4.1 Fouling

In heterogeneous catalysis, fouling refers to the accumulation of various contaminants such as carbon deposits on the surface of a catalyst. These contaminants can clog the catalyst's active sites, preventing the reactants from reaching them. Carbon deposition has been a major concern for many industrial processes that involve heterogeneous catalysis as it prevents efficient conversion. The carbon formed during these processes may hinder catalyst performance through the occlusion of their active sites or fouling of their pores (Wang et al., 2017). The extent of catalyst deactivation resulting from carbon deposition depends on the nature of the carbon formed while the nature of carbon formed is strongly influenced by the reaction operating conditions (Jana et al., 2013). According to Bartholomew (2001), the carbon

deposited during CO decomposition on nickel can exist in different forms depending on the operating temperature (Table 2.7), and these forms of carbon deposits may be reactive or non-reactive. The commonest forms of carbon deposits are the adsorbed atomic carbon, amorphous carbon, whisker or filamentous carbon, and graphitic carbon.

Table 2.7 The possible forms of carbon deposits by decomposition of CO on nickel (Bartholomew, 2001).

Morphologies of carbon deposits	Classification	Formation temperature (K)	Maximum temperature for reaction with H_2 (K)
Adsorbed, atomic (surface carbide)	C_α	473 to 673	473
Polymeric, amorphous films or filaments	C_β	523 to 773	673
Vermicular filaments, fibres, and/or whiskers	C_v	573 to 1,273	673 to 873
Nickel carbide (bulk)	C_γ	423 to 523	548
Graphitic (crystalline) platelets or film	C_c	773 to 823	823 to 1,123

2.4.1.1 Adsorbed atomic carbon

Adsorbed atomic carbon is a well-known catalyst deactivation species that can be deposited on the surface of various catalysts during chemical reactions. When carbon-containing molecules react on the catalyst surface, they can break down into smaller species, including atomic carbon. This atomic carbon can then adsorb onto the surface of the catalyst, forming carbon deposits that can cover active sites and reduce the catalyst's ability to catalyse reactions.

Adsorbed atomic carbon deposit is a reactive carbon formed at peak temperature within 523 to 623 K and can easily be removed from catalyst surfaces by passing a stream of H_2 through the catalyst system (Takahara et al., 2013). Pour et al. (2010) stated that the adsorbed atomic carbon is formed because of the dissociative adsorption of CO during Fischer–Tropsch synthesis (FTS) and is favoured with the increase in basicity of the catalyst surface. Swart et al. (2008) reported

that adsorbed atomic carbon possesses high mobility in reaction conditions similar to that of Fischer-Tropsch synthesis owing to its low barrier of diffusion estimated to be around 40 to 50 kJ/mol. However, high operating temperatures around 773 to 1,173 K may cause atomic carbon to deactivate a Ni catalyst because it can dissolve and precipitate into the catalyst framework within a depth greater than 50 to 70 nm at such high temperatures (Argyle and Bartholomew, 2015).

The formation of adsorbed atomic carbon is a complex process that depends on various factors, including the type of catalyst, the reaction conditions, and the nature of the carbon-containing molecules. The rate and extent of carbon deposition can vary widely, but in general, it tends to increase with increasing temperature, pressure, and carbon-containing molecule concentration. The presence of adsorbed atomic carbon can have several negative effects on catalyst performance. First, it can block active sites on the catalyst surface, reducing its ability to catalyse reactions. Second, it can alter the electronic properties of the catalyst surface, making it less active or selective. Third, it can promote the formation of other deactivation species, such as coke or carbonaceous deposits, which can further reduce catalyst performance.

Several strategies can be used to mitigate the effects of adsorbed atomic carbon on catalyst performance. One approach is to use catalysts that are less prone to carbon deposition, such as those with high metal dispersion or high surface area. Another approach is to modify the catalyst surface to make it more resistant to carbon deposition, for example, by adding metal oxides or other surface modifiers. Additionally, operating the reaction under conditions that minimise carbon deposition, such as low temperature or low reactant concentrations, can also be effective in reducing catalyst deactivation due to adsorbed atomic carbon. Finally, catalyst elements can be added to promote the oxidation of deposited carbon, thus tilting the equilibrium towards CO_2 formation and therefore carbon removal.

2.4.1.2 Amorphous carbon

Amorphous carbon is a moderately reactive carbon which is favourably formed at temperatures within the range of 523 to 773 K during the reforming of hydrocarbons, Fischer–Tropsch synthesis (FTS) or the methanation reaction by CO dissociation (Xu & Bartholomew, 2005). The accumulation of amorphous carbon on catalyst surfaces blocks the access of the reacting

species to the active sites, thereby causing catalyst deactivation. Unlike adsorbed atomic carbon, which forms on the catalyst surface, amorphous carbon can form within the catalyst bulk or on the support material. The formation of amorphous carbon can occur due to several reasons, including the incomplete oxidation of carbon-containing molecules, and the decomposition of hydrocarbons.

Several techniques can be employed to mitigate the effects of amorphous carbon on catalyst performance. One approach is to remove the amorphous carbon through techniques such as oxidation at temperatures within the range of 500 to 850 K (Cao et al., 2022a) or steam treatment (Tobias et al., 2006). However, these methods may also remove active catalyst species, leading to a decrease in catalytic activity. Another approach is to use catalysts that are more resistant to amorphous carbon formation, such as those with a high metal dispersion or those that utilise support materials that are less prone to carbon deposition. Additionally, operating the reaction under conditions that minimise the formation of amorphous carbon, such as using lower temperatures or reducing the concentration of carbon-containing molecules, can also help to reduce catalyst deactivation due to amorphous carbon.

2.4.1.3 Whisker carbon

Whisker carbon is a filamentous carbon with a diameter in the range of 10 to several hundred nm generally formed during the dissociation of CO, a reaction involving carbonaceous gases and metal catalyst particles at around 673 to 1273 K (Baker et al., 1975), or incomplete combustion of hydrocarbons, which can produce soot particles that agglomerate and form whisker carbon (Tibbetts, 1984). A filamentous carbon usually carries the catalyst particles at its growing end. In some cases, the catalyst particles are either found at the middle of the filament or the filament completely originates from a single particle (Figueiredo and Bernardo, 1990). Whisker carbon, which is believed to be the most destructive form of carbon (Aasberg-Petersen et al., 2011), can cause catalyst deactivation by physically blocking the active sites of the catalyst and prevent reactants from accessing them. This decreases the efficiency of the catalyst and ultimately leads to its deactivation.

In addition to physically blocking the active sites of the catalyst, whisker carbon can also affect the chemistry of the reaction. Whisker carbon can cause the fragmentation of catalyst pellets

when the growing whisker is forced into the catalyst supports' pore wall owing to its relatively higher mechanical strength (Baharudin et al., 2020). This catalyst fragmentation may result in increased pressure drop and loss of activity to reactor blockage in steam reformers, and hot spots/hot bands that can lead to reactor failure (Aramouni et al., 2018). Finally, Whisker carbon can act as a support for other materials that are not part of the desired reaction, such as metal impurities or other contaminants. These impurities can then interact with the reactants and produce unwanted by-products, leading to decreased selectivity and efficiency of the catalyst.

Furthermore, whisker carbon can also alter the electronic properties of the catalyst. The formation of whisker carbon can change the electronic structure of the catalyst, leading to a change in its catalytic activity. This can lead to decreased efficiency or even complete deactivation of the catalyst. There are still discrepancies in the understanding of the mechanism for whisker carbon growth, but detailed work on this topic can be found in the literature (Helveg et al., 2011). Overall, the formation of whisker carbon can have significant effects on catalyst deactivation. Understanding the mechanisms by which whisker carbon forms and its impact on catalysts is crucial for developing strategies to mitigate its effects and improve the efficiency and selectivity of industrial processes.

2.4.1.4 Graphitic carbon

Graphitic carbon is a type of carbon that is highly stable and resistant to oxidation, and this makes it a common by-product that causes catalyst deactivation in many catalytic reactions. Graphitic carbon is formed at higher temperatures due to its stability. This implies that both the atomic and amorphous carbons can be converted to graphitic carbon under high temperature (>700 K) conditions over a long duration. Nakamura and Toyoshima (1988) stated that carbidic carbon formed on the surface of a cobalt catalyst at 500 K by the Boudouard reaction was transformed into graphitic carbon at 700 K. Agrawal et al. (1981) stated that the formation of graphite over a Ni catalyst during methanation is more favourable at temperatures above 598 K, while the graphitisation rate slows at temperatures below 573 K. Apart from the operating temperature, it has been reported that a reaction involving a lower ratio between H_2 and CO can favour the conversion of both atomic and amorphous carbon into graphitic carbon (Chen et al., 2018).

When graphitic carbon accumulates on the surface of a catalyst, it blocks the active sites, resulting in deactivation, and this can hinder or end the catalytic reaction. The deactivation of catalysts by graphitic carbon can occur via various mechanisms, including blocking the active sites, adsorption of reactant molecules onto the graphitic carbon surface, and reducing the availability of reactive species. Additionally, graphitic carbon can act as a barrier to the diffusion of reactants and products, which can further limit the activity of the catalyst. It is also worth noting that graphitic carbon can grow into a whisker carbon between catalyst support and metal particle resulting in the mechanical destruction of the catalyst (Kihlman and Simell, 2022).

To mitigate the effects of graphitic carbon on catalyst deactivation, several strategies have been developed. One approach is to modify the catalyst surface to prevent the accumulation of graphitic carbon. This can be achieved through the addition of active metals or metal oxides to the catalyst surface, which can promote the oxidation of carbon species and prevent the formation of graphitic carbon. For example, Siang et al. (2021) reported that a modified fibrous silica alumina supported rhodium catalyst employed for CO_2 methanation reaction exhibited high resistance to the formation of graphite. The author attributed the excellent resistance of the catalyst to the improvement of the catalyst surface for CO_2 adsorption, which effectively removed the amorphous carbon deposits via a CO_2 gasification process. Shakir et al. (2022) modified a $Ni/MgAl_2O_4$ catalyst by introducing boron into the structure, testing in DRM. The B-modified catalyst was found to show a superior resistance to the deposition of graphitic carbon compared to the unmodified catalyst. The high resistance was ascribed to the promotional effect of B leading to the formation of Ni-B species along with metallic Ni, particle size control, the stabilisation of the metallic state, and the weakening of the Ni-C interaction, and these helped to improve the catalyst activity and decrease the rate of deactivation.

2.4.2 Poisoning

Catalyst poisoning is the loss of activity of a catalyst due to its exposure to contaminants that act as poisons. These poisons can bond with active sites on the catalyst surface and alter its chemical or physical properties, reducing its ability to catalyse the desired reaction. Poisons can be introduced to the catalyst in various ways, such as through the feedstock or the catalyst

preparation process. Some common examples of catalyst poisons include sulfur, heavy metals, and halides depending on the type of reaction to be catalysed. In DRM or the methanation reaction, sulfur is a common poison that can deactivate catalysts by forming stable compounds with active sites on the catalyst surface, reducing their availability for the desired reaction. This is a particular problem in the petrochemical industry, where crude oil and natural gas often contain high levels of sulfur compounds (Shi and Wu, 2021). The problem could also arise from employing CO_2 derived from industrial exhaust gases since they often contain sulfur (Wolf et al., 2019). In some cases, the presence of sulfur can also promote the formation of carbon deposits on the catalyst surface, further reducing its activity (Xie et al., 2011).

Catalyst poisoning can be managed by (1) modifying the catalyst with lanthanides such as La and Ce, or alkaline (K) and alkaline-earth (Mg, Ca, Ba) metals for improved tolerance to sulfur poisoning; (2) carefully selecting feedstock sources with high purity, and (3) employing operating conditions that are unfavourable for the activity of the contaminants or poisons (Yeo et al., 2019; Nirmal Kumar et al., 2021). Xie et al. (2012) investigated the sulfur tolerance and carbon resistance of supported noble metal catalysts in steam reforming of liquid hydrocarbons. In this study, Al_2O_3, CeO_2, SiO_2, and MgO were employed as the catalyst supports while Rh, Ru, Pt, and Pd were the active metal. The activity test results revealed that CeO_2-supported Rh and Pt catalysts displayed excellent performances despite the presence of sulfur. The high sulfur tolerance and catalytic activity of these catalysts were attributed to the promotional effect of CeO_2 which also influenced the carbon gasification, resulting in high resistance to carbon deposition compared with other catalysts tested. In another study, the addition of CeO_2 into a Ni/Al_2O_3 catalyst was reported to enhance the catalyst's resistance to sulfur poisoning in CO_2 methanation (Alarcón et al., 2020). The various studies reported indicate that the use of catalyst supports and/or metal components (the active metal or promoter) with low affinity for H_2S adsorption is crucial in developing high sulfur-tolerant heterogeneous catalysts.

2.4.3 Thermal deactivation

Thermal deactivation is a common form of catalyst deactivation that occurs when a catalyst is exposed to high temperatures, which can lead to irreversible changes in its structure and activity (Argyle and Bartholomew, 2015). Thermal deactivation can occur in automotive three-way

catalysts during fuel shutoff used for enhancing fuel economy (Zheng et al., 2015b). This phenomenon can be particularly problematic in industrial processes that involve high-temperature reactions, such as petrochemical refining, where catalysts are used to promote chemical reactions. When a catalyst is undergoing thermal deactivation, the high temperatures can cause physical changes in the catalyst, such as sintering or melting, which can alter its surface area, pore size distribution, and other key properties (Fu et al., 2012). These changes can reduce the catalyst's ability to interact with reactants, leading to reduced activity and selectivity.

In addition to physical changes, thermal deactivation can also cause chemical changes in the catalyst. For example, high temperatures can lead to the formation of new phases or the migration of metals within the catalyst structure, which can alter its catalytic properties. These changes can be particularly pronounced for catalysts containing active metals such as platinum or palladium, which are known to be susceptible to high-temperature deactivation. Another important factor in thermal deactivation is the rate at which the temperature changes occur. Rapid changes in temperature, such as those that occur during shutdowns or startup procedures, can cause thermal shock and thermal stress, which can lead to cracking, deformation, or other forms of damage to the catalyst structure (Argyle and Bartholomew, 2015; Bartholomew, 2001). This damage can further reduce the catalyst's activity and stability.

To mitigate the effects of thermal deactivation, catalysts are often designed with heat-resistant materials and structures, and operating conditions are carefully controlled to minimise thermal stress and shock (Zhang et al., 2015). In some cases, catalysts may be periodically regenerated or replaced to maintain their performance over time. Overall, thermal deactivation remains a significant challenge in the development and use of catalysts for industrial processes, and ongoing research is focused on developing new materials and strategies to improve their thermal stability and durability.

2.4.4 Structural changes

Catalysts can also undergo structural changes over time, leading to a decrease in the surface area available for catalysis. There are different types of structural changes that can lead to catalyst deactivation. One type of structural change is sintering. Sintering occurs when the

catalyst particles undergo a physical change that causes them to coalesce or agglomerate. This can happen when the catalyst is exposed to high temperatures, which causes the particles to reduce their surface area and activity. A common example when this situation can arise is in the calcination stage during catalyst synthesis which is usually a high-temperature process (Yoshitake et al., 2003; Shi et al., 2020). The result is a loss of catalytic activity and reduced selectivity.

In addition to sintering and poisoning, catalyst deactivation can also occur due to structural changes caused by carbon deposition or coke formation (Takenaka et al., 2002). A structural change can occur when burning off the excessive coke deposition during the regeneration process of the spent catalyst if subject to extreme conditions such as high temperature and fast heating rate (Ma et al., 2018). Therefore, it is recommended to employ optimum conditions such as slow or moderate heating rates during regeneration processes involving the burning of excess coke deposits on a catalyst. To prevent catalyst deactivation, it is essential to select appropriate catalyst materials and operating conditions, as well as to monitor the catalyst's performance regularly. Additionally, researchers are continually developing new catalysts that are more resistant to deactivation and more efficient at accelerating chemical reactions.

2.3 Concluding remark

CO_2 methanation is a highly exothermic reaction which is thermodynamically feasible but kinetically unfavourable at low temperatures. Therefore, suitable catalysts are usually employed to enhance the CO_2 conversion and CH_4 selectivity. Before conducting CO_2 methanation, the choice of the type of reactor, the heat management in the system and the catalyst to be employed are crucial in designing an efficient process. The most common type of methanation reactor is the fixed-bed reactor which can exist in various configurations, including the single fixed-bed and multi-tubular fixed bed reactors. Another type of reactor is the fluidised bed due to its ability to achieve a highly uniform temperature distribution in the reactor. Other forms of reactors include the honeycomb monolith reactors which are structured forms of fixed bed reactors, microchannel reactors, flat bed reactors, membrane reactors, and three-phase slurry reactors. Different pathways have been proposed for the formation of CH_4 during CO_2 methanation. Among the suggested pathways, the most proposed mechanisms are

(1) the CO intermediate route which involves the formation and cleavage of CO intermediates, (2) the formate/formyl route which involves the formation of a CH_xO_y complex or complexes (formyl, formates, bicarbonate species, etc), and (3) the reverse water gas shift (RWGS). Notwithstanding the discrepancies, several studies have shown that the reaction pathways leading to CH_4 are influenced by the type of catalyst employed. The catalysts employed in CO_2 methanation are often categorised under heterogeneous catalysts. These catalysts have two main components, namely, the support and the active metal. The metal generally provides the site for the adsorption and activation of H_2 while the support provides the surface for the metal dispersion, and the adsorption and activation of CO_2 In this study, the active metals discussed were the noble metals including Ru, Rh and Pd, and Ni which is a non-noble metal. Surveying through various literature studies, these metals have shown to be highly selective to CH_4 formation. Among the reviewed metals, Ni is the most extensively employed for the synthesis of methanation catalysts due to economic reasons. However, Ni is more prone to deactivation compared to the noble metals. Therefore, a second metal, also known as promoter, is usually recommended to improve the stability of Ni-based catalysts. The introduction of alkali and alkaline earth metals can help to (1) increase the surface area for high metal dispersion and more active sites for the reactants to adsorb and react; (2) enhance the basic sites which favour CO and CO_2 adsorption. This also helps to inhibit carbon deposition since the improved CO_2 adsorption will result in a high conversion rate; (3) alter the reaction pathways: Alkali and alkaline earth metals can alter the reaction pathways of catalytic reactions. Similarly, the addition of lanthanide promoters can; (1) influence the dispersion of the active metal on the catalyst surface through a particle size reduction effect; (2) enhance the redox performance of the catalyst by encouraging the electron transfer of the metal species, and more active sites are generated; (3) provide sufficient oxygen vacancies and enhanced basic sites which are crucial for suppressing the carbon deposition and improving the CO_2 adsorption and activation capacity of the catalyst. Ceria, YSZ, alumina and SBA-15 supports were reviewed because of their excellent properties in aiding metal dispersion, and CO/CO_2 adsorption and activation. YSZ and Ceria have exceptional redox properties and a high oxygen storage capacity. As support, their oxygen vacancies behave as active sites where a high oxygen mobility favours the activation and conversion of carbon oxides. After the activation and adsorption, these oxygen vacancies also help in breaking the C-O bond in the adsorbed carbon oxides. The C-O bond breaking result in the release of oxygen which fills the vacancies while the carbon

undergoes hydrogenation to CH_4. Finally, catalyst deactivation is a major challenge in many heterogeneous catalytic reactions. Catalyst deactivation can occur in various ways including fouling, poisoning, thermal deactivation, and structural changes. The general strategies for preventing or suppressing the deactivation of a catalyst include the use of reaction conditions unfavourable to the activity of contaminants such as sulfur and carbon, catalyst modification either through the synthesis method or the addition of a promoter, and the effective design of the reactor system.

CHAPTER 3

Research Methodology

3.1 Introduction

This chapter provides details of materials and equipment used for the experiments conducted in this research. A comprehensive procedure for the preparation, characterisation, and testing of the samples in methanation reactions will also be presented in this chapter.

3.2 Materials and equipment

The equipment and materials employed in this research are given in Table 3.1 and Table 3.2, respectively. It is worth mentioning that deionised water (diH_2O) with a resistivity of 18.2 megaohms was used for the preparation of all the catalysts for this research.

Table 3.1 List of equipment used for catalyst preparation.

Equipment	Model/Manufacturer	Application
Electronic balance	Sartorius Quintix Analytical Balance	Sample's weight measurement
Millipore Milli-Q		For deionised water (diH_2O)
Hot plate stirrer	IKA™ RCT Basic Hot Plate Stirrer (Fisher Scientific)	Temperature-controlled Stirring
Oil-less Vacuum pump	Autobo Elec. Tech. Ltd (AP-1400C/V	Filtration of as-synthesised SBA-15
Benchtop Oven	GenLab	Drying of samples
Carbolite & Split tube furnaces	Carbolite Gero (CWF1300) and Vecstar	Calcination of samples
Teflon-lined autoclave		Hydrothermal treatment
Quartz-tube reactor		Catalyst testing
Personal Protective Equipment (PPE)		Protect against skin contact with corrosive chemicals and inhalation of poisonous gases during samples preparation
Micromeritics® TriStar II Plus analyser		BET surface, pore size and volume measurement of catalysts
Proto Benchtop AXRD		Powder X-ray diffraction for crystal phase identification
Environmental Scanning Electron Microscope	Zeiss Evo10	Imaging of catalyst's surface morphology
Tabletop electron microscope with an energy dispersive spectrometer (EDS)	Hitachi TM3030	Imaging of catalyst's surface morphology and determination of elemental distribution on the surface
Transmission electron microscope	Jeol 1400 TEM	Imaging of catalyst's surface morphology
Mass spectrometer	MKS Cirrus	H_2 temperature programmed-reduction (H_2-TPR), temperature-programmed oxidation (TPO) and CO_2 methanation

Table 3.1 List of equipment used for catalyst preparation (continuation)**.**

Temperature-controlled furnace	Elite Thermal Systems. Ltd.: Model THH12/90/305	CO_2 methanation
Gas chromatography	Shimadzu GC-2014	Product analysis after CO_2 methanation
Thermogravimetric analysis (TGA)	TG 209 F1 - NETZSCH Analysing & Testing instrument	Temperature-programmed calcination
Transmission electron microscope	Jeol 1400 TEM	Imaging of catalyst's surface morphology
Raman spectroscopy	inVia^{TM} Qontor confocal Raman microscope	Tool for inspecting the chemical structure, phase and polymorphy, crystallinity and molecular interactions on a surface.

Table 3.2 List of main materials used for sample preparation and testing.

Chemical/Gas	Formula	Purity (%)	Supplier	Application
Pluronic P-123	$EO_{20}PO_{70}EO_{20}$	–	Sigma-Aldrich Chemicals	Silica synthesis (catalyst support)
Tetraethyl orthosilicate (TEOS)	$SiC_8H_{20}O_4$	98.00	Fisher Scientific	Silica synthesis (catalyst support)
Hydrochloric acid, pure, fuming	HCl	37	Fisher Scientific	Silica synthesis (catalyst support)
Nickel (II) nitrate hexahydrate	$Ni(NO_3)_2{\cdot}6H_2O$	Extra Pure	Fisher Scientific	Metal precursor for catalysts
Lanthanum(III) nitrate hexahydrate	$La(NO_3)_3{\cdot}6H2O$	99.99	Sigma-Aldrich Chemicals	Promoter for catalysts
Tosoh-zirconia (TZ-8YS)	YSZ	99.98	Tosoh corporation	Catalyst support
Alumina 16-SG powder	Al_2O_3	99.5	Almatis®	Catalyst support
Cerium(IV) oxide powder	CeO_2	99.5	Alfa Aesar	Catalyst support
Carbon dioxide	CO_2	99.99	Air Products & Chemicals	Methanation reactant
Hydrogen	H_2	99.99	Air Products & Chemicals	Methanation reactant & catalyst reduction
Nitrogen	N_2	99.99	Air Products & Chemicals	Diluent for the reacting gases
Argon	Ar	99.99	Air Products & Chemicals	Carrier gas for GC
Oxygen	O_2	99.99	Air Products & Chemicals	Temperature-programmed oxidation
Vapour trap	$CaSO_4$	98.90	W.A. Hammond Drierite Company	Trap condensed moisture from the products stream

3.2 Catalysts Preparation

The SBA-15 support was synthesised by following the method reported in a previous study (Omoregbe et al., 2017) and summarised in Figure 3.1. A dilute solution of HCl (dil HCl) was obtained by adding concentrated HCl (37%, Fisher Scientific) dropwise into 350 mL of diH_2O until the pH of the solution was around 1. Thereafter, Pluronic® P123 triblock copolymer (Sigma-Aldrich) was dissolved in the HCl solution which was stirred at 1000 rpm (rev min^{-1}) at 303 K. Subsequently, a silica precursor tetraethylorthosilicate (TEOS, Fisher Scientific) was added dropwise into the mixture at 310 K with stirring for 24 h. The mass ratio of the dil $HCl_{(aq)}$, P123 and TEOS was 26:1:2. After 24 hours, the mixture was transferred to a Teflon-lined autoclave and aged in a static air environment at 393 K for 24 hours in the GenLab Benchtop oven with an exhaust connection. The as-synthesised SBA-15 was then taken out of the autoclave, washed with diH_2O until the HCl was removed and pH was about 7. The washed SBA-15 was then filtered and dried in the GenLab Benchtop oven at 353 K for 24 h. Finally, the dried as-synthesised SBA-15 was calcined at 823 K with heating and cooling rates of 10 K min^{-1}. The Ni/SBA-15 catalyst was prepared using wet impregnation deposition-precipitation, and sol-gel methods.

The Ni/SBA-15, Ni/YSZ, Ni/CeO_2 and Ni/Al_2O_3 catalysts were prepared by the wetness impregnation method summarised in

Figure 3.2. A controlled quantity of Ni precursor $Ni(NO_3)_2.6H_2O$ (extra pure, Fisher Scientific) was first dissolved in diH_2O to form a solution. The $Ni(NO_3)_2.6H_2O$ solution was then mixed with a calculated amount of the support X (SBA-15, YSZ, CeO_2 or Al_2O_3) and stirred at 323 K until a slurry was formed. The catalyst formed was dried at 353 K and calcined at 923 K with heating and cooling rates of 5 K min^{-1}.

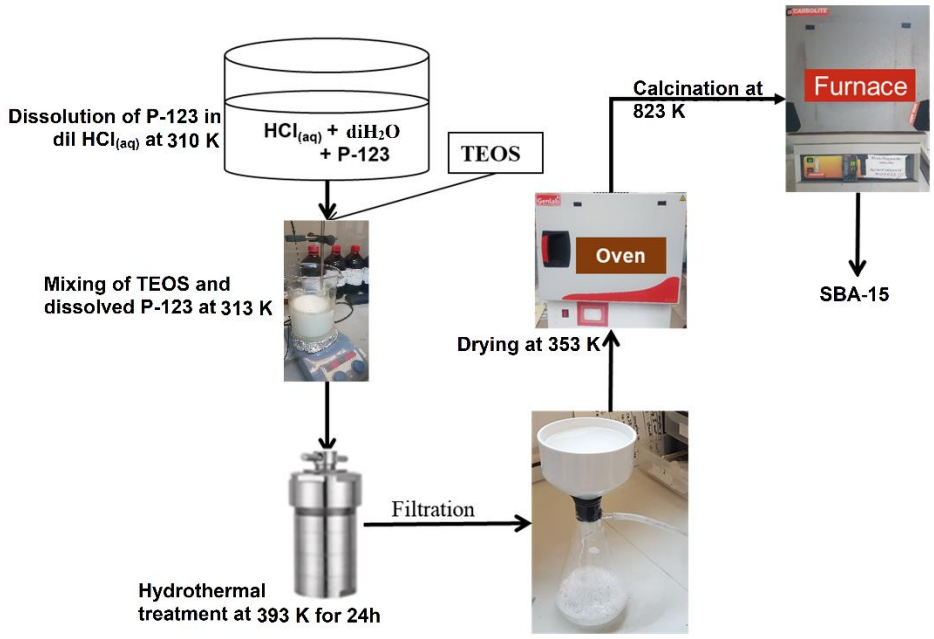


Figure 3.1 Flowchart for the preparation of SBA-15 support.

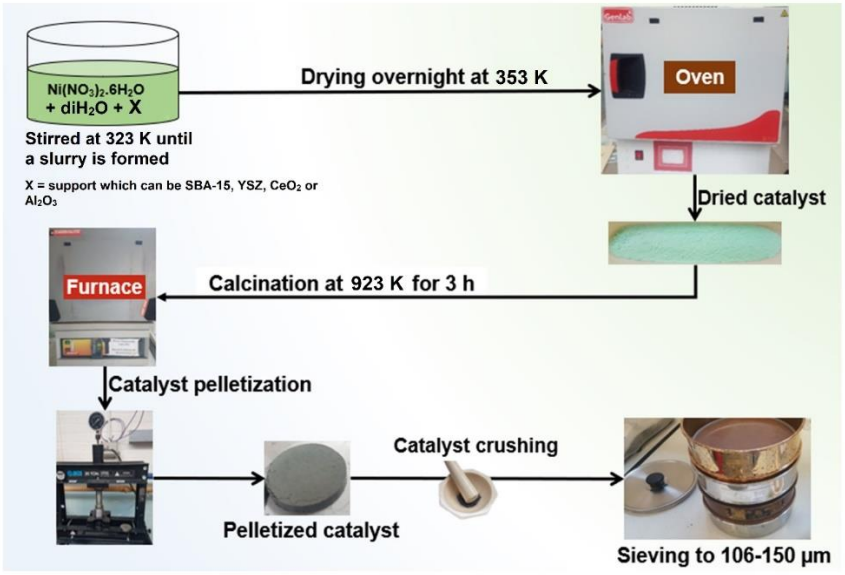


Figure 3.2 Flowchart for catalyst synthesis using the wetness impregnation method.

3.3 Catalyst characterisation

3.4.1 Textural Analysis

The textural properties of porous materials were investigated by Brunauer-Emmett-Teller (BET) surface measurement. A comprehensive study on the theory behind BET is found at Naderi (2015). This analysis enables the determination of the surface areas, pore sizes and pore volumes of the samples. The data from this analysis also enabled the calculation of the average crystallite sizes of the active Ni metal in the samples, where applicable. In this study, the BET surface areas of the samples were measured using a Micromeritics® TriStar II Plus analyser (Figure 3.3) at a temperature of 77.15 K. For each run, the sample tube was loaded such that the oval shape at the bottom was half filled. The weight used ranged from 0.25 to 3.00 g, depending on the quantity of sample needed to achieve a half-filled level in the tube. Before the adsorption/desorption step, the material was degassed for about 6 hours at 373 K to expel moisture and contaminants. Once the degassing process was complete, the sample tubes were transferred to the BET surface equipment for BET surface and porosity measurement. A Dewar flask in the equipment contained liquid N_2, whose movement (up and down) was automated by an acquisition computer software connected to the instrument.

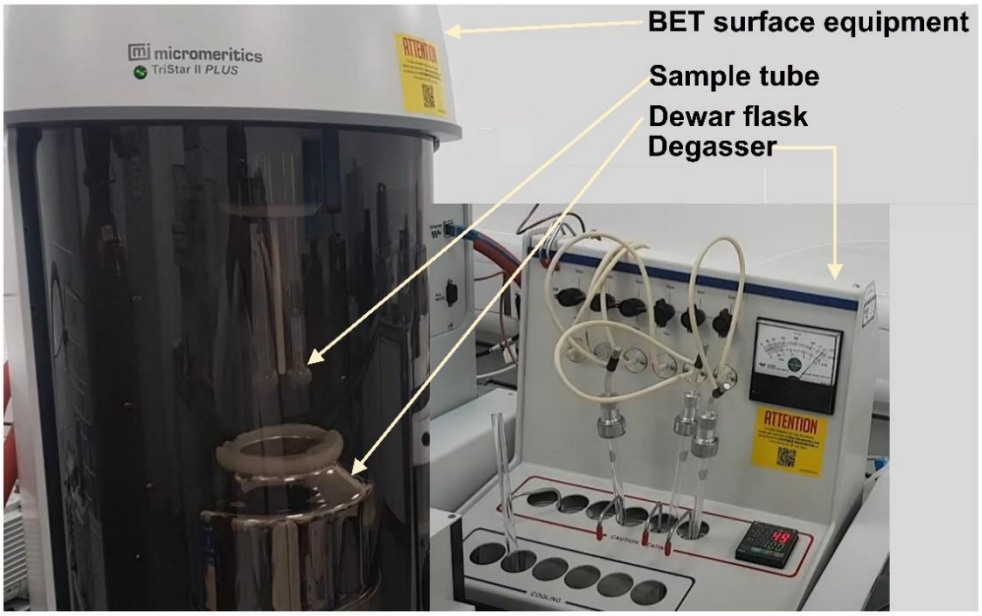


Figure 3.3 Micromeritics® TriStar II Plus analyser with degasser.

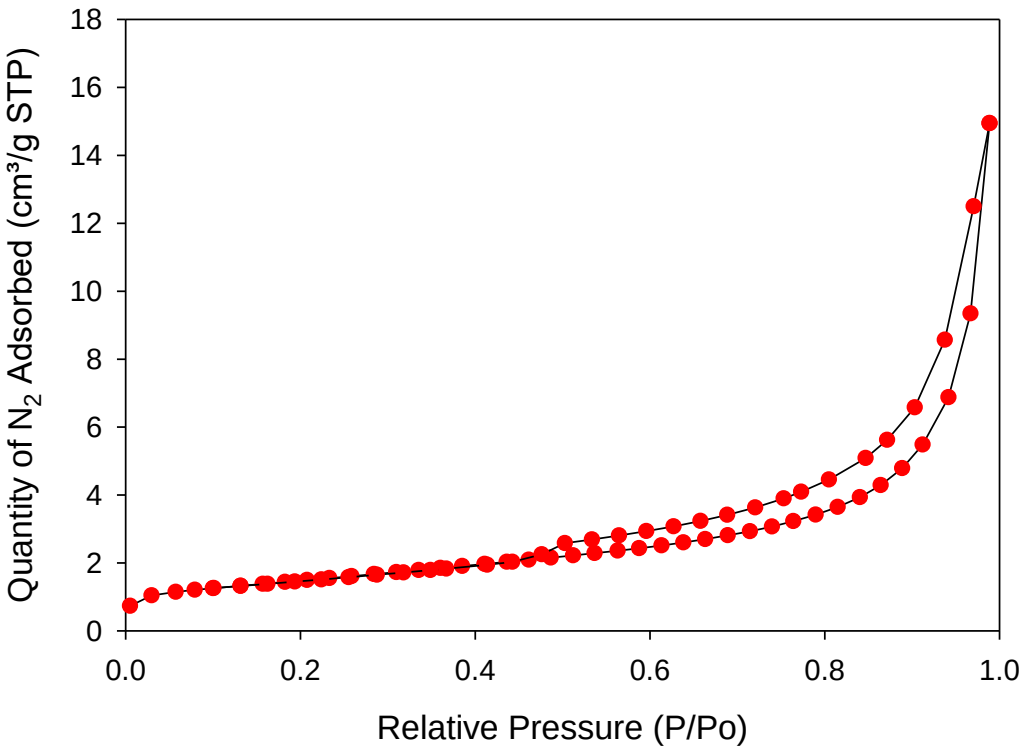


Figure 3.4 A typical N_2 adsorption–desorption isotherm profile from a Micromeritics® TriStar II Plus analyser.

During the process, the flask moves up enabling the sample tubes to be immersed inside liquid N_2 until the analysis is complete. At the end of the process, the software acquires a series of data, among which is an isotherm profile for adsorption-desorption processes such as the one shown in Figure 3.4. As seen, P and P_0 represent the equilibrium pressure of the adsorbed gas and saturation pressure of the adsorbate gas (which is N_2 in this case), respectively. The dimensionless quantity P/P_0, which is also referred to as the relative pressure, is used to describe the amount of gas adsorbed on the solid material relative to the maximum amount it can hold at a particular temperature. From the BET data, the sample's pore volume could be estimated by using the quantity of gas adsorbed at the relative pressure of about 1 provided the pores were completely saturated with the liquid adsorbate (liquid N_2). The volume of liquid N_2 was evaluated using Eq. **(**3.1**)**.

$$V_{N_2} = \frac{P_a V_{ads} v_m}{RT_a} \quad \textbf{(}3.1\textbf{)}$$

where V_{N2} = Volume of liquid N_2 (cm^3),

V_{ads} = Volume of adsorbed N_2 (cm^3),

P_a = Ambient pressure (atm),

R = universal gas constant ($cm^3 \cdot atm \cdot K^{-1} \cdot mol^{-1}$)

T_a = Ambient temperature (K)

v_m = Molar volume of the adsorbate (34.7 cm^3 mol^{-1} for N_2).

On the premise that the pore geometry was cylindrical, the Kelvin equation (Eq. **(**3.2**)**) was used to determine the pore size (Gregg and Sing, 1982).

$$r_K = \frac{-2\gamma_s v_m}{RT_b \ln \frac{P}{P_0}} \quad \textbf{(}3.2\textbf{)}$$

where γ_s = the surface tension of liquid N_2 at boiling point (N m^{-1}),

v_m = molar volume of the liquid N_2 (m^3),

T_b = boiling point of nitrogen (T),

r_K = the Kelvin radius (m).

It is important to note that the Kelvin equation does not accurately gives the pore's true size considering that there is a high probability of some adsorption taken place on the pore wall prior to condensation. Furthermore, an adsorbed layer remains on the walls during evaporation.

Therefore, the thickness of the adsorbed layer should also be considered when estimating the pore true size. This can be achieved by applying Eq. **(**3.3**)**:

$$r_P = r_K + t_{ads} \quad \textbf{(}3.3\textbf{)}$$

where t_{ads} = The thickness of the adsorbed layer

Eq. (3.4) suggested, by de Boer (Singh, 2008), can be applied in estimating the thickness of the adsorbed layer (t_{ads}):

$$t_{ads} = \left(\frac{13.99}{\log(P_0 / P) + 0.034}\right)^{\frac{1}{2}} \quad \textbf{(}3.4\textbf{)}$$

3.4.2 X-ray diffraction measurement

X-ray diffraction (XRD) is a characterisation technique that is mostly used in investigating the crystalline structure of samples. It can also be used to estimate the average spacings between atomic planes, study the orientation of an individual crystal or a grain, or evaluate the size, shape, and internal stress of small crystalline regions. X-ray diffraction operates on the principle of diffraction and transmission of X-rays when incident on a crystalline material (see Figure 3.5 (a)-(c)). A cathode ray tube inside the equipment generates the X-rays which are filtered to produce monochromatic radiation and focussed on the sample. The incident rays thereafter interact with the samples to create a constructive interference and a diffracted ray according to Bragg's Law (Eq **(**3.5)).

$$n\lambda = 2d \sin\theta \quad \textbf{(}3.5\textbf{)}$$

In Bragg's equation, n is an integer, the order of the reflection, λ is the wavelength of the X-ray, d is the distance between two lattice planes, and θ is the angle between the incident X-rays and the scattering plane (angle of diffraction). The angle of diffraction can be obtained from the XRD diffraction peaks of the sample while the crystalline phases associated with these peaks are identified using standard reference patterns. The most common standard for

identifying the phases from XRD peaks is the Joint Committee for Powder Diffraction Studies (JCPDS) database for peak identification (Hybler, 1985; Wong-Ng et al., 1982).

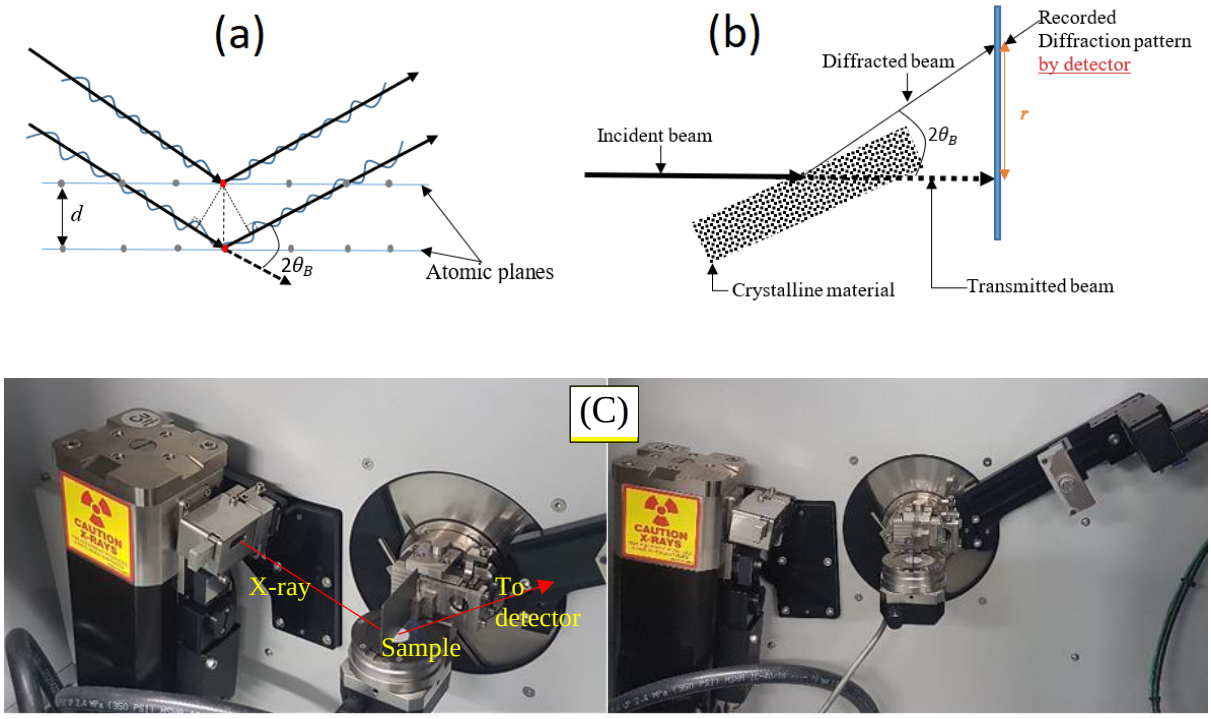


Figure 3.5 Diagrams (a) and (b) represent the principle of X-rays diffraction as proposed by Bragg's Law, and (c) shows the inner chamber of a Proto Benchtop AXRD equipment during a typical XRD analysis.

In addition, the average crystallite size for the crystals of each sample can be determined from XRD data by the Scherrer equation (Patterson, 1939) (Eq. **(**3.6**)**):

$$d_p \text{ (nm)} = \frac{K\lambda}{\beta \cos \theta} \qquad \textbf{(}3.6\textbf{)}$$

Where d_p = Particle size in nm,

K = Shape factor with the value of 0.9 (assuming a spherical particle),

λ = X-ray wavelength of the X-ray source Cu Kα (1.5406 Å),

β = Line broadening at half the maximum intensity (FWHM) of the NiO or Ni^0 diffraction peak,

θ = is the Bragg angle in radian.

The crystalline phases of the catalysts were investigated by X-ray powder diffraction analysis on a Proto Benchtop AXRD at 30.5 kV and 20.5 mA scanning from a 2θ of 5° to 85° with an increment of 0.0149° using Cu-K_α at room temperature in ambient air.

3.4.3 Thermogravimetric analysis

Thermogravimetric analysis (TGA) is a technique that is employed in determining the thermal stability of a material by subjecting it to a temperature-controlled environment either in the presence or absence of a gaseous medium. In this technique, the change in the sample's mass over time is measured in relation to the change in temperature. The TGA technique is used in different ways depending on the information that is needed about a sample. The commonest among these TGA techniques includes temperature-programmed calcination (TPC), temperature-programmed oxidation (TPO), and H_2 temperature-programmed reduction (H_2-TPR).

3.4.3.1 Temperature-programmed calcination TPC

Temperature-programmed calcination (TPC) is a type of thermogravimetric analysis (TGA) that measures the weight change of a sample over time when it is subjected to a controlled temperature programme in a regulated atmosphere (in air or inert medium). The weight change of the sample can give vital information such as the nature of a sample (organic or inorganic), the decomposition temperature, or the safe operating temperature in different gaseous media and the types of volatiles removed from the sample before or during decomposition.

In this study, the TPC of samples were carried out to determine their optimal calcination temperatures (the minimum temperature required for all the volatiles and physically adsorbed moisture to be removed and the samples' weights to become stable). Such information allowed to set the furnace to specific temperatures for calcination during sample preparation. The TPC of samples was performed on a TG 209 F1 - NETZSCH Analysing & Testing instrument (Figure 3.6). The TPC of all the prepared samples was carried out under N_2 environment flowing at 20 mL min^{-1} and temperature up to 1,073 K at a heating rate of 10 K min^{-1}. The mass of the samples was in the range of 10 to 70 mg, depending on their density. The TA analysis software "NETZSCH Proteus" was employed in evaluating the measured data and obtaining the TPC profile such as the one shown in Figure 3.7.



Figure 3.6 NETZSCH Analysing & Testing instrument for Temperature-programmed calcination.

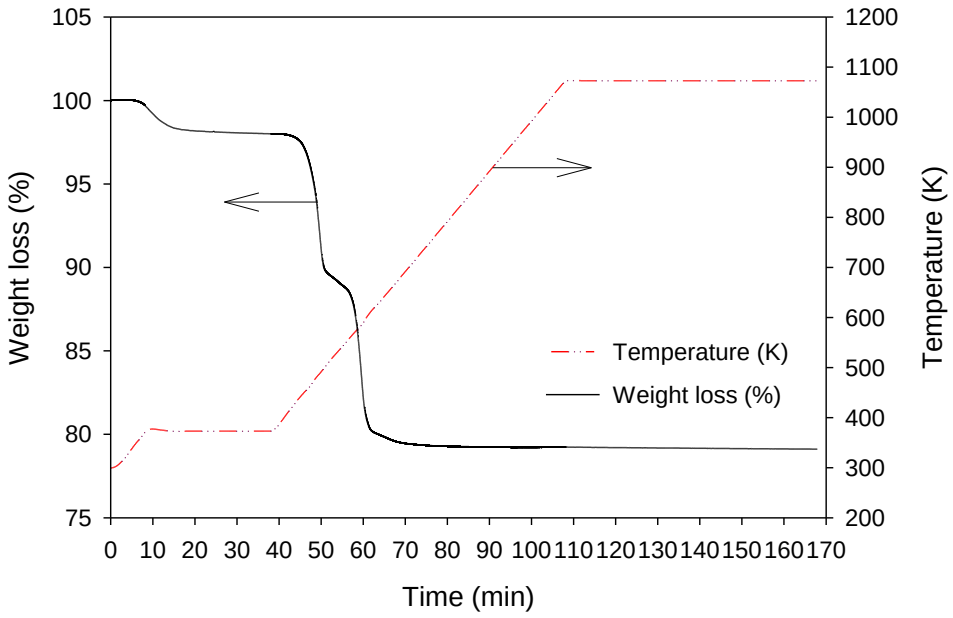


Figure 3.7 Representation of a typical temperature and weight change profile from a TPC analysis conducted with the NETZSCH Analysing & Testing instrument in Figure 3.6.

3.4.3.2 Temperature-programmed oxidation

Temperature-programmed oxidation (TPO) is a TGA technique commonly used in heterogeneous catalysis to determine the amount and nature of the carbon species formed on the surface of a catalyst after a reaction. Basically, a known mass of the catalyst is heated at a controlled temperature in air or O_2 until the change in the catalyst weight becomes zero. The amount of carbon is then determined by the weight loss of the catalyst since carbon is expected to burn off the sample resulting in weight loss. However, this step can be sometimes complicated when the catalyst contains an active metal such as Ni. During the TPO analysis, not only the carbon is combusted and oxidised to CO_2, but Ni is most likely oxidised into NiO according to Eq. (3.7):

$$2Ni + C + 2O_2 \rightarrow 2NiO + CO_2 \quad \textbf{(3.7)}$$

Therefore, the quantity of carbon formed after a CO_2 methanation reaction was determined by focusing on the amount of CO_2 formed and not the catalyst weight change. This was achieved by heating the spent catalyst in a quartz-tube reactor that was directly connected to a MKS Cirrus mass spectrometer. The furnace was heated up to 1073 K at a heating rate of 5 K min^{-1}. Gaseous stream of O_2 and N_2 with flowrates of 5 mL min^{-1} and 20 mL min^{-1}, respectively was used for the TPO analysis. The data from the mass spectrometer readings supplied a profile such as the one shown in Figure 3.8.

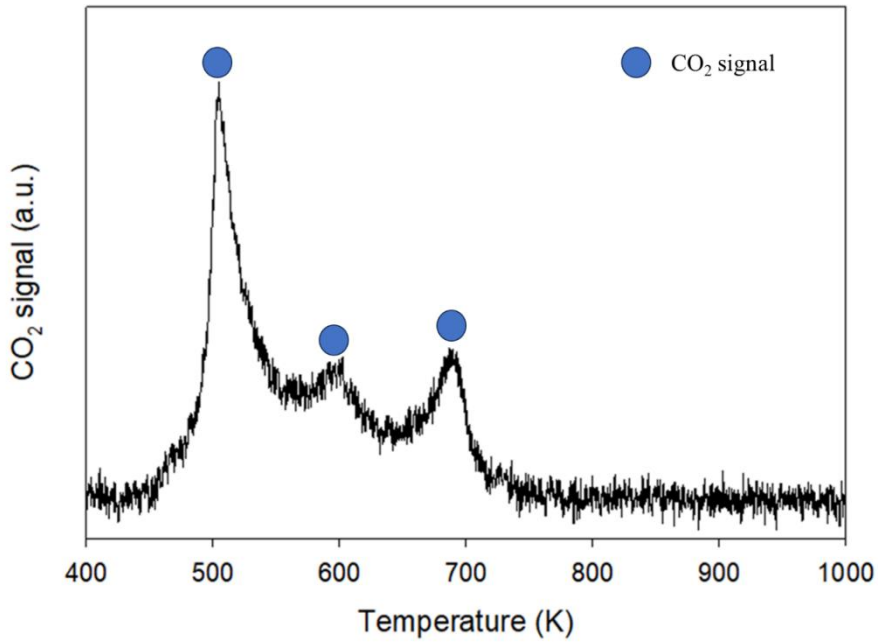


Figure 3.8 TPO profile showing CO_2 signal as a function of the oxidation temperature.

3.4.3.3 H_2 temperature-programmed reduction

H_2 temperature-programmed reduction (H_2-TPR) is a TGA technique that is mainly used to determine the reducibility of a heterogeneous catalyst. This technique involves the heating of a freshly prepared (calcined) catalyst in H_2 environment until the weight change becomes zero. The reaction that takes place during the H_2-TPR of a Ni-based catalyst is described by Eq. (3.8). Basically, the NiO component of the catalyst is reduced into Ni (catalyst activation) when the catalyst is heated at elevated temperature in a H_2 environment. The reduction temperature depends on the nature of the bond between the NiO and the catalyst surface. Therefore, the

different catalysts undergo complete reduction at different temperatures. As a rule of thumb, a catalyst with lower reduction temperature is said to have a high degree of reduction. However, it has been argued that a high degree of reduction may also be due to low NiO dispersion on the surface (Swaan et al. 1994). This could result in a weak bond, and hence result in a high degree of reduction.

$$NiO + H_2 \rightarrow Ni + H_2O \qquad \textbf{(}3.8\textbf{)}$$

The H_2-TPR was carried out in a quartz tube reactor connected to the MKS Cirrus mass spectrometer by passing a stream of H_2/N_2 under monitored temperature according to a procedure reported by (Huang et al., 2017). For each catalyst reduced, 200 mg of sample was heated to 1273 K under the flow of 5 mL min^{-1} H_2 and 20 mL min^{-1} N_2 and at a heating rate of 5 K min^{-1}. The amount of hydrogen consumed was determined by the readings from the mass spectrometer, and the temperature profile was like the one shown in Figure 3.9.

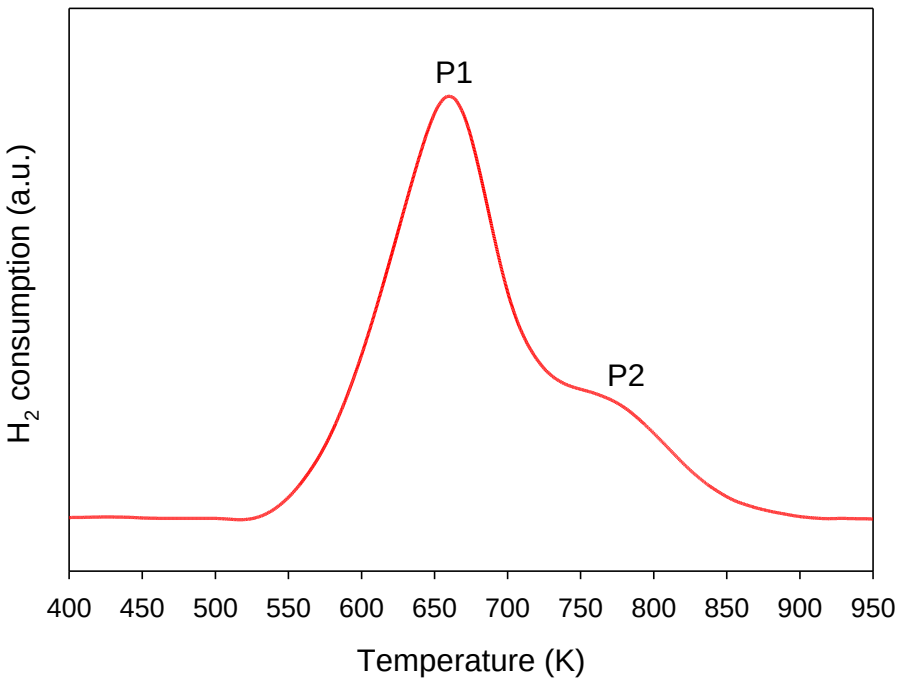


Figure 3.9 H_2-TPR profile showing H_2 consumption as a function of temperature. The reduction peaks P1 and P2 are signals indicating the consumption of hydrogen at the lower and higher temperatures, respectively.

3.4.4 Scanning electron microscopy

A scanning electron microscope is a type of electron microscope that creates an image by scanning a focused beam of electrons over the surface of a sample. In this measurement, various signals containing information about the sample's morphology are produced during the interaction of electrons in the beam with atoms in the sample. In this study, a Tabletop Scanning Electron Microscope Hitachi TM3030 with energy-dispersive X-ray (EDX) spectroscopic option (Figure 3.10) and environmental Scanning Electron Microscope Zeiss Evo10 were employed in determining the morphologies of the samples. Prior to the imaging, samples were coated with platinum using the Quorum - Q150T ES Sputter coater. The thin platinum metal layer helped to create a conductive surface that prevented static charging and improved the secondary electron signal required for imaging. The chemical elemental composition of sintered samples (without coating) was analysed using EDX. The deviation of the Ni content determined in this way from the theoretical value was below 2 %.



Figure 3.10 Diagrams representing the Tabletop Scanning Electron Microscope Hitachi TM3030.

3.4.5 Raman spectroscopy

Raman Spectroscopy is a powerful tool used for chemical analysis to provide detailed information about the molecular interactions, chemical structure, crystallinity, and phase of samples. This technique works according to the interaction of light with the chemical bonds

within a sample. Basically, the molecules within the sample scatter incident light that is originating from a high intensity laser light source. The scattered light with a different wavelength from the laser source (Raman Scatter) is used in providing useful information about the sample (HORIBA Scientific, 2022). In this study, Raman spectroscopy was carried out in the inVia^{TM} Qontor confocal Raman microscope (M&M 2A04) (Figure 3.11) equipped with a Renishaw Centrus 0C4E47 detector. A laser excitation of 532 nm laser (green), laser power of 10 mW, dispersed by 1800 lines/mm grating and exposition for 10 sec, 3 accumulations and a spectra range of 100 to 4000 cm^{-1} were employed. The silicon reference peak intensity was set to 520 cm^{-1} while cosmic ray removal was enabled.



Figure 3.11 inVia^{TM} Qontor confocal Raman microscope (M&M 2A04).

3.5 Catalytic activity test

The performance of the synthesised catalysts for CO_2 methanation was examined in a continuous flow quartz tube fixed-bed reactor (I.D. = 5.5 mm, wall thickness = 2 mm) at a temperature range of 473 to 823 K under atmospheric pressure. The catalyst weight range was from 150 mg to 600 mg depending on test setup. An average particle size of 150 µm was employed to eliminate mass transport resistances. For each experiment, the catalyst was supported by an inert quartz wool, forming a bed at both ends. The reactor was horizontally positioned in a temperature-controlled furnace (Elite Thermal Systems. Ltd.: Model THH12/90/305). Three reactor settings were employed in this study and are presented in Figure 3.12.

Prior to the actual methanation reaction, the catalyst in the reactor was first reduced by passing a stream of 20 mL min^{-1} H_2 and 60 mL min^{-1} N_2 through it at 973 K for 1 h. Subsequently, the reactor was cooled to the reaction temperature whilst being purged by passing a stream of N_2 (60 mL min^{-1}). Thereafter, a gaseous feed stream containing N_2 (60 mL min^{-1}), H_2 (60 mL min^{-1}) and CO_2 (15 mL min^{-1}) was introduced at the respective reaction temperatures under atmospheric pressure. The reactant flowrates were controlled using calibrated mass flow controllers. The products of the reaction were channelled through a drying system before sending them to a Shimadzu GC-2014 gas chromatograph for analysis. The GC was equipped with a thermal conductivity detector and column (ShimCarbon ST, length 200 m, inner diameter 0.35 mm) and was operated under argon as the carrier gas. The performances of tested catalysts, carbon balance (C_b) and the rate of carbon deposition (C_d) were estimated by applying Eqs. (3.9) to (3.13).

$$X_{CO_2} = \left(\frac{F_{CO_{2,in}} - F_{CO_{2,out}}}{F_{CO_{2,in}}}\right) \times 100\% \quad (3.9)$$

$$Y_{CH_4} = \left(\frac{F_{CH_4,out}}{F_{CO_{2,in}}}\right) \times 100\% \quad (3.10)$$

$$S_i = \left(\frac{F_{i,out}}{F_{CH_4,out} + F_{CO,out}}\right) \times 100\% \quad (3.11)$$

$$C_b(\%) = \frac{\left(F_{CO_{2,out}} + F_{CO,out} + F_{CH_4,out}\right)}{F_{CO_{2,in}}} \times 100 \quad (3.12)$$

$$C_d\ (mol\ S^{-1} g_{cat}^{-1}) = \frac{F_{CO_{2,in}} - \left(F_{CO_{2,out}} + F_{CO,out} + F_{CH_4,out}\right)}{W_{cat}} \quad (3.13)$$

Where F_i= molar flowrate for any species *i* (CO or CH_4) in mol s^{-1},

X_{CO2} = CO_2 conversion (%); Y_{CH4} = CH_4 yield (%); S_i = CH_4 or CO selectivity (%),

$F_{CO_{2,in}}$= The flowrate of inlet CO_2 in mol s^{-1},

$F_{CO_{2,out}}$, $F_{CO,out}$ and $F_{CH_{4,out}}$= The flowrate of CO_2, CO and CH_4 in the outlet in mol s^{-1},

W_{cat} = Catalyst mass (g).

The molar flowrate (F_i) was obtained by converting the equivalent volumetric flowrate using the ideal gas law with the assumption that the external temperature was 298 K. The carbon balance was determined by assuming that the main carbon sources are CO_2, CO, C and CH_4 while other side products are negligible.

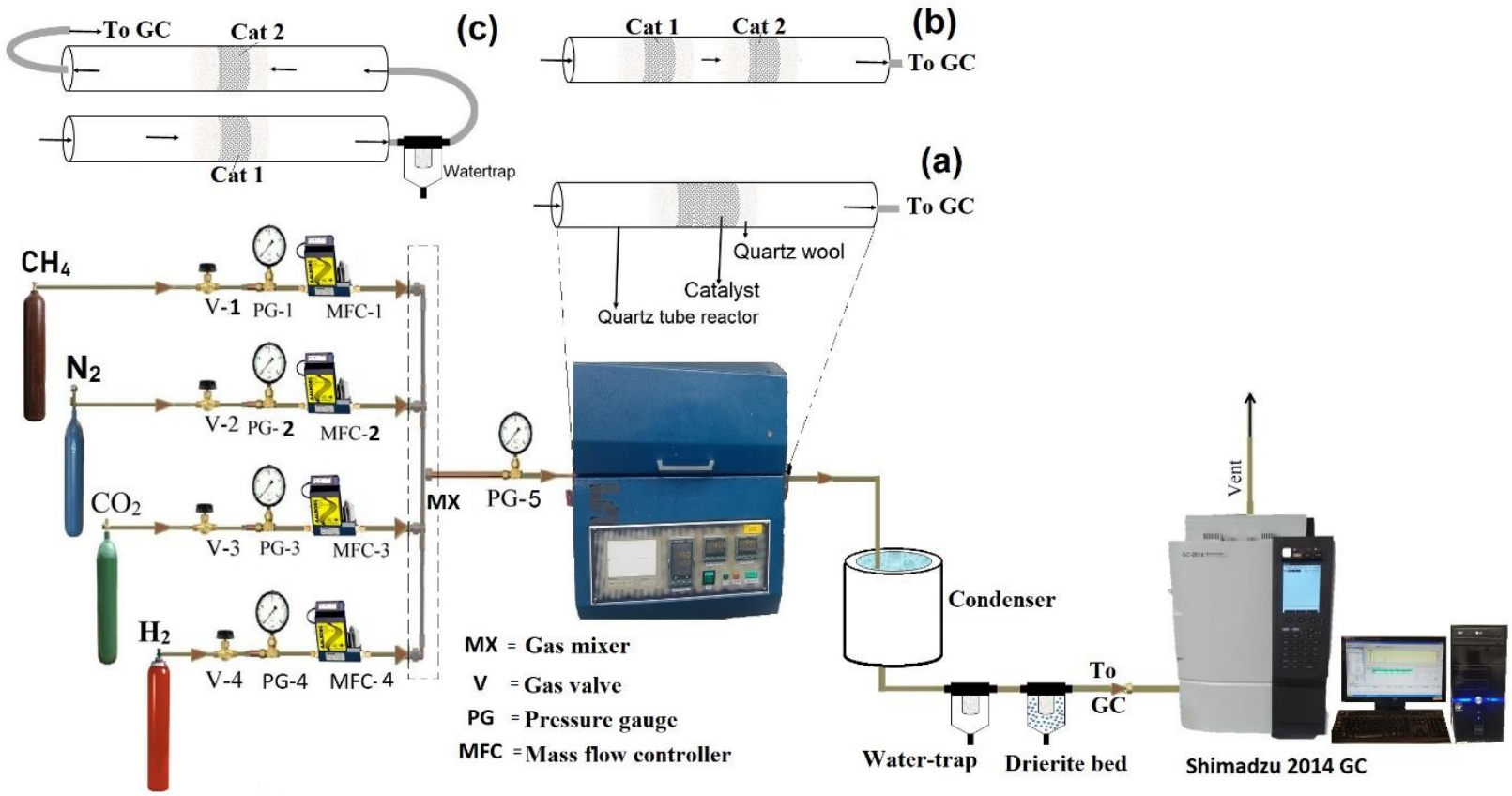


Figure 3.12 Scheme of (a) a single fixed-bed quartz reactor containing one catalyst bed, (b) a single fixed-bed quartz reactor containing two catalyst beds, and (c) two fixed-bed quartz reactors arranged in series with a water trap placed between them for the CO_2 methanation reaction.

CHAPTER 4

Characterisation results and discussion

4.1 Textural Analysis

This section presents and discusses the textural properties of all the synthesised catalysts used in this work, such as the Ni-based YSZ, Al_2O_3, CeO_2 and SBA-15 catalysts by the N_2-physisorption analysis.

4.1.1 Textural properties of Ni-based YSZ catalysts

The N_2-adsorption/desorption properties of YSZ and the freshly prepared Ni/YSZ catalysts were investigated. Their adsorption curves are presented in Figure 4.1. As seen in the Figure, the adsorption curves of all the samples developed into a type-IV isotherm with an H3-type hysteresis loop based on the IUPAC classifications (Al-Fatesh et al., 2022a; Feng et al., 2022). Type-IV isotherm is a type of isotherm formed by the capillary condensation and evaporation within the porous structure of the adsorbent at high relative pressures (P/P_0) within the range of 0.8 to 1. Type-IV adsorption isotherms is typical for mesoporous and macroporous substances that possess a network of interconnected channels with slit-shaped pores (Chang et al., 2016; Sing et al., 1985). The distinctive H3-type hysteresis loop observed in these isotherms suggests strong interactions between the adsorbent and adsorbate, making it a valuable tool for identifying and characterising porous materials with unique surface properties and pore structures.

In addition, the similarity in the N_2-adsorption/desorption isotherms of both the YSZ and Ni/YSZ catalysts revealed that there was no significant alteration in the YSZ support's framework after the impregnation with Ni. Notwithstanding, there were changes in the BET surface area, pore size and pore volume after the impregnation process as shown in

Table 4.1. The BET surface area initially decreased with increasing Ni content from 5% to 10% and then increased until 30% Ni loading declining again with high Ni loading of above 40%.

The observed decrease in the surface area can be attributed to the partial blockage of the pores due to the dispersion of Ni in the support.

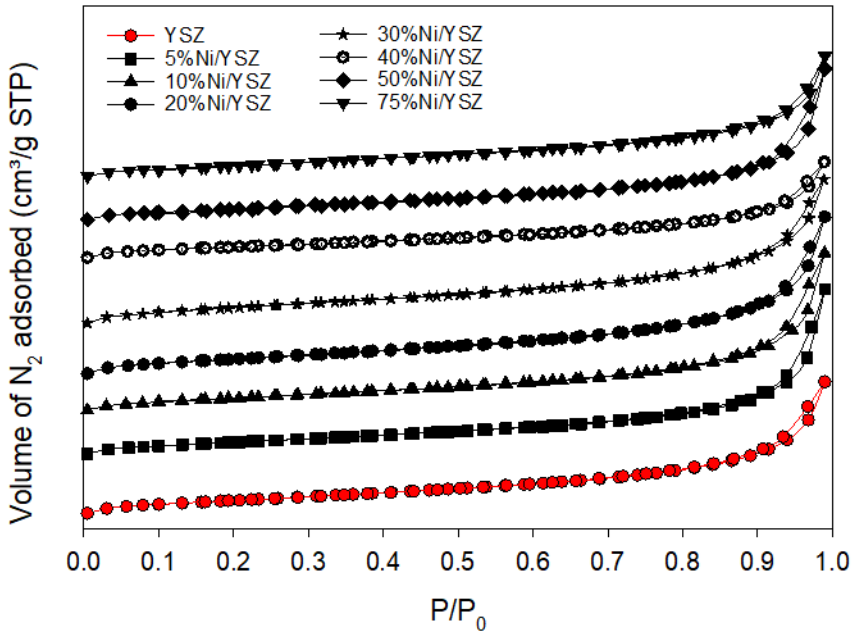


Figure 4.1 N_2-adsorption/desorption isotherms of the YSZ support and the calcined Ni/YSZ catalysts with various Ni-loading before the reaction.

Furthermore, the average pore size and pore volume relatively increased with higher Ni loading until 30%Ni loading and decreased above 30%Ni loading. The N_2-adsorption/desorption isotherms of YSZ support, and 10%Ni/YSZ and La-promoted Ni/YSZ catalysts are shown in Figure 4.2. Just like the YSZ and 10%Ni/YSZ catalyst (Figure 4.1), the N_2-adsorption/desorption isotherms of all the La-promoted Ni/YSZ catalysts developed into a type-IV isotherms with an H3-type hysteresis loop. However, these hysteresis loops resulting from capillary condensation and evaporation, shifted to lower P/P_0 values (about 0.8 to 1 for 10%Ni/YSZ to about 0.75 to 1 for the 5La%-10%Ni/YSZ catalyst) as the amount of La content increased. This shift in the hysteresis loop of the YSZ indicates that the addition of the La-promoter resulted in the modification of the pore structure. Indeed, the BET surface area, pore size and volume of YSZ (see Table 4.2) were greatly improved after the addition of La-promoter. This upgrade in the pore structure may be attributed to the enhanced resistance to

sintering of the NiO particles, which likely resulted in the enhanced dispersion of the (smaller) NiO particles.

Table 4.1 Physicochemical properties of the YSZ support and the calcined Ni/YSZ catalysts before reduction in H_2.

Samples	BET surface area ($m^2\ g^{-1}$)	Pore size (nm)[a]	Pore volume ($cm^3\ g^{-1}$)[b]
YSZ	5.8248 ± 0.0057	5.63887	0.008211
5%Ni/YSZ	5.2464 ± 0.0052	6.02938	0.007908
10%Ni/YSZ	5.3354 ± 0.0128	6.35586	0.008478
20%N/YSZ	6.2207 ± 0.0071	5.92179	0.009209
30%N/YSZ	6.0809 ± 0.0193	5.84615	0.008887
40%N/YSZ	4.2374 ± 0.0053	5.67500	0.006012
50%Ni/YSZ	4.8420 ± 0.0093	6.06354	0.007340
75%Ni/YSZ	4.7306 ± 0.0143	5.92908	0.007012

[a] Data were obtained from the BJH adsorption average pore diameter (4 v/A); [b] Data were obtained from the BJH single point adsorption at P/Po = 0.95.

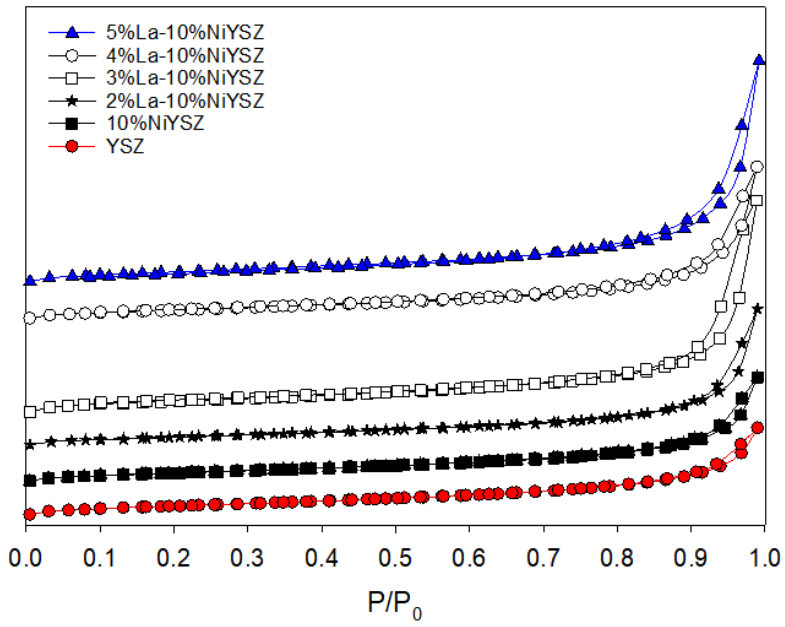


Figure 4.2 Nitrogen adsorption/desorption isotherms of YSZ support, 10%Ni/YSZ and La-promoted Ni/YSZ catalysts before reduction in H_2.

Table 4.2 Physicochemical properties of the YSZ support, 10%Ni/YSZ and La-promoted Ni/YSZ catalysts before reduction in H_2.

Samples	BET surface area (m^2 g^{-1})	Pore size (nm)[a]	Pore volume (cm^3 g^{-1})[b]
YSZ	5.8248 ± 0.0057	5.63887	0.008211
10%Ni/YSZ	5.2464 ± 0.0052	6.02938	0.007908
2%La-10%Ni/YSZ	5.7929 ± 0.0065	6.28439	0.009101
3%La-10%Ni/YSZ	6.2861 ± 0.0066	7.75140	0.012182
4%La-10%Ni/YSZ	5.8290 ± 0.0051	7.36956	0.010739
5%La-10%Ni/YSZ	7.0489 ± 0.0053	7.29750	0.012860

[a] Data were obtained from the BJH adsorption average pore diameter (4 v/A); [b] Data were obtained from the BJH single point adsorption at P/Po = 0.95.

4.1.2 Textural properties of Ni-based Al_2O_3, CeO_2 and SBA-15 catalysts

The N_2-adsorption/desorption of the SBA-15, CeO_2, and Al_2O_3 supports with their Ni-based catalysts was also investigated and the adsorption curves are presented in Figure 4.3 to 4.5. As seen in the figures, the adsorption curves of all the samples developed into type-IV isotherms which is indicative that these samples are mesoporous. However, the curves take different hysteresis loops for the various catalysts.

Figure 4.3 represents the N_2-adsorption/desorption of the SBA-15 support and 10%Ni/SBA-15 catalyst. It can be seen that both SBA-15 and 10%Ni/SBA-15 catalyst developed into type IV isotherms with H1-type hysteresis loop (Thommes et al., 2015). This is characteristic of a mesoporous material with a well-defined hexagonal structure (Al-Fatesh et al., 2022b). The combination of type IV isotherm and H1-type hysteresis loop is indicative of a porous material with relatively narrow pore size distribution and capillary condensation occurring within the mesopores. Considering that both SBA-15 support and 10%Ni/SBA-15 catalyst displayed similar isotherms after the impregnation of Ni, this suggests that the framework of the SBA-15 was not significantly altered after impregnation.

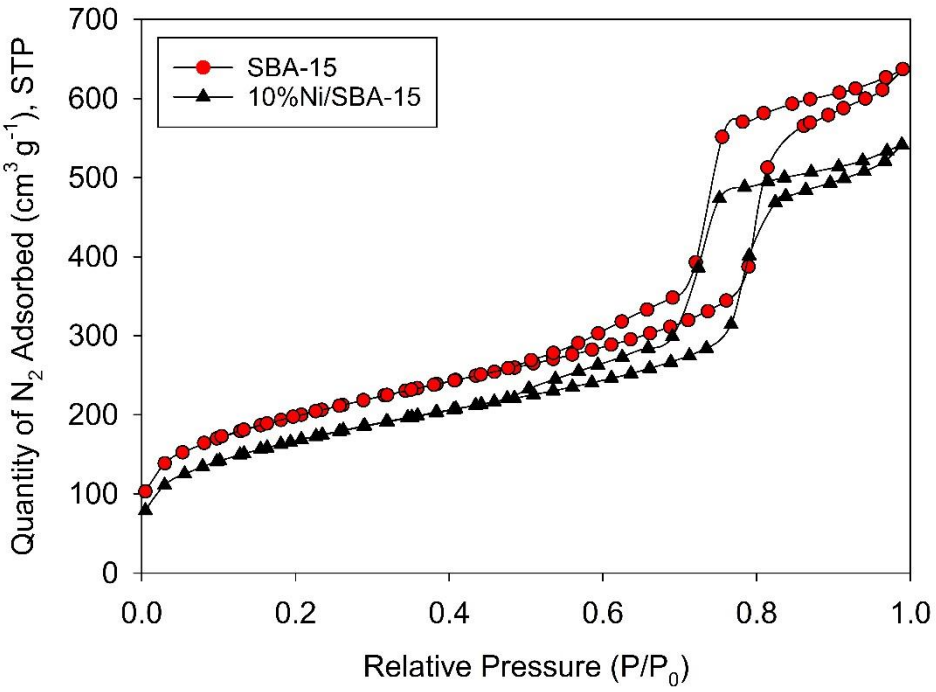


Figure 4.3 Nitrogen adsorption/desorption isotherms of SBA-15 and 10%Ni/SBA-15 before reduction in H_2.

The textural properties including BET surface area, pore size and pore volume for SBA-15 support and 10%Ni/SBA-15 catalyst are given in Table 4.3. SBA-15 exhibits a high surface area of 664.4107 ± 1.1197 m^2 g^{-1}. However, the surface area decreased to 609.868 ± 1.0902 m^2 g^{-1} after the impregnation of Ni into its framework. Similarly, the pore size and pore volume also decreased from 5.47447 nm and 0.909324 cm^3 g^{-1}, to 5.18621 nm and 0.790725 cm^3 g^{-1}, respectively, and this was attributed to partial pore blockage by the NiO species.

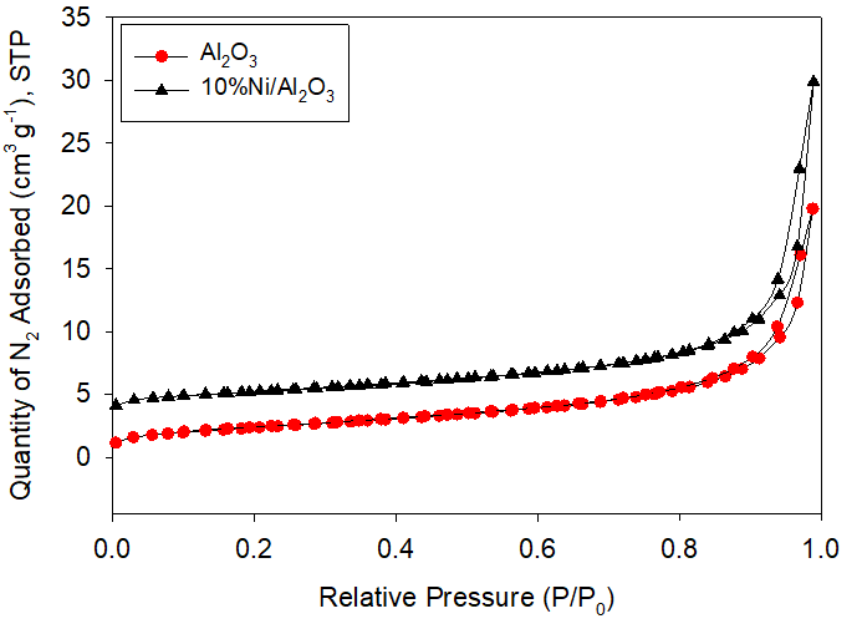


Figure 4.4 Nitrogen adsorption/desorption isotherms of Al2O3 and 10%Ni/Al2O3 before reduction in H2.

depicts the N_2 adsorption/desorption isotherms of Al_2O_3 and 10%Ni/Al_2O_3 catalyst where both materials developed into type IV isotherms with H3-type hysteresis loop in the relative pressure range of 0.78 to 1.0. The similarity in the isotherms of both Al_2O_3 and 10%Ni/Al_2O_3 catalyst suggest that there was no significant alteration in the Al_2O_3 support's pore structure after the impregnation of NiO.

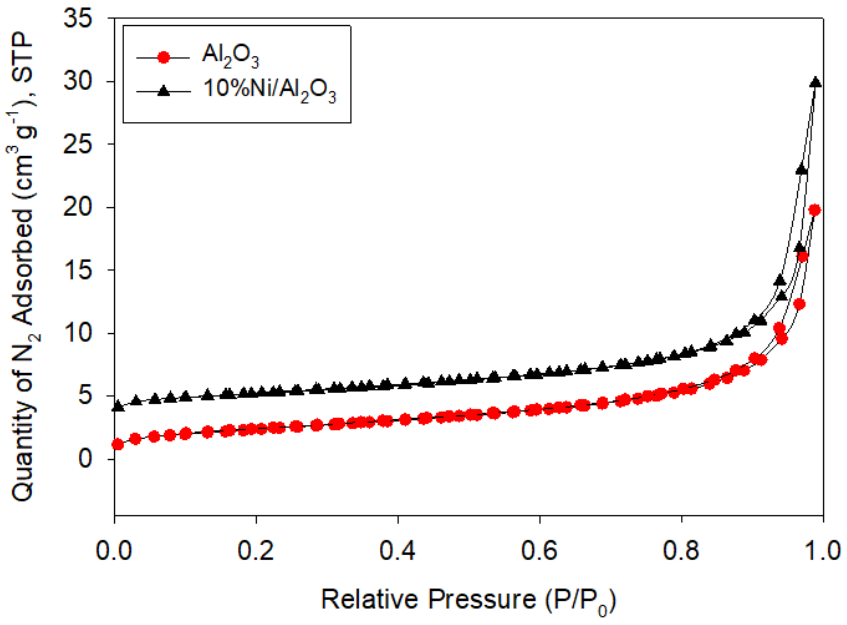


Figure 4.4 Nitrogen adsorption/desorption isotherms of Al_2O_3 and 10%Ni/Al_2O_3 before reduction in H_2.

Table 4.3 Textural properties of SBA-15, CeO_2, Al_2O_3 and YSZ supports and their Ni-based catalysts before reduction in H_2.

Samples	BET surface area (m^2 g^{-1})	Pore size (nm)[a]	Pore volume (cm^3 g^{-1})[b]
SBA-15	664.4107 ±1.1197	5.47447	0.909324
10%Ni/SBA-15	609.8681 ± 1.0902	5.18621	0.790725
CeO_2	5.2883 ± 0.0156	8.46286	0.011189
10%Ni/CeO_2	4.3261 ± 0.0214	9.63428	0.010420
Al_2O_3	8.4632 ± 0.0327	7.19775	0.015229
10%Ni/Al_2O_3	8.0257 ± 0.0130	7.77670	0.015603
YSZ	5.8248 ± 0.0057	5.63887	0.008211
10%Ni/YSZ	5.2464 ± 0.0052	6.02938	0.007908

a Data was obtained from the BJH adsorption average pore diameter (4v/A by BET); b Data was obtained from the BJH single point adsorption at P/P_o = 0.95.

Figure 4.5 shows the N_2-adsorption/desorption isotherms of CeO_2 and the 10%Ni/CeO_2 catalyst. The isotherms developed into type IV isotherms with H3-type hysteresis loop (Sun et al., 2022b). However, the capillary condensation and evaporation were found to start at a low relative pressure of P/P0 = 0.45. This indicates that the CeO_2 supported catalyst has more micropores than the SBA-15, Al_2O_3 and YSZ supported catalysts since less pressure is required to fill micropores than to fill mesopores (Zhou et al., 2023; Shivakumar and Maitra, 2023).

Furthermore, the textural data shown in Table 4.3 revealed that there was a decrease in the BET surface area and pore volume of CeO_2 after impregnation with the NiO to form the 10%Ni/CeO_2 catalyst. The decrease in the surface area and pore volume after the incorporation of the NiO species may be attributed to the dispersion of the metals into the support pore channels, resulting in partial pore blockage.

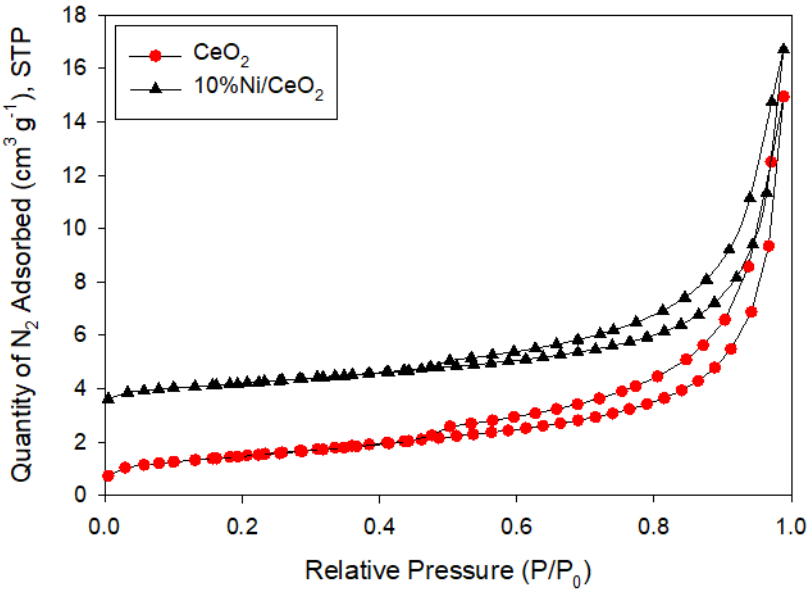


Figure 4.5 Nitrogen adsorption/desorption isotherms of CeO_2 and 10%Ni/CeO_2 before reduction in H_2.

4.2 X-ray diffraction measurement

The crystalline phases present in all the catalysts were investigated by powder XRD. The recorded diffractograms of both the freshly prepared and reduced catalysts are presented in

Figure 4.6 to 4.8. The X-ray peaks were matched with the Joint Committee on Powder Diffraction Standards (JCPDS) database (Wong-Ng et al., 1982; JCPDS Powder Diffraction File, 2000). The NiO and Ni^0 particle sizes were estimated using the Debye–Scherrer equation (Eq. **(**3.6**)**).

4.2.1 XRD of Ni-based YSZ catalysts

Figure 4.6 (a) represents the XRD patterns of the freshly prepared YSZ and Ni/YSZ catalysts. The recorded diffractograms indicates the existence of YSZ peaks (JCPDS 81–1550) at 2θ = 29.9° (1 1 1), 34.6° (2 0 0), 50.0° (2 2 0), 59.4° (2 2 2), 62.3° and 73.5° (4 0 0) (Zhou et al., 2020; Kesavan et al., 2018). NiO peaks (JCPDS 73–1519) were observed at 2θ = 37.4°, 43.4°, 75.6° and 79.5° for the 30%Ni, 50% and 75%Ni catalysts, while the NiO peak intensities observed at 2θ = 37.4°, 43.4° and 75.6° for the 5%Ni and 10%Ni catalysts were very weak. In addition, there was an overlap between the YSZ and NiO phases at 2θ = 62.8°.

Figure 4.6 (b) shows the XRD patterns of the reduced Ni/YSZ catalysts. After the catalyst reduction in H_2, the peak at 2θ = 37.4° disappeared while the peak at 43.4° shifted to around 44.5° to 45°, indicating the presence of Ni^0 metal. A new peak appeared at about 52°, and this was ascribed to the presence of Ni^0 metal. Furthermore, the particle size calculation using the Scherrer equation showed that there was a relative increase in Ni particle size after the reduction in H_2 (Table 4.4).

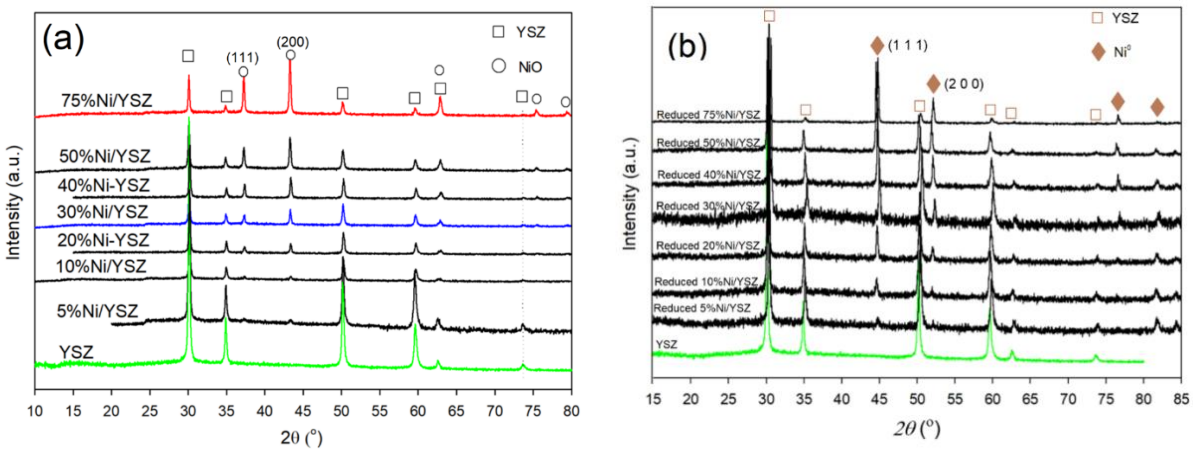


Figure 4.6 XRD patterns of (a) fresh and (b) reduced Ni/YSZ catalysts with different Ni-loading.

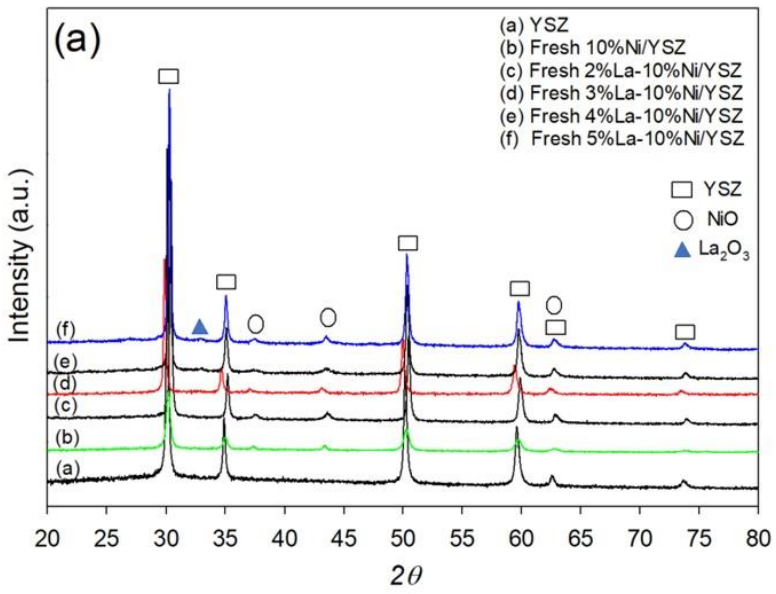
Table 4.4 Crystallite size of Ni and NiO in both fresh and reduced Ni/YSZ catalysts. Estimation from Scherrer equation with the (2 0 0) reflection for NiO phase in the unreduced Ni/YSZ catalysts and (1 1 1) for Ni phase in the reduced Ni/YSZ catalysts in the XRD data.

Samples	Crystallite size, d (nm)	
	d_{NiO}	d_{Ni}
YSZ	-	-
5%Ni/YSZ	21.73 ± 0.000689782	25.74 ± 0.002541344
10%Ni/YSZ	31.36 ± 0.002251982	34.39 ± 0.000924852
20%N/YSZ	31.24 ± 0.004910579	36.52 ± 0.002787709
30%N/YSZ	33.73 ±0.003514915	36.22 ± 0.002392454
40%N/YSZ	35.75 ± 0.003048091	39.11 ± 0.000208785
50%Ni/YSZ	35.83 ± 0.004208775	40.30 ± 0.002971849
75%Ni/YSZ	35.92 ± 0.000465413	41.08 ± 0.0006851

The increase in Ni particle size after the reduction of NiO was unexpected. However, the reduction of the catalyst at elevated temperature has been reported to encourage crystal growth through migration and coalescence or atom diffusion (Villarba and Jónsson, 1994; Ruckenstein and Pulvermacher, 1973; Ghaani and Catti, 2019; Lee, 1980). Yi et al. (2022) employed the atom diffusion mechanism to conduct a sintering kinetic study for the growth of Ni during the reduction of a series of Ni-based catalysts. The authors stated from their findings that the distance between the diffused Ni species and metal-support interactions (MSI) or variation in pore size and shape influenced the order of sintering kinetics of Ni. Notwithstanding the occurrence of Ni crystal growth, all the reduced catalysts exhibited similar XRD patterns,

which indicated that the Ni/YSZ structure was not significantly altered after the reduction process.

Figure 4.7 (a) and (b) illustrate the XRD patterns of the freshly prepared and reduced La-promoted Ni/YSZ catalysts. The XRD patterns of the unreduced La-promoted Ni/YSZ catalysts in Figure 4.7 (a) exhibited a similar pattern with that of the unreduced 10%Ni/YSZ catalyst. However, the NiO peaks slightly shifted to the left at 2θ = 37.0°, 43.1° and 62.4° for the 3%La-10%Ni/YSZ catalyst indicating that the 3%La addition likely aided the modification of the catalyst structure. Furthermore, the presence of lanthanum oxide (La_2O_3) could not be detected for La contents below 3%. When the La contents was raised above 3% (4%La-10%Ni/YSZ and 5%La-10%Ni/YSZ catalysts), a diffraction peak which can be assigned to La_2O_3 (JCPDS-ICDD: 05-0602) was observed at 2θ = 32.9° (Xiao et al., 2014; Wang et al., 2014).



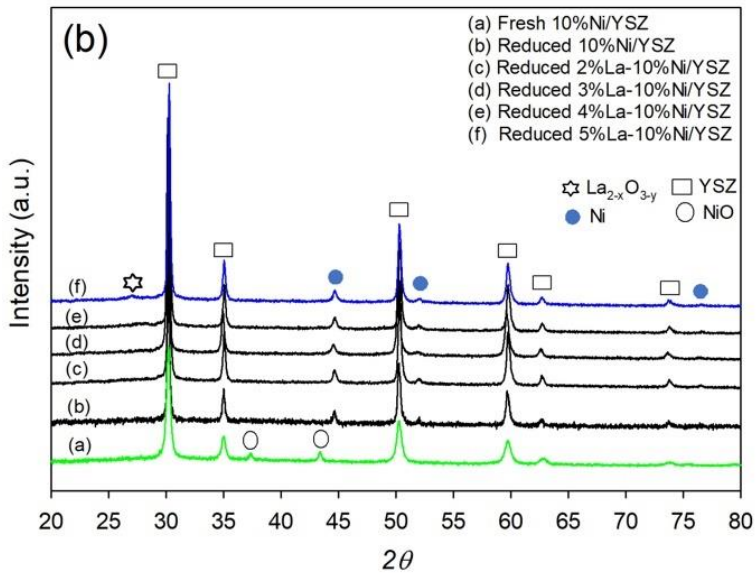


Figure 4.7 XRD patterns of (a) fresh and (b) reduced La-promoted Ni/YSZ catalysts.

Table 4.5 Crystallite size of Ni and NiO in both fresh and reduced 10%Ni/YSZ and La-promoted Ni/YSZ catalysts. Estimation from Scherrer Equation with the (2 0 0) reflection for NiO phase in the unreduced Ni/YSZ catalysts and (1 1 1) for Ni phase in the reduced Ni/YSZ catalysts in the XRD data

Samples	Crystallite size (nm)	
	d_{NiO}	d_{Ni}
YSZ	-	-
10%Ni/YSZ	31.36 ± 0.002251982	34.39 ± 0.000924852
2%La-10%Ni/YSZ	17.27 ± 0.0020528	24.93 ± 0.002414165
3%La-10%Ni/YSZ	16.33 ± 0.002199891	20.40 ± 0.004741212
4%La-10%Ni/YSZ	14.87 ± 0.002683365	23.24 ± 0.000859852

5%La-10%Ni/YSZ	23.06 ± 0.002592261	24.00 ± 0.003078849

Figure 4.7 (b) depicts the XRD patterns of the reduced La-promoted Ni/YSZ catalysts where Ni peaks were detected at 2θ = 44.7°, 52° and 76.6°. Interestingly, a new peak with weak intensity appeared at 2θ = 27.1° for the 5%La-10%Ni/YSZ catalyst. This may be attributed to the presence of La species ($La_{2-x}O_{3-y}$) where $0 \leq x < 2$, and $0 \leq y < 3$. In this study, x and y are assumed to be zero suggesting that the La species at 2θ = 27.1° is La_2O_3, and this is in agreement with literature data (Liu et al., 2016). Notwithstanding, it has been suggested that in a situation where reduction takes place, the La species may be reduced into La_2O_{3-x} (Li et al., 2012) or LaO_x (x<1.5) (Bernal et al., 1997). However, it could not be confirmed if there was reduction of any La species based on the available data. Therefore, additional analysis is suggested to determine whether there would be a reduction of La species during a H_2-TPR of La-promoted Ni/YSZ catalysts. The estimation of the particle sizes of the La-promoted catalyst using the Scherrer equation (see Table 4.5) revealed the catalyst size was greatly reduced after the La-promotion. Therefore, it was inferred that the addition of the La-promoter helped in suppressing the sintering process during the catalyst synthesis. It also suggested that the presence of the La-promoter in the Ni/YSZ catalyst aided enhancement of the Ni particles distribution over the surface. It is worth mentioning that the promotional influence of La was significant for the La contents below 5%.

4.2.2 XRD of Ni-based Al_2O_3, CeO_2 and SBA-15 catalysts

The X-ray diffraction patterns of fresh and reduced 10%Ni/Al_2O_3, 10%Ni/SBA-15 and 10%Ni/CeO_2 catalysts were also examined, and the results are represented in Figure 4.8 to 4.10. Figure 4.8 illustrates the XRD pattern of SBA-15, and unreduced and reduced 10%Ni/SBA-15 catalysts. As seen in the figure, a phase appeared around 2θ = 15 – 30°. This broad peak may be attributed to the SiO_2 structure of the SBA-15 (JCPDS card No. 29-0085) (Zhang et al., 2023a). This SiO_2 phase was also noticed in the XRD pattern of the unreduced and reduced 10%Ni/SBA-15 catalysts indicating that the mesoporous structure of the silica was

not significantly altered after synthesis. In Figure 4.8 (b), the peaks detected at 2θ = 37.1°, 43.2°, 62.8°, 75.5° and 78.2° are ascribable to the (1 1 1), (2 0 0), (2 2 0), (3 1 1) and (2 2 2) reflections, respectively, of the NiO phase (JCPDS card No. 47-1049).

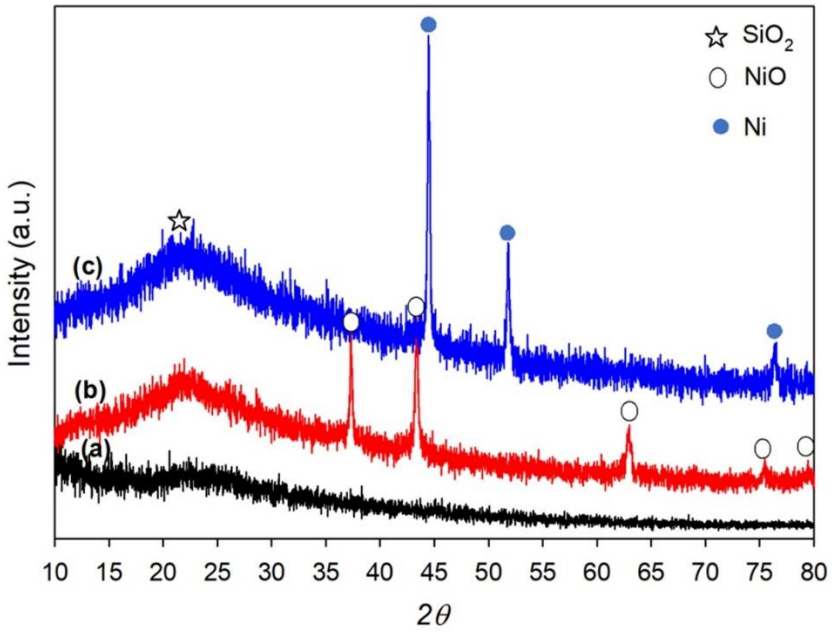


Figure 4.8 XRD patterns of (a) SBA-15, (b) unreduced 10%Ni/SBA-15 and (c) reduced 10%Ni/SBA-15 catalysts.

In Figure 4.8 (c), the peaks observed at 2θ = 44.6°, 52.0° and 76.6° may be assigned to the Ni phase. The NiO particle and Ni crystallite sizes were also estimated using the Scherrer equation, and the results are given in Table 4.6. The Ni crystallite size for the 10%Ni/SBA-15 catalyst was higher than the NiO particle size, indicating that sintering occurred during the catalyst reduction in H_2.

Table 4.6 Crystallite size of Ni and NiO in both fresh and reduced 10%Ni/YSZ, 10%Ni/Al_2O_3, 10%Ni/SBA-15 and 10%Ni/CeO_2 catalysts.

Samples	Crystallite size, d (nm)		
	d_{NiO}	d_{Ni}^{*}	d_{Ni}^{**}
10%Ni/YSZ	31.36 ± 0.002251982	34.39 ± 0.000924852	23.91471
10%Ni/Al_2O_3	28.42 ± 0.001217952	32.08 ± 0.001411639	28.66058
10%Ni/SBA-15	27.63 ± 0.001075886	29.53 ± 0.002685854	15.01891
10%Ni/CeO_2	41.28 ± 0.004535681	44.43 ± 0.000728086	38.6412

* Estimation was obtained from the Scherrer Equation using the highest FWHM of NiO and Ni peaks in the XRD data of the catalysts; ** Particle size was obtained from TEM results.

Figure 4.9 represents the XRD patterns of Al_2O_3, unreduced and 10%Ni/Al_2O_3 catalysts. The Al_2O_3 phase (JCPDS 65 – 3102) was noticed at 2θ = 25.6°, 35.2°, 37.8°, 43.4°, 52.6°, 57.6°, 61.2°, 66.5°, 68.4° and 76.8°. For the unreduced 10%Ni/Al_2O_3 catalyst, the peaks located around 2θ = 37.4°, 62.8° and 75.6° and 79.4° represent NiO phases (JCPDS 47–1049). Although it was reported in the literature that a surface nickel aluminate ($NiAl_2O_4$) spinel is formed when NiO interacts with Al_2O_3 at temperatures ≥ 673 K during calcination (Cesteros et al., 2000), the $NiAl_2O_4$ phase (JCPDS 10–0339) was not visible in the XRD results obtained in this study. This is likely due to the overlapping effect between the Al_2O_3 and $NiAl_2O_4$ phases (Qiu et al., 2022). For the unreduced 10%Ni/Al_2O_3 catalyst, the peaks located around 2θ = 44.6° and 51.8° may be assigned to the Ni phase. The sizes of the NiO and Ni particles were calculated according to the Scherrer equation, and the results are given in Table 4.6. The results of the particle size calculation revealed that there was particle growth leading to larger Ni sizes after the reduction of the 10%Ni/Al_2O_3 catalyst in H_2.

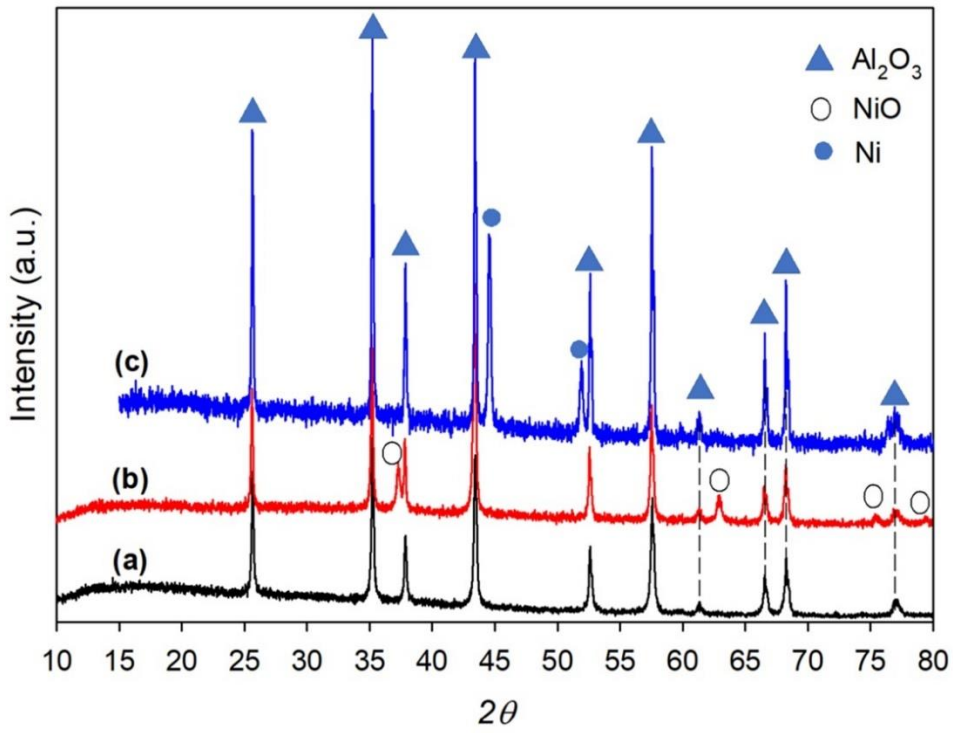


Figure 4.9 XRD patterns of (a) Al_2O_3, (b) unreduced 10%Ni/Al_2O_3 and (c) reduced 10%Ni/Al_2O_3 catalysts.

Figure 4.10 illustrates the XRD patterns of unreduced and reduced 10%Ni/CeO_2 catalysts. Figure 4.10 (a) represents the XRD pattern of unreduced 10%Ni/CeO_2 catalyst where eight peaks ascribable to the CeO_2 phase (JCPDS number 34-0394) appeared at 2θ = 28.5°, 33.2°, 47.6°, 56.4°, 59.2°, 69.6°, 76.6° and 79.1° (Zhou et al., 2017). Three peaks attributable to NiO were observed at 2θ = 37.4°, 43.4° and 62.8°. The weak intensities of the NiO phase suggests a fine dispersion of the NiO particles within the CeO_2 support framework. Figure 4.10 (b) illustrates the XRD pattern of the 10%Ni/CeO_2 catalyst after reduction in H_2. As seen in the figure, two diffraction peaks credited to the Ni phase appeared at 2θ = 44.5° and 51.9°. Meanwhile, the particle size calculation (see Table 4.6) revealed that the Ni particle size was higher than the NiO size indicating the occurrence of particle growth resulting from the reduction of the 10%Ni/CeO_2 catalyst. This growth is also evident in the diffraction peaks where the Ni phases have higher peak intensities compared to the NiO phases.

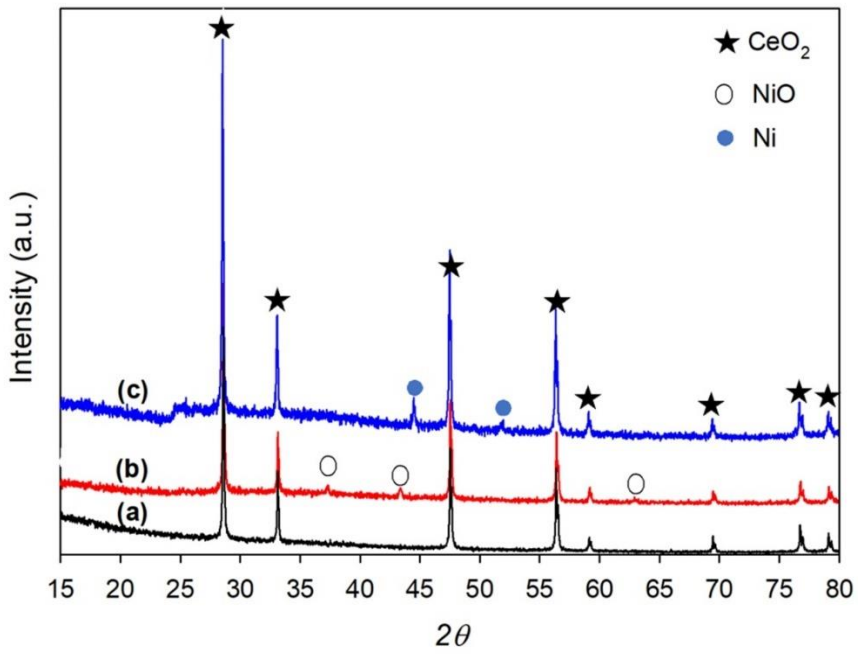


Figure 4.10 XRD patterns of (a) CeO_2 (b) unreduced 10%Ni/CeO_2 and (c) reduced 10%Ni/CeO_2 catalysts.

4.3 Thermogravimetric analysis

4.3.1 Temperature-programmed calcination (TPC)

Figure 4.11 represents the temperature-programmed calcination (TPC) profile of uncalcined SBA-15. As seen in Figure 4.11, the drastic weight loss around 573 and 673 K for the SBA-15 support may be attributed to the degradation of the residual copolymer surfactant and any other impurities covering the sample. For the Ni/SBA-15 catalyst, the rapid decrease in weight was observed around 423 and 573 K. This trend can be attributed to the decomposition of $Ni(NO_3)_2.6H_2O$ or $Ni(OH)_2$ into NiO (Burattin et al., 1999; Wang et al., 2006). Figure 4.12 represents the TPC for 10%Ni/YSZ, 10%Ni/Al_2O_3, 10%Ni/SBA-15 and 10%Ni/CeO_2 catalysts. According to previous studies (Brockner et al., 2007; Sietsma et al., 2008; Mentus et al., 2007), the decomposition process of these catalysts was grouped into three stages: (a), (b), and (c), as shown in Eqs. **(**4.1) to **(**4.4). Stage (a) involves the removal of chemisorbed water, as represented by Eq **(**4.1). Stage (b) involves nitrate decomposition, as represented by Eq. **(**4.2). Stage (c) involves the decomposition of two different oxides of nickel to NiO, as

represented by Eqs. **(**4.3) and **(**4.4). It is worth noting that the decomposition of the nitrates in all the samples was completed at slightly different temperatures.

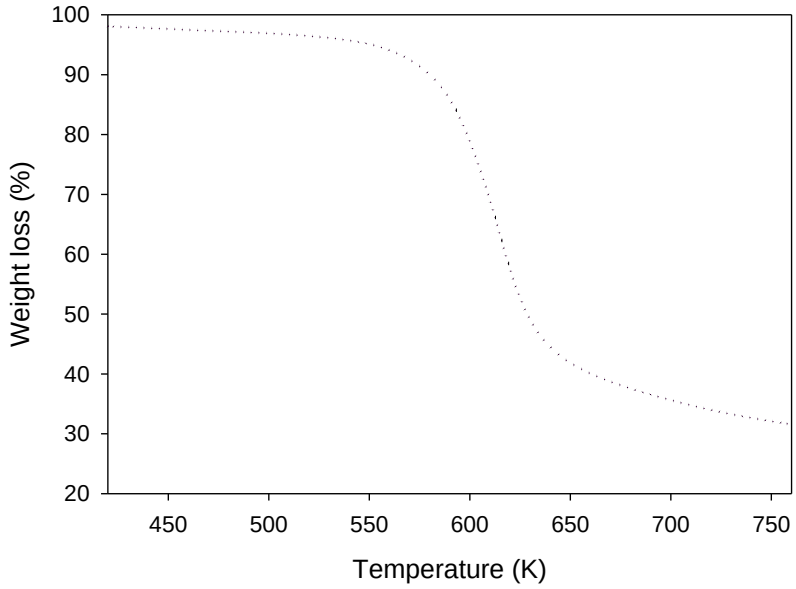


Figure 4.11 Temperature-programmed calcination profile of uncalcined SBA-15 at heating rate of 10 K min^{-1} under N_2 atmosphere. Equipment model: NETZSCH - TG 209 F1.

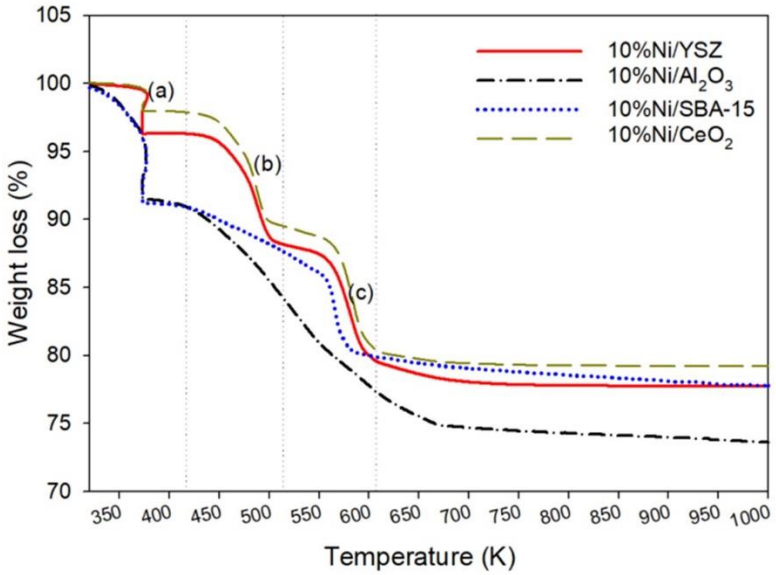


Figure 4.12 TPC profile of 10%Ni/YSZ, 10%Ni/Al_2O_3, 10%Ni/SBA-15 and 10%Ni/CeO_2 catalysts at heating rate of 10 K min^{-1} under N_2 atmosphere. Equipment model: NETZSCH - TG 209 F1.

For example, the decomposition to form 10%Ni/SBA-15, 10%Ni/YSZ, 10%Ni/Al_2O_3 catalysts was completed at about 573, 623 and 673 K, respectively. This variation is likely due to the differences in the support-metal interactions where the least bonded species encouraged a complete decomposition at a lower temperature.

$$Ni(NO_3)_2.6H_2O \rightarrow Ni(NO_3)(OH)_{1.5}.O_{0.25}H_2O \quad (4.1)$$

$$Ni(NO_3)(OH)_{1.5}.O_{0.25}H_2O \rightarrow 0.5Ni_2O_3 + HNO_3 + 1.25H_2O \quad (4.2)$$

$$3Ni_2O_3 \rightarrow 2Ni_3O_4 + 0.5O_2 \quad (4.3)$$

$$Ni_3O_4 \rightarrow 3NiO + 0.5O_2 \quad (4.4)$$

4.3.2 H_2 temperature-programmed reduction

The reduction behaviour of all the catalysts was investigated using the TPR-MS technique in the 5%H_2/20%N_2 environment.

4.3.2.1 H_2-TPR profiles for YSZ catalysts

The H_2-TPR profiles of Ni/YSZ catalysts with variation in Ni loading are shown in Figure 4.13. As seen in the figure, both the 5%Ni and 10%Ni loading exhibited similar behaviour at temperatures ranging from 567 to 810 K. Meanwhile the reduction of 30%Ni, 50% and 75%Ni catalysts was in the range of 520 to 860 K. The reduction peak temperatures for all the catalysts are given in Table 4.7. The first peak observed at lower temperatures for all the catalysts can be attributed to the reduction of bulk NiO with weak support interaction to Ni^0, while the second peak at higher temperatures can be ascribed to the reduction of the highly dispersed NiO particles with stronger MSI (Lopera et al., 2022; Shahid et al., 2020).

These results revealed that higher Ni loading of around 30 to 40% decreases the reducibility of the catalysts as seen in the shift in the reduction peaks to the right and enlarged peak 2, which means that a higher temperature is required for the complete reduction of the NiO particles. This indicated higher interaction with the support and was in line with the BET results. Further increase in Ni loading to 50 to 75% resulted in the availability of more NiO with weak MSI. This also led to the shift in reduction temperatures of NiO to the left (lower region) as indicated by the enlarged peak 1 (Figure 4.13).

Notwithstanding, the reduction of all the catalysts was completed before reaching 973 K. Therefore, 973 K was selected as the catalysts' reduction temperature to ensure that the NiO species were completely reduced before testing their activities in this study.

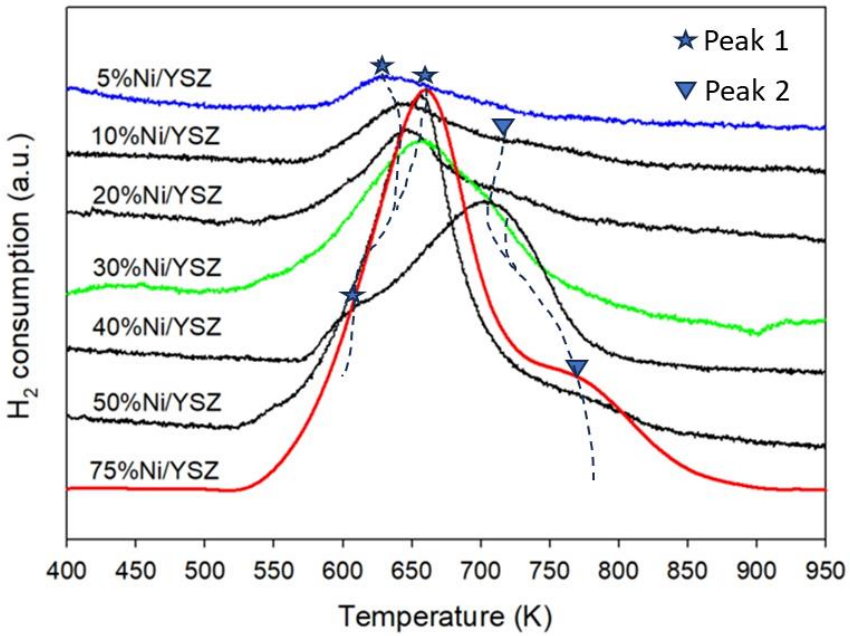


Figure 4.13 H_2-TPR profiles of 5%Ni/YSZ, 10%Ni/YSZ, 20%Ni/YSZ, 30%Ni/YSZ, 40%Ni/YSZ, 50%Ni/YSZ and 75%Ni/YSZ calcined catalysts before the reaction.

Table 4.7 Reduction peak temperatures during the H2-TPR of calcined Ni/YSZ catalysts.

Samples	Reduction Peak temperatures (K)*	
	Peak 1	Peak 2
5%Ni/YSZ	629	-
10%Ni/YSZ	641	734
20%N/YSZ	645	724
30%N/YSZ	654	748
40%N/YSZ	601	706
50%Ni/YSZ	654	778

75%Ni/YSZ	659	764

* Reduction peak temperatures were obtained from H_2-TPR profiles.

Figure 4.14 represents the H_2-TPR profiles of La-promoted catalysts. As seen in the figure, there was a slight shift in the reduction temperature towards the lower region after the La-promoter was introduced into the Ni/YSZ catalyst. This indicates that the presence of La-promoter enhanced the catalyst's reducibility.

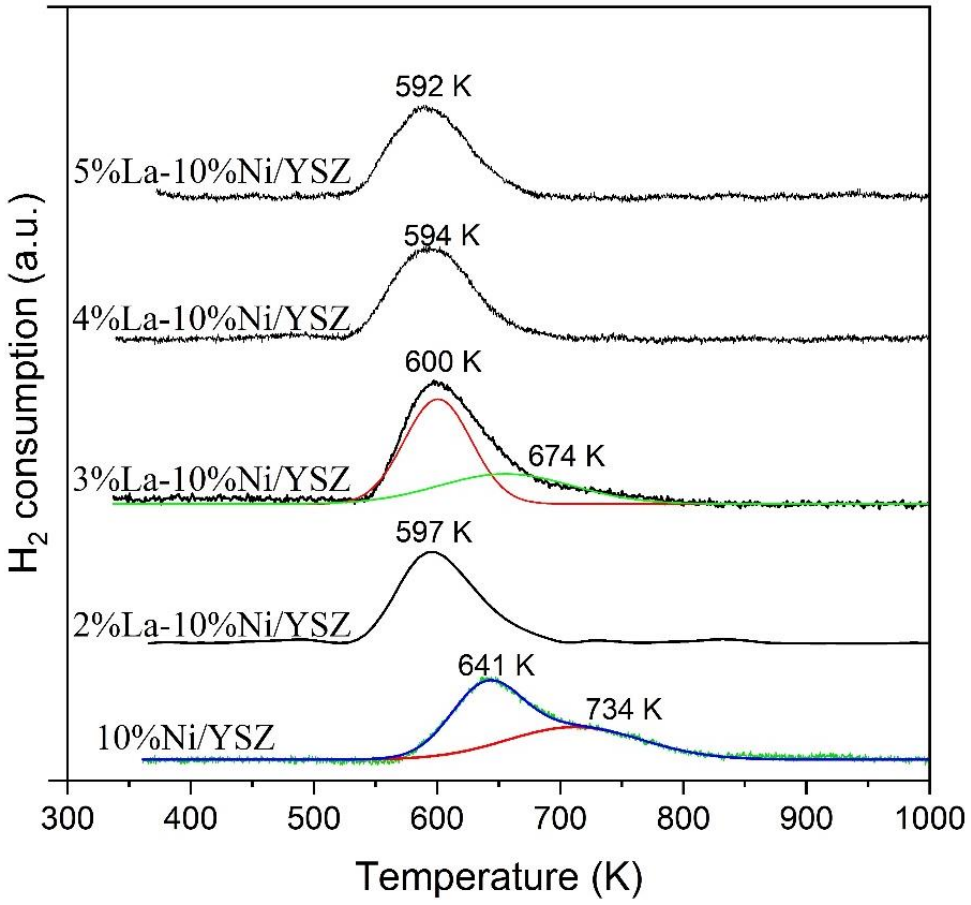


Figure 4.14 H_2-TPR profiles of 10%Ni/YSZ and La-promoted Ni/YSZ catalysts.

4.3.2.2 H2-TPR profiles of 10%Ni/SBA-15, 10%Ni/CeO_2, 10%Ni/Al_2O_3 catalysts

The H_2-TPR profiles of 10%Ni/SBA-15, 10%Ni/CeO_2, 10%Ni/Al_2O_3, and 10%Ni/YSZ catalysts are shown in Figure 4.15. As seen in the figure, the H_2-TPR profile of 10%Ni/SBA-

15 catalyst exhibited two peaks at 640 K and 826 K. In the first peak, reduction started from about 570 K and attained a maximum at 640 K.

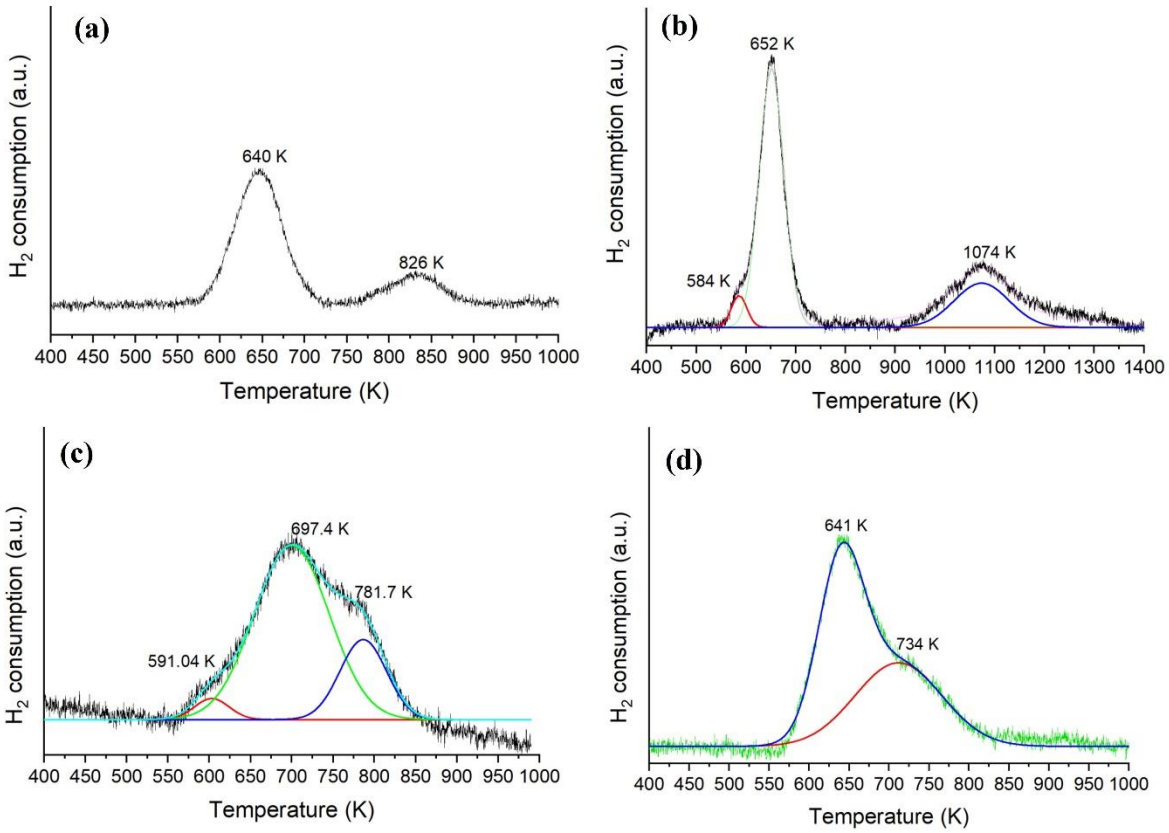


Figure 4.15 H_2-TPR profiles and peak deconvolution of (a) 10%Ni/SBA-15, (b) 10%Ni/CeO_2, (c) 10%Ni/Al_2O_3, and (d) 10%Ni/YSZ catalysts.

This peak can be ascribed to the reduction of bulk NiO particles with the weak MSI which are mainly deposited on the surface (Narksri et al., 2022). The second peak started from about 739 K and attained a maximum at 826 K. This peak can be accredited to the reduction of the highly dispersed NiO species in the SBA-15 support's mesopores which could also indicate the reduction of NiO species with medium-strength MSI with the SBA-15 support (Al-Fatesh et al., 2022b).

Figure 4.15 (b) represents the H_2-TPR profile of the 10%Ni/CeO_2 catalyst. As seen from the figure, a weak shoulder peak appeared at about 584 K, an intense peak at about 652 K and a

broad peak at about 1074 K. The low temperature peak at 584 K can be attributed to the reduction of NiO with weak interaction on the CeO_2 surface while the high temperature peak at 652 K can be ascribed to the reduction of the strongly bonded and highly dispersed NiO species in the pore structure of CeO_2 (Wang et al., 2013).The broad peak displayed at the high temperature of about 1074 K may be attributed to the reduction of CeO_2 (Ma et al., 2022). It was also reported in the literature that during the reduction process Ni^{2+} with an ionic radius of 0.069 nm dissolves into the ceria framework replacing some of the Ce^{4+} ions (radius 0.101 nm) to form Ni-Ce-O species (Wang et al., 2013; Zhou et al., 2022). This alteration of the ceria lattice and the disequilibrium of charges caused by the incorporation of the Ni^{2+} ions usually result in the formation of surface oxygen vacancies which is crucial for many catalytic processes.

Figure 4.15 (c) represents the H_2-TPR profile of the 10%Ni/Al_2O_3 catalyst where three reduction peaks appeared at around 591 K, 697.4 K and 781.7 K. The peak at about 591 K is ascribable to the reduction of NiO particles weakly interacted with the catalyst's support and the peak at about 697.4 K is attributed to the reduction of NiO species with medium-strong interaction with the catalyst's support. The third peak at about 781.7 K may be attributed to the reduction of $NiAl_2O_4$ (Weber et al., 2022). It is worth noting that the $NiAl_2O_4$ species is formed by the incorporation of Ni^{2+} into the alumina framework when NiO interacts with Al_2O_3 during the calcination stage of catalyst synthesis (Younis et al., 2022; He et al., 2022a). Notwithstanding, it was difficult to differentiate between the Al_2O_3 and Al_2O_4 lattices within the catalyst system in the XRD analysis due to their similar crystallographic structures.

4.4 SEM analysis

The SEM imaging was conducted to examine the external morphology and elemental composition of all the catalysts.

4.4.1 SEM images of Ni/YSZ catalysts

The SEM images of the calcined Ni/YSZ catalysts and SEM-EDS elemental mapping of the reduced catalysts are represented in Figure 4.16 and Figure 4.17, respectively. The YSZ support (Figure 4.16 (a)) showed a rough surface with uniform morphology. The SEM image of the 5%Ni/YSZ catalyst Figure 4.16 (b)) showed a uniform surface, which indicates an even

distribution of the Ni particles. This even distribution and absence of sintering of the NiO particles is likely due to the low content of NiO particles with the YSZ support's high surface availability. With increasing Ni content (Figure 4.16 (c) to (f)), the clustering of NiO particles became evident, which is in line with the BET analyses.

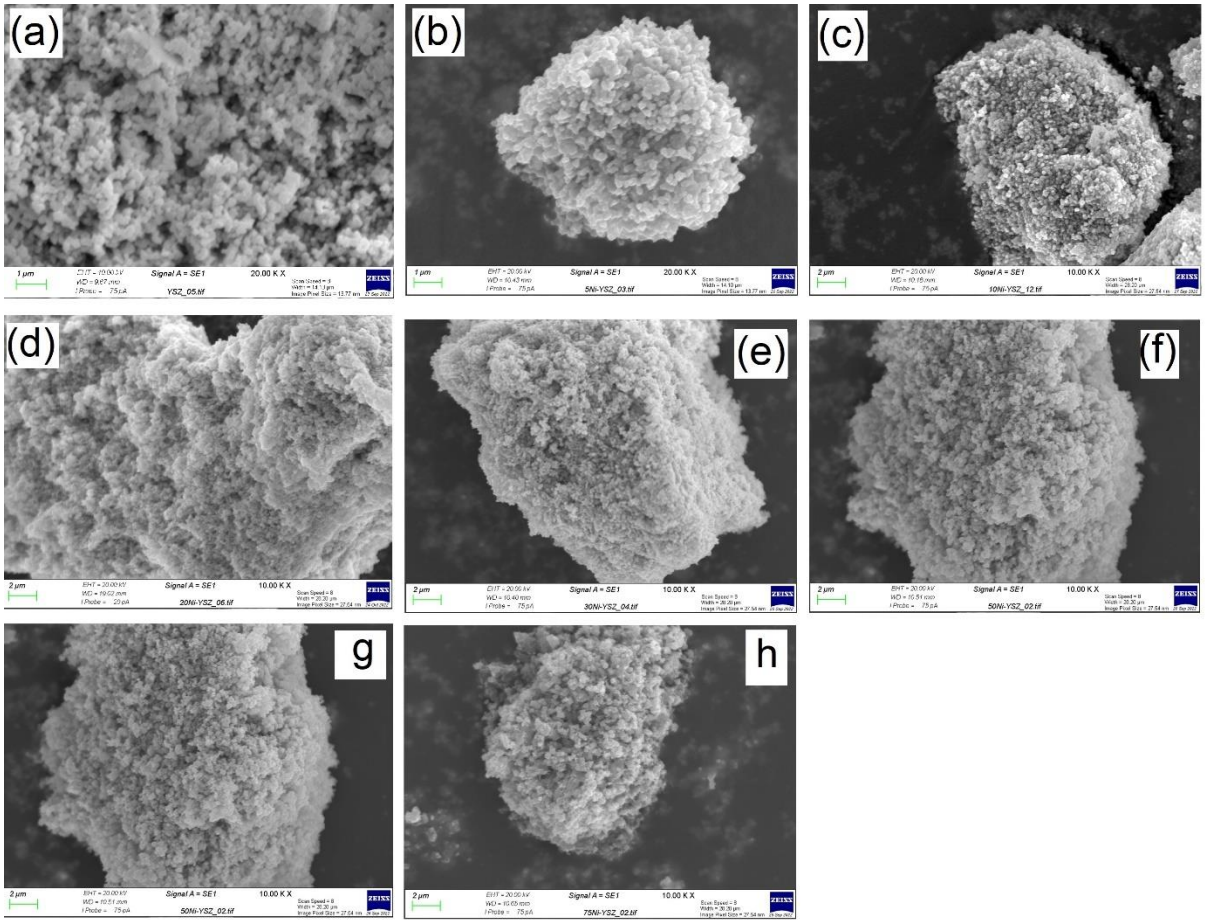


Figure 4.16 SEM images of (a) YSZ, (b) 5%Ni/YSZ, (c) 10%Ni/YSZ, (d) 20%Ni/YSZ, (e) 30%Ni/YSZ, (f) 40%Ni/YSZ, (g) 50%Ni/YSZ and (h) 75%Ni/YSZ calcined catalysts before the reaction. Note: Images were taken in Zeiss Evo10.

The EDS mapping of the reduced catalysts shown in Figure 4.17 gives an insight into how Ni particles are distributed on the catalyst surfaces. At 5%Ni, the Ni particles which were rarely noticed in the mapped image were well dispersed on the surface. The presence of Ni particles started getting more visible as the loading increased from 10% to 75%. However, the mappings of the catalysts with higher Ni loadings from 30% to 75% showed uneven distribution of Ni particles. In addition, the regions showing the presence of Ni clusters also increased with the

Ni loading. This result further supports other analysis indicating the occurrence of significant sintering at higher Ni-loading. The uneven distribution of Ni particles in catalysts can have significant implications on their catalytic activity and stability. A uniform distribution of active catalytic sites is essential for efficient catalytic reactions. Non-uniform dispersion of Ni particles can lead to reduced active surface area and uneven catalytic performance.

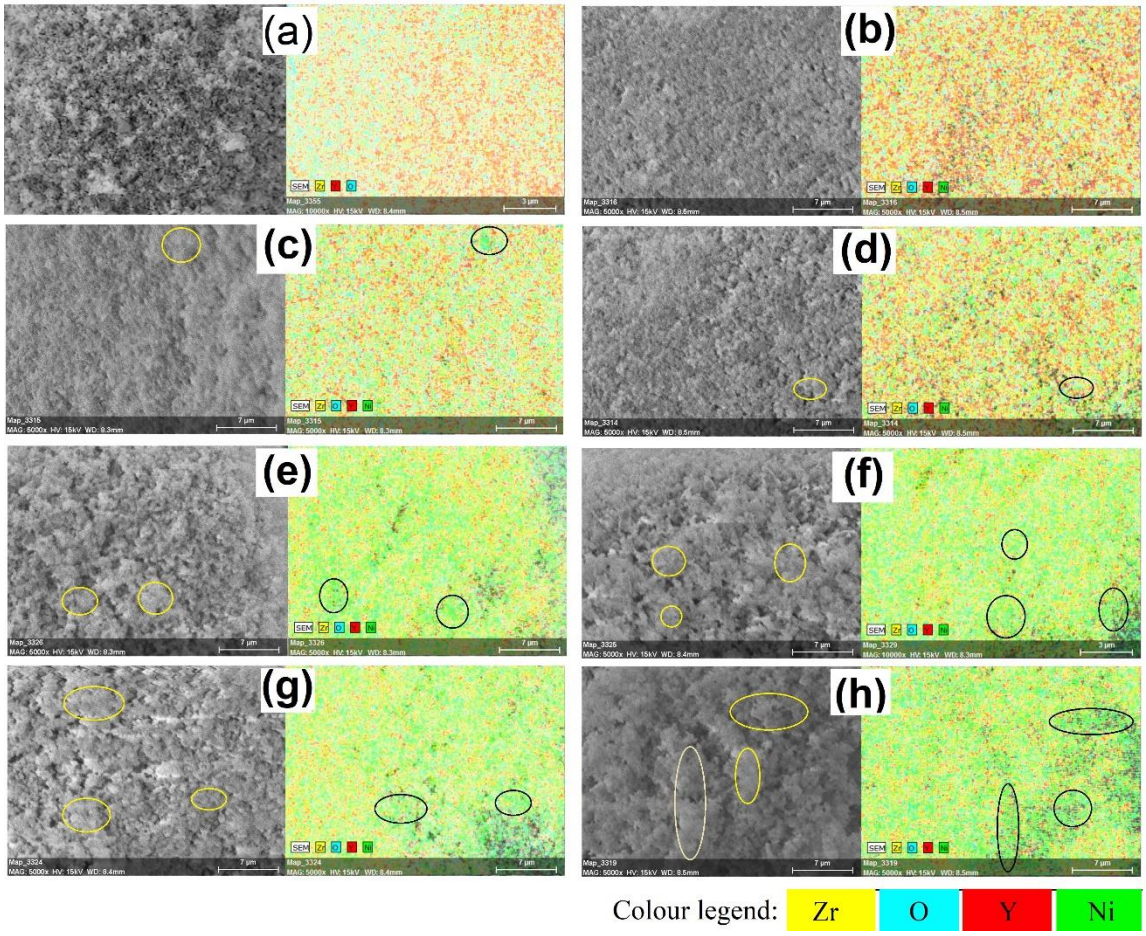


Figure 4.17 SEM-EDS images of (a) YSZ, (b) 5%Ni/YSZ, (c) 10%Ni/YSZ, (d) 20%Ni/YSZ, (e) 30%Ni/YSZ, (f) 40%Ni/YSZ, (g) 50%Ni/YSZ and (h) 75%Ni/YSZ calcined catalysts after reduction.

Figure 4.18 shows the SEM-EDS imaging of YSZ, 10%Ni/YSZ, 2%La-10%Ni/YSZ, 3%La-10%Ni/YSZ, 4%La-10%Ni/YSZ, and 5%La-10%Ni/YSZ. As seen, the SEM-EDS mapping of YSZ shows a uniform distribution of Zr, O, and Y throughout the material. This uniform

distribution indicates that the YSZ substrate does not contain any distinct phases or elemental clustering. The presence of Zr and Y elements confirms the successful stabilisation of zirconia with yttria. The SEM-EDS mapping of the 10%Ni/YSZ catalyst indicates that the Ni particles are well distributed on the YSZ support as discussed earlier. Similar to the 10%Ni/YSZ catalyst, the SEM-EDS mappings of the 2%La-10%Ni/YSZ and 3%La-10%Ni/YSZ catalysts also show well-distributed Ni particles.

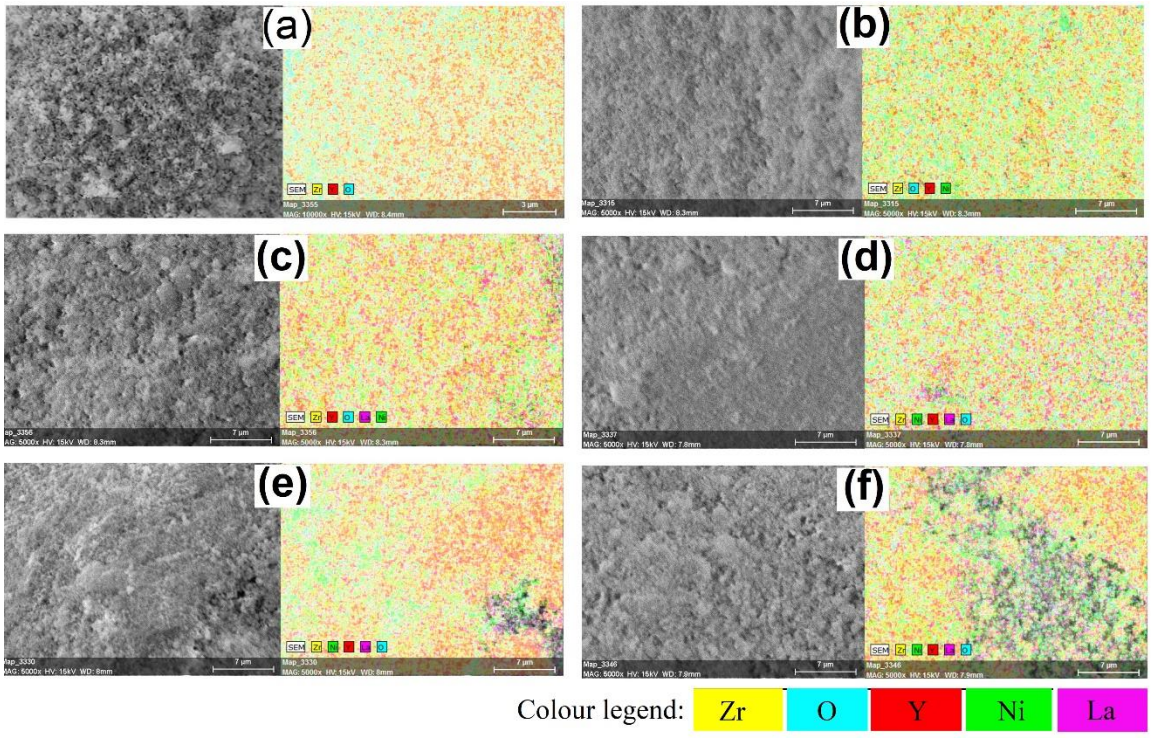


Figure 4.18 SEM-EDS images of (a) YSZ, (b) 10%Ni/YSZ, (c) 2%La-10%Ni/YSZ, (d) 3%La-10%Ni/YSZ, (e) 4%La-10%Ni/YSZ, (f) 5%La-10%Ni/YSZ, catalysts after reduction.

In contrast to the lower La loadings (2% and 3%La), the SEM-EDS mappings of the 4%La and 5%La promoted 10%Ni/YSZ catalysts reveal an uneven distribution of Ni particles. The presence of large Ni agglomerates and uneven clustering of Ni particles suggests that the introduction of higher amounts of La negatively influenced the Ni dispersion, which also resulted in the sintering of some of the Ni particles. The presence of La in the catalysts was not detected by SEM-EDS analysis. The absence of detected La in the SEM-EDS analysis could be due to the relatively low concentration of La in the catalysts or its distribution in such a way that it falls below the detection limit of the EDS technique.

4.4.2 SEM images of 10%Ni/SBA-15, 10%Ni/CeO_2, 10%Ni/Al_2O_3 catalysts

The external morphologies of SBA-15 and 10%Ni/SBA-15 catalysts before and after reduction are given in Figure 4.19 (a) to (c) while the EDX mapping of the reduced 10%Ni/SBA-15 catalyst is illustrated in Figure 4.19 (d). As seen in Figure 4.19 (a), the SBA-15 exhibits uniform cylindrical shaped particles with diameters around 500 to 1200 nm. In Figure 4.19 (b), the 10%Ni/SBA-15 catalyst took a rod-like shape indicating that the support's structure was not significantly altered after NiO incorporation. The image also shows the presence of NiO particles evenly distributed over the surface of the SBA-15 support.

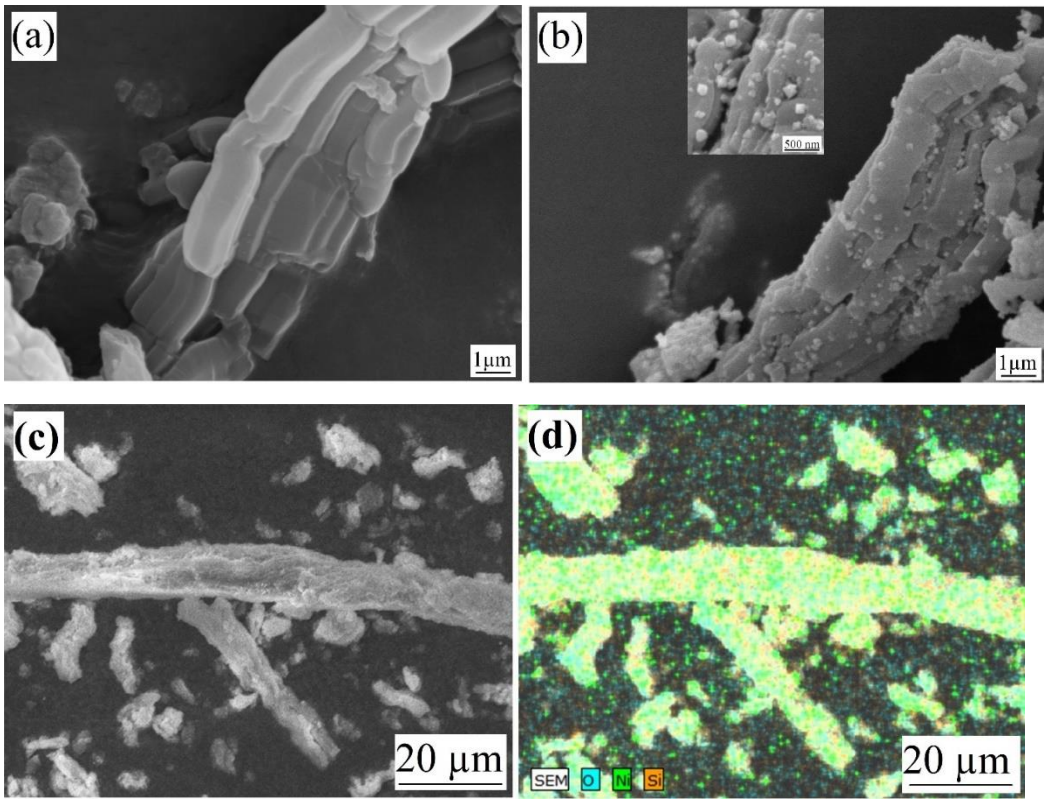


Figure 4.19 SEM-EDS images of (a) SBA-15, (b) 10%Ni/SBA-15, (c) reduced 10%Ni/SBA-15 and (d) EDX mapping of reduced 10%Ni/SBA-15.

After reduction in H_2 environment, Figure 4.19 (c) indicates that the reduced 10%Ni/SBA-15 catalyst maintained the rod-like shape. The EDS mapping of the reduced 10%Ni/SBA-15 catalyst revealed the presence of Si, O, and Ni which were evenly distributed over the surface.

It can also be seen that there was no noticeable agglomeration of the Ni particles over the surface indicating that the catalyst is highly resistant to metal sintering at the high temperatures required for both calcination and reduction processes. This can also be attributed to the high dispersion of the Ni into the support's pores due to its high surface area and pore volume as mentioned in the BET results (see Table 4.3).

The SEM images of CeO_2 and the 10%Ni/CeO_2 catalyst (before and after reduction) are illustrated in Figure 4.20 (a) – (c).

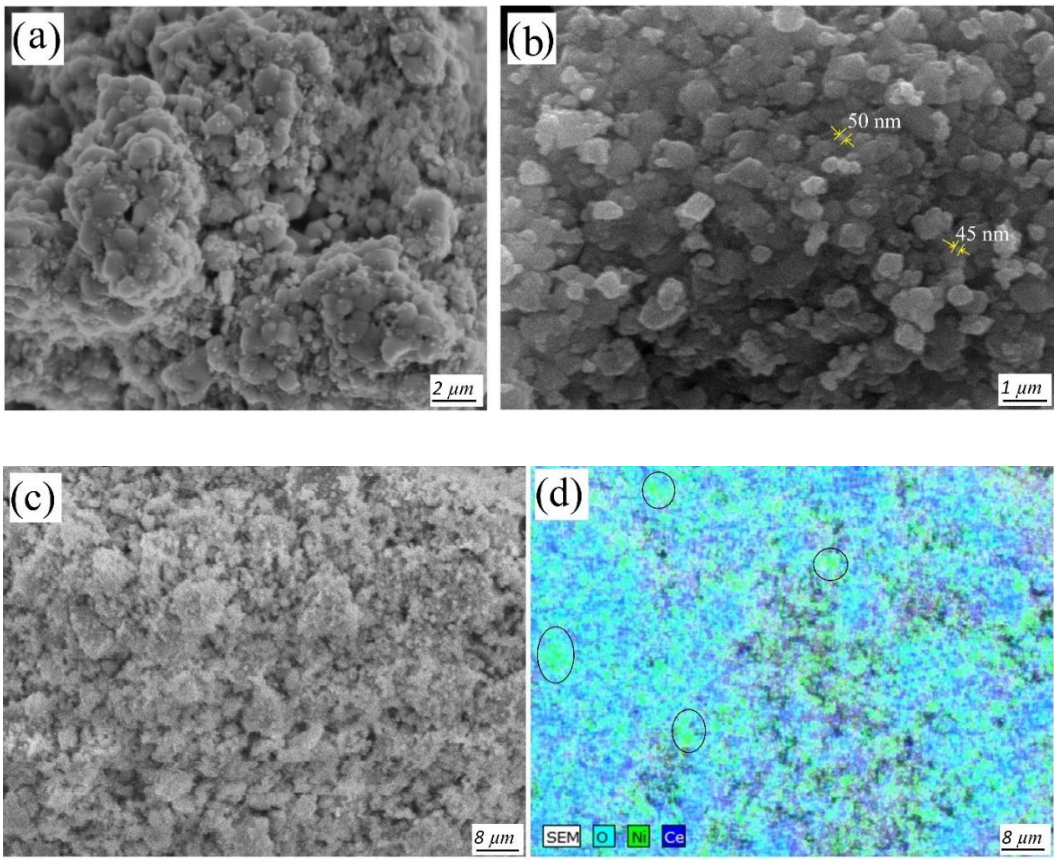


Figure 4.20 SEM-EDS images of (a) CeO_2, (b) 10%Ni/ CeO_2, (c) reduced 10%Ni/ CeO_2 and (d) EDX mapping of reduced 10%Ni/ CeO_2.

As seen in Figure 4.20 (a), the ceria support is comprised of an aggregation of particles with mainly spherical shape. The 10%Ni/CeO_2 catalyst in Figure 4.20 (b) also shows the presence of smaller particles which are evenly distributed. However, it is difficult to identify the NiO

particles within the structure. Therefore, EDX elemental mapping was employed to identify the presence of Ni particles after the reduction of the 10%Ni/CeO_2 catalyst. EDX mapping illustrated in Figure 4.20 (d) reveals the presence of cerium, oxygen, and nickel with unform distribution within the catalyst's framework. The EDX mapping also revealed the occurrence of Ni sintering, where some of the sintered Ni particles are marked in circles. This means that ceria has a suitable surface for the unform distribution of Ni particles while the 10%Ni/CeO_2 catalyst is relatively resistant to Ni sintering at high temperatures.

Figure 4.21 (a) to (c) illustrate the morphologies of the Al_2O_3 support and 10%Ni/Al_2O_3 catalyst before and after reduction, respectively, while Figure 4.21 (d) represents the EDX mapping of the reduced 10%Ni/Al_2O_3 catalyst.

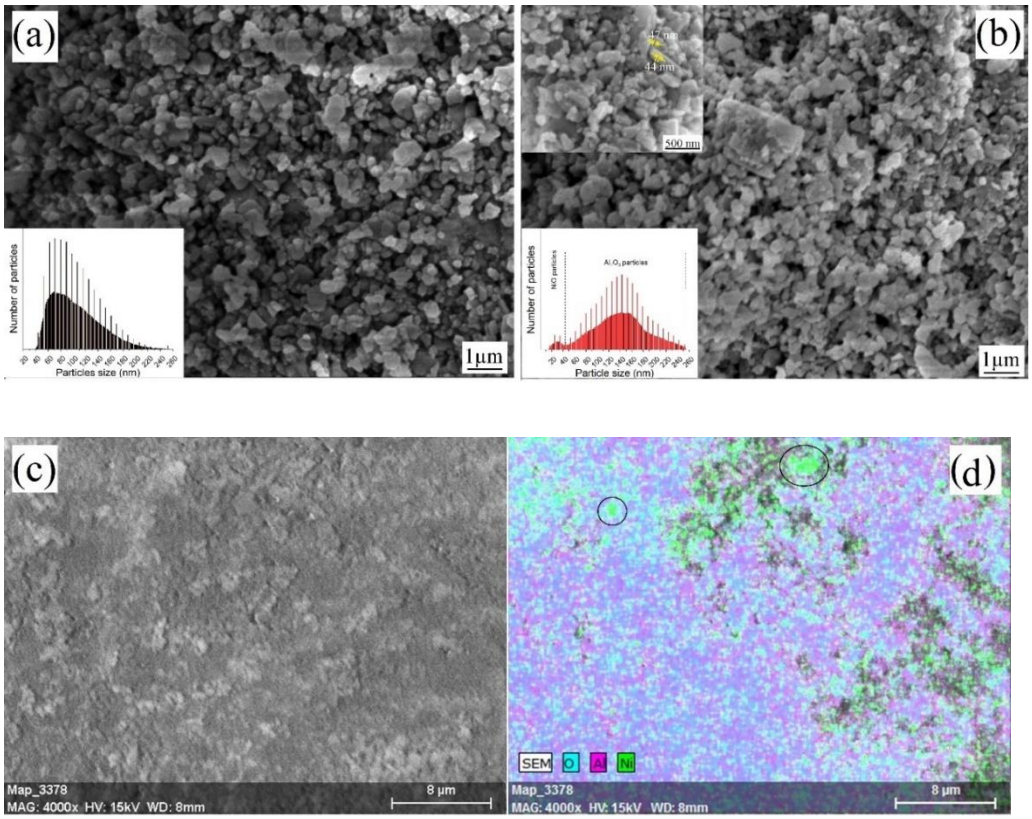


Figure 4.21 SEM-EDS images of (a) Al_2O_3, (b) 10%Ni/Al_2O_3, (c) reduced 10%Ni/Al_2O_3 and (d) EDX mapping of reduced 10%Ni/Al_2O_3.

As seen in Figure 4.21 (a), the Al_2O_3 support comprises aggregation of particles with sizes within the range of 38 and 254 nm as obtained from ImageJ software. After the incorporation

of NiO to form the 10%Ni/Al_2O_3 catalyst as given in Figure 4.21 (b), no noticeable change in the alumina framework was observed. The particle size distribution of the 10%Ni/Al_2O_3 catalyst obtained from ImageJ showed two regions in which the first region can be attributed to the distribution of the NiO particles over the surface and the second region may be ascribed to the distribution of Al_2O_3. The NiO particles size distribution started from about 8 nm to about 50 nm.

This result agrees well with the XRD result (see Table 4.6) since the highest concentration of the NiO particle size can be found within the range of 25 and 35 nm. Figure 4.21 (c) and (d) are the SEM image and EDX mapping, respectively, of the reduced 10%Ni/Al_2O_3 which was carried out to examine the distribution of the Ni particles over the surface and to determine the level of Ni particles sintering. As seen from the EDX mapping, the Ni particles are uniformly distributed over the alumina surface. However, some sintering of Ni particles, marked by circles, was observed. This result shows that the 10%Ni/Al_2O_3 catalyst did not completely resist the occurrence of Ni sintering during the reduction process at a high temperature.

CHAPTER 5

Determination of transport limitations

5.1 Blank test

The blank test involves passing the feed gases (CO_2 and H_2 in the ratio of 1:4) and N_2 as the carrier gas into a reactor under the CO_2 methanation conditions but without a catalyst. in this study, the feed gases (15 mL $min^{-1}CO_2$ and 60 mL $min^{-1}H_2$) and 60 mL $min^{-1}N_2$ were sent into a blank tubular reactor under atmospheric pressure and the reaction temperature was uniformly increased to 773 K. The outlet gases from the reactor were sent to a gas chromatograph (Shimadzu GC-2014) for analysis. At any of the temperatures taken into consideration, there was no evidence of CH_4, most likely because the amount of CH_4 produced was too small for the GC to pick up. This suggests that, in the absence of a catalyst, CO_2 methanation is unfavourable. Therefore, before conducting a thorough analysis of the performances of all the synthesised catalysts, the following sections will identify and discuss the various resistances that could arise when using a heterogeneous catalyst for CO_2 methanation.

5.2 Mass & heat transport limitations

In heterogeneous catalysis, mass transport refers to the movement of reactant molecules, products, and intermediates between the bulk phase (gas or liquid) and the catalyst's surface (Kakaei et al., 2019). This phenomenon plays a crucial role in determining the overall catalytic rate and can significantly influence the efficiency and selectivity of the catalytic process. According to Fogler (2006), heterogeneous catalytic reactions at the various phases follow an orderly manner namely: 1. mass transport of reactants from the bulk fluid to the external surface of the catalyst takes place first; 2. At the external surface of the catalyst, reactants travel through the catalyst's pores to reach the internal surface of the catalyst; 3. This is followed by the adsorption of the reactants onto the catalyst surface; 4. The adsorbed species then undergo reaction on the internal surface of the catalyst; 5. After the reaction has taken place, the products are desorbed from the catalyst surface and 6; diffuse through the pores to the external surface of the catalyst particle; 7. Finally, the products at the external surface of the catalyst travel to the bulk fluid through mass transport phenomena.

The slowest of the seven steps is usually used to determine the overall rate of reaction. Steps 3, 4 and 5 are used in determining the existing chemical reaction kinetics occurring in a heterogeneous catalytic reaction while steps 2 and 6 represent the internal transport processes. Steps 1 and 7 indicate external transport processes. When the diffusion steps are faster than the reaction steps, then the reaction steps become rate-limiting during the heterogeneous catalytic reactions and the overall reaction will be a representative of the true kinetics. However, the reaction rate is said to be transport-limited if the diffusion steps are slower than the reaction steps. Therefore, the occurrence of mass and heat transport resistances can affect the analysis of chemical reaction rate data. This is why it is important to determine the conditions for minimum or absent mass and heat transfer intrusions in reaction kinetics data.

This section aims to establish the conditions that favour mass and heat transport resistances during CO_2 methanation and how to prevent or minimise them. Specifically, the criteria for determining transport limitations will be obtained using the YSZ-supported Ni catalyst, which was found to be the optimal catalyst among the four supported catalysts considered in this study. This will be discussed extensively in the next chapter. Table 5.1 contains a list of some of the parameters that were employed for the estimations.

Table 5.1 Parameters for the estimation of transport limitations.

Parameters	Value	Source
Reactor diameter, d, (m)	5.5×10^{-3}	-
Reaction rate at 523 K, r_{exp} (mol g_{cat}^{-1} s^{-1})	5.41×10^{-5}	Experimental condition
Catalyst particle diameter, d_p (m)	1.50×10^{-4}	Experimental condition
Total feed flowrate, $\dot{V}$ (m^3 s^{-1})	2.25×10^{-6}	Experimental condition
Heat of reaction at 523 K, ΔH_r (kJ mol^{-1})	-174.95	Experimental condition

Table continues on next page

Activation energy, E_A (kJ mol^{-1})	49.91	Experimental condition
Catalyst's porosity (ε)	0.6022	From Pycnometer
Catalyst's density (ρ_c), (kg m^{-3})	5682.2	From Pycnometer

5.3 External Mass Transfer

External mass transfer resistance refers to the resistance across the solid–gas interface in the methanation catalyst systems resulting from the formation of a boundary layer around the catalyst particles. For homogeneous catalytic reactions, where all reactants, products, and catalysts are present in the same phase, mass transfer resistance is generally insignificant (Zuliani et al., 2018). However, in heterogeneous catalytic reactions, mass transfer limitations arise due to the movement of molecules through the film layer that separates the bulk fluid from the external catalyst surface. Since different phases are involved in these reactions, the rate of the reaction is largely dependent on the mass transfer or diffusion between these phases. To ensure that the external mass transfer regime does not control the reaction rate, criteria such as the Mears' criterion (Mears, 1971) was utilised as shown in Eq. **(**5.1) with the detailed calculation given in Appendix E.

$$\frac{(-r_{\exp})\rho_b R_p n}{k_c C_{Ab}} < 0.15 \qquad \textbf{(}5.1\textbf{)}$$

($-r_{exp}$) = rate of reaction obtained experimentally (mol kg_{cat}^{-1} s^{-1})

ρ_b = bulk density of catalyst bed (kg m^{-3})

R_p = catalyst particle radius (m)

n = reaction order

C_{Ab} = Concentration of reactant A (CO_2) in the bulk gas-phase (mol m^{-3})

k_c = mass transfer coefficient (m s^{-1})

The calculated value for the left-hand side of the Mears criterion using the parameters from Table 5.1 was 0.003026 indicating that the external mass transfer resistance can be ignored for the CO_2 methanation reaction. See the detailed calculation in Appendix E.1.

5.4 Internal Mass Transfer (Pore Diffusion)

Internal mass transfer resistance pertains to the impediment encountered during the diffusion of reactants within the catalyst's pore structure. When the external mass transfer resistance surpasses both the internal mass transfer resistance and the intrinsic reaction in terms of their impact on the overall reaction rate, it indicates that the reaction is predominantly regulated by external mass transfer, and vice versa (Tadepalli et al., 2007). After the transfer of reactants from the bulk fluid to the outer surface of the catalyst (referred to as external mass transfer), the reactants further diffuse through the catalyst's internal pores where the reaction takes place. The resistances encountered by these reactants during internal mass transfer can be neglected under the condition that the experimental conditions and rate data adhere to the Weisz-Prater criterion given in Eq. **(**5.2) (Weisz and Prater, 1954; Chen et al., 1999).

$$\frac{(-r_{\exp})\rho_c R_p^2}{D_{eff} C_{As}} < 1 \qquad \textbf{(}5.2\textbf{)}$$

ρ_c = density of catalyst pellet (kg m^3)

R_p = radius of catalyst particles (m)

C_{As} = concentration of CO_2 at the catalyst surface (mol m^{-3})

D_{eff} = effective diffusivity of CO_2 in the feed mixture of CO_2, N_2 and H_2 (m^2 s^{-1})

The Weisz-Prater criterion was estimated using the parameters from Table 5.1 as 0.01418 which suggests that the internal mass transfer resistance can be ignored for the CO_2 methanation reaction. See the detailed calculation in Appendix E.2

5.5 External Heat Transfer

External heat transfer resistance is a significant factor that can affect the efficiency of CO_2 methanation over heterogeneous catalysts since the reaction is exothermic. The heat released during the reaction must be properly managed to maintain optimal conditions for the reaction. External heat transfer resistance refers to the resistance to heat transfer between the reactor and its surroundings. There are various factors that influence this resistance, such as the reactor's surface roughness and diameter, the thermal conductivity of the reactor walls etc (Liu et al., 2019). Other influencing factors for external heat transfer resistance are the temperature difference between the reactor and its surroundings, and the convective heat transfer coefficient between the reactor and the surrounding fluid (usually air or water). The higher the external heat transfer resistance, the less efficient the heat transfer will be, and the more difficult it will be to control the reactor temperature. During CO_2 methanation, external heat transfer resistance can be especially problematic because the reaction rate is highly dependent on temperature. The catalyst activity is optimal at a certain temperature range, which must be maintained for the reaction to proceed efficiently. If the reactor temperature is too high, the catalyst may become deactivated or damaged, reducing its effectiveness. On the other hand, if the temperature is too low, the reaction rate will be slow, and the process will be less efficient.

To minimise the external heat transfer resistance during CO_2 methanation, several strategies can be employed. One is to increase the convective heat transfer coefficient between the reactor and the surrounding fluid by using a cooling fluid with high flowrate or by increasing the surface area of the reactor. Another strategy is to improve the thermal conductivity of the reactor walls by using materials with higher thermal conductivity, such as copper. Additionally, insulation can be added to the reactor walls to reduce heat losses to the surroundings. In this study, the Mears criterion given by Eq. (5.3) was employed in determining the effect of external heat transfer since it was established that the impact of heat transfer resistance can be ignored at a criterion value less than 0.15.

$$\frac{\left|\left(-\Delta H_r\right)\right|\left(-r_{\exp}\right)\rho_b R_p E_A}{hRT_b^2} < 0.15 \qquad (5.3)$$

$-\Delta H_r$ = heat of reaction (J mol^{-1})

E_A = activation energy (J mol^{-1})

h = heat transfer coefficient between the gas mixture and catalyst (J m^{-2} s^{-1} K^{-1})

R = ideal gas constant (J mol^{-1} K^{-1})

T_b = reactant gas bulk temperature (K)

After the substitution of the various parameters in Eq. (5.3), the left-hand side gave 0.03215 which is less than 0.15. This indicates that external heat transfer resistance can be neglected for the experimental conditions employed. In conclusion, external heat transfer resistance is an important consideration during CO_2 methanation over a heterogeneous catalyst. Controlling the reactor temperature is crucial for maintaining optimal catalyst activity and ensuring efficient conversion of CO_2 to CH_4. By minimising the external heat transfer resistance, the process can be optimised for maximum yield and reduced energy consumption. See the detailed calculation in Appendix E.3.

5.6 Intraparticle Heat Transfer

Intraparticle heat transfer refers to the transfer of thermal energy within the particles of a catalyst, from the external surface to the pores within. While intraparticle heat transfer has less impact on the reaction rate compared to external heat transfer, it still plays a role. To address limitations in internal heat transfer, catalysts with smaller particle sizes can be used. However, using extremely small particles can lead to a significant drop in pressure across the catalyst bed (Foo, 2012). Therefore, it is crucial to determine the appropriate range of particle sizes that minimise internal heat transfer effects. The Anderson criterion, described by Eq. (5.4), can be employed to determine if the internal heat transfer effect is negligible in a heterogeneous catalytic reaction.

$$\frac{\left|\left(-\Delta H_r\right)\right|\left(-r_{\exp}\right)\rho_b R_p^2 E_A}{\lambda_p R T_s^2} < 0.75 \tag{5.4}$$

Where

λ_p = thermal conductivity of catalyst pellet (J m^{-2} s^{-1} K^{-1})

T_s = surface temperature of reactant gas

Upon plugging in the various parameters in Eq. (5.4), the calculated Anderson criterion value was determined to be 0.001246. This value suggests that the resistance to internal heat transfer is negligible. See the detailed calculation in Appendix E.4.

5.7 Wall and Radial Heat Dispersion Effects

The phenomenon of wall heat transfer involves the exchange of thermal energy between the reactor wall and the catalyst, which occurs through either conduction within the catalyst pellet or convection via the movement of gaseous reactant(s) through the catalyst bed. Previous studies have indicated that the effects of wall heat transfer are influenced by the ratio of reactor tube diameter (d_t) to the diameter of the catalyst particles (d_p) (Ibrahim et al., 2016). The tube-particle diameter (d_t/d_p) is an important parameter that can be used to manage the pressure drop for a system involving the use of a heterogeneous tubular reactor (Quintana-Solórzano et al., 2018). d_t/d_p can also influence the radial thermal conductivity (K_{er}) and the radial heat transfer depending on the shape (Aparicio-Mauricio et al., 2017; Zare and Hashemabadi, 2020).

According to Dixon (1997), when the ratio of *dt/dp* exceeds 4 (assuming a spherical particle), the impact of wall heat transfer effects becomes negligible. Similarly, Yang et al. (2015) found that the impact of wall effects associated with *dt/dp* on flow transitions within the central areas of packed beds would be insignificant when *dt/dp* is equal to or greater than 9.9. It is worth noting that the unitless d_t/d_p parameter can be employed when the particle is assumed to be spherical. For non-spherical particles, equivalent diameters are used for d_p (von Seckendorff and Hinrichsen, 2021; Allen, 2013; Wadell, 1935).

In the present study, the calculated d_t/d_p value was determined to be 36.67, indicating a negligible influence of wall heat transfer effects. However, it should be noted that when d_t/d_p reaches high values, the radial heat transfer effect becomes more prominent. To ascertain that

both the tube-particle diameter ratio and the experimental conditions applied in this investigation fall within the acceptable range for negligible radial heat transfer, the Mears criterion, as presented in Equation (5.5), was employed.

$$\left(\frac{E_a}{RT_w}\right)\left(\frac{\left|\left(-\Delta H_r\right)\right|\left(-r_{\exp}\right)\rho_b R_p^2\left[\left(1-\varepsilon\right)/\left(1-b\right)\right]}{4\lambda_p T_w}\right)\left(\frac{1}{8}+\frac{B_p}{Bi_w R_t}\right)<0.05 \qquad (5.5)$$

where

T_w = temperature of the tube wall (K)

ε = void fraction in the catalyst bed

b = inert solids fraction of the catalyst bed

R_t = radius of the tubular reactor (m)

Bi_w = wall Biot number

After substitutions into Equation (5.5), the left-hand side gave 0.001607, suggesting that radial heat dispersion effects are insignificant for the experimental conditions employed in this work. See the detailed calculation in Appendix E.5.

CHAPTER 6

Catalyst activity

This chapter discusses the results from various catalyst testing experiments including the influence of reaction conditions, effect of reactor configuration and effect of promoters.

6.1 Effect of Catalyst support

The catalytic performance of Ni supported on CeO_2, SBA-15, Al_2O_3, and YSZ were evaluated in the CO_2 methanation studied within the temperature range of 473 to 713 K at a pressure of 1 bar, and GHSV of 20250 mL h^{-1} g_{cat}^{-1}.

6.1.1 Temperature dependency of the catalyst activity

Figure 6.1 (a) and (b) represent the CO_2 conversion (X_{CO2}) and CH_4 yield (Y_{CH4}) obtained. As seen in Figure 6.1 (a), the X_{CO2} for all the catalysts exhibited an increasing trend with temperature until reaching maximum conversion at individual optimum temperatures beyond which the X_{CO2} started to decrease. The 10%Ni/YSZ catalyst demonstrated a maximum X_{CO2} of about 84% at the optimum temperature of 643 K. This indicates that the catalyst exhibits the highest activity of all tested catalysts for CO_2 methanation at this temperature range. The 10%Ni/Al_2O_3 catalyst achieved a maximum X_{CO2} of about 80% at the optimum temperature of 630 K. This suggests that the catalyst also possesses good performance for X_{CO2} and at a lower temperature compared with the 10%Ni/YSZ catalyst.

The 10%Ni/SBA-15 catalyst showed a maximum X_{CO2} of approximately 78% at the optimum temperature of 693 K. Although this value is not too far below what was obtained for Ni/YSZ and Ni/Al_2O_3 catalysts, a higher temperature was required to achieve this maximum conversion. The X_{CO2} for Ni/CeO_2 catalyst continued to increase with temperature with no significant decline within the temperature range.

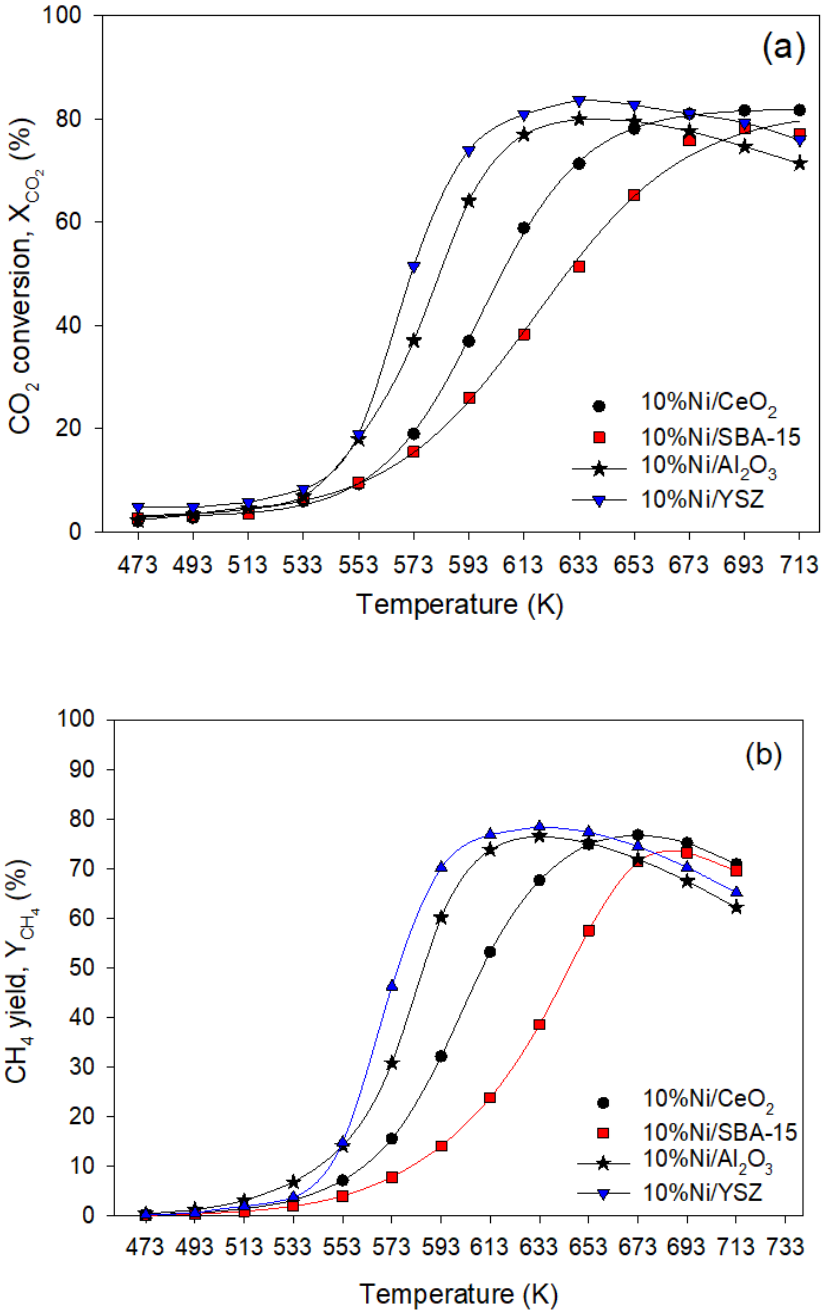


Figure 6.1 Activity profiles of various supported Ni catalysts showing (a) CO_2 conversion and (b) CH_4 yield in a CO_2 methanation conducted within the temperature range of 473 to 713K at a pressure of 1 bar, GHSV 20250 mL h^{-1} g^{-1}_{cat} and H_2:CO_2:N_2 ratio of 4:1:4. The heating rate and holding time were 10 K min^{-1} and 1 h, respectively.

In terms of Y_{CH4} (Figure 6.1 (b)), the trend follows a similar pattern to X_{CO2}. The Y_{CH4} for the Ni/CeO_2 catalyst was observed to start decreasing above 673 K even though its X_{CO2} did not show any significant decrease within the temperature range. This indicates the presence of side reactions that reduce the selectivity towards CH_4 at higher temperatures.

Figure 6.2 depicts the selectivity to CH_4 and CO formation within the range of temperatures adopted. For all the catalysts, the CH_4 selectivity (S_{CH4}) was close to 100% at the starting temperature but gradually decreased while the CO selectivity increased with increasing temperature. This behaviour further confirms that there was an occurrence of side reactions which favoured CO production as the temperature rose. This trend where S_{CH4} is high and S_{CO} low at lower temperatures, aligns with results from other studies. Chen et al. (2023) discovered in their research using a manganese promoted Ni/Al_2O_3 catalyst that lower temperatures restrict the reverse water gas shift (RWGS) reaction, which is an endothermic process. Consequently, the S_{CH4} increases while the S_{CO} decreases with lower temperatures.

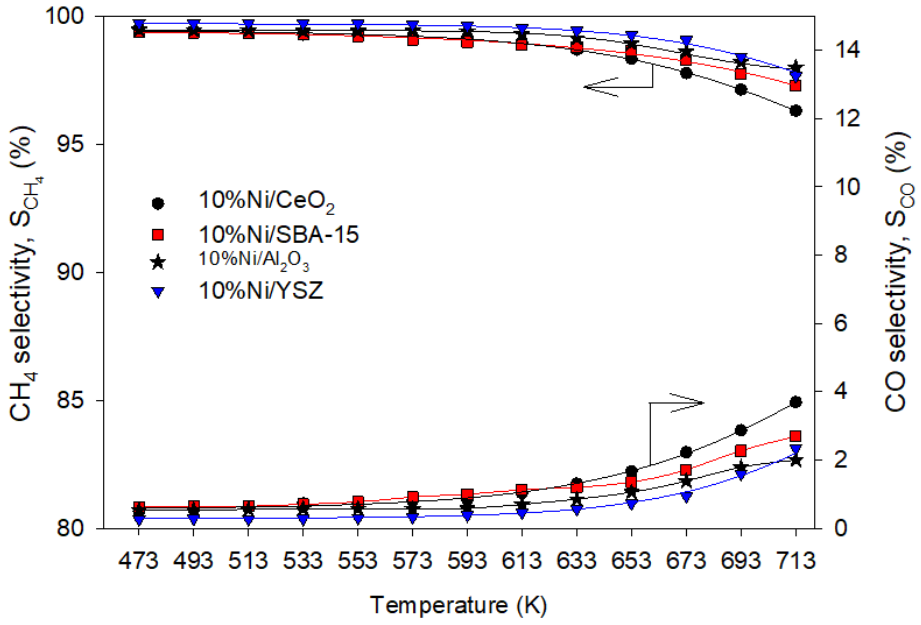


Figure 6.2 Activity profiles of various supported Ni catalysts showing CH_4 and CO selectivity in a CO_2 methanation conducted within the temperature range of 473 to 713K at a pressure of 1 bar, GHSV 20250 mL h^{-1} g^{-1}_{cat} and H_2:CO_2:N_2 ratio of 4:1:4.

6.1.2 Arrhenius coefficient and energy of activation

The activation energy represents the energy barrier that reactant molecules must overcome to transform into products. A lower activation energy indicates a more favourable reaction, as it implies that the reaction can proceed more easily at a given temperature. The higher the activation energy, the slower the reaction rate, as more energy is required to initiate the reaction. In the case of CO_2 methanation, the activation energies of the catalysts can provide insights into their performance and reactivity. A lower activation energy suggests that the catalyst is more efficient in facilitating the conversion of CO_2 to CH_4. The activation energies for the CO_2 methanation reaction over Ni/CeO_2, Ni/SBA-15, Ni/Al_2O_3, and Ni/YSZ catalysts were estimated to provide insights into the energy barriers involved. The apparent activation energies of these catalysts were determined by utilising the Arrhenius formula given in Eq. (6.1), and the details of the calculations is given in Appendix D.

$$k = Ae^{-\frac{E_A}{RT}} \tag{6.1}$$

k = rate constant,

A = frequency or collision factor,

T = reaction temperature (K),

E_A = activation energy (J mol^{-1}),

R = gas constant (8.314 J mol^{-1} K^{-1}),

The tests were carried out at temperatures 513, 523, 533, and 543 K such that the X_{CO2} was lower than 15% to avoid mass transfer limitation and to minimise the inhibitory effect of water. Kesavan et al. (2018) avoided the mass and heat transport limitations by employing a temperature region within which X_{CO2} was lower than 15%. Meanwhile, Tsiotsias et al. (2022) reported that the effect of mass transfer limitation was avoided while estimating the CO_2 activation energies of CeO_2 supported Ni catalysts by assuming pseudo-first order kinetics and employing a temperature range where X_{CO2}< 20%. Irrespective of the temperature region

considered, it is important to avoid or minimise the effect of mass transfer limitations when calculating the apparent activation energy and for kinetic studies.

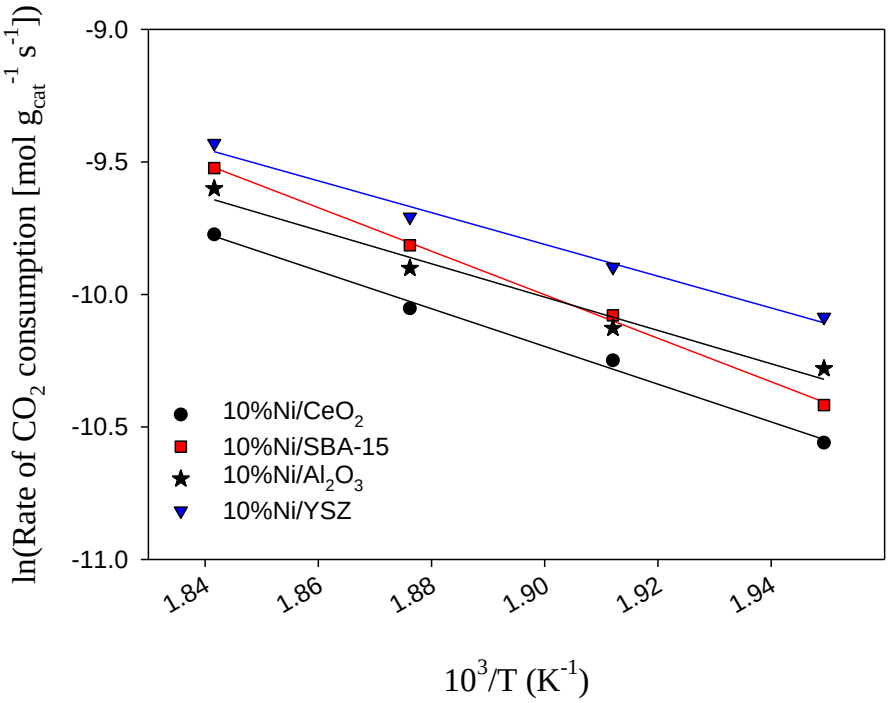


Figure 6.3 The apparent activation energies for CO_2 conversion during methanation over various supported catalysts estimated within the temperature range of 473-713 K. Other reaction conditions: pressure of 1 bar, GHSV 20250 mL h^{-1} g^{-1}_{cat} and H_2:CO_2:N_2 ratio of 4:1:4.

The results of these calculations are represented in Figure 6.3. Comparing the apparent activation energies of the catalysts, Ni/YSZ exhibits the lowest value of 49.9 kJ mol^{-1}, indicating that it has the lowest energy barrier for the CO_2 methanation reaction. The Ni/Al_2O_3 and Ni/CeO_2 catalysts have activation energies of 52.0 and 59.2 kJ mol^{-1}, respectively. Although these values are higher than for Ni/YSZ, they are still relatively low compared to Ni/SBA-15, which has the highest activation energy of 68.0 kJ mol^{-1}. This suggests that the Ni/YSZ catalyst can promote the reaction at a faster rate and is more favourable for CO_2 conversion to CH_4 compared to the other catalysts. The lower performance exhibited by Ni/SBA-15 is attributed to its higher energy barrier compared to the other catalysts. The apparent activation energies obtained for the Ni-based YSZ, Al_2O_3, CeO_2 and SBA-15 catalysts

employed in this study are compared with the values reported in the literature for CO_2 methanation as presented in Table 6.1.

Table 6.1 Range of activation energies for CO_2 conversion during methanation over different catalysts reported in the literature.

Catalyst	Activation energy (kJ/mol)	Temp range (K)	References
Ni/CeO_2	59.2±0.012878	513-543	This work
	94.9	473-573	(Lin et al., 2021)
	124	523-623	(Tsiotsias et al., 2022)
	26.409	523-673	(Li et al., 2023)
	53.3	483-513	(Yu et al., 2018)
	112.17	417-513	(Bian et al., 2018)
Ni/Al_2O_3	52.4±0.03844688	513-543	This work
	74		(Mutschler et al., 2018)
	80.1	588-703	(Quindimil et al., 2022)
	~66	493-543	(Michalska et al., 2019)
	75 (Ni/Al hydrotalcite)	543-660	(Marocco et al., 2018)
Ni/YSZ	49.9±0.00051839	513-543	This work
	17.033 (Ni/ZrO_2)	523-673	(Li et al., 2023)
	99.1	573-608	(Kesavan et al., 2018)
	3.46		(Kristiani and Takeishi, 2022)
Ni/SBA-15	68.3±0.013478	513-543	This work
	70.36		(Lu et al., 2015)
	82	473-673	(Zhao et al., 2023)
	101.5 (Ni/SiO_2)	473-723	(Xu et al., 2023)
	66.3 (Ni/SiO_2)	623-698	(Wu et al., 2021)

As seen in the Table, the apparent activation energies reported in the literature for CO_2 methanation for the different catalysts is consistent with the range of values obtained in this study. The variation in the activation energy observed in the literature work can be associated with the influence of different factors including changes in the reaction mechanism, adsorption effects and surface restructuring which are mainly dependent on temperature.

Surface restructuring may occur at high temperatures, causing the surface of the catalyst to become less ordered and more defective. This could change the number of active sites and the energy of those sites, thereby influencing the activation energy. Other conditions that could influence the activation energy include the catalyst preparation method, the catalyst composition such as the Ni loading and the addition of promoters, and the reaction conditions. Therefore, it is important to consider a wide range of influencing factors when comparing the activation energy for different catalysts in CO_2 methanation. It is also important to conduct extensive characterisation on catalysts to understand the specific mechanisms and surface phenomena that contribute to the observed activation energies for each catalyst.

In summary, the experimental results demonstrate the temperature-dependent behaviour of the investigated catalysts during CO_2 methanation. The catalysts exhibited a maximum X_{CO2} at different optimum temperatures, beyond which the conversion declined. The Ni/YSZ catalyst exhibited the highest X_{CO2} and excellent S_{CH4}, indicating its superior performance, followed by Ni/Al_2O_3, Ni/CeO_2 and Ni/SBA-15. The results also show that while the Ni/Al_2O_3 and Ni/YSZ catalyst are very active at intermediate temperatures, both Ni/SBA-15 and Ni/CeO_2 catalysts are best suited for high temperature methanation processes. These findings provide valuable insights into the catalytic performance and temperature effects, facilitating the optimisation of CO_2 methanation processes for efficient CO_2 utilisation. The remaining part of this chapter will now focus on the stability of the preferred catalyst (Ni/YSZ) in comparison to Ni/SBA-15 (the least active according to the order of arrangement). The rationale behind this is rooted in the understanding that a catalyst's activity alone cannot be deemed as the sole criterion for assessing its superiority. It is entirely plausible for a catalyst to demonstrate high activity levels but suffer from inherent shortcomings in terms of stability. Therefore, a comprehensive

examination of the catalysts' stability becomes imperative to truly gauge their overall performance and reliability.

6.1.3 Longevity test

The long-term stability test of Ni/YSZ and Ni/SBA-15 catalysts in CO_2 methanation was performed at 643 K and a GHSV of 20250 mL h^{-1} g^{-1} under atmospheric pressure for a duration of 72 h on-stream. The experimental findings are presented in Figure 6.4 (a) and (b). As seen in Figure 6.4 (a), the X_{CO2} for both Ni/SBA-15 and Ni/YSZ catalysts was relatively stable with only a slight decrease of 4.1% and 1.9%, respectively, during the 72 h on-stream. In Figure 6.4 (b), the S_{CH4} of the Ni/SBA-15 and Ni/YSZ catalysts decreased from 98.8% to 96.2% and 99.1% to 99.0%, respectively. In addition, the CO selectivity data clearly showed that the amount of CO produced over the Ni/SBA-15 started to pick up after 50 h on-stream indicating the decline in activity or deactivation. The S_{CO} of Ni/YSZ was almost steady throughout the test.

The moderate stability exhibited by the Ni/SBA-15 catalyst can be attributed to the presence of accessible mesoporous channels in the SBA-15 supports, which resulted in high dispersion of the metallic Ni nanoparticles, but the gradual deactivation observed after 50 h on-stream can be linked to sintering of the metallic active sites, which are mainly responsible for the dissociation of H_2 into H atoms. The gradual increase in S_{CO} may be ascribed to the decrease in the rate of CO dissociation which is an important step in the pathway leading to CH_4 formation. A similar trend was reported by Hongmanorom et al. (2021) where the Ni/SBA-15 catalyst prepared by the wetness impregnation method displayed an obvious deactivation during the stability test. The catalyst's performance was enhanced by adopting a different synthesis method (ammonia evaporation technique) and the addition of Mg. The authors found that the metal-support interaction, confinement effect and the anti-sintering properties of the modified SBA-15 catalyst were greatly enhanced, and this resulted in improved stability.

On the other hand, the exceptional stability displayed by Ni/YSZ catalyst can be related to the availability of a high oxygen vacancy concentration, enhanced basic sites and the anti-metal sintering properties because of the presence of yttrium and zirconium in the YSZ support (Tang et al., 2023; Guo and Chen, 2022; Sun et al., 2022a). Overall, the Ni/YSZ catalyst exhibited

exceptional performance in terms of both low-temperature activity and catalytic stability compared to Ni/SBA-15 catalyst.

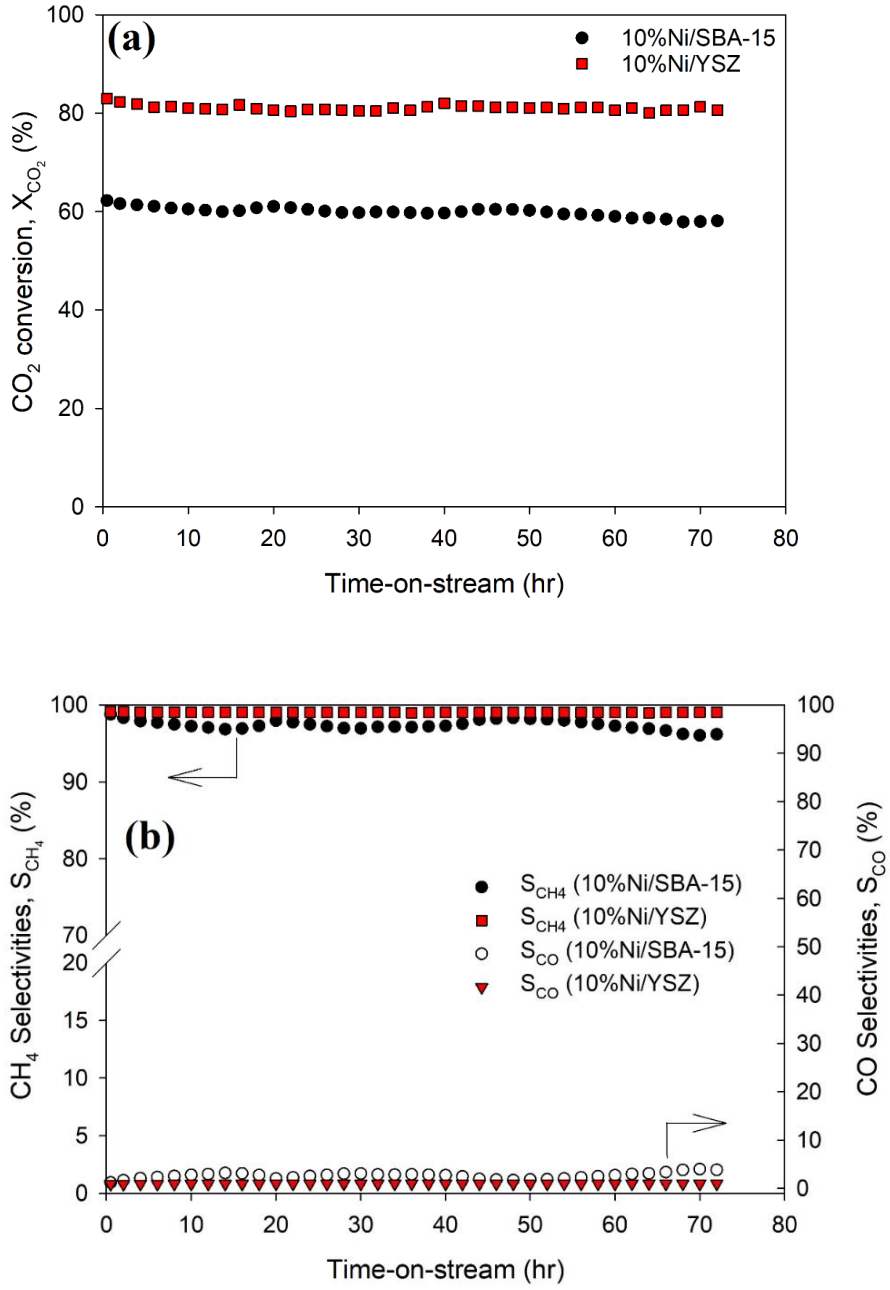


Figure 6.4 Longevity test profile for 10%Ni/SBA-15 and 10%Ni/YSZ catalysts in CO_2 methanation conducted under atmospheric pressure, temperature of 643 K, GHSV 20250 mL h^{-1} g^{-1}_{cat} and 72 h on-stream.

6.2 The role of catalyst position in the reactor

When the catalyst position is varied in a fixed-bed reactor during a CO_2 methanation reaction, several factors are likely to change, influencing the overall performance of the reactor and the catalytic process. The specific changes will depend on the position of the catalyst relative to the reactant and product flow streams. Some potential changes that are expected are: 1. The residence time of reactants. A longer residence time allows more opportunities for contact between reactant molecules (H_2 and CO_2) and the catalyst, thus increasing the CO_2 conversion (Anoop et al., 2021). However, a longer residence time can also increase the risk of thermal runaway and catalyst deactivation due to the exothermic nature of the CO_2 methanation reaction. Therefore, proper residence time control is essential to optimising the catalyst's performance; 2. Product selectivity. The variation of the catalyst position may favour the formation of undesired by-products or side reactions; 3. The heat management and thermal gradients in the reactor may be influenced since heat will be released during the methanation reaction (exothermic). These variations in the temperature profile along the reactor length can favour the occurrence of hot-spot, and affect the catalyst stability and lifetime if not properly managed (Türks et al., 2017; Serrer et al., 2021). Therefore, careful consideration of catalyst position and reactor design is necessary to optimising the CO_2 methanation process.

The effect of position in the reactor was investigated by loading 400 mg of 10%Ni/YSZ catalyst into a 300 mm long quartz tube reactor for each experiment. Seven different positions were considered namely 20, 50, 100, 150, 200, 250 and 280 mm from the inlet of the reactor for this study. The CO_2 methanation reaction was conducted at a temperature of 643 K and 1 bar. The temperature of each position was calibrated to ensure that 643 K was maintained since a temperature gradient was expected along the different positions in the reactor. The result of this study is shown in Figure 6.5. As seen, both the CO_2 conversion (X_{CO2}) and selectivity to CH_4 (S_{CH4}) increased as the catalyst position (from inlet) shifted from 20 to 150 mm of the reactor length but a decline in activity set in when the catalyst was positioned beyond 150 mm from the inlet. The variation in the catalyst activity at the various positions can be attributed to the alteration in the preheating of the reacting species which likely changed the temperature distribution throughout the reactor (Gao et. al. 2021).

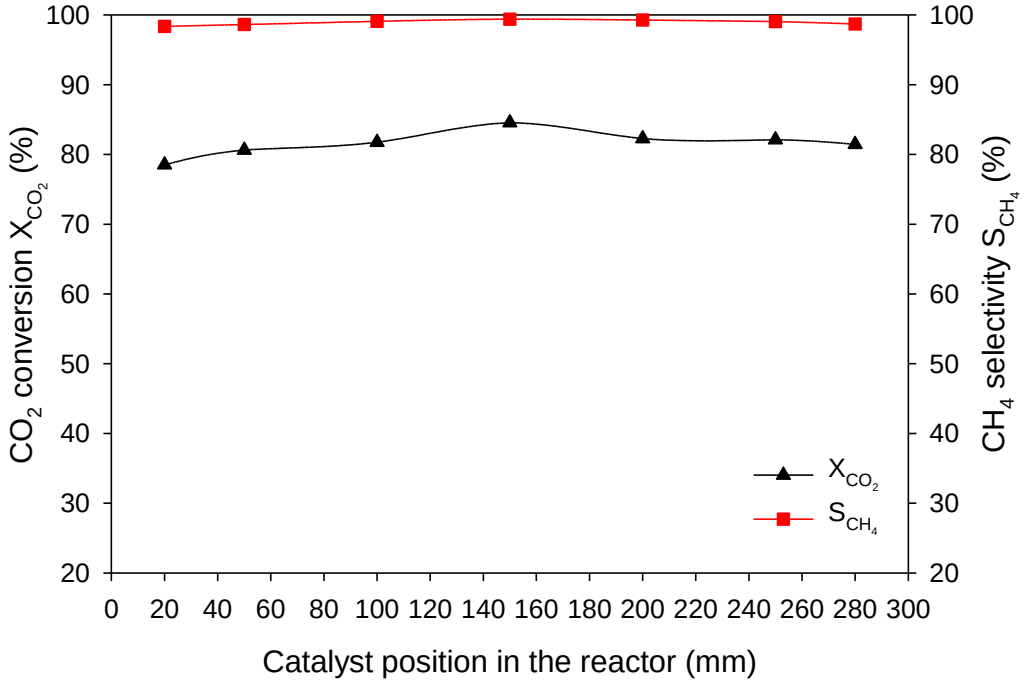


Figure 6.5 Effect of catalyst position in the reactor on CO_2 conversion and CH_4 selectivity in CO_2 methanation over 10%Ni/YSZ catalyst at 643K, 1 bar, GHSV 20250 mL h^{-1} g^{-1}_{cat} and reactor length of 30 cm. The colours were used to show the variation in temperature along the reactor: The light and dark colours represent the low and high temperature regions, respectively.

The optimal catalyst position was at 150 mm or between the 100 and 200 mm (33.3 and 66.7% of the reactor length) where X_{CO2} and S_{CH4} of 84.5% and 99.6%, respectively, were achieved.

6.3 Effect of varying Ni loading

The effect of varying the amount of Ni in the Ni/YSZ catalyst for CO_2 methanation reaction was investigated next. The catalysts were prepared by wetness impregnation of Ni on a YSZ support to achieve 5, 10, 20, 30, 40, 50 and 75wt.% Ni/YSZ catalysts. The performance of these catalysts was tested in CO_2 methanation within a temperature range of 473 to 703 K under atmospheric pressure. For each test, 200 mg of the catalyst was loaded into the reactor containing inert quartz wool at both ends as the catalyst bed.

The results of the activity test over the Ni/YSZ catalyst during CO_2 methanation are shown in Figure 6.6 (a) and (b). As seen in Figure 6.6 (a), there was a steady but low X_{CO2} at temperatures

between 473 to 553 K. But beyond 553 K, a sharp increase in the CH_4 formation was observed. The increase in X_{CO2} continued with increasing temperature until around 633 K for all tested catalysts. Thereafter, the X_{CO2} declined slowly at higher temperatures. Therefore, the optimal temperature range for high X_{CO2} was between 613 and 653 K. All the catalysts exhibited relatively high activity at the optimal temperature. These superior properties of the catalysts are likely related to the unique physicochemical properties of the YSZ support which include the presence of defect sites such as the oxygen vacancies (Jia et al., 2019; Alves et al., 2021). These properties aid the adsorption and activation of CO_2 (Ilsemann et al., 2021) which is a crucial step in the mechanism of CH_4 formation during the CO_2 methanation reaction.

In Figure 6.6 (b), a similar trend was observed for $Y_{CH4,}$ where the amount of CH_4 produced was initially favoured as the temperature increased, and then decreased when the temperature was raised above the optimum value. It is worth noting that the CO_2 methanation reaction is thermodynamically feasible at low temperatures due to its exothermic nature (see Figure 6.7), but the results from this study revealed that a high Y_{CH4} cannot be achieved at low temperatures. This is due to the substantial kinetic limitations associated with the cleavage of CO_2 bonds during the reduction process to produce other carbon species, which leads to the formation of CH_4 (Yang et al., 2020b; Ashok et al., 2020). Mebrahtu et al. (2019a) acknowledged that the CO_2 methanation reaction is thermodynamically feasible at low temperatures, but the authors stated that high operating pressure will be required to conduct CO_2 methanation at low temperatures for a favourable equilibrium composition.

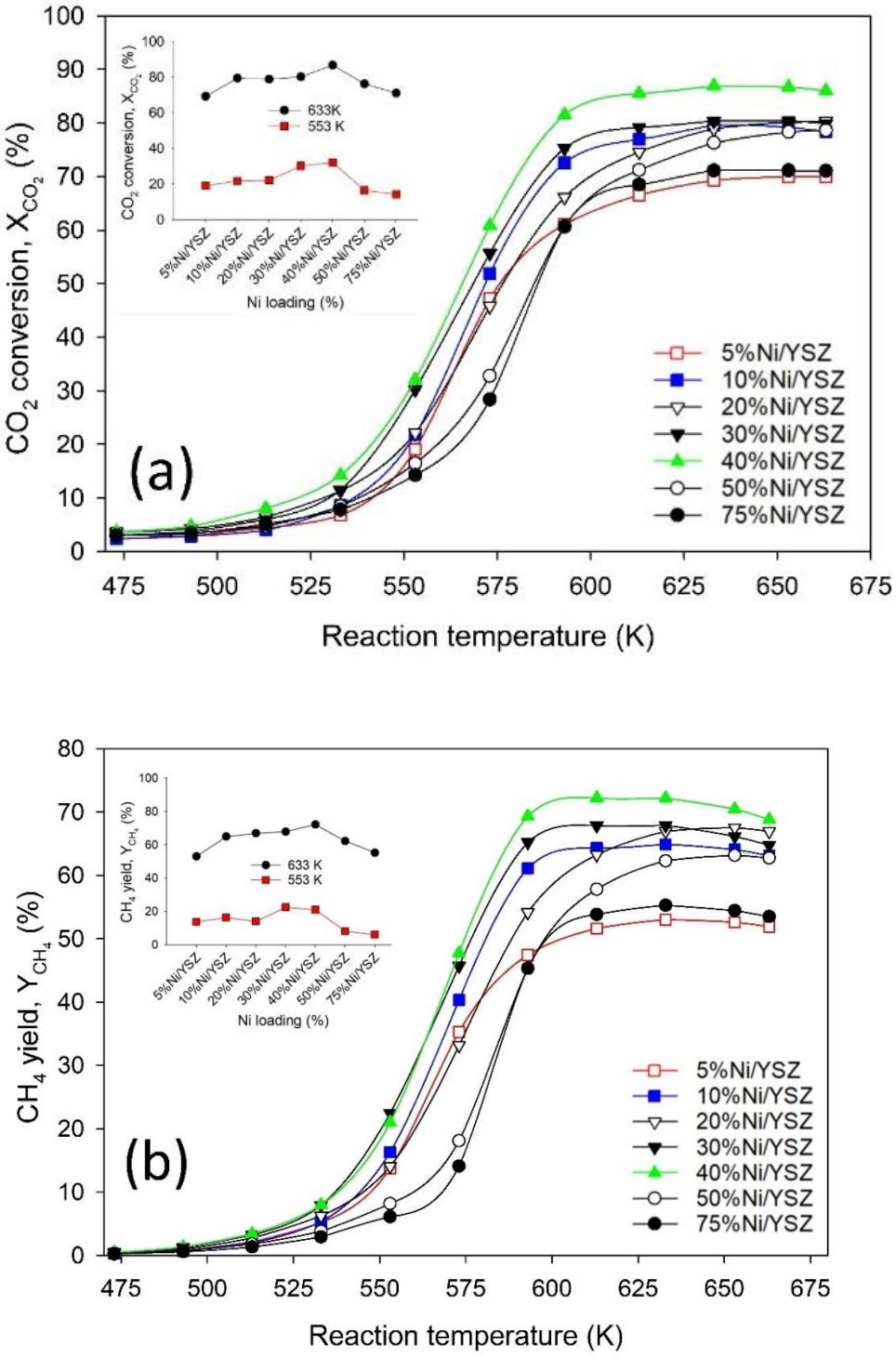


Figure 6.6 Activity test profile showing (a) CO_2 conversion and (b) CH_4 yield during CO_2 methanation over Ni/YSZ catalysts. Reaction conditions: Total flow = 135 mL min^{-1}, H_2:CO_2 ratio = 4, pressure = 1 bar, temperature = 473 – 703 K, GHSV 40,500 mL h^{-1} g^{-1}_{cat}.

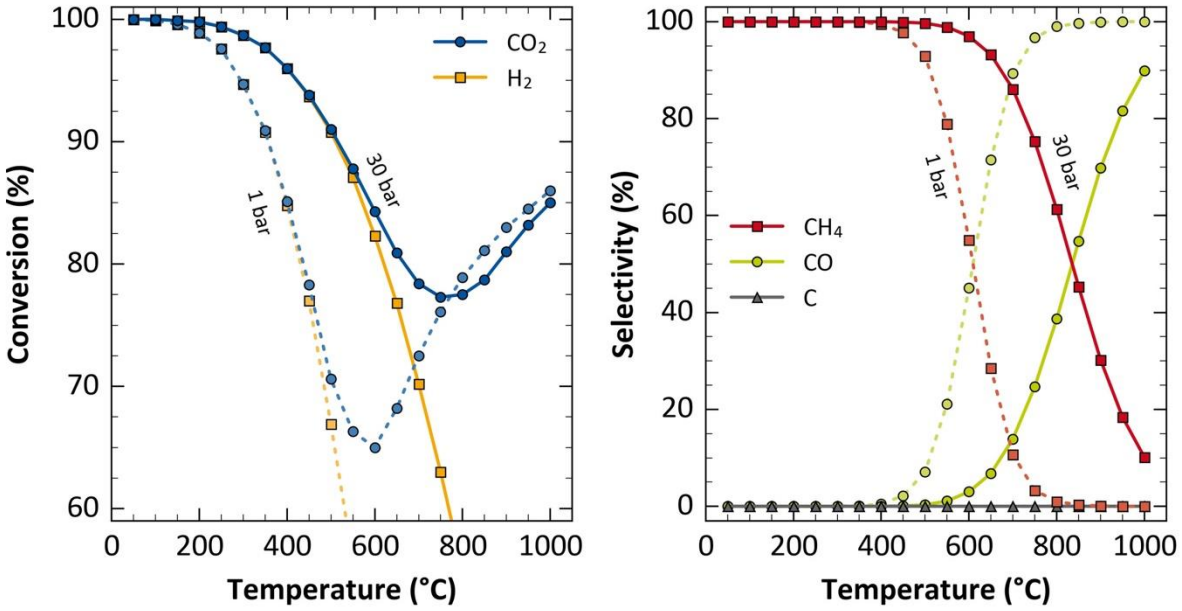


Figure 6.7 Activity profile showing the influence of temperature and pressure on CO_2 equilibrium conversion and selectivity for CO_2 methanation conducted at a H_2:CO_2 ratio of 4. These results were achieved by minimising the Gibbs energy based on the NASA database. Adapted with permission from ref (Mebrahtu et al., 2019). Copyright 2019 Elsevier B.V.

On the other hand, conducting CO_2 methanation at elevated reaction temperatures favours side reactions such as CH_4 dry reforming (Eq. (6.2)), CH_4 steam reforming (Eq. (6.3)), reverse-Boudouard (Eq. (6.4)), and RWGS reactions (Eq. (6.5)), which usually causes low Y_{CH4} (Ashok et al., 2020; El-Salamony et al., 2021).

$$CO_2 + CH_4 \rightleftharpoons 2CO + 2H_2 \quad \Delta H_{298K} = 247.3k\ Jmol^{-1} \tag{6.2}$$

$$CH_4 + H_2O \rightleftharpoons CO_2 + 3H_2 \quad \Delta H_{298K} = 206\ kJmol^{-1} \tag{6.3}$$

$$CO_2 + C \rightleftharpoons 2CO \quad \Delta H_{298K} = 172.4\ kJmol^{-1} \tag{6.4}$$

$$CO_2 + H_2 \rightleftharpoons CO + H_2O \quad \Delta H_{298K} = 41.2\ kJmol^{-1} \tag{6.5}$$

Most likely, the occurrence of these side reactions was responsible for the observed steady and slow decrease in X_{CO2} at temperatures above the optimum value of 650 K since CO_2 was consumed during most of these reactions while the decline in Y_{CH4} was visible. Moreover, the exothermic nature of the CO_2 methanation reaction and the likelihood of hot-spot formation makes it difficult to control the heat in the reactor. Razzaq et al. (2013) reported that instead of the Y_{CH4} increasing at high temperatures, CO formation via RWGS reaction was favoured at temperatures above 673 K. Similarly, Panagiotopoulou et al. (2009) observed that at reaction temperatures greater than 633 K, the formation rate of CO through RWGS was greater than the rate at which CO was consumed in the hydrogenation reaction, which in total led to the decrease in CO conversion.

The catalyst performance improved as the Ni loading increased until reaching optimal performance for a loading of 40%Ni. Any further increase in Ni loading reduced the catalyst activity for the methanation reaction. The initial increase in the catalyst's activities with Ni loading can be ascribed to more availability of active sites resulting from the improved pore size as seen in the BET results (see

Table 4.1) and the improvement in MSI as seen in their reducibility at lower temperatures (see Figure 4.13). Figure 6.8 reveals that the increase in Ni loading resulted in a decrease in CO selectivity up to 40%Ni loading. Studies have shown that Ni loading, together with Ni^0 particle size and morphology, influences the reaction pathways during CO_2 methanation owing to its role in the adsorption and activation of H_2 on the catalyst surface (Choi et al., 2021). A small Ni^0 particle size will likely encourage a longer adsorption-dissociation route through which CH_4 or C is formed. The small Ni^0 particles may also have low coverage for H_2 dissociation which favours the desorption of CO from the surface without hydrogenation to CH_4 (Kesavan et al., 2018; Wu et al., 2015).

Large Ni^0 particle size can influence the intermediate carbon species to be hydrogenated to CH_4 since there is a large coverage for H_2. This means more CH_4 production and less CO formation. Accordingly, the decrease in CO selectivity as shown in Figure 6.8 can be attributed to the favoured reaction route towards the formation of CH_4 as the Ni content increases. Other studies have also shown that an increase in Ni loading encourages the H_2 chemisorption and increased H_2 uptake, indicating high H_2 coverage on the catalyst surface (Wu et al., 2015; Li

et al., 2005). However, high Ni loading of over 40% affects the catalyst morphology, reducing the overall catalyst activity.

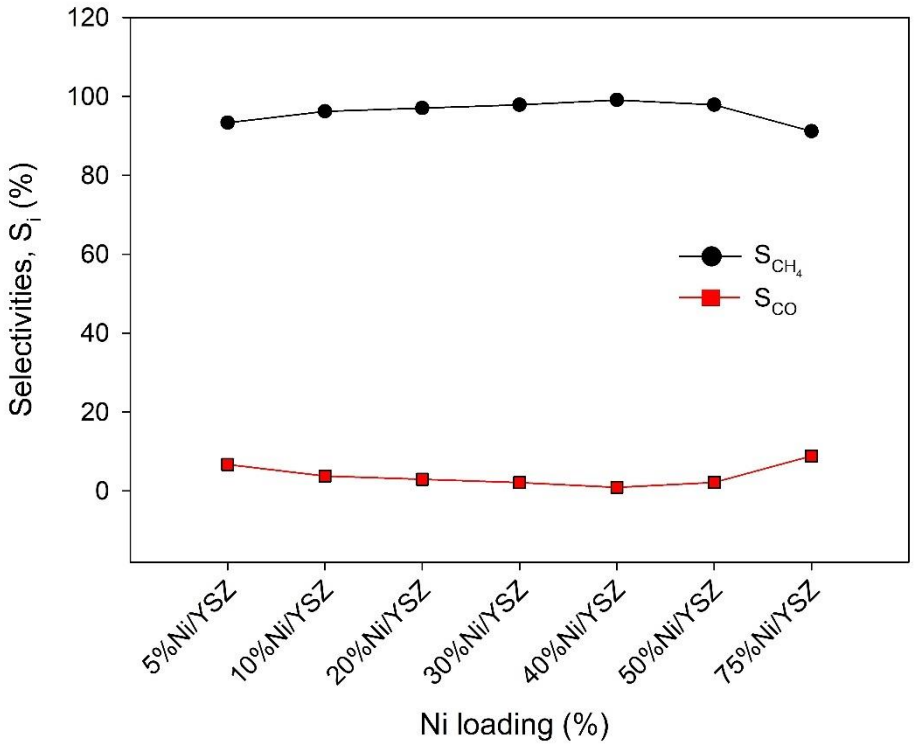


Figure 6.8 Activity test profile showing the selectivity to CH_4 and CO formation during CO_2 methanation at 643 K over a Ni/YSZ catalysts. Reaction conditions: Total flow = 135 mL min^{-1}, H_2:CO_2 ratio = 4, pressure = 1 bar, GHSV 40,500 mL h^{-1} g^{-1}_{cat}.

From our results, the catalyst performance significantly declined after increasing the Ni% loading beyond 40%. This indicates that there was likely a change in the reaction path at higher Ni loading or inaccessibility of the reacting species to the active sites due to pore blockage. In any case, further study is required to determine the relationship between Ni loading and the number of active sites, as well as the optimum Ni^0 particle size that favours high CH_4 production and minimises or inhibits CO formation. Overall, the performance of the catalysts was in the order 40%Ni/YSZ > 30%Ni/YSZ > 20%Ni/YSZ > 50%Ni/YSZ > 10%Ni/YSZ > 5%Ni/YSZ > 75%Ni/YSZ at temperatures beyond 613 K. Therefore, the optimum catalyst choice was 40%Ni/YSZ. It is worth mentioning that this comparative study was carried out

using an equal mass of catalysts. It was also found that the catalyst bed length in the reactor increased with higher Ni loading, indicating an increase in the volume and a decrease in the bulk density. This means that the Ni/YSZ catalysts at higher Ni loading would likely have a longer contact time for the reacting species to react than the catalysts at low Ni loading. The longer contact time may also explain why there was an improvement in the performance with higher Ni loading.

However, the catalyst activity dropped when the loading was increased beyond 40%Ni despite a favoured higher contact time. This is likely due to enhanced clustering of the Ni particles as seen in the SEM images and the increase in crystallite size at higher Ni loading (see Table 4.4).

6.4 Effect of H_2/CO_2 ratio

The effect of H_2/CO_2 molar ratio on both CO_2 conversion and CH_4 yield is represented in Figure 6.9. As seen, CO_2 conversion is favoured at high H_2/CO_2 molar ratios. This is because H_2 in the feed stream at lower H_2/CO_2 molar ratios is the limiting reactant and not sufficient to convert all the CO_2 in contact with it.

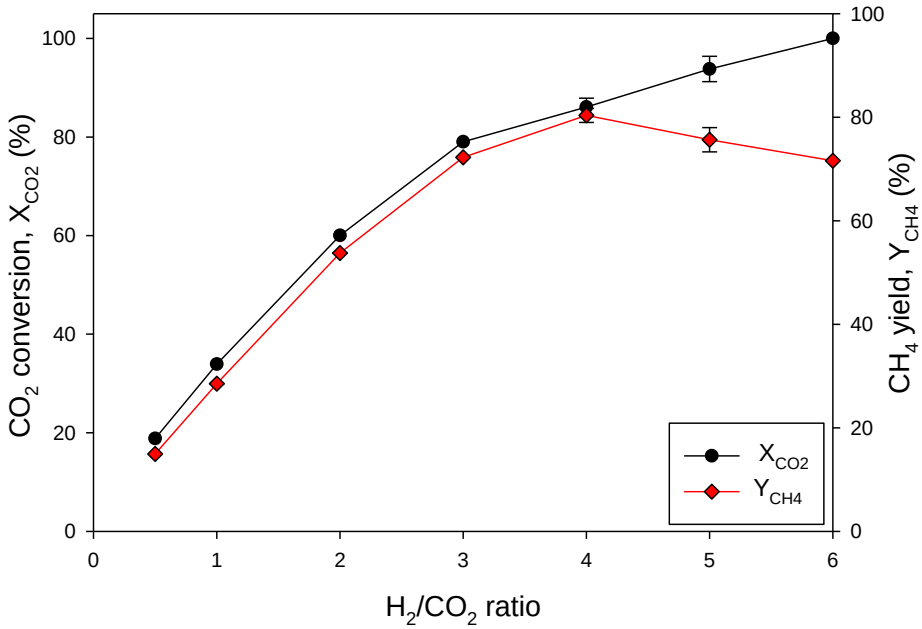


Figure 6.9 Activity test profile showing the effect of varying the H_2/CO_2 ratio on CO_2 conversion and CH_4 yield during CO_2 methanation over a 10%Ni/YSZ

catalyst. Reaction conditions: Total flow = 135 mL min^{-1}, H_2:CO_2 ratio = 4, pressure = 1 bar, temperature = 643 K, GHSV 20,250 mL h^{-1} g^{-1}_{cat}.

The results from this study also revealed that more CO was formed at low H_2/CO_2 molar ratios indicating the occurrence of RWGS reaction. This also explains the reason for the low CH_4 yield at the lower ratios. Moreover, higher concentration of CO_2 favours coke formation and this will enhance catalyst deactivation over time. However, excess H_2 in the feed stream did not favour both CO_2 conversion and CH_4 yield. This observation can be attributed to the presence of excess H_2 hindering CO_2 from reaching the adsorption sites. Thus, CO_2 becomes the limiting reactant, and the extent of conversion or product yield will depend on how many CO_2 molecules can reach the adsorption sites and be reduced for the methanation reaction to take place.

6.5 Effect of Gas Hourly Space Velocity (GHSV)

The Gas Hourly Space Velocity (GHSV) of a feed stream is defined as the volumetric flow rate of reactants divided by the total catalyst volume under standard conditions. GHSV is commonly given in h^{-l} or in mL h^{-l} g^{-1}_{cat} for a heterogeneous catalyst. In this study, GHSV was varied from 16500 to 39000 mL h^{-l} g^{-1}_{cat} under atmospheric pressure and at 643K. The result of this investigation is shown in Figure 6.10.

As seen, both X_{CO2} and Y_{CH4} decreased from 85.6% to 58.9% and 81.9% to 47.8%, respectively, as the GHSV was raised from 16500 to 39000 mL h^{-l} g^{-1}_{cat}. This observation can be attributed to the decrease in the contact time needed for the reacting species to completely react at higher GHSV. A similar trend was observed in S_{CH4} with an increase in GHSV. This decrease in S_{CH4} as GHSV increases can be ascribed to favoured side reactions leading to the formation of CO instead of complete conversion into CH_4. This is expected since the reacting species may not be able to complete the series of chain reactions required for CH_4 formation because of short contact at higher GHSVs.

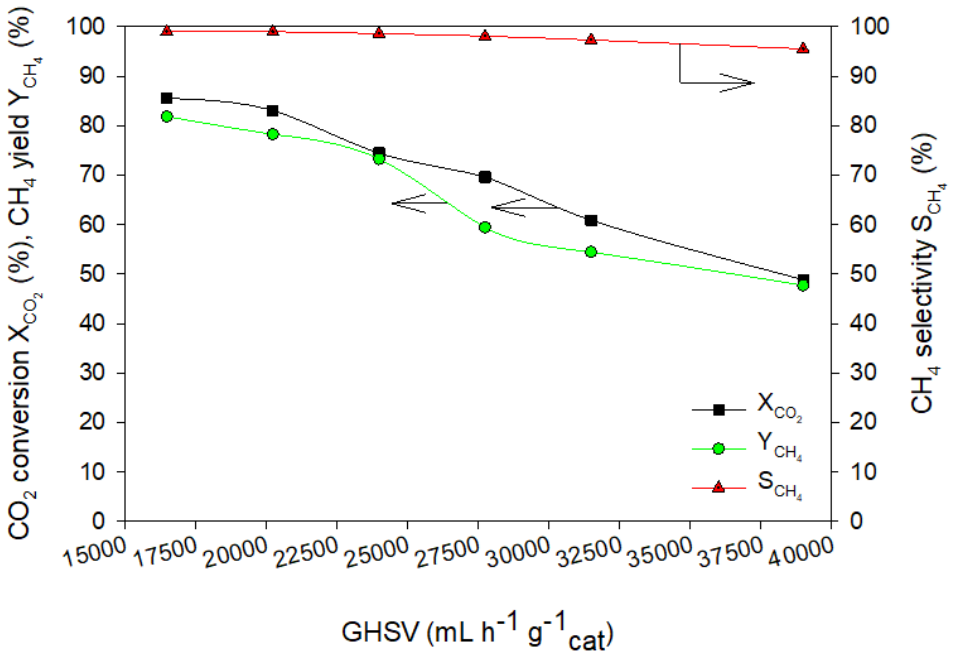


Figure 6.10 Influence of varying the GHSV on CO_2 conversion, CH_4 yield and selectivity during CO_2 methanation conducted over the 10%Ni/YSZ catalyst at 643 K and 1 bar.

A similar trend in X_{CO2} and Y_{CH4} at varying GHSV over different catalysts has been reported in literature (Rahmani et al., 2014b; Stangeland et al., 2017a). Rahmani et al. (2014) stated that the reactants can reach the catalyst active sites with enough contact time to react and form products when the GHSV is low. Therefore, employing higher GHSV for a CO_2 methanation reaction is not favourable.

6.6 Effect of adding CH_4 to the reactants

The effect of the initial CH_4 concentration in the feed stream during CO_2 methanation was investigated over 400 mg of 10%Ni/YSZ at 643 K. The total feed flow was maintained at 135 mL min^{-1} by varying N_2 flow from 60 to 35 mL min^{-1} while increasing the CH_4 concentration from 0 to 25 mL min^{-1}. The H_2 and CO_2 flows were kept constant at 60 and 15 mL min^{-1}, respectively. The result of this investigation is represented in Figure 6.11. As seen in the Figure, the addition of CH_4 caused an inhibitory effect on the catalyst activity, leading to a decrease in X_{CO2} from 84.8 to 78.5% and S_{CH4} from 99.95 to 99.76% while S_{CO}

increased from 0.055 to 0.24%. This observation can be explained by applying the collision theory. The collision frequency of H_2 and CO_2 molecules likely decreased as the concentration of CH_4 in the feed is increased, resulting in a decrease in the forward reaction. This condition also favoured the formation of CO indicating that the presence of CH_4 likely influenced the chain reactions leading to the complete CO_2 methanation. A similar trend was reported by Stangeland et al. (2017b). The authors explained the inhibitory effect of adding CH_4 to the feed stream using the Le Chatelier's principle. Notwithstanding, our study reveals that the 10%Ni/YSZ catalyst will be efficient in CO_2 methanation where the feed is obtained from biogas since the loss of activity was not severe.

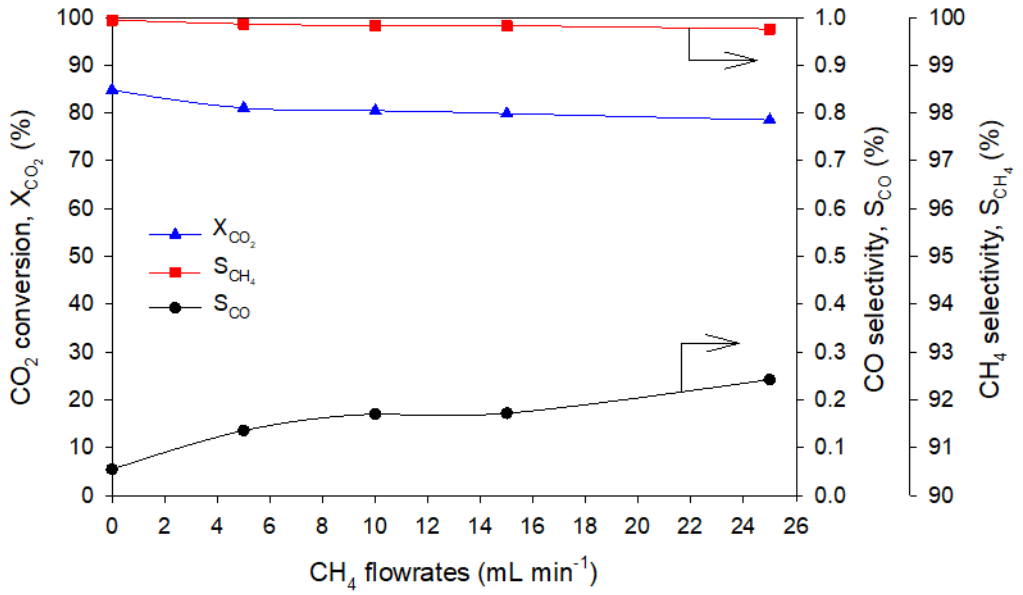


Figure 6.11 Effect of adding CH_4 to the feed on CO_2 conversion and CH_4 and CO selectivity during CO_2 methanation conducted over 10%Ni/YSZ catalyst at 643 K, 1 bar and GHSV 20250 mL h^{-1} g^{-1}_{cat}.

6.7 Effect of pressure

Among other parameters, it is important to study the effect of pressure in the design of a CO_2 methanation system to ensure safety and optimum performance. Apart from other parameters,

optimising the performance of a power-to-gas (PtG) technology can be achieved by operating the CO_2 methanation reactor at high pressure within the range of 5 to 100 bar (Falbo et al., 2018; Stiegler et al., 2019). High pressure in the system can help to lower the activation energy of the forward reaction and cause the molecules to collide faster which will lead to a higher rate of reaction (Chandraker et al., 2022; Engelbrecht et al., 2017). In addition, this pressure range offers the advantage of relaxed thermodynamic constraints and reduced equipment volumes (Falbo et al., 2018). In this study, the effect of pressure was investigated over the 10%Ni/YSZ catalyst at 573 K, H_2:N_2:CO_2 = 4:4:1 and pressures ranging from 0.5 to 3 bar. The result is demonstrated in Figure 6.12. As expected, X_{CO2} increased with pressure. The goal of this work is to look at methanation closer to solid oxide electrolyser (SOE) conditions, i.e., atmospheric pressure, for efficient integration. Slight pressurisation could be a future option.

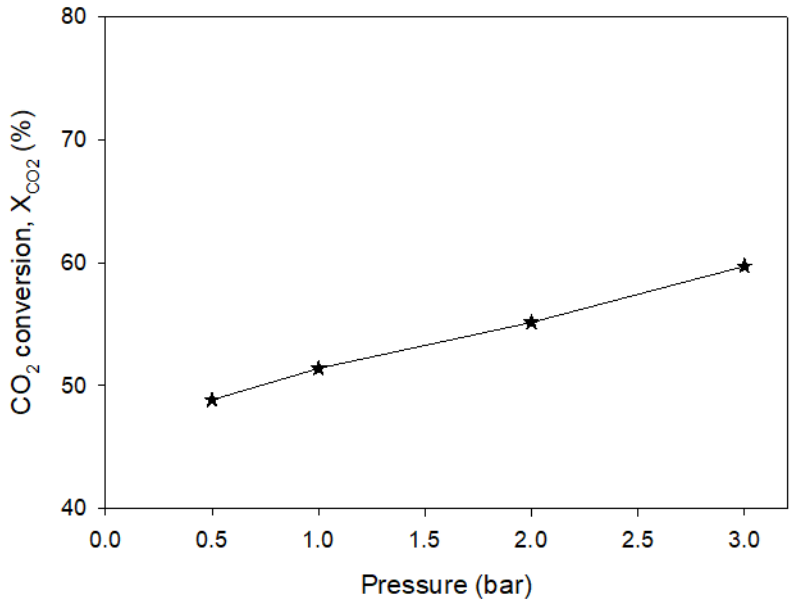


Figure 6.12 Effect of pressure on the performance of 10%Ni/YSZ catalyst in CO_2 methanation conducted over at 573 K and GHSV 20250 mL h^{-1} g^{-1}_{cat}.

6.8 Effect of La-promoter

The effect of incorporating a La-promoter into the framework of the Ni/YSZ was investigated because several reports showed that the addition of La can greatly enhance the performance of

a catalyst as discussed in chapter 2. Zhang et al. (2019) ascribed the improvement in the activity of Ni/Al_2O_3 catalyst during CO methanation after adding La-promoter to the enhanced anti-sintering, increased resistance to coke formation, improved reducibility of Ni particles, and the decrease in the size of the Ni crystallites resulting in a high dispersion on the alumina support. Similarly, Ho et al. (2020) attributed the exceptional activity of the La-promoted Ni/Al_2O_3 catalyst to a synergistic impact of dissociative and associative CO_2 activation which was induced by the presence of more reduced, finely distributed, and stable Ni nanoparticles, as well as basic sites within the La_2O_3/Al_2O_3 matrix. Mihet et al. (2021) attributed the improved performance of the La-promoted Ni/SiO_2 catalyst in CO_2 methanation to the enhancement of Ni particle dispersion, better capacity for H_2 and CO_2 adsorption and activation, improved anti-sintering capacity, the combined effect of Ni nanoparticles stabilisation inside the medium sized mesopores, and the facilitated access of reagents to active centers due to the large mesopores. However, no report focussing on the promoting effect of La on the performance of Ni/YSZ catalyst for CO_2 methanation was identified.

The results of this study are presented in Figure 6.13. As seen, the addition of the La-promoter slightly improved the activity of the Ni/YSZ catalyst, but a significant decline in the catalyst's performance occurred at La-contents beyond 3%. This trend could not be compared with a similar study on the promoting effect of La on Ni/YSZ catalyst in CO_2 methanation because such study was not found. The closest study found on the effect of La on Ni/YSZ focused on CH_4 dry reforming and not methanation. According to a study by Tu et al. (2020), the addition of a La-promoter improved the activity of a Ni-YSZ catalyst in methane cracking during a CH_4 dry reforming reaction. Deducing from the authors' observation, the addition of a La-promoter to a Ni/YSZ catalyst for CO_2 methanation in the current research encouraged the cracking of CH_4. Therefore, the S_{CH4} was not increased as the La-content increased. This is also evident in the S_{CO} which increased as the La-content increased since part of the CH_4 produced likely underwent cracking.

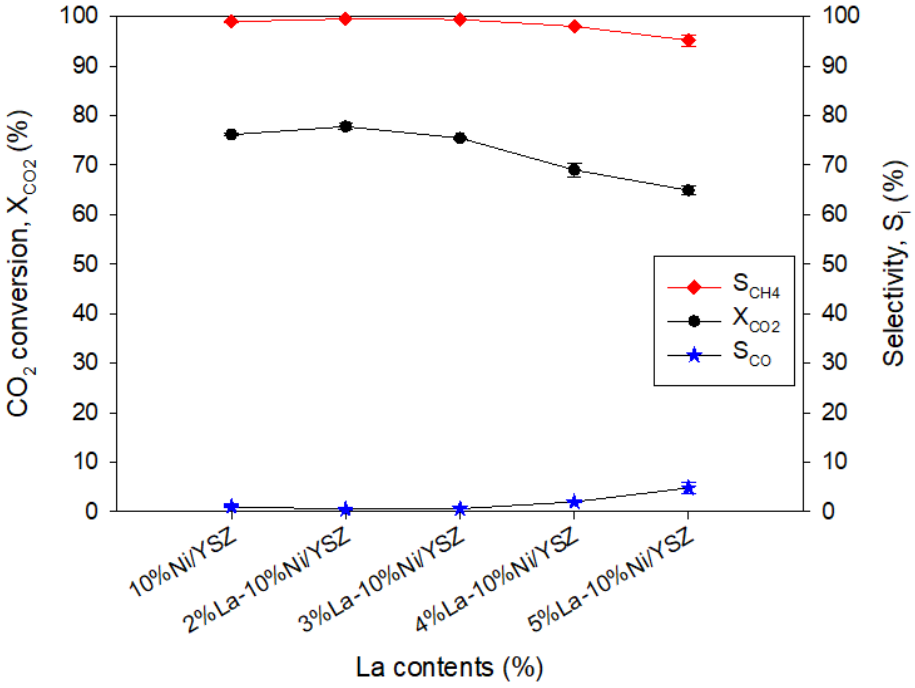


Figure 6.13 Performance of 10%Ni/YSZ with the variation in the La-content in CO_2 methanation conducted under atmospheric pressure at 643 K and GHSV 40500 mL h^{-1} g^{-1}_{cat}.

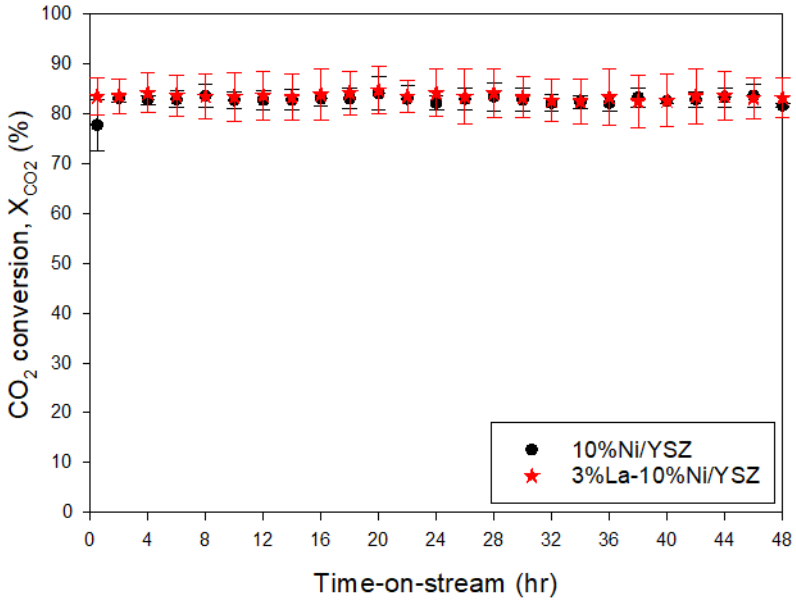


Figure 6.14 Longevity test profiles showing the stability of 10%Ni/YSZ and 3%La-10%Ni/YSZ catalysts in CO_2 methanation conducted under atmospheric pressure at 643 K, GHSV 20250 mL h^{-1} g^{-1}_{cat} and 48 h on-stream.

Figure 6.14 shows the results obtained during a 48 h on-stream longevity test over 10%Ni/YSZ and 3%La-10%Ni/YSZ catalysts at 643 K and 1 bar. As seen in the figure, the addition of the La-promoter to the catalyst did not offer any significant change to the catalyst's performance and stability within the time-on-stream. This result further proves that the addition of La-promoter to Ni/YSZ catalysts is not economically ideal when employing such catalysts for CO_2 methanation.

6.9 Effect of reactor configuration

This section presents the results from the investigation of the influence of reactor configuration for CO_2 methanation. Specifically, three reactor configurations, namely, a single reactor with one catalyst bed, a single reactor with two catalyst beds, and two reactors in series configuration were employed. For the results for a single catalyst bed, the reader can refer to all the results presented in previous sections of this chapter. The following will therefore focus on the latter two concepts.

6.9.1 A single fixed-bed quartz reactor containing two catalyst beds

For this reactor configuration, the weights of the catalysts in the first and second beds from the feed inlet were varied in the ratios 20%-80%, 40%-60%, 60%-40%, 80%-20% and were compared with a single bed reactor (100%-0). Figure 6.15 (a) and (b) depict the results of this study.

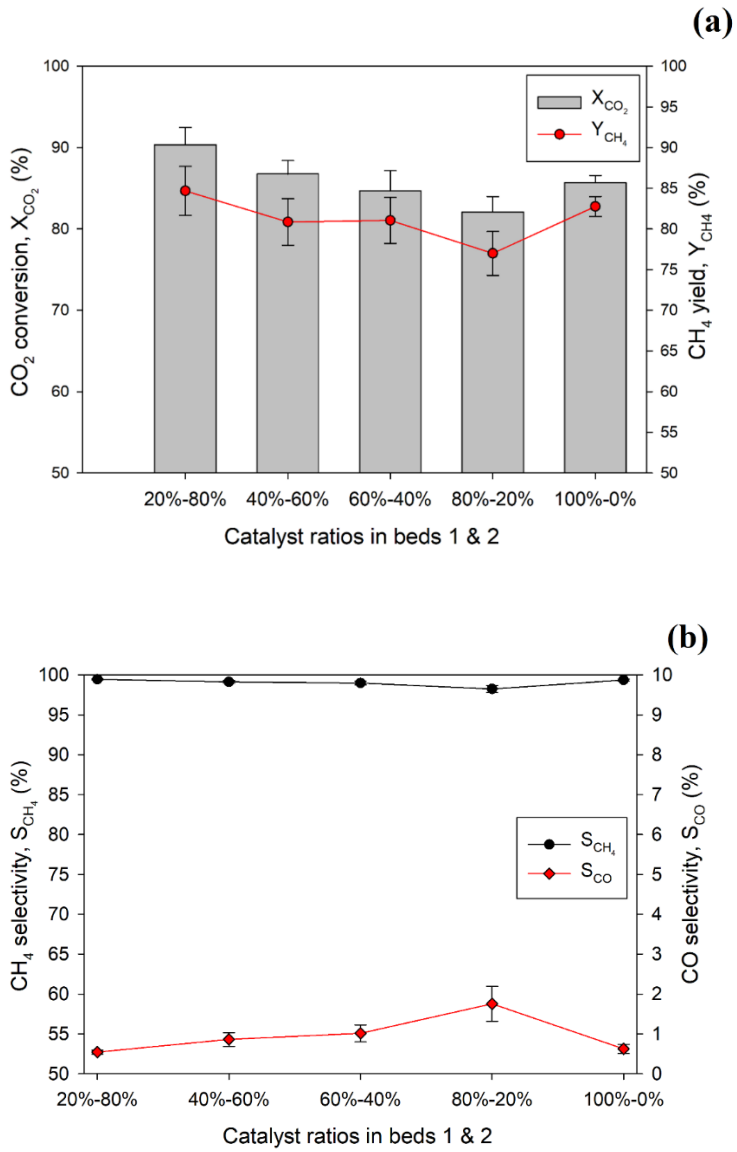


Figure 6.15 Effect of varying the catalyst ratio in a single fixed-bed quartz reactor containing two catalyst beds on (a) CO_2 conversion and CH_4, and (b) CH_4 and CO selectivities during CO_2 methanation conducted at total feed flow = 135 mL min^{-1}, N_2:H_2:CO_2 ratio = 4:4:1, pressure = 1 bar, temperature = 643 K, GHSV 13,500 mL h^{-1} g^{-1}_{cat}.

As seen in Figure 6.15 (a), the CO_2 conversion and CH_4 yield were favoured when the reaction was conducted with less amount of catalyst in the first bed than in the second bed. This observation was explained by relating the interaction of the products from the first catalyst with the second catalyst. At lower catalyst weight in the first bed, the products such as CH_4, CO, and H_2O are low compared with what will be obtained with a higher amount of catalyst in the

first bed. In this regard, the effect of water produced from the first catalyst was not significant because of the availability of active sites in the second catalyst for CO, the unreacted CO_2 and H_2 to further react. As the quantity of the first catalyst increased, the amount of water produced also increased. The increasing amount of water molecules then diluted the stream of reactants and prevented some of the unreacted species from reaching the active sites of the second catalyst. This occurrence was evidenced in the amount of CO produced as shown in Figure 6.15 (b) The amount of CO from the first catalyst bed being converted in the second catalyst bed decreased as more water was brought in from the first catalyst, hence the CO increase. While the 20%-80% catalyst bed ratio displayed the best in terms of CO_2 conversion, the CH_4 yield was comparable with a single catalyst bed system (100% to 0%). It should also be noted that the temperature around the first catalyst bed was slightly higher than the temperature within the region before the second catalyst bed. This temperature difference could also be responsible for the observed performances in a single reactor with two catalyst beds. From this observation, it is not economical to design a reactor system with two catalyst beds within a single reactor.

6.9.2 Two fixed-bed quartz reactors arranged in series

The effect of two fixed-bed quartz reactors arranged in series was also studied after the results from the single reactor system with dual catalyst beds revealed that such a setting is not effective for improved performance in CO_2 methanation. The motivation for installing a water-removing device at the outlet of the first reactor in a series of fixed-bed quartz reactors was that the presence of high amounts of water could have potential adverse effects on the CO_2 methanation process in the second reactor. This strategy is expected to help mitigate the negative impact of water on the catalyst activity, selectivity, stability, and overall process efficiency, ultimately leading to enhanced and optimised performance of the entire reactor system.

Prior to the actual experiment, an initial investigation was conducted where the two reactors were connected without a water trap device at the outlet of the first reactor (Figure 6.16).



Figure 6.16 Pictorial view of the two-reactors in series configuration without water-trap.

In this reactor configuration, all the output from the first reactor flowed into the second reactor. A CO_2 conversion of about 97% was obtained in the first one hour and decreased to about 94% after four hours of operation. Subsequently, the CO_2 conversion continued to drop after 4h on-stream and became stabilised at about 76% after 15 h on-stream. The reaction was eventually stopped because the pressure buildup resulting from the condensation of water at the outlet of the first reactor caused the catalyst in the second reactor to completely shift out of position. The initial high CO_2 conversion in the first four hours of the reaction was attributed to the longer dwelling time of the reactants across the two reactors and less interference of water with the second catalyst which enabled more active sites for the unreacted CO_2 leaving the first reactor to be converted in the second reactor. But as the operation proceeded beyond four hours, the amount of condensed water became significant, and some flowed alongside the gaseous mixture entering the second reactor causing an inhibitory effect on the catalyst in the second reactor. This condensed water also resulted in a significant back pressure causing the catalyst bed in the second reactor to shift.

The inhibiting effect of water has been reported in several studies. For instance, Marwood et al. (1997, 1994) investigated the impact of water on the performance of Ru/TiO_2 catalyst in CO_2 methanation by employing transient in-situ DRIFT experiments. Their findings revealed that the presence of water leads to a decrease in the CO_2 conversion rate. This negative effect of water was attributed to the inhibitory role of water, which reduced the rate of CO_2 activation, thereby limiting the amount of adsorbed CO on the Ru active sites. The inhibitory effect of

water was also attributed to its participation in both the reverse water gas shift and the methanation processes resulting in the formation of byproducts other than CH_4. Falbo et al. (2018) examined the influence of water by co-feeding water with other reactants into the reactor at a partial pressure of 0.08. It was observed that catalyst activity in terms of CO_2 conversion significantly dropped as the inlet water pressure increased. The X_{CO2} recorded a drop close to 59% due to the inhibitory effect of water. Lim et al. (2016) investigated the effect of water during a kinetic study of CO_2 methanation over a Ni/γ-Al_2O_3 catalyst. The addition of water was found to result in a decrease in the rate of CH_4 formation. Hence, it was recommended that the inhibitory effect of water on the rate of reaction be accounted for whenever data from kinetic study of CO_2 methanation are being analysed at higher conversion rates. Duyar et al. (2015) estimated the order of reaction with respect to H_2O to be -0.23 during a kinetic study of CO_2 methanation over a Ru/γ-Al_2O_3 catalyst. The negative order of H_2O was attributed to its inhibitory effect on the reaction during methanation.

The problem of pressure buildup resulting from extreme condensation of water at the outlet of the first reactor was resolved by installing a water-trap at the exit of the first reactor before the connection to the second reactor as shown in Figure 6.17. This enabled the condensed water from the first reactor to be removed while the unreacted CO_2, H_2, N_2, CH_4 and CO passed into the second reactor. This configuration was subjected to a 48 h on-stream longevity tests, and the results are presented in Figure 6.18.

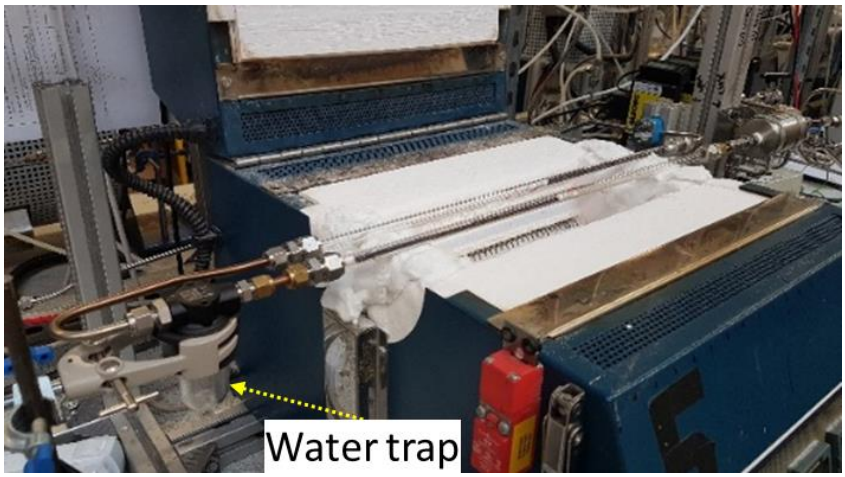


Figure 6.17 Pictorial view for two-reactors in series configuration with a water-trap.

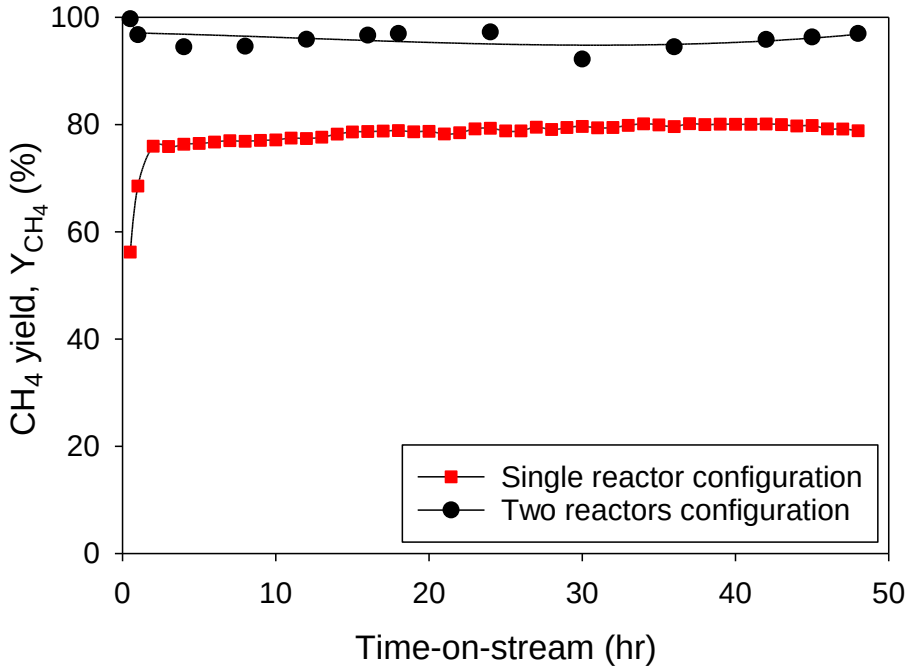


Figure 6.18 Longevity test profiles showing the CH_4 yield during CO_2 methanation conducted for 4 8h on-stream over 10%Ni/YSZ catalyst in a single and two reactors in series configurations with a water-removing device at GHSV 20250 mL h^{-1} g^{-1}_{cat}, H_2:CO_2:N_2 ratio of 4:1:4, 1 bar and at 643 K.

The results from this new setup indicated that the effect of water was significantly reduced resulting in about 99% conversion of CO_2 with negligible backpressure as observed during the study. The CH_4 yield was in the range of 96 to 98% throughout the test. This observation is in agreement with a previous study by Hernandez et al. (2020) in which the addition of water in the feed caused a negative effect during CO_2 methanation. Hashemi et al. (2021) also found that the removal of water significantly improved the average reaction rate within the reactor, leading to an increase in CO_2 conversion within a reactor operating at static conditions. It is also believed that the removal of water before the reactant stream enters the second reactor helps to overcome the thermodynamic limitations of conversion (Götz et al., 2014).

Furthermore, the effect of varying the catalyst ratio in the two-reactor configuration in series with a water trap for CO_2 methanation was investigated over the 10%Ni/YSZ catalyst. The results are represented in Figure 6.19. As seen in Figure 6.19, the CO_2 conversion and CH_4

yield vary with the catalyst ratio in the two reactors. It was expected that the configuration with a higher quantity of catalyst in the first reactor than in the second reactor would perform better because of the higher amount of water produced and potentially removed in the water trap. Since this water was removed before entering the second reactor, the water interference would be minimal. However, the results revealed that the reactor configurations with less catalyst in the first reactor than in the second reactor generally showed better performance. These interesting results can be attributed to the fact that as most of the water produced in the first reactor was trapped before entering the second reactor, the reacting species entering reactor 2 had more active sites for the reaction to take place.

On the other hand, the initially higher concentration of reactants in the first reactor would imply an over proportional production of water. It is worth mentioning that the presence of small amounts of water may behave differently if the same experiment was to be conducted under high pressures. However, the reactors used in this study could not handle pressures beyond 4 bar. Therefore, it is recommended that a further study be carried out on the influence of water in CO_2 methanation under high operating pressure in a pressure vessel.

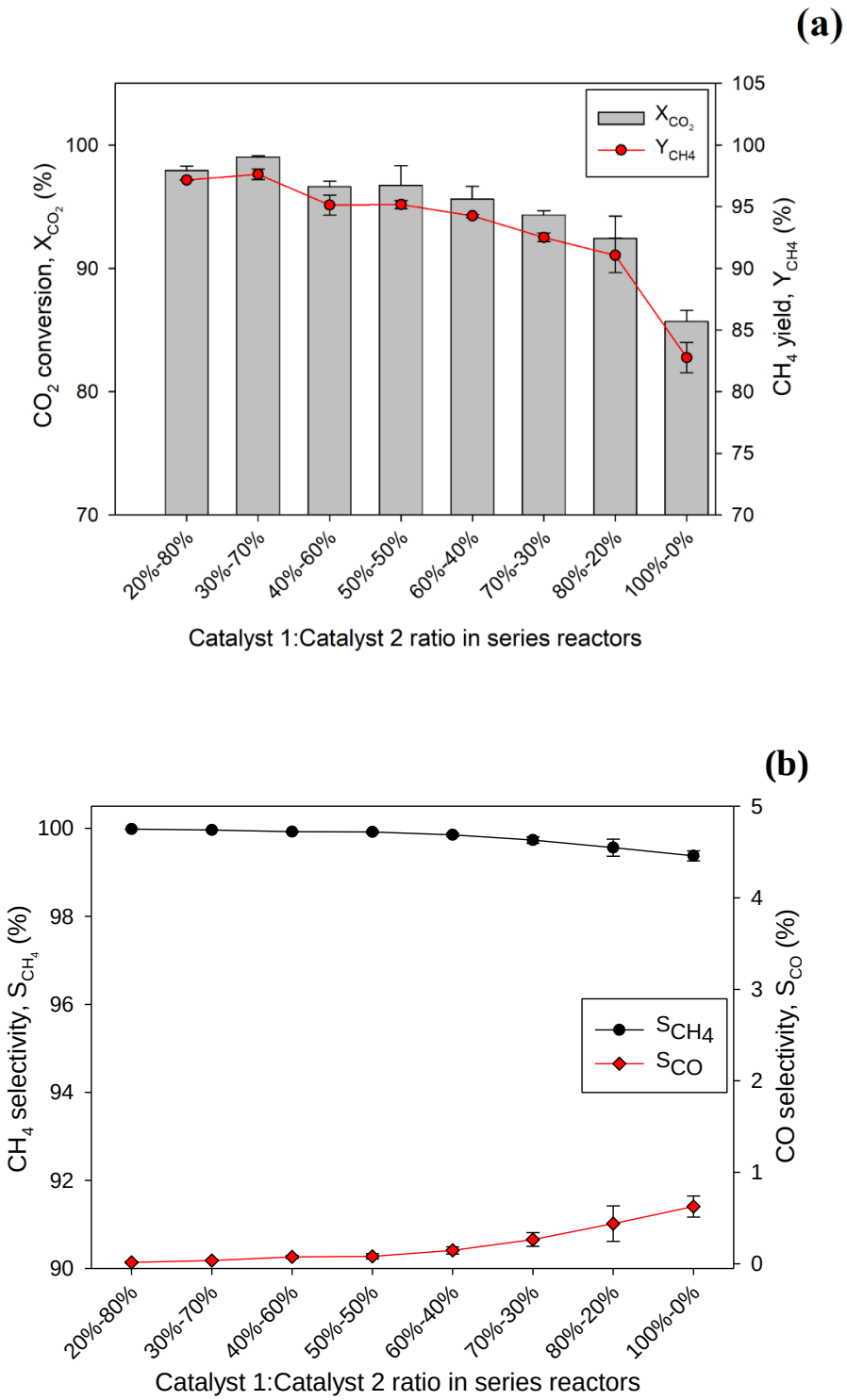


Figure 6.19 Effect of varying the catalyst ratio in the two fixed-bed quartz reactors setup arranged in series with a water trap on (a) CO_2 conversion and CH_4, and (b) CH_4 and CO selectivities during CO_2 methanation conducted at total feed flow = 135 mL min^{-1}, N_2:H_2:CO_2 ratio = 4:4:1, pressure = 1 bar, temperature = 643 K, GHSV 13,500 mL h^{-1} g^{-1}_{cat}.

CHAPTER 7

Post-reaction Characterisation results and discussion

7.1 XRD measurement

Figure 7.1 illustrates the XRD pattern of the spent Ni/SBA-15, unpromoted and La-promoted Ni/YSZ catalysts following a 48-hour on-stream longevity test. Notably, no distinct changes in peaks were observed, and these results are very similar to the XRD patterns of the fresh samples (see Figure 4.7 and 4.8). This is an indication of the remarkable structural stability of the catalysts during methanation reactions. However, there was a slight increase in the sizes of the Ni particles for the spent catalysts as presented in Table 7.1. This increase in Ni particle size is potentially attributed to sintering or carbon deposition. To further investigate this subtle change, additional characterisation was undertaken to determine the underlying cause.

Table 7.1 Crystallite size of Ni in the reduced catalysts before (d_{Ni}) and after (d_{Ni}^{*}) CO_2 methanation reaction.

Samples	Crystallite size, d (nm)	
	d_{Ni}	d_{Ni}^{*}
10%Ni/YSZ	34.39 ± 0.000924852	35.18 ± 0.002643312
10%Ni/SBA-15	29.53 ± 0.002685854	31.46 ± 0.002231267
3%La-10%Ni/YSZ	20.40 ± 0.004741212	21.44 ± 0.002656643

Crystallite size estimation was obtained from the Scherrer Equation using the highest FWHM of the Ni peaks in the XRD data of the catalysts.

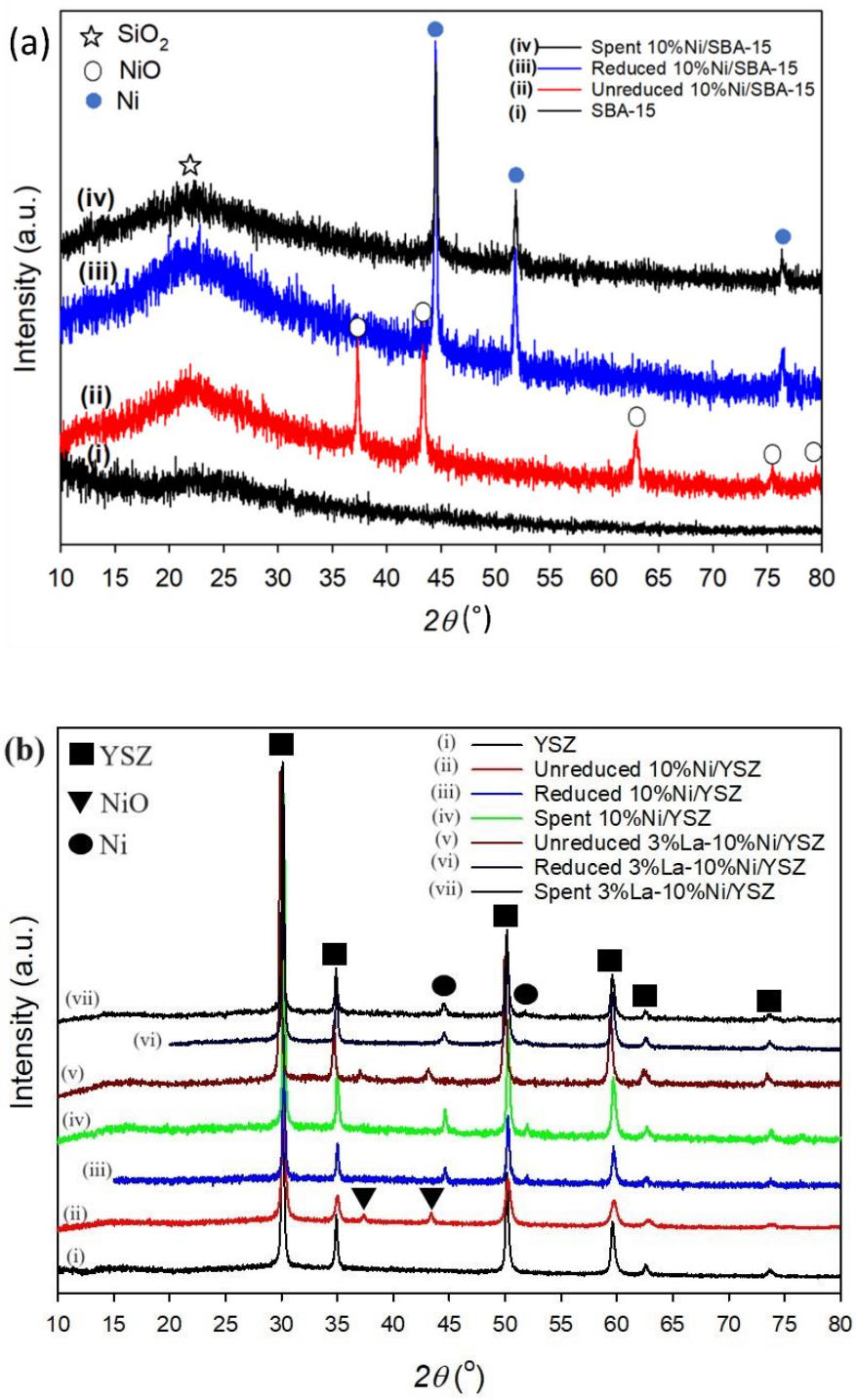


Figure 7.1 XRD patterns of (a) SBA-15 supported, and (b) YSZ supported catalysts before and after 48 h on-stream longevity tests under the following CO_2 methanation conditions: Total feed flow = 135 mL min^{-1}, N_2:H_2:CO_2 ratio = 4:4:1, pressure = 1 bar, temperature = 643 K, GHSV 13,500 mL h^{-1} g^{-1}_{cat}.

7.2 Raman spectroscopy

Figure 7.2 illustrates the Raman spectra of the spent catalysts following a 48-hour CO_2 methanation operation at 643 K. Notably, no discernible peaks were observed in the Raman shift range of 1000 to 3000 cm^{-1}, where carbon peaks are typically expected. Typically, any peak that manifests within the range of 1250 to 1350 cm^{-1} is ascribed to the presence of an amorphous carbon, and is designated as the D band, while a peak within the range of 1500 to 1700 cm^{-1} corresponds to the in-plane vibration of graphitic carbon layers and designated as G band) (Wu et al., 2021; Wang et al., 2012; Li et al., 2023b). Additionally, there are other bands such as the D' band which show the presence of disordered carbons. In this study, the absence of peaks associated with carbon could either indicate that there were no carbon deposits on the catalysts, or the amount of the carbon deposits might be below the detection limit of the Raman spectroscope. Hence, further characterisation was carried out to ascertain the actual situation.

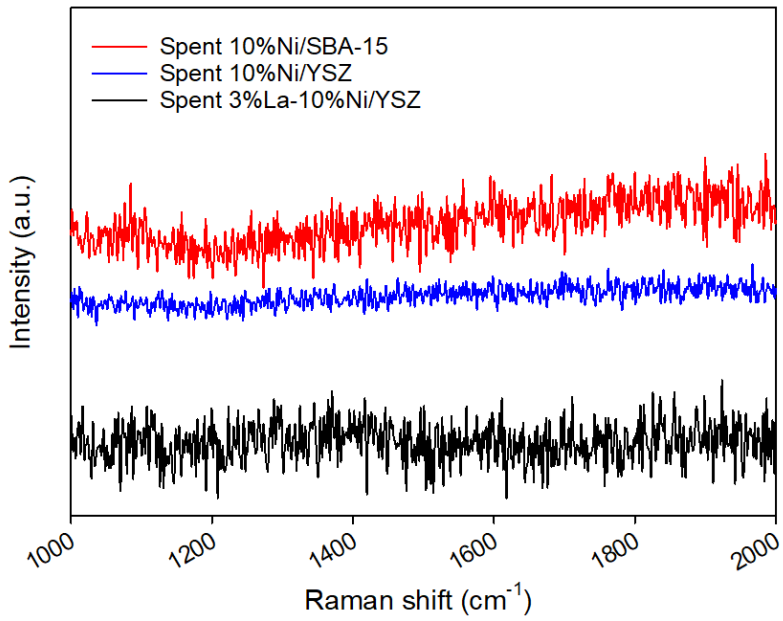


Figure 7.2 Raman spectra of spent SBA-15 supported, and YSZ supported catalysts after 48 h on-stream longevity tests under the following CO_2 methanation conditions: Total feed flow = 135 mL min^{-1}, N_2:H_2:CO_2 ratio = 4:4:1, pressure = 1 bar, temperature = 643 K, GHSV 13,500 mL h^{-1} g^{-1}_{cat}.

7.3 Scanning electron microscopy (SEM)

SEM analysis was conducted to characterise the spent catalysts following the stability test. The images are shown in Figure 7.3.

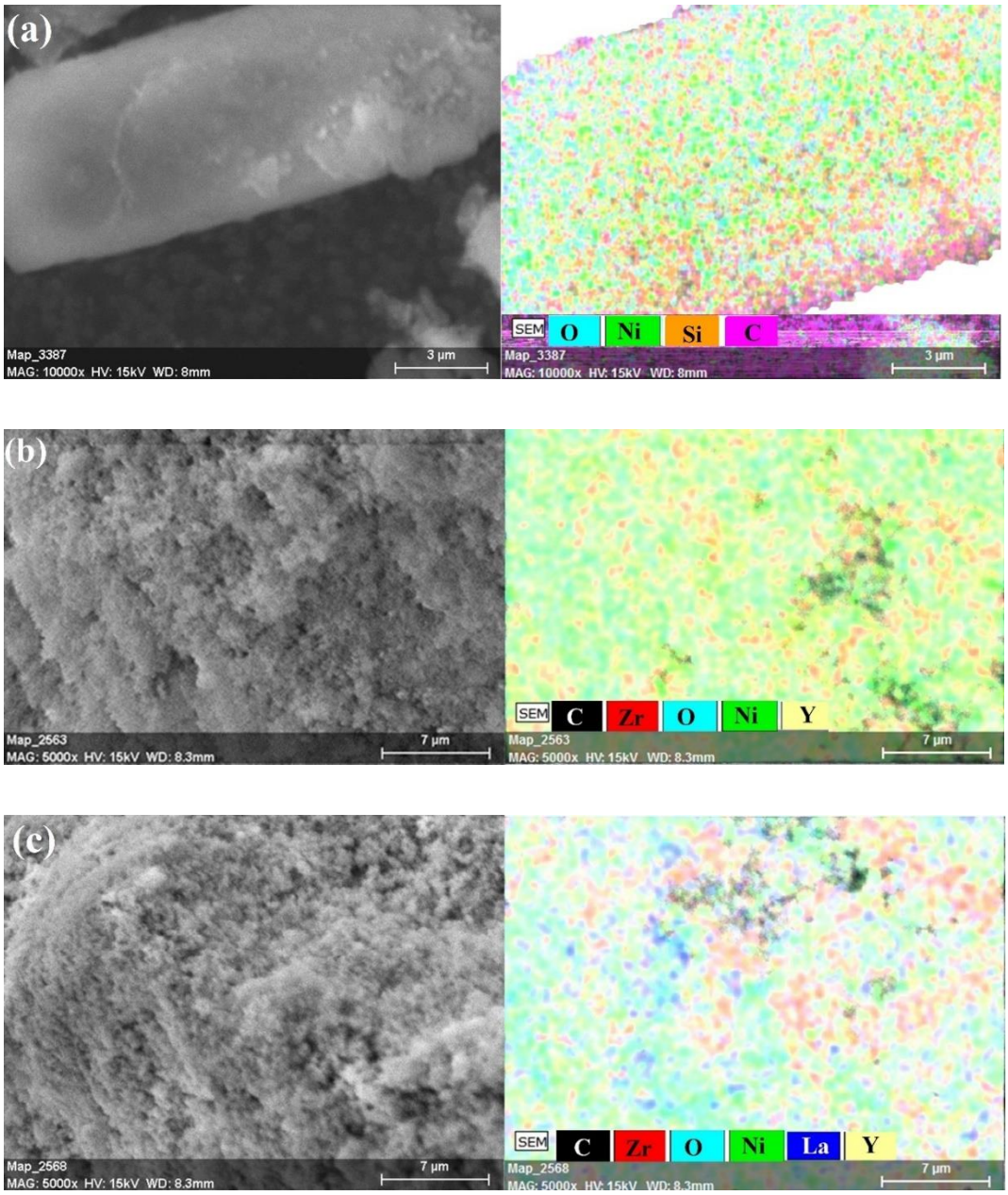


Figure 7.3 SEM micrographs of spent (a) 10%Ni/SBA-15, (b) 10%Ni/YSZ and (c) 3%La-10%Ni/YSZ catalysts after 48 h on-stream longevity tests under the following CO_2 methanation conditions: Total feed flow = 135 mL min^{-1}, N_2:H_2:CO_2 ratio = 4:4:1, pressure = 1 bar, temperature = 643 K, GHSV 13,500 mL h^{-1} g^{-1}_{cat}.

The acquired micrographs revealed negligible carbon deposition on the catalysts' surfaces. Although there was no significant sintered region observed on any of the catalysts, the XRD results showed a slight increase in the crystallite sizes of all the catalysts after the longevity tests (Table 7.1). This indicated that the catalysts had high resistance to sintering. These findings can explain the high stability exhibited by the catalysts, especially the La-promoted Ni/YSZ. This improvement can be attributed to the increased Ni dispersion on the YSZ support and the reduction in Ni particle size.

7.4 Temperature-programmed oxidation (TPO)

Figure 7.4 displays the TPO profiles of used catalysts from 48 h on-stream longevity tests. The catalysts exhibited distinct patterns with three primary segments based on the oxidation temperature as given in Table 7.2. The first segment can be attributed to the removal of moisture adsorbed on the surface and pores. The subsequent segment can be linked to the oxidation of residual Ni^0 following the stability tests according to previous studies (Dias and Perez-Lopez, 2023; Miao et al., 2022).

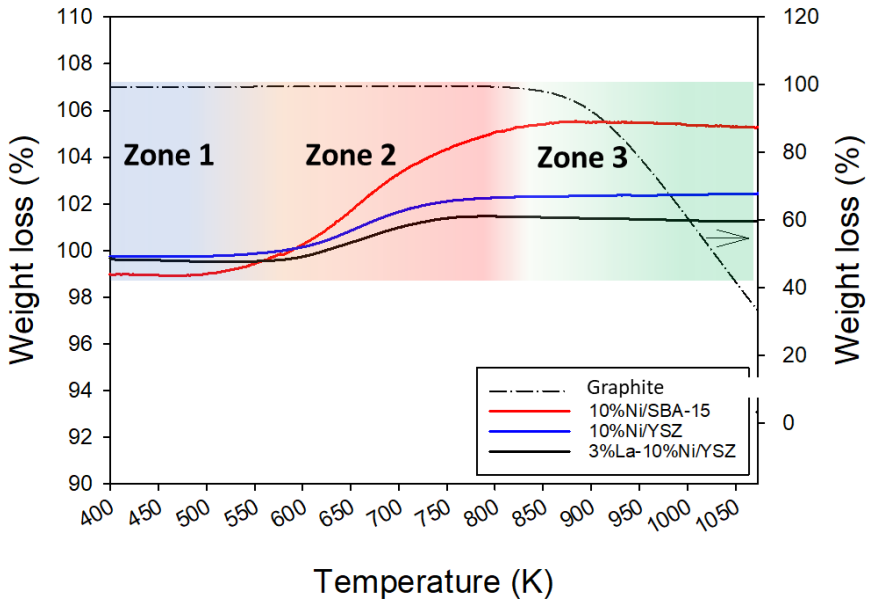


Figure 7.4 TPO profiles showing the weight loss of graphite and spent catalysts after 48 h on-stream longevity tests under the following CO_2 methanation conditions:

Total feed flow = 135 mL min^{-1}, N_2:H_2:CO_2 ratio = 4:4:1, pressure = 1 bar, temperature = 643 K.

Table 7.2 Estimated weight gain/loss percent for the Ni^0 and carbon oxidation zones during the TPO of catalysts used in a 48 h on-stream longevity test for CO_2 methanation at 643 K.

Samples	Initial sample weight $\times 10^{-3}$ (g)	Weight gained during Ni^0 oxidation (%)	Mass of carbon deposited in zone 3 $(g_{carbon}\ g_{cat}^{-1})$
10%Ni/SBA-15	8.80	6.6102	0.0036
10%Ni/YSZ	41.1	2.4771	0
3%La-10%Ni/YSZ	66.7	1.9500	0.0034

Although studies have established the high chances of Ni^0 oxidation within the temperature range of the second zone, other studies have also reported the oxidation of amorphous carbon within this temperature range (Xu et al., 2023; da Fonseca et al., 2022). Therefore, zone 2 could be the result of both Ni^0 and carbon oxidation where the rate of Ni^0 oxidation was greater than the rate of carbon oxidation. To ascertain the actual species being oxidised in this zone, further characterisation is required. A characterisation technique capable of detecting and quantifying the CO_2 produced from the oxidation of carbon deposits at various temperatures will be suitable.

The third zone displayed a minor decline in weight for the 10%Ni/SBA-15 and 3%La-10%Ni/YSZ catalysts while no weight loss was observed for the 10%Ni/YSZ catalyst. The weight loss in the third zone has been attributed to the oxidation of carbon deposits in a previous study (Aieamsam-Aung et al., 2023). To verify this claim, graphite was subjected to the same TPO conditions, and the weight loss observed corresponded with the trend in this region (see Figure 7.4). Table 7.2 also displays the estimated quantity of carbon deposits based on the weight loss observed in the third zone. Overall, the three spent catalysts showed an insignificant amount of carbon deposit. The limited deposition of carbon suggests that all the samples possess high anti-coking properties.

Considering that the change in weight of the catalysts due to carbon deposit obtained from the TG experiment may not be reliable, further carbon study of the spent catalysts was conducted

using a mass spectrometer to confirm the approximate quantity, and the nature of carbon deposited. This confirmation test was also necessary since the TG experiment could not differentiate between the oxidation of Ni^0 and amorphous carbon in zone two, and there was no visible weight loss observed for the spent 10%Ni/YSZ catalyst in the third zone. The mass spectrometer was operating using the conditions: O_2 and N_2 flows of 5 and 20 $mL.min^{-1}$, respectively; heating rate of 5 K min^{-1}. The use of a mass spectrometer for quantifying the amount of carbon deposited on catalysts has also been reported in the literature (da Fonseca et al., 2022). Figure 7.5 represents the TPO profile conducted with the mass spectrometer, and Table 7.3 shows the amount of carbon deposited on each of the catalysts. As seen from the figure, two peaks were detected for all the spent catalysts where the first peak is about the same temperature range but peak 2 is at different temperature ranges. Peak 1 can be ascribed to the oxidation of adsorbed atomic carbon (Takahara et al., 2013). The temperature range of the second peak for 10%Ni/YSZ and 10%Ni/SBA-15 catalysts corresponds to the oxidation temperature range of polymeric carbons while the second peak for the 3%La-10%Ni/YSZ catalyst corresponds to graphitic carbon (Xu & Bartholomew, 2005).

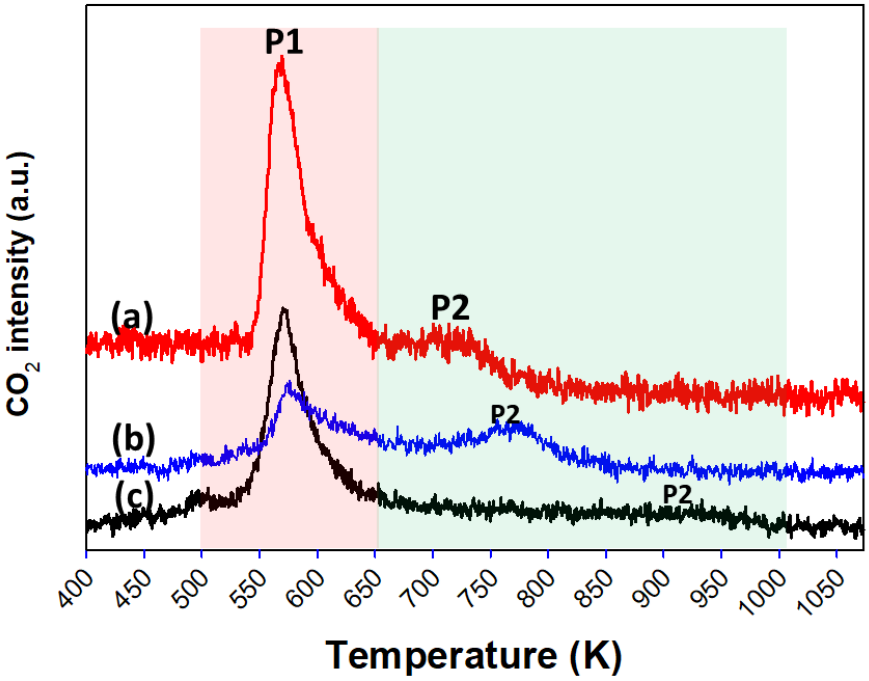


Figure 7.5 TPO profiles showing the CO_2 signals from carbon oxidation of spent (a) 10%Ni/YSZ, (b) 10%Ni/SBA-15 and (c) 3%La-10%Ni/YSZ catalysts after 48 h on-stream

longevity tests under the following CO_2 methanation conditions: Total feed flow = 135 mL min^{-1}, N_2:H_2:CO_2 ratio = 4:4:1, pressure = 1 bar, temperature = 643 K.

While the adsorbed atomic carbon is reactive and easily oxidised, the graphitic carbon is very difficult to be oxidised. From Table 7.3, the order of carbon deposited per mg of catalyst is as follows: 10%Ni/SBA-15 > 10%Ni/YSZ > 3%La-10%Ni/YSZ. It should be noted that the amount of carbon deposited as given in Table 7.2 is lower than the amount estimated in Table 7.3 because the former was obtained using only one segment while the latter was obtained using all temperature zones. In addition, the observed weak peak intensities for polymeric or graphitic carbon indicates that all the catalysts are highly resistant to the formation of graphitic carbon, and this may be connected to the relatively high stability displayed during the longevity tests.

The results of the carbon balance for the 10%Ni/SBA-15, 10%Ni/YSZ and 3%La-10%Ni/YSZ catalysts are presented in Table 7.4. The carbon balance results revealed a notable trend, with the 3%La-10%Ni/YSZ catalyst demonstrating the highest carbon balance and lowest carbon deposition rate. Interestingly, the 10%Ni/SBA-15 catalyst, with a higher surface area than the two other catalysts (according to BET measurements), exhibited the lowest carbon balance and the highest carbon deposition rate.

Table 7.3 Total mass of carbon deposited during a 48 h on-stream longevity test for CO_2 methanation at 643 K estimated from TPO of the spent catalysts in a mass spectrometer.

Samples	Initial sample weight $\times 10^{-3}(g)$	Mass of carbon deposited $(g_{carbon}\, g_{cat}^{-1})$
10%Ni/SBA-15	37.5	0.00812014
10%Ni/YSZ	100	0.00403213
3%La-10%Ni/YSZ	100	0.00368136

Table 7.4 Results of carbon balance and carbon deposition rates obtained from the GC data during a 48 h on-stream longevity test for CO_2 methanation at 643 K.

Samples	Carbon balance (%)	carbon deposition rates $\times 10^{-6}$ $(mol\ g_{cat}^{-1}\ s^{-1})$
10%Ni/SBA-15	93.01169595	1.97975
10%Ni/YSZ	94.32572463	1.60749
3%La-10%Ni/YSZ	95.80715087	1.07294

This variation in the carbon balance and deposition rates may be attributable to the difference in the catalyst composition and structure, which can influence the extent of suppression of side reactions such as the Boudouard reaction (Siang et al., 2021). As discussed in chapter 4, the H_2-TPR of 3%La-10%Ni/YSZ showed a lower reduction temperature than those of the unpromoted 10%Ni/YSZ and the 10%Ni/SBA-15 catalysts. Another observation was in the overlapping between the NiO phase and the YSZ phase at 2θ = 62.8° degree in the XRD patterns of both the unpromoted 10%Ni/YSZ and the 3%La-10%Ni/YSZ catalysts (see Figure 4.6 (a) and Figure 4.7 (a), respectively), while the XRD pattern of the 10%NiSBA-15 indicated the presence of NiO at the 2θ = 62.8° (see Figure 4.8 (b)). Therefore, the synergistic effect between Ni and YSZ support in both the 3%La-10%Ni/YSZ and the unpromoted 10%Ni/YSZ catalysts likely enhanced Ni dispersion and reducibility, leading to abundant active sites for efficient CO_2 conversion to CH_4 and minimising carbon deposition.

This observation suggest that surface area alone is not the sole determinant of catalyst performance. Rather, a combination of factors, including dispersion, reducibility, and intrinsic activity, plays a crucial role in dictating the overall catalytic efficiency in CO_2 methanation.

CHAPTER 8

Conclusions and future work

8.1 Conclusions

The research reported in this thesis focused on the performance of Ni-based catalysts in CO_2 methanation with the aim of producing synthetic natural gas (SNG). The study aimed to contribute to the mitigation of climate change by exploring an efficient and sustainable method for converting CO_2 into a valuable energy resource. The subsequent paragraphs provide a concise summary and exemplify the key discoveries made throughout this research endeavour.

The characterisation results revealed insights into the catalyst supports and their corresponding Ni-based catalysts. The N_2-adsorption/desorption isotherms provided information about the pore structures of the different supports, with modifications observed after impregnation with Ni or a La-promoter. XRD analysis indicated the high dispersion of Ni particles on all catalysts. H_2-TPR results highlighted the varying reducibility properties of the catalysts, with Ni/YSZ demonstrating the highest reducibility. SEM images showed the even distribution of Ni particles in some catalysts, while others exhibited Ni agglomerations.

The effect of transport limitations using the Mears' and Weisz-Prater criteria was negligible, indicating that the selected catalyst particle size of 150 µm is appropriate for the CO_2 methanation operation. The catalyst activity tests demonstrated that Ni/YSZ exhibited the highest CO_2 conversion of about 83%, attributed to its high oxygen vacancies, enhanced basic sites, and resistance to metal sintering. The estimated activation energies of the catalysts showed that Ni/YSZ exhibits the lowest value of 49.9±0.00051839 kJ mol^{-1} followed by Ni/Al_2O_3 (52.4±0.03844688 kJ mol^{-1}), Ni/CeO_2 (59.2±0.012878 kJ mol^{-1}) and Ni/SBA-15 (68.3±0.013478 kJ mol^{-1}). This suggests that the lower performance exhibited by Ni/SBA-15 is attributed to its higher energy barrier compared to the other catalysts.

Operating conditions, such as temperature, pressure, H_2:CO_2 ratio and gas space velocity, were found to influence the methanation reaction, with an optimum range identified for best performance of Ni/YSZ.

Although the characterisation results indicated that the La-promoter to Ni/YSZ modified the catalyst physicochemical properties, its activity in CO_2 methanation was not significantly different from that of the unpromoted Ni/YSZ catalyst. Therefore, more advanced characterisation such as NH_3 temperature-programmed desorption and XPS is recommended to unravel other properties of these catalyst. Notwithstanding, the observed modification in the structure of Ni/YSZ after adding La-promoter suggested its potential for enhanced performance in other reforming reactions.

The reactor configuration study emphasised the superiority of a two-reactor system in series with a water-removing device, outperforming other configurations.

The investigation of spent catalysts indicated minimal carbon deposition and sintering, contributing to their high stability.

8.2 Future work

The following suggestions are provided based on the observations in this study:

8.2.1 Synthesis of SBA-15

In the synthesis of SBA-15, the as-synthesised SBA-15 was thoroughly washed with deionised water before calcination during the synthesis of SBA-15. But results show that when the as-synthesised SBA-15 was calcined without washing, a black residue was formed instead of the white-coloured powder associated with SBA15. Future research could involve: Characterising the black residue using techniques like X-ray diffraction (XRD), Fourier-transform infrared spectroscopy (FTIR), and X-ray photoelectron spectroscopy (XPS) to identify its chemical composition and potential impurities. Conducting high-resolution microscopy (SEM, TEM) to examine the morphological and structural changes in SBA-15.

8.2.2 Water effect at high pressure

Building upon the inhibiting effect of water on the catalyst performance, a comprehensive study at high pressures (> 20 bar) is suggested: Performing CO_2 methanation experiments using a high-pressure reactor setup to assess water impact on catalyst behaviour at elevated pressures. Advanced techniques such as in-situ spectroscopy (Raman, FTIR) could be employed to monitor catalyst performance and water interactions under high-pressure conditions. The potential alteration of reaction pathways and intermediates due to water presence at high pressures could be studied. Compare the results with the inhibitory effect observed at lower pressures to unveil pressure-dependent water-related deactivation mechanisms.

8.2.3 In-depth study on the Ni-YSZ Interaction

While the current study has revealed that Ni/YSZ catalyst is highly active for CO_2 methanation, the study on the interaction between Ni and YSZ has not been fully exhausted. Further characterisation techniques, such as in-situ spectroscopy and advanced microscopy, could provide deeper insights into the catalyst-support interaction dynamics during CO_2 methanation. Thermodynamic studies could elucidate the underlying mechanisms governing Ni-YSZ interactions under different reaction conditions, helping to optimise catalyst performance and stability. An in-depth comparison with the CeO_2 support would be useful.

8.2.4 Reactor configuration

Expanding on the results from the reactor configuration systems, future work could delve into a comprehensive investigation of the catalyst distribution and reaction kinetics within the reactors. By employing advanced computational fluid dynamics (CFD) simulations, the flow dynamics, temperature distribution, and species concentration profiles could be precisely modelled and analysed. This would provide a detailed understanding of how the spatial distribution of catalyst beds influences reaction performance and product selectivity. A comprehensive study on the reaction thermodynamics is also suggested. This would involve examining the impact of varying operating conditions, such as pressure and temperature, on the thermodynamic feasibility of the CO_2 methanation process. Such analysis could lead to the identification of optimal conditions that enhance methane yield and minimise energy losses, contributing to process efficiency.

8.2.5 Integration of methanation and co-electrolysis

To further advance the sustainable utilisation of surplus electrical power, the integration of methanation with co-electrolysis in a reversible solid oxide electrolyser (RSOE) system holds great promise. Future research could focus on designing, fabricating, and characterising a novel RSOE setup that combines CO_2 methanation and electrolysis of H_2O and CO_2 to produce syngas. This integrated system could offer a pathway for the efficient conversion of renewable energy into a versatile energy carrier.

8.2.6 Scale-up and techno-economic analysis

Transitioning from laboratory-scale experiments to practical applications involves challenges related to catalyst scale-up, reactor engineering, and economic feasibility. Future work could involve a comprehensive techno-economic analysis, considering factors such as catalyst production costs, reactor design, and energy consumption. This analysis would provide valuable insights into the viability of large-scale CO_2 methanation processes as a key component of the clean energy transition.

Addressing these future research directions will contribute positively to the advancement of knowledge in CO_2 methanation and its integration with innovative energy conversion technologies, furthering our understanding of sustainable energy solutions.

References

Aasberg-Petersen, K., Dybkjær, I., Ovesen, C. V., et al. (2011) Natural gas to synthesis gas - Catalysts and catalytic processes. *Journal of Natural Gas Science and Engineering*, 3 (2): 423–459. doi:10.1016/j.jngse.2011.03.004.

Ab Halim, A.Z., Ali, R. and Bakar, W.A.W.A. (2015) CO_2/H_2 methanation over M*/Mn/Fe-Al_2O_3 (M*: Pd, Rh, and Ru) catalysts in natural gas; optimization by response surface methodology-central composite design. *Clean Technologies and Environmental Policy*, 17 (3): 627–636. doi:10.1007/s10098-014-0814-8.

Abate, S., Mebrahtu, C., Giglio, E., et al. (2016) Catalytic performance of γ-Al_2O_3-ZrO_2-TiO_2-CeO_2 composite oxide supported Ni-Based catalysts for CO_2 methanation. *Industrial and Engineering Chemistry Research*, 55 (16): 4451–4460. doi:10.1021/acs.iecr.6b00134.

Abdalla, A.M., Hossain, S., Nisfindy, O.B., et al. (2018) Hydrogen production, storage, transportation and key challenges with applications: A review. *Energy Conversion and Management*, 165: 602–627. doi:10.1016/J.ENCONMAN.2018.03.088.

Agrawal, P.K., Katzer, J.R. and Manogue, W.H. (1981) Methanation over transition metal catalysts. II. carbon deactivation of Co Al_2O_3 in sulfur-free studies. *Journal of Catalysis*, 69 (2): 312–326. doi:10.1016/0021-9517(81)90168-8.

Ahmad, Y.H., Mohamed, A.T., Kumar, A., et al. (2021) Solution combustion synthesis of Ni/La_2O_3 for dry reforming of methane: Tuning the basicity via alkali and alkaline earth metal oxide promoters. *RSC Advances*, 11 (53): 33734–33743. doi:10.1039/d1ra05511a.

Ahn, J., Bu, H., Kim, C., et al. (1996) Structural Study of the Ni{100}-(2 x 2)-C Surface by Time-of-flight Scattering and Recoiling Spectrometry. *Journal of Physical Chemistry*, 100 (21): 9088–9092. doi:10.1021/jp960346p.

Ahn, J.Y., Chang, S.W., Lee, S.M., et al. (2019) Developing Ni-based honeycomb-type catalysts using different binary oxide-supported species for synergistically enhanced CO_2 methanation activity. *Fuel*, 250: 277–284. doi:10.1016/J.FUEL.2019.03.123.

Aieamsam-Aung, P., Srifa, A., Koo-Amornpattana, W., et al. (2023) Upgradation of methane in the biogas by hydrogenation of CO_2 in a prototype reactor with double pass

operation over optimized Ni-Ce/Al-MCM-41 catalyst. *Scientific Reports*, 13 (1): 1–16. doi:10.1038/s41598-023-36425-5.

Al-Fatesh, A. (2015) Suppression of carbon formation in CH_4–CO_2 reforming by addition of Sr into bimetallic Ni–Co/γ-Al_2O_3 catalyst. *Journal of King Saud University - Engineering Sciences*, 27 (1): 101–107. doi:10.1016/j.jksues.2013.09.006.

Al-Fatesh, A.S., Ibrahim, A.A., Osman, A.I., et al. (2022a) Effect of holmium oxide loading on nickel catalyst supported on yttria-stabilized zirconia in methane dry reforming. *ACS Omega*, 7 (48): 43700–43709. doi:10.1021/acsomega.2c04320.

Al-Fatesh, A.S., Kasim, S.O., Ibrahim, A.A., et al. (2022b) Greenhouse gases utilization via catalytic reforming with Sc promoted Ni/SBA-15. *Fuel*, 330 (June): 125523. doi:10.1016/j.fuel.2022.125523.

Alarcón, A., Guilera, J., Soto, R., et al. (2020) Higher tolerance to sulfur poisoning in CO_2 methanation by the presence of CeO_2. *Applied Catalysis B: Environmental*, 263 (August 2019): 118346. doi:10.1016/j.apcatb.2019.118346.

Albers, P., Pietsch, J. and Parker, S.F. (2001) Poisoning and deactivation of palladium catalysts. *Journal of Molecular Catalysis A: Chemical*, 173 (1–2): 275–286. doi:10.1016/S1381-1169(01)00154-6.

Allen, J.W. and Martin, R.M. (1982) Kondo volume collapse and the y-a transition in cerium. *Physical Review Letters*, 49 (15): 1106–1110. Available at: https://journals.aps.org/prl/pdf/10.1103/PhysRevLett.49.1106.

Allen, T. (2013) *Particle size measurement*. Powder Technology Series. Springer US. Available at: https://books.google.co.uk/books?id=7dsFCAAAQBAJ.

Alves, L.M.N.C., Almeida, M.P., Ayala, M., et al. (2021) CO_2 methanation over metal catalysts supported on ZrO_2: Effect of the nature of the metallic phase on catalytic performance. *Chemical Engineering Science*, 239: 116604. doi:10.1016/j.ces.2021.116604.

Amin, M.H., Putla, S., Bee Abd Hamid, S., et al. (2015) Understanding the role of lanthanide promoters on the structure–activity of nanosized Ni/γ-Al_2O_3 catalysts in carbon dioxide reforming of methane. *Applied Catalysis A: General*, 492: 160–168. doi:http://dx.doi.org/10.1016/j.apcata.2014.12.038.

Ambrose, J. (2023) Greenhouse gas emissions from global energy industry still rising – report. Available at: https://www.theguardian.com/business/2023/jun/26/greenhouse-

gas-emissions-from-global-energy-industry-still-rising-report#:~:text=The report%2C undertaken by the,world used more energy overall. (Accessed: 28 July 2023).

Anderson, J.B. (1963) A criterion for isothermal behaviour of a catalyst pellet. *Chem. Eng. Sci.*, 18 (2): 147–148.

Anoop, N., Sundaramurthy, S., Jha, J.M., et al. (2021) Plasma catalysis: a feasible solution for carbon dioxide valorization? Clean Technologies and Environmental Policy, 23 (10): 2789–2811. doi:10.1007/s10098-021-02203-y.

Aparicio-Mauricio, G., Ruiz, R.S., López-Isunza, F., et al. (2017) A simple approach to describe hydrodynamics and its effect on heat and mass transport in an industrial wall-cooled fixed bed catalytic reactor: ODH of ethane on a MoVNbTeO formulation. *Chemical Engineering Journal*, 321: 584–599. doi:10.1016/j.cej.2017.03.043.

Apostolescu, N., Tataru Farmus, R.E., Harja, M., et al. (2023) Photocatalytic Removal of Antibiotics from Wastewater Using the CeO_2/ZnO Heterojunction. *Materials*, 16 (2). doi:10.3390/ma16020850.

Aramouni, N.A.K., Touma, J.G., Tarboush, B.A., et al. (2018) Catalyst design for dry reforming of methane: Analysis review. *Renewable and Sustainable Energy Reviews*, 82 (September 2017): 2570–2585. doi:10.1016/j.rser.2017.09.076.

Arandiyan, H., Wang, Y., Scott, J., et al. (2018) In situ exsolution of bimetallic Rh-Ni nanoalloys: A highly efficient catalyst for CO_2 methanation. *ACS Applied Materials and Interfaces*, 10 (19): 16352–16357. doi:10.1021/acsami.8b00889.

Argyle, M. and Bartholomew, C. (2015) Heterogeneous catalyst deactivation and regeneration: A Review. *Catalysts*, 5 (1): 145–269. doi:10.3390/catal5010145.

Arrhenius, S. (1896) XXXI. On the influence of carbonic acid in the air upon the temperature of the ground. *The London, Edinburgh, and Dublin Philosophical Magazine and Journal of Science*, 41 (251): 237–276. doi:10.1080/14786449608620846.

Ashok, J., Pati, S., Hongmanorom, P., et al. (2020) A review of recent catalyst advances in CO_2 methanation processes. *Catalysis Today*, 356: 471–489. doi:10.1016/j.cattod.2020.07.023.

Aziz, H.S., Wan, C., Xing, Y., et al. (2022) Low radiative heat transfer realized by 8YSZ/$LaAl_{11}O_{18}$ composites for high-temperature applications. *Journal of Materials Science*, 57 (40): 18754–18769. doi:10.1007/s10853-022-07840-2.

Aziz, M.A.A., Jalil, A.A., Triwahyono, S., et al. (2015) CO_2 methanation over heterogeneous

catalysts: recent progress and future prospects. *Green Chemistry*, 17 (5): 2647–2663. doi:10.1039/c5gc00119f.

Babakouhi, R., Alavi, S.M., Rezaei, M., et al. (2023) Combined CO_2 reforming and partial oxidation of methane over mesoporous nanostructured Ni/M-Al_2O_3 catalyst: Effect of various support promoters and nickel loadings. *Journal of CO_2 Utilization*, 70 (February): 102427. doi:10.1016/j.jcou.2023.102427.

Bacariza, M.C., Graça, I., Bebiano, S.S., et al. (2018) Micro- and mesoporous supports for CO_2 methanation catalysts: A comparison between SBA-15, MCM-41 and USY zeolite. *Chemical Engineering Science*, 175: 72–83. doi:10.1016/j.ces.2017.09.027.

Baharudin, L., Yip, A.C.K., Golovko, V., et al. (2020) Potential of metal monoliths with grown carbon nanomaterials as catalyst support in intensified steam reformer: A perspective. *Reviews in Chemical Engineering*, 36 (4): 459–491. doi:10.1515/revce-2018-0007.

Baker, R.T.K., Gadsby, G.R., Thomas, R.B., et al. (1975) The production and properties of filamentous carbon. *Carbon*, 13 (3): 211–214. doi:10.1016/0008-6223(75)90234-1.

Baran Aydın, E., Ateş, S. and Yazıcı, B. (2022) Production of nanoporous alumina membranes modified with multi-walled carbon nanotube, polyacrylamide and polystyrene and use in wastewater treatment. *Water and Environment Journal*, 36 (4): 598–607. doi:10.1111/wej.12790.

Bärnighausen, H. and Schiller, G. (1985) The crystal structure of A-Ce_2O_3. *Journal of The Less-Common Metals*, 110 (1–2): 385–390. doi:10.1016/0022-5088(85)90347-9.

Barreto, A.R. (2018) Fossil fuels, alternative energy and economic growth. *Economic Modelling*, 75: 196–220.

Bartholomew, C.H. (2001) Mechanisms of catalyst deactivation. *Applied Catalysis A: General*, 212 (1–2): 17–60. doi:10.1016/S0926-860X(00)00843-7.

Bartholomew, C.H. and Farrauto, R.J. (2011) Fundamentals of industrial catalytic processes.

Bernal, S., Blanco, G., Calvino, J.J., et al. (1997) Influence of the preparation procedure on the chemical and microstructural properties of lanthana promoted Rh/SiO2 catalysts a FTIR spectroscopic study of chemisorbed CO. *Journal of Alloys and Compounds*, 250 (1–2): 461–466. doi:10.1016/S0925-8388(96)02835-6.

Berzelius, J.J. (1835) Ueber die Destillationsproducte der Traubensäure. *Annalen der Physik*, 112: 1–29.

Beuls, A., Swalus, C., Jacquemin, M., et al. (2012) Methanation of CO_2: Further insight into the mechanism over Rh/γ-Al_2O_3 catalyst. *Applied Catalysis B: Environmental*, 113–114: 2–10. doi:10.1016/J.APCATB.2011.02.033.

Bhatia, S.K., Joo, H.-S. and Yang, Y.-H. (2018) Biowaste-to-bioenergy using biological methods – A mini-review. *Energy Conversion and Management*, 177: 640–660. doi:10.1016/J.ENCONMAN.2018.09.090.

Bian, Y., Xu, C., Wen, X., et al. (2023) CO_2 methanation over the Ni-based catalysts supported on nano-CeO_2 with varied morphologies. *Fuel*, 331 (P1): 125755. doi:10.1016/j.fuel.2022.125755.

Bian, Z., Chan, Y.M., Yu, Y., et al. (2018) Morphology dependence of catalytic properties of Ni/CeO_2 for CO_2 methanation: A kinetic and mechanism study. *Catalysis Today*. doi:10.1016/j.cattod.2018.04.067.

Blanco, A., Caroca, J., Tamayo, R., et al. (2022) CO_2 methanation activity of Ni-doped perovskites. *Fuel*, 320 (December 2021): 1–8. doi:10.1016/j.fuel.2022.123954.

Borgohain, X., Das, E. and Rashid, M.H. (2022) Facile synthesis of CeO_2 nanoparticles for enhanced removal of malachite green dye from an aqueous environment. *Materials Advances*, 4: 683–693. doi:10.1039/d2ma01019d.

Borodziński, A. and Bond, G.C. (2006) Selective hydrogenation of ethyne in ethene-rich streams on palladium catalysts. Part 1. Effect of changes to the catalyst during reaction. *Catalysis Reviews - Science and Engineering*. 48 (2) pp. 91–144. doi:10.1080/01614940500364909.

Bortnovsky, O., Sazama, P. and Wichterlova, B. (2005) Cracking of pentenes to C_2-C_4 light olefins over zeolites and zeotypes: Role of topology and acid site strength and concentration. *Applied Catalysis A: General*, 287 (2): 203–213. doi:10.1016/j.apcata.2005.03.037.

Botzolaki, G., Goula, G., Rontogianni, A., et al. (2020) CO_2 methanation on supported Rh nanoparticles: The combined effect of support oxygen storage. *Catalysts*, 10 (8): 944.

Boukha, Z., Bermejo-López, A., Pereda-Ayo, B., et al. (2022) Study on the promotional effect of lanthana addition on the performance of hydroxyapatite-supported Ni catalysts for the CO_2 methanation reaction. *Applied Catalysis B: Environmental*, 314 (January). doi:10.1016/j.apcatb.2022.121500.

BP (2019) *BP Statistical review of world energy*. London, UK. doi:10.1111/j.1468-

0351.1993.tb00076.x.

Breidenich, C., Magraw, D., Rowley, A., et al. (1998) The Kyoto Protocol to the United Nations Framework Convention on climate change. *The American Journal of International Law*, 92 (2): 315–331. doi:10.2307/2998044.

Brockner, W., Ehrhardt, C. and Gjikaj, M. (2007) Thermal decomposition of nickel nitrate hexahydrate, $Ni(NO_3)_2 \cdot 6H_2O$, in comparison to $Co(NO_3)_2 \cdot 6H_2O$ and $Ca(NO_3)_2 \cdot 4H_2O$. *Thermochimica Acta*, 456 (1): 64–68. doi:10.1016/J.TCA.2007.01.031.

Bulfin, B., Lowe, A.J., Keogh, K.A., et al. (2013) Analytical model of CeO_2 oxidation and reduction. *Journal of Physical Chemistry C*, 117 (46): 24129–24137. doi:10.1021/jp406578z.

Burattin, P., Che, M. and Louis, C. (1999) Metal particle size in Ni/SiO_2 materials prepared by deposition-precipitation: Influence of the nature of the Ni(II) phase and of its interaction with the support. *Journal of Physical Chemistry B*, 103 (30): 6171–6178. doi:10.1021/jp990115t.

Burger, T., Koschany, F., Thomys, O., et al. (2018) CO_2 methanation over Fe- and Mn-promoted co-precipitated Ni-Al catalysts: Synthesis, characterization and catalysis study. *Applied Catalysis A: General*, 558: 44–54. doi:10.1016/J.APCATA.2018.03.021.

Busca, G. (2019) Catalytic materials based on silica and alumina: Structural features and generation of surface acidity. *Progress in Materials Science*, 104 (February): 215–249. doi:10.1016/j.pmatsci.2019.04.003.

Cai, J., Fu, Y., Sun, Q., et al. (2013) Effect of acidic promoters on the titania-nanotubes supported V_2O_5 catalysts for the selective oxidation of methanol to dimethoxymethane. *Chinese Journal of Catalysis*, 34 (11): 2110–2117. doi:10.1016/S1872-2067(12)60690-1.

Cao, A.N.T., Pham, C.Q., Nguyen, T.M., et al. (2022a) Dysprosium promotion on Co/Al_2O_3 catalysts towards enhanced hydrogen generation from methane dry reforming. *Fuel*, 324 (PC): 124818. doi:10.1016/j.fuel.2022.124818.

Cao, A.N.T., Pham, C.Q., Pham, L.K.H., et al. (2022b) Boosted methane dry reforming for hydrogen generation on cobalt catalyst with small cerium dosage. *International Journal of Hydrogen Energy*, 47 (100): 42200–42212. doi:10.1016/j.ijhydene.2021.11.077.

Cesteros, Y., Salagre, P., Medina, F., et al. (2000) Preparation and characterization of several high-area $NiAl_2O_4$ spinels. Study of their reducibility. *Chemistry of Materials*, 12 (2):

331–335. doi:10.1021/cm990154h.

Chai, S., Men, Y., Wang, J., et al. (2019) Boosting CO_2 methanation activity on Ru/TiO_2 catalysts by exposing (001) facets of anatase TiO_2. *Journal of CO_2 Utilization*, 33: 242–252. doi:10.1016/j.jcou.2019.05.031.

Champon, I., Bengaouer, A., Chaise, A., et al. (2019) Carbon dioxide methanation kinetic model on a commercial Ni/Al_2O_3 catalyst. *Journal of CO_2 Utilization*, 34: 256–265. doi:10.1016/j.jcou.2019.05.030.

Chandraker, V., Paramasivan, G. and Chandy, A.J. (2022) Computational investigations of enrichment effects for CO_2 methanation in Sabatier microchannel reactors. *Chemical Engineering Research and Design*, 182: 51–65. doi:10.1016/j.cherd.2022.03.035.

Chang, B. and Starcher, K. (2019) Evaluation of wind and solar energy investments in Texas. *Renewable Energy*, 132: 1348–1359. doi:10.1016/j.renene.2018.09.037.

Chang, H., Chen, H., Shao, Z., et al. (2016) In situ fabrication of (Sr,La)FeO_4 with CoFe alloy nanoparticles as an independent catalyst layer for direct methane-based solid oxide fuel cells with a nickel cermet anode. *Journal of Materials Chemistry A*, 4 (36): 13997–14007. doi:10.1039/c6ta04639h.

Chang, R. (2008) General chemistry: the essential concepts. Boston: McGraw-Hill.

Chaudhary, V. and Sharma, S. (2017) An overview of ordered mesoporous material SBA-15: synthesis, functionalization and application in oxidation reactions. *Journal of Porous Materials*, 24 (3): 741–749. doi:10.1007/s10934-016-0311-z.

Chein, R.Y., Yu, C.T. and Wang, C.C. (2016) Numerical simulation on the effect of operating conditions and syngas compositions for synthetic natural gas production via methanation reaction. *Fuel*, 185: 394–409. doi:10.1016/j.fuel.2016.07.123.

Chen, D., Rebo, H.P., Moljord, K., et al. (1999) Methanol conversion to light olefins over SAPO-34. Sorption, diffusion, and catalytic reactions. *Industrial and Engineering Chemistry Research*, 38 (11): 4241–4249. doi:10.1021/ie9807046.

Chen, H.-W., Wang, C.-Y., Yu, C.-H., et al. (2004) Carbon dioxide reforming of methane reaction catalyzed by stable nickel copper catalysts. *Catalysis Today*, 97 (2–3): 173–180. doi:10.1016/j.cattod.2004.03.067.

Chen, W., Kimpel, T.F., Song, Y., et al. (2018) Influence of Carbon Deposits on the Cobalt-Catalyzed Fischer-Tropsch Reaction: Evidence of a Two-Site Reaction Model. *ACS Catalysis*, 8 (2): 1580–1590. doi:10.1021/acscatal.7b03639.

Cheng, C., Shen, D., Xiao, R., et al. (2017) Methanation of syngas (H_2/CO) over the different Ni-based catalysts. *Fuel*, 189: 419–427. Available at: https://www.sciencedirect.com/science/article/pii/S0016236116310894 (Accessed: 13 April 2019).

Cheng, Z., Wu, Q., Li, J., et al. (1996) Effects of promoters and preparation procedures on reforming of methane with carbon dioxide over Ni/Al_2O_3 catalyst. *Catalysis Today*, 30 (1–3): 147–155. doi:10.1016/0920-5861(95)00005-4.

Cheung, H., Bromley, L.A. and Wilke, C.R. (1962) Thermal conductivity of gas mixtures. *AIChE Journal*, 8 (2): 221–228. Available at: https://aiche.onlinelibrary.wiley.com/doi/10.1002/aic.690080219.

Chevalier, J., Gremillard, L., Virkar, A. V., et al. (2009) The tetragonal-monoclinic transformation in zirconia: Lessons learned and future trends. *Journal of the American Ceramic Society*, 92 (9): 1901–1920. doi:10.1111/j.1551-2916.2009.03278.x.

Cho, E.H., Park, Y.K., Park, K.Y., et al. (2022) Simultaneous impregnation of Ni and an additive via one-step melt-infiltration: Effect of alkaline-earth metal (Ca, Mg, Sr, and Ba) addition on Ni/γ-Al_2O_3 for CO_2 methanation. *Chemical Engineering Journal*, 428 (July 2021): 131393. doi:10.1016/j.cej.2021.131393.

Choi, C., Khuenpetch, A., Zhang, W., et al. (2021) Determination of kinetic parameters for CO_2 methanation (Sabatier reaction) over Ni/ZrO_2 at a stoichiometric feed-gas composition under elevated pressure. *Energy and Fuels*, 35 (24): 20216–20223. doi:10.1021/ACS.ENERGYFUELS.1C01534/ASSET/IMAGES/LARGE/EF1C01534_0008.JPEG.

Chuang, S.S.C. and Pien, S.I. (1992) Infrared study of the CO insertion reaction on reduced, oxidized, and sulfided Rh/SiO_2 catalysts. *Journal of Catalysis*, 135 (2): 618–634. doi:10.1016/0021-9517(92)90058-P.

Cimino, S., Boccia, F. and Lisi, L. (2020) Effect of alkali promoters (Li, Na, K) on the performance of Ru/Al_2O_3 catalysts for CO_2 capture and hydrogenation to methane. *Journal of CO_2 Utilization*, 37: 195–203. doi:10.1016/j.jcou.2019.12.010.

Comba, A., Baldi, A., Tempesta, R.M., et al. (2021) Do chemical-based bonding techniques affect the bond strength stability to cubic zirconia? *Materials*. 14 (14). doi:10.3390/ma14143920.

Cousland, G.P., Cui, X.Y., Ringer, S., et al. (2014) Electronic and vibrational properties of

yttria-stabilised zirconia from first-principles for 10–40 mol% Y_2O_3. *Journal of Physics and Chemistry of Solids*, 75 (11): 1252–1264. doi:10.1016/J.JPCS.2014.05.015.

Cui, Y., Chen, B., Xu, L., et al. (2023) CO_2 methanation over the Ni-based catalysts supported on the hollow ZSM-5 zeolites: Effects of the hollow structure and alkaline treatment. *Fuel*, 334 (P2): 126783. doi:10.1016/j.fuel.2022.126783.

Damyanova, S., Pawelec, B., Arishtirova, K., et al. (2009) The effect of CeO_2 on the surface and catalytic properties of Pt/CeO_2-ZrO_2 catalysts for methane dry reforming. *Applied Catalysis B: Environmental*, 89 (1–2): 149–159. doi:10.1016/j.apcatb.2008.11.035.

Daroughegi, R., Meshkani, F. and Rezaei, M. (2017) Enhanced activity of CO_2 methanation over mesoporous nanocrystalline Ni–Al_2O_3 catalysts prepared by ultrasound-assisted co-precipitation method. *International Journal of Hydrogen Energy*, 42 (22): 15115–15125. doi:10.1016/j.ijhydene.2017.04.244.

Daroughegi, R., Meshkani, F. and Rezaei, M. (2020) Characterization and evaluation of mesoporous high surface area promoted Ni- Al_2O_3 catalysts in CO_2 methanation. *Journal of the Energy Institute*, 93 (2): 482–495. doi:10.1016/j.joei.2019.07.003.

Daza, C.E., Gallego, J., Mondragón, F., et al. (2010) High stability of Ce-promoted Ni/Mg–Al catalysts derived from hydrotalcites in dry reforming of methane. *Fuel*, 89 (3): 592–603. doi:10.1016/j.fuel.2009.10.010.

Delgado, J.M.P.Q. (2006) A simple experimental technique to measure tortuosity in packed beds. *The Canadian Journal of Chemical Engineering*, 84 (December): 651–655.

Deraz, N.M. (2018a) The comparative jurisprudence of catalysts preparation methods: I. precipitation and impregnation methods. *Journal of Industrial and Environmental Chemistry*, 2 (1): 19–21.

Deraz, N.M. (2018b) The comparative jurisprudence of catalysts preparation methods: II. Deposition-precipitation and adsorption methods. *Journal of Industrial and Environmental Chemistry*, 2 (2): 1–3. Available at: http://www.alliedacademies.org/journal-industrial-environmental-chemistry/.

Dias, Y.R. and Perez-Lopez, O.W. (2023) CO_2 methanation over Ni-Al LDH-derived catalyst with variable Ni/Al ratio. *Journal of CO_2 Utilization*, 68 (December 2022): 102381. doi:10.1016/j.jcou.2022.102381.

Didenko, L.P., Sementsova, L.A., Chizhov, P.E., et al. (2019a) Pure hydrogen production by steam reforming of methane mixtures with various propane contents in a membrane

reactor with the industrial nickel catalyst and a Pd–Ru alloy foil. *International Journal of Hydrogen Energy*, 44 (48): 26396–26404. doi:10.1016/j.ijhydene.2019.08.083.

Didenko, L.P., Sementsova, L.A., Chizhov, P.E., et al. (2019b) Steam reforming of methane and its mixtures with propane in a membrane reactor with industrial nickel catalyst and palladium–ruthenium foil. *Petroleum Chemistry*, 59 (4): 394–404. doi:10.1134/S0965544119040054.

Dixon, A.G. (1997) Heat transfer in fixed beds at very low (<4) tube-to-particle diameter ratio. *Industrial & Engineering Chemistry Research*, 36 (8): 3053–3064. doi:Doi 10.1021/Ie9605950.

Dou, L., Fu, M., Gao, Y., et al. (2021) Efficient sulfur resistance of Fe, La and Ce doped hierarchically structured catalysts for low-temperature methanation integrated with electric internal heating. *Fuel*, 283 (August 2020): 118984. doi:10.1016/j.fuel.2020.118984.

Du, D., Wolf, M.J., Hermansson, K., et al. (2018) Screened hybrid functionals applied to ceria: Effect of Fock exchange. *Physical Review B*, 97 (23): 1–14. doi:10.1103/PhysRevB.97.235203.

Du, Z., Petru, C., Yang, X., et al. (2023) Development of stable $La_{0.9}Ce_{0.1}NiO_3$ perovskite catalyst for enhanced photothermochemical dry reforming of methane. *Journal of CO_2 Utilization*, 67 (September 2022): 102317. doi:10.1016/j.jcou.2022.102317.

Durmaz, T. (2018) The economics of CCS: Why have CCS technologies not had an international breakthrough? *Renewable and Sustainable Energy Reviews*, 95: 328–340. doi:10.1016/J.RSER.2018.07.007.

Duyar, M.S., Ramachandran, A., Wang, C., et al. (2015a) Kinetics of CO_2 methanation over $Ru/\gamma\text{-}Al_2O_3$ and implications for renewable energy storage applications. *Journal of CO_2 Utilization*, 12: 27–33. doi:10.1016/J.JCOU.2015.10.003.

Duyar, M.S., Treviño, M.A.A. and Farrauto, R.J. (2015b) Dual function materials for CO_2 capture and conversion using renewable H_2. *Applied Catalysis B: Environmental*, 168–169: 370–376. doi:10.1016/J.APCATB.2014.12.025.

Dwivedi, P. and Upadhyay, S. (1977) Particle-fluid mass transfer in fixed and fluidized beds. *Industrial & Engineering Chemistry Process Design and Development*, 16 (2): 157–165. doi:10.1021/i260062a001.

Edenhofer, O., Pichs-Madruga, R., Sokona, Y., Minx, J.C., Farahani, E., Kadner, S., Seyboth,

K. (2015) Climate change 2014 mitigation of climate change summary for policymakers and technical summary, working group III contribution to the fifth assessment report of the intergovernmental panel on climate change (IPCC). doi:10.1146/annurev-environ-021113-095626.

Eigenberger, G., Werther, J., Schoenfelder, H., et al. (2008) "Reaction engineering." In Gerhard Ertl, Helmut Knözinger, Ferdi Schüth, J.W. (ed.) *Handbook of Heterogeneous Catalysis*. 2nd Editio. John Wiley & Sons Inc. doi:https://doi.org/10.1002/9783527619474.ch10.

Eilers, H., González, M.I. and Schaub, G. (2016) Lab-scale experimental studies of Fischer–Tropsch kinetics in a three-phase slurry reactor under transient reaction conditions. *Catalysis Today*, 275: 164–171. doi:10.1016/j.cattod.2015.11.011.

El-Salamony, R.A., El-Sharaky, S.A., Al-Temtamy, S.A., et al. (2021) CO_2 valorization into synthetic natural gas (SNG) using a Co–Ni bimetallic Y_2O_3 based catalysts. *International Journal of Chemical Reactor Engineering*, 19 (6): 571–583. doi:10.1515/ijcre-2020-0163.

Energy Institute (2023) Statistical review of world energy. 72nd ed. Available at: https://www.energyinst.org/statistical-review.

Engelbrecht, N., Chiuta, S., Everson, R.C., et al. (2017) Experimentation and CFD modelling of a microchannel reactor for carbon dioxide methanation. *Chemical Engineering Journal*, 313: 847–857. doi:10.1016/j.cej.2016.10.131.

Erdőhelyi, A. (2020) Hydrogenation of carbon dioxide on supported rh catalysts. *Catalysts*, 10 (2): 155. doi:10.3390/catal10020155.

Erdöhelyi, A., Pásztor, M. and Solymosi, F. (1986) Catalytic hydrogenation of CO_2 over supported palladium. *Journal of Catalysis*, 98 (1): 166–177. doi:10.1016/0021-9517(86)90306-4.

Ermakova, M.A., Ermakov, D.Y., Plyasova, L.M., et al. (1999) XRD studies of evolution of catalytic nickel nanoparticles during synthesis of filamentous carbon from methane. *Catalysis Letters*, 62 (2–4): 93–97. doi:10.1023/A:1019079929435.

Ezzeddine, Z., Batonneau-gener, I. and Pouilloux, Y. (2023) Zinc removal from water via EDTA-modified mesoporous SBA-16 and SBA-15. *Toxics*, 11 (3): 205.

Fakeeha, A.H., Al Fatesh, A.S., Ibrahim, A.A., et al. (2021) yttria modified ZrO_2 supported Ni catalysts for CO_2 reforming of methane: The role of Ce promoter. *ACS Omega*, 6

(2): 1280–1288. doi:10.1021/acsomega.0c04731.

Falbo, L., Martinelli, M., Visconti, C.G., et al. (2018) Kinetics of CO_2 methanation on a Ru-based catalyst at process conditions relevant for power-to-gas applications. *Applied Catalysis B: Environmental*, 225 (December 2017): 354–363. doi:10.1016/j.apcatb.2017.11.066.

Fan, M., Jimenez, J.D., Shirodkar, S.N., et al. (2019) Atomic Ru immobilized on porous h-BN through simple vacuum filtration for highly active and selective CO_2 methanation. *ACS Catalysis*, 9 (11): 10077–10086. doi:10.1021/acscatal.9b02197.

Fan, Z., Wang, Y., Zhang, Y., et al. (2021) Influence of oxygen vacancy compensation on the structure, electronic and mechanical properties of yttrium stabilized tetragonal zirconia. *Materials Science in Semiconductor Processing*, 135 (July): 106082. doi:10.1016/j.mssp.2021.106082.

Felder, M.R. and Rousseau, W.R. (2005) *Elementary principles of chemical processes*. 3rd editio. Welter, J. and Rosado, J. (eds.). John Wiley & Sons Inc.

Feng, R., Liu, S., Bai, P., et al. (2014) Preparation and characterization of γ-Al_2O_3 with rich Brønsted acid sites and its application in the fluid catalytic cracking process. *Journal of Physical Chemistry C*, 118 (12): 6226–6234. doi:10.1021/jp411405r.

Feng, Z., Zhang, X. and Luo, D. (2022) Evolution and effect on electrolysis performance of pores in YSZ electrolyte films prepared by screen-printing. *Ceramics International*, (November). doi:10.1016/j.ceramint.2022.11.263.

Figueiredo, J.L. and Bernardo, C.A. (1990) "Filamentous carbon formation on metals and alloys." In Figueiredo, J.L., Bernardo, C.A., Baker, R.T.K., et al. (eds.) *Carbon Fibers Filaments and Composites*. Dordrecht: Springer Netherlands. pp. 441–457. doi:10.1007/978-94-015-6847-0_19.

Fogler, H.S. (2006) *Elements of Chemical Reaction Engineering*. 4th ed. Upper Saddle River, NJ, USA: Pearson Education.

da Fonseca, R.O., Ponseggi, A.R., Rabelo-Neto, R.C., et al. (2022) Controlling carbon formation over Ni/CeO_2 catalyst for dry reforming of CH_4 by tuning Ni crystallite size and oxygen vacancies of the support. *Journal of CO_2 Utilization*, 57 (November 2021). doi:10.1016/j.jcou.2021.101880.

Foo, S.Y., Cheng, C.K., Nguyen, T.H., et al. (2011) Evaluation of lanthanide-group promoters on Co-Ni/Al_2O_3 catalysts for CH_4 dry reforming. *Journal of Molecular*

Catalysis A: Chemical, 344 (1–2): 28–36. doi:10.1016/j.molcata.2011.04.018.

Frontera, P., Macario, A., Ferraro, M., et al. (2017) Supported catalysts for CO_2 methanation: A review. *Catalysts*. 7 (2) p. 59. doi:10.3390/catal7020059.

Fu, G., Jiang, M., Liu, J., et al. (2021) Rh/Al nanoantenna photothermal catalyst for wide-spectrum solar-driven CO_2 methanation with nearly 100% selectivity. *Nano Letters*, 21 (20): 8824–8830. doi:10.1021/acs.nanolett.1c03215.

Fu, P., Hu, S., Xiang, J., et al. (2012) Evaluation of the porous structure development of chars from pyrolysis of rice straw : Effects of pyrolysis temperature and heating rate. *Journal of Analytical and Applied Pyrolysis*, 98: 177–183. doi:10.1016/j.jaap.2012.08.005.

Fuller, E.N., Schettler, P.D. and Giddings, J.C. (1966) A new method for prediction of binary gas-phase diffusion coefficients. *Industrial and Engineering Chemistry*, 58 (5): 18–27. doi:10.1021/ie50677a007.

Fulvio, P.F., Pikus, S. and Jaroniec, M. (2005) Short-time synthesis of SBA-15 using various silica sources. *Journal of Colloid and Interface Science*, 287 (2): 717–720. doi:10.1016/j.jcis.2005.02.045.

Gac, W., Zawadzki, W., Rotko, M., et al. (2020) Effects of support composition on the performance of nickel catalysts in CO_2 methanation reaction. *Catalysis Today*, 357: 468–482. doi:10.1016/J.CATTOD.2019.07.026.

Gallucci, F., Comite, A., Capannelli, G., et al. (2006) Steam reforming of methane in a membrane reactor: An industrial case study. *Industrial and Engineering Chemistry Research*, 45 (9): 2994–3000. doi:10.1021/ie058063j.

Gamliel, D.P., Wilcox, L. and Valla, J.A. (2017) The effects of catalyst properties on the conversion of biomass via catalytic fast hydropyrolysis. *Energy and Fuels*, 31 (1): 679–687. doi:10.1021/acs.energyfuels.6b02781.

Gao, J., Liu, Q., Gu, F., et al. (2015) Recent advances in methanation catalysts for the production of synthetic natural gas. *RSC Advances*, 5 (29): 22759–22776. doi:10.1039/c4ra16114a.

Gao, M., Zhang, J., Zhu, P., et al. (2022) Unveiling the origin of alkali metal promotion in CO_2 methanation over Ru/ZrO_2. *Applied Catalysis B: Environmental*, 314 (January): 121476. doi:10.1016/j.apcatb.2022.121476.

Gao, Y., Golmakani, A., Nabavi, S.A., et al. (2021) Simulative optimization of catalyst configuration for biogas dry reforming. *International Journal of Hydrogen Energy*, 46

(24): 12835–12845. doi:10.1016/j.ijhydene.2021.01.059.

García-Bordejé, E., Dongil, A.B., Conesa, J.M., et al. (2022) Promotion of Ru or Ni on alumina catalysts with a basic metal for CO_2 hydrogenation: Effect of the type of metal (Na, K, Ba). *Nanomaterials*, 12 (7): 1–17. doi:10.3390/nano12071052.

Ghaani, M.R. and Catti, M. (2019) Investigation on the kinetic mechanism of the reduction of Fe_2O_3/CoO-decorated carbon xerogels: A non-isothermal study. *Journal of Solid State Chemistry*, 277: 368–375. doi:10.1016/J.JSSC.2019.06.034.

Ghaib, K., Nitz, K. and Ben-Fares, F.-Z. (2016) Chemical methanation of CO_2: A review. *ChemBioEng Reviews*, 3 (6): 266–275. doi:10.1002/cben.201600022.

Ghillanyova, K. and Galusek, D. (2011) "Ceramic oxides." In Riedel, R. and Chen, I.-W. (eds.) *Ceramics Science and Technology, Materials and Properties*. 2nd ed. John Wiley & Sons.

Gibbins, J., Chalmers, H. (2008) Carbon capture and storage. *Energy Policy*, 36: 4317–4322.

Gírio, F. (2019) "Innovation on bioenergy." In *The role of bioenergy in the bioeconomy*. Academic Press. pp. 405–433. doi:10.1016/B978-0-12-813056-8.00009-1.

Goodarzi, F., Kang, L., Wang, F.R., et al. (2018) Methanation of carbon dioxide over zeolite-encapsulated nickel nanoparticles. *ChemCatChem*, 10 (7): 1566–1570. doi:10.1002/cctc.201701946.

Götz, M., Lefebvre, J., Schollenberger, D., et al. (2014) Novel methanation concepts for the production of substitute natural gas. *International Gas Research Conference Proceedings*, 3 (January): 2313–2320.

Gregg, S.J. and Sing, K.S.W. (1982) *Adsorption, surface area and porosity*. 2nd ed. New York, USA: Academic Press, Inc.

Gudkov, S. V., Burmistrov, D.E., Smirnova, V. V., et al. (2022) A mini review of antibacterial properties of Al_2O_3 nanoparticles. *Nanomaterials*, 12 (15): 1–17. doi:10.3390/nano12152635.

Guo, M. and Lu, G. (2014) The difference of roles of alkaline-earth metal oxides on silica-supported nickel catalysts for CO_2 methanation. *RSC Advances*, 4 (102): 58171–58177. doi:10.1039/c4ra06202g.

Guo, W. and Chen, H. (2022) Mechanochemical synthesis of Ni-Y/CeO_2 catalyst for nonthermal plasma catalytic CO_2 methanation. *Industrial and Engineering Chemistry Research*, 61 (4): 1666–1674. doi:10.1021/acs.iecr.1c04456.

Hashemi, S.E., Lien, K.M., Hillestad, M., et al. (2021) Thermodynamic insight in design of methanation reactor with water removal considering nexus between CO_2 conversion and irreversibilities. *Energies*, 14 (23). doi:10.3390/en14237861.

Hasrack, G., Bacariza, M.C., Henriques, C., et al. (2022) On the effect of cobalt promotion over Ni/CeO_2 catalyst for CO_2 thermal and plasma assisted methanation. *Catalysts*, 12 (1): 21–24. doi:10.3390/catal12010036.

Hassanzadeh-Afruzi, F., Esmailzadeh, F., Asgharnasl, S., et al. (2022) Efficient removal of Pb(II)/Cu(II) from aqueous samples by a guanidine-functionalized SBA-15/Fe_3O_4. *Separation and Purification Technology*, 291 (March). doi:10.1016/j.seppur.2022.120956.

Hatta, A.H., Jalil, A.A., Hassan, N.S., et al. (2023) A short review on informetric analysis and recent progress on contribution of ceria in Ni-based catalysts for enhanced catalytic CO methanation. *Powder Technology*, 417 (January): 118246. doi:10.1016/j.powtec.2023.118246.

Hausfather, Z. (2023) State of the climate: 2023 now likely hottest year on record after extreme summer. Available at: https://www.carbonbrief.org/state-of-the-climate-2023-now-likely-hottest-year-on-record-after-extreme-summer/ (Accessed: 29 July 2023).

He, L., Chen, X., Ren, Y., et al. (2022a) Improving catalytic stability and coke resistance of Ni/Al_2O_3 catalysts with Ce promoter for relatively low temperature dry reforming of methane reaction. *Chemical Research in Chinese Universities*, 38 (4): 1032–1040. doi:10.1007/s40242-021-1281-5.

He, Y., Shen, H., Bai, Y., et al. (2022b) Construction of the low-loading Ni/CeO_2 catalyst with a boosted CO_2 methanation performance via the facile pyrolysis CeO_2 support. *Industrial and Engineering Chemistry Research*, 61 (43): 15948–15960. doi:10.1021/acs.iecr.2c02822.

He, Z., Wang, X., Gao, S., et al. (2015) Effect of reaction variables on CO methanation process over NiO–La_2O_3–MgO/Al_2O_3 catalyst for coal to synthetic natural gas. *Applied Petrochemical Research*, 5 (4): 413–417. doi:10.1007/s13203-015-0127-9.

Helveg, S., Sehested, J. and Rostrup-Nielsen, J.R. (2011) Whisker carbon in perspective. *Catalysis Today*, 178 (1): 42–46. doi:10.1016/j.cattod.2011.06.023.

Hemmingsson, F., Schaefer, A., Skoglundh, M., et al. (2020) CO_2 methanation over Rh/CeO_2 studied with infrared modulation excitation spectroscopy and phase sensitive detection.

Catalysts, 10 (6). doi:10.3390/catal10060601.

Hernandez Lalinde, J.A., Roongruangsree, P., Ilsemann, J., et al. (2020) CO_2 methanation and reverse water gas shift reaction. Kinetic study based on in situ spatially-resolved measurements. *Chemical Engineering Journal*, 390: 124629. doi:10.1016/j.cej.2020.124629.

Ho, P.H., de Luna, G.S., Angelucci, S., et al. (2020) Understanding structure-activity relationships in highly active La promoted Ni catalysts for CO_2 methanation. *Applied Catalysis B: Environmental*, 278 (April): 119256. doi:10.1016/j.apcatb.2020.119256.

Ho, S. Van and Harriott, P. (1980) The kinetics of methanation on nickel catalysts. *Journal of Catalysis*, 64 (2): 272–283. doi:10.1016/0021-9517(80)90502-3.

Hofer, T.S., Kilchert, F.M. and Tanjung, B.A. (2019) An effective partial charge model for bulk and surface properties of cubic ZrO_2, Y_2O_3 and yttrium-stabilised zirconia. *Phys. Chem. Chem. Phys*, 21: 25635. doi:10.1039/c9cp04307a.

Hongmanorom, P., Ashok, J., Zhang, G., et al. (2021) Enhanced performance and selectivity of CO_2 methanation over phyllosilicate structure derived Ni-Mg/SBA-15 catalysts. *Applied Catalysis B: Environmental*, 282 (September 2020): 119564. doi:10.1016/j.apcatb.2020.119564.

HORIBA Scientific (2022) *What is Raman Spectroscopy?* Available at: https://www.horiba.com/int/scientific/technologies/raman-imaging-and-spectroscopy/raman-spectroscopy/#:~:text=Raman Spectroscopy is a non,chemical bonds within a material.

Horowitz, C.A. (2016) Paris Agreement. *International Legal Materials*, 55 (4): 740–755. doi:10.1017/S0020782900004253.

Horváth, A., Stefler, G., Geszti, O., et al. (2011) Methane dry reforming with CO_2 on CeZr-oxide supported Ni, NiRh and NiCo catalysts prepared by sol-gel technique: Relationship between activity and coke formation. *Catalysis Today*, 169 (1): 102–111. doi:10.1016/j.cattod.2010.08.004.

Hossain, S., Akama, H., Verma, P., et al. (2023) Effect of twist angle in spiral-type Ru/CeO_2 catalysts on CO_2 auto-methanation performance. *Journal of Chemical Engineering of Japan*, 56 (1). doi:10.1080/00219592.2023.2182628.

Hou, T., Lei, Y., Zhang, S., et al. (2015) Ethanol dry reforming for syngas production over Ir/CeO_2 catalyst. *Journal of Rare Earths*, 33 (1): 42–45. doi:10.1016/S1002-

0721(14)60381-1.

Hou, Z., Chen, Y., Wang, C., et al. (2023) The promotional effects of Mn on Ni/SiO_2 catalysts for CO methanation. *Reaction Kinetics, Mechanisms and Catalysis*, (0123456789). doi:10.1007/s11144-023-02377-0.

Hu, D., Gao, J., Ping, Y., et al. (2012) Enhanced investigation of CO methanation over Ni/Al_2O_3 catalysts for synthetic natural gas production. *Industrial and Engineering Chemistry Research*, 51 (13): 4875–4886. doi:10.1021/ie300049f.

Hu, F., Ye, R., Jin, C., et al. (2022) Ni nanoparticles enclosed in highly mesoporous nanofibers with oxygen vacancies for efficient CO_2 methanation. *Applied Catalysis B: Environmental*, 317 (April): 121715. doi:10.1016/j.apcatb.2022.121715.

Hu, X., Zhang, L., Wang, W., et al. (2023) Mitochondria-targeted and multistage synergistic ROS-elevated drug delivery system based on surface decorated MnO_2 with CeO_2 for enhanced chemodynamic/chemotherapy. *Colloids and Surfaces A: Physicochemical and Engineering Aspects*, 656: 130495. doi:10.1016/j.colsurfa.2022.130495.

Huang, X., Ji, C., Wang, C., et al. (2017) Ordered mesoporous CoO-NiO-Al_2O_3 bimetallic catalysts with dual confinement effects for CO_2 reforming of CH_4. *Catalysis Today*, 281: 241–249. doi:10.1016/J.CATTOD.2016.02.064.

Huynh, H.L. and Yu, Z. (2020) CO_2 Methanation on hydrotalcite-derived catalysts and structured reactors: A Review. *Energy Technology*. doi:10.1002/ente.201901475.

Hybler, J. (1985) Phase-analysis utilizing the JCPDS powder diffraction file. *CHEMICKE LISTY*, 79 (11): 1121–1130.

Ibrahim, H.G., Alshuiref, A.A., Maraie, A.A., et al. (2016) Radial heat transport in packed beds-III : Correlations of effective transport parameters at high pressure. *International Journal of Engineering Science Invention*, 5 (5): 77–83.

IEA (2023) CO_2 emissions in 2022. Available at: https://www.iea.org/reports/co2-emissions-in-2022 (Accessed: 28 July 2023).

Ilsemann, J., Murshed, M.M., Gesing, T.M., et al. (2021) On the support dependency of the CO_2 methanation - decoupling size and support effects. *Catalysis Science and Technology*, 11 (12): 4098–4114. doi:10.1039/d1cy00399b.

Imperor-Clerc, M., Davidson, P. and Davidson, A. (2000) Existence of a microporous corona around the mesopores of silica-based SBA-15 materials templated by triblock copolymers. *Journal of the American Chemical Society*, 122 (48): 11925–11933.

doi:10.1021/ja002245h.

IPCC (2023) AR6 synthesis report: Climate change 2023. doi:10.4324/9781315071961-11.

Iruretagoyena, D., Huang, X., Shaffer, M.S.P., et al. (2015) Influence of alkali metals (Na, K, and Cs) on CO_2 adsorption by layered double oxides supported on graphene oxide. *Industrial and Engineering Chemistry Research*, 54 (46): 11610–11618. doi:10.1021/acs.iecr.5b02762.

Italiano, C., Ashraf, M.A., Pino, L., et al. (2018) Rh/CeO_2 thin catalytic layer deposition on alumina foams: Catalytic performance and controlling regimes in biogas reforming processes. *Catalysts*, 8 (10): 1–25. doi:10.3390/catal8100448.

Jacquemin, M., Beuls, A. and Ruiz, P. (2010) "Catalytic production of methane from CO_2 and H_2 at low temperature: Insight on the reaction mechanism." In *Catalysis Today*. 17 November 2010. Elsevier. pp. 462–466. doi:10.1016/j.cattod.2010.06.016.

Jana, P., De La Peña O'Shea, V.A., Coronado, J.M., et al. (2013) H_2 production by CH_4 decomposition over metallic cobalt nanoparticles: Effect of the catalyst activation. *Applied Catalysis A: General*, 467: 371–379. doi:10.1016/j.apcata.2013.08.004.

Jang, W.-J., Shim, J.-O., Kim, H.-M., et al. (2019) A review on dry reforming of methane in aspect of catalytic properties. *Catalysis Today*, 324: 15–26. doi:10.1016/J.CATTOD.2018.07.032.

JCPDS Powder Diffraction File (2000) *International Centre for Diffraction Data*. doi:10.6028/jres.101.027.

Jia, X., Zhang, X., Rui, N., et al. (2019) Structural effect of Ni/ZrO_2 catalyst on CO_2 methanation with enhanced activity. *Applied Catalysis B: Environmental*, 244 (November 2018): 159–169. doi:10.1016/j.apcatb.2018.11.024.

Jiang, H., Zhao, Y., Lin, J., et al. (2021) Highly-dispersed Pd nanoparticles on UiO-66 in assistance of supercritical fluid and its catalytic performance of CO_2 methanation. *Journal of Porous Materials*, 28 (6): 1737–1747. doi:10.1007/s10934-021-01117-w.

Jiang, L., Gonzalez-Diaz, A., Ling-Chin, J., et al. (2019) Post-combustion CO_2 capture from a natural gas combined cycle power plant using activated carbon adsorption. *Applied Energy*, 245: 1–15. doi:10.1016/J.APENERGY.2019.04.006.

Jiang, Y., Lang, J., Wu, X., et al. (2020) Electronic structure modulating for supported Rh catalysts toward CO_2 methanation. *Catalysis Today*, 356 (January): 570–578. doi:10.1016/j.cattod.2020.01.029.

Jlidi, M., Hamidi, F., Barambones, O., et al. (2023) An Artificial Neural Network for Solar Energy Prediction and Control Using Jaya-SMC. Electronics (Switzerland), 12 (3). doi:10.3390/electronics12030592.

Johansson, B. (1974) The α-γ transition in cerium is a mott transition. *Philosophical Magazine*, 30 (3): 469–482. doi:10.1080/14786439808206574.

Jomjaree, T., Sintuya, P., Srifa, A., et al. (2021) Catalytic performance of Ni catalysts supported on CeO_2 with different morphologies for low-temperature CO_2 methanation. *Catalysis Today*, 375 (November 2019): 234–244. doi:10.1016/j.cattod.2020.08.010.

Jordal, K., Anheden, M., Yan, J., et al. (2005) Oxyfuel combustion for coal-fired power generation with CO_2 capture-opportunities and challenges. *Greenhouse Gas Control Technologies*, 1: 201–209. Available at: https://www.sciencedirect.com/science/article/pii/B9780080447049500215 (Accessed: 25 June 2019).

Jung, S., Park, Y.-K. and Kwon, E.E. (2019) Strategic use of biochar for CO_2 capture and sequestration. *Journal of CO_2 Utilization*, 32: 128–139. doi:10.1016/j.jcou.2019.04.012.

Kakaei, K., Esrafili, M.D. and Ehsani, A. (2019) Chapter 1 - Introduction to Catalysis. *Interface Science and Technology*, 27: 1–21. doi:10.1016/B978-0-12-814523-4.00001-0.

Kalita, P., Ghosh, S., Gutierrez, G., et al. (2021) Grain size effect on the radiation damage tolerance of cubic zirconia against simultaneous low and high energy heavy ions: Nano triumphs bulk. *Scientific Reports*, 11 (1): 10886. doi:10.1038/s41598-021-90214-6.

Karakoyun, E.C., Avci, H., Kocaman, A.S., et al. (2023) Deviations from commitments: Markov decision process formulations for the role of energy storage. International Journal of Production Economics, 255 (November 2022): 108711. doi:10.1016/j.ijpe.2022.108711.

Kang, W.R. and Lee, K.B. (2013) Effect of operating parameters on methanation reaction for the production of synthetic natural gas. *Korean Journal of Chemical Engineering*, 30 (7): 1386–1394. doi:10.1007/s11814-013-0047-2.

Karelovic, A. and Ruiz, P. (2012) CO_2 hydrogenation at low temperature over Rh/γ-Al_2O_3 catalysts: Effect of the metal particle size on catalytic performances and reaction mechanism. *Applied Catalysis B: Environmental*, 113–114: 237–249.

doi:10.1016/j.apcatb.2011.11.043.

Karelovic, A. and Ruiz, P. (2013) Improving the hydrogenation function of Pd/γ-Al_2O_3 catalyst by Rh/γ-Al_2O_3 Addition in CO_2 methanation at low temperature. *ACS Catalysis*, 3 (12): 2799–2812. doi:10.1021/cs400576w.

Kesavan, J.K., Luisetto, I., Tuti, S., et al. (2018) Nickel supported on YSZ: The effect of Ni particle size on the catalytic activity for CO_2 methanation. *Journal of CO_2 Utilization*, 23: 200–211. doi:10.1016/j.jcou.2017.11.015.

Keshavarz, A.R., Rezaei, M. and Yaripour, F. (2010) Nanocrystalline gamma-alumina: A highly active catalyst for dimethyl ether synthesis. *Powder Technology*, 199 (2): 176–179. doi:10.1016/j.powtec.2010.01.003.

Kiewidt, L. and Thöming, J. (2015) Predicting optimal temperature profiles in single-stage fixed-bed reactors for CO_2-methanation. *Chemical Engineering Science*, 132: 59–71. doi:10.1016/j.ces.2015.03.068.

Kihlman, J. and Simell, P. (2022) Carbon formation in the reforming of simulated biomass gasification gas on nickel and rhodium catalysts. *Catalysts*, 12 (4): 410. doi:10.3390/catal12040410.

Kikuzono, Y., Kagami, S., Naito, S., et al. (1981) Selective hydrogenation of carbon monoxide on palladium catalysts. *Faraday Discussions of the Chemical Society*, 72: 135–143. doi:10.1039/DC9817200135.

Kim, A., Debecker, D.P., Devred, F., et al. (2018) CO_2 methanation on Ru/TiO_2 catalysts: On the effect of mixing anatase and rutile TiO_2 supports. *Applied Catalysis B: Environmental*, 220: 615–625. doi:10.1016/j.apcatb.2017.08.058.

Kim, J., Ha, H., Doh, W.H., et al. (2020) How Rh surface breaks CO_2 molecules under ambient pressure. *Nature Communications*, 11 (1): 5649. doi:10.1038/s41467-020-19398-1.

Kirchner, J., Baysal, Z. and Kureti, S. (2020) Activity and structural changes of Fe-based catalysts during CO_2 hydrogenation towards CH_4 – A mini review. *ChemCatChem*. 12 (4) pp. 981–988. doi:10.1002/cctc.201901956.

Kocs, E.A. (2017) The global carbon nation: Status of CO_2 capture, storage and utilization. *EPJ Web of Conferences*, 148: 00002. doi:10.1051/epjconf/201714800002.

Köpfle, N., Götsch, T., Grünbacher, M., et al. (2018) Zirconium-assisted activation of palladium to boost syngas production by methane dry reforming. *Angewandte Chemie*,

130 (44): 14823–14828. doi:10.1002/ange.201807463.

Kosaka, F., Yamaguchi, T., Ando, Y., et al. (2020) Effect of Ni content on CO_2 methanation performance with tubular-structured Ni-YSZ catalysts and optimization of catalytic activity for temperature management in the reactor. *International Journal of Hydrogen Energy*, 45 (23): 12911–12920. doi:10.1016/J.IJHYDENE.2020.02.221.

Koschany, F., Schlereth, D. and Hinrichsen, O. (2016) On the kinetics of the methanation of carbon dioxide on coprecipitated $NiAl(O)_x$. *Applied Catalysis B: Environmental*, 181: 504–516. doi:10.1016/j.apcatb.2015.07.026.

Kouva, S., Honkala, K., Lefferts, L., et al. (2015) Review: Monoclinic zirconia, its surface sites and their interaction with carbon monoxide. *Catalysis Science and Technology*, 5 (7): 3473–3490. doi:10.1039/c5cy00330j.

Koytsoumpa, E.I., Bergins, C. and Kakaras, E. (2018) The CO_2 economy: Review of CO_2 capture and reuse technologies. *Journal of Supercritical Fluids*, 132: 3–16. doi:10.1016/j.supflu.2017.07.029.

Kress, M.E. and Tielens, A.G.G.M. (2001) The role of Fischer-Tropsch catalysis in solar nebula chemistry. *Meteoritics and Planetary Science*, 36 (1): 75–91. doi:10.1111/j.1945-5100.2001.tb01811.x.

Krishnan J N, U., Jakka, S.C.B. and Jivanlal, S.A. (2023) Effective tri-metallic TiO_2 supported catalyst for hydrocarbon production from carbon dioxide. *Journal of the Indian Chemical Society*, 100 (1): 100859. doi:10.1016/j.jics.2022.100859.

Kristiani, A. and Takeishi, K. (2022) CO_2 methanation over nickel-based catalyst supported on yttria-stabilized zirconia. *Catalysis Communications*, 165: 106435. doi:10.1016/J.CATCOM.2022.106435.

Kustov, A.L., Frey, A.M., Larsen, K.E., et al. (2007) CO methanation over supported bimetallic Ni-Fe catalysts: From computational studies towards catalyst optimization. *Applied Catalysis A: General*, 320: 98–104. doi:10.1016/j.apcata.2006.12.017.

Kuznecova, I. and Gusca, J. (2017) "Property based ranking of CO and CO_2 methanation catalysts." In *Energy Procedia*. 2017. pp. 255–260. doi:10.1016/j.egypro.2017.09.068.

Lanatà, N., Yao, Y.X., Wang, C.Z., et al. (2013) γ-α Isostructural transition in cerium. *Physical Review Letters*, 111 (19): 1–5. doi:10.1103/PhysRevLett.111.196801.

Lanatà, N., Yao, Y.X., Wang, C.Z., et al. (2014) Interplay of spin-orbit and entropic effects in cerium. *Physical Review B - Condensed Matter and Materials Physics*, 90 (16): 1–4.

doi:10.1103/PhysRevB.90.161104.

Lavagna, M., Lacroix, C. and Cyrot, M. (1982) Volume collapse in the Kondo lattice. *Physics Letters A*, 90 (4): 210–212. doi:10.1016/0375-9601(82)90689-2.

Lázaro, M.J., Echegoyen, Y., Alegre, C., et al. (2008) TiO_2 as textural promoter on high loaded Ni catalysts for methane decomposition. *International Journal of Hydrogen Energy*, 33 (13): 3320–3329. doi:10.1016/j.ijhydene.2008.03.050.

Le, T.A., Kim, M.S., Lee, S.H., et al. (2017) CO and CO_2 methanation over supported Ni catalysts. *Catalysis Today*, 293–294: 89–96. doi:10.1016/j.cattod.2016.12.036.

Lechkar, A., Barroso Bogeat, A., Blanco, G., et al. (2018) Methanation of carbon dioxide over ceria-praseodymia promoted Ni-alumina catalysts. Influence of metal loading, promoter composition and alumina modifier. *Fuel*, 234: 1401–1413. doi:10.1016/j.fuel.2018.07.157.

Lee, C.J., Lee, D.H. and Kim, T. (2017) Enhancement of methanation of carbon dioxide using dielectric barrier discharge on a ruthenium catalyst at atmospheric conditions. *Catalysis Today*, 293–294: 97–104. doi:10.1016/J.CATTOD.2017.01.022.

Lee, H.H. (1980) Kinetics of sintering of supported metal catalysts: The mechanism of atom diffusion. *Journal of Catalysis*, 63 (1): 129–137. doi:10.1016/0021-9517(80)90066-4.

Lefebvre, J., Trudel, N., Bajohr, S., et al. (2018) A study on three-phase CO_2 methanation reaction kinetics in a continuous stirred-tank slurry reactor. *Fuel*, 217 (May 2017): 151–159. doi:10.1016/j.fuel.2017.12.082.

Leung, D.Y.C., Caramanna, G. and Maroto-Valer, M.M. (2014) An overview of current status of carbon dioxide capture and storage technologies. *Renewable and Sustainable Energy Reviews*, 39: 426–443. doi:10.1016/j.rser.2014.07.093.

Lewis, S.N. (2007) Toward cost-effective solar energy use. *Science*, 315 (5813): 798–801. doi:10.1126/science.1137014.

Li, B., Watanabe, R., Maruyama, K., et al. (2005) Effect of Ni Loading on catalyst bed temperature in oxidative steam reforming of methane over r-Al_2O_3-supported Ni Catalysts. *Ind. Eng. Chem. Res.*, 44: 485–494. doi:10.1016/j.cattod.2005.03.037.

Li, D., Ding, X., Liu, X., et al. (2023) CO_2 hydrogenation to methane over Ni/ZrO2 and Ni/CeO2 catalysts: experimental and DFT studies. *Journal of Materials Science*, 58 (31): 12584–12595. doi:10.1007/s10853-023-08814-8.

Li, H., Xia, P., Pan, S., et al. (2020) The advances of ceria nanoparticles for biomedical

applications in orthopaedics. *International Journal of Nanomedicine*, 15: 7199–7214. doi:10.2147/IJN.S270229.

Li, J., Zhang, C., Cheng, X., et al. (2013) Effects of alkaline-earth metals on the structure, adsorption and catalytic behavior of iron-based Fischer-Tropsch synthesis catalysts. *Applied Catalysis A: General*, 464–465: 10–19. doi:10.1016/j.apcata.2013.04.042.

Li, N., Zou, X., Liu, M., et al. (2017) Enhanced visible light photocatalytic hydrogenation of CO_2 into methane over a Pd/Ce-TiO_2 nanocomposition. *Journal of Physical Chemistry C*, 121 (46): 25795–25804. doi:10.1021/acs.jpcc.7b07298.

Li, Q., Li, Z., Du, Y., et al. (2012) Palladium nanoparticles supported on γ-Al_2O_3 for hydrogenation of 2-tertiary butyl anthraquinone to produce H_2O_2. *Journal of Dispersion Science and Technology*, 33 (5): 660–667. doi:10.1080/01932691.2011.579825.

Li, S., Xu, Y., Wang, H., et al. (2023a) Tuning the CO_2 hydrogenation selectivity of rhodium single-atom catalysts on zirconium dioxide with alkali ions. *Angewandte Chemie*, 300457. doi:10.1002/ange.202218167.

Li, W., Wang, H., Jiang, X., et al. (2018) A short review of recent advances in CO_2 hydrogenation to hydrocarbons over heterogeneous catalysts. *RSC Advances*, 8 (14): 7651–7669. doi:10.1039/c7ra13546g.

Li, X., Everitt, H.O. and Liu, J. (2019a) Confirming nonthermal plasmonic effects enhance CO_2 methanation on Rh/TiO_2 catalysts. *Nano Research*, 12 (8): 1906–1911. doi:10.1007/s12274-019-2457-x.

Li, Y., Liu, Z., Rao, Z., et al. (2022a) Experimental and theoretical insights into an enhanced CO_2 methanation mechanism over a Ru-based catalyst. *Applied Catalysis B: Environmental*, 319 (June): 121903. doi:10.1016/j.apcatb.2022.121903.

Li, Y., Zhang, H., Zhang, L., et al. (2019b) Bimetallic Ni-Pd/SBA-15 alloy as an effective catalyst for selective hydrogenation of CO_2 to methane. *International Journal of Hydrogen Energy*, 44 (26): 13354–13363. doi:10.1016/j.ijhydene.2019.03.276.

Li, Y., Zhang, X., Gao, S., et al. (2022b) synthesis of the CeO_2 support with a honeycomb-lantern-like structure and its application in dry reforming of methane based on the surface spatial confinement strategy. *Journal of Physical Chemistry C*, 127: 1032–1048. doi:10.1021/acs.jpcc.2c07401.

Li, Z., Bian, L., Zhu, Q., et al. (2014) Ni-based catalyst derived from Ni/Mg/Al hydrotalcite-like compounds and its activity in the methanation of carbon monoxide. *Kinetics and*

Catalysis, 55 (2): 217–223. doi:10.1134/s0023158414020049.

Li, Z., Deng, L., Kinloch, I.A., et al. (2023b) Raman spectroscopy of carbon materials and their composites: Graphene, nanotubes and fibres. *Progress in Materials Science*, 135 (February): 101089. doi:10.1016/j.pmatsci.2023.101089.

Li, Z., Zhang, B., Zhang, Z., et al. (2023c) Vitamin needed: Lanthanides in optoelectronic applications of metal halide perovskites. *Materials Science and Engineering R: Reports*, 152 (November 2022): 100710. doi:10.1016/j.mser.2022.100710.

Lian, Z., Olanrele, S.O., Si, C., et al. (2020) Critical role of interfacial sites between nickel and CeO_2 support in dry reforming of methane: Revisit of reaction mechanism and origin of stability. *Journal of Physical Chemistry C*, 124 (9): 5118–5124. doi:10.1021/acs.jpcc.9b09856.

Liang, C., Wei, T., Wang, H., et al. (2019) Impacts of La addition on formation of the reaction intermediates over alumina and silica supported nickel catalysts in methanation of CO_2. *Journal of the Energy Institute*. doi:10.1016/j.joei.2019.05.009.

Liang, L., Gu, W., Jiang, J., et al. (2022a) Effective CO_2 methanation over site-specified ruthenium nanoparticles loaded on TiO_2/palygorskite nanocomposite. *Journal of Colloid And Interface Science*, 623: 703–709. doi:10.1016/j.jcis.2022.05.071.

Liang, L., Miao, C., Chen, S., et al. (2022b) Effective CO_2 methanation at ambient pressure over Lanthanides (La/Ce/Pr/Sm) modified cobalt-palygorskite composites. *Journal of CO_2 Utilization*, 63 (June): 102114. doi:10.1016/j.jcou.2022.102114.

Liang, Z., Zhang, Y., Zhang, G., et al. (2023) Promotion effect of different lanthanide doping on Co/Al_2O_3 catalyst for dry reforming of methane. *International Journal of Hydrogen Energy*, (xxxx): 1–13. doi:10.1016/j.ijhydene.2023.01.301.

Lim, Y.J., McGregor, J., Sederman, A.J., et al. (2016) Kinetic studies of CO_2 methanation over a $Ni/\gamma\text{-}Al_2O_3$ catalyst using a batch reactor. *Chemical Engineering Science*, 141: 28–45. doi:10.1016/J.CES.2015.10.026.

Lin, F., Si, M., Lu, Y., et al. (2023) Surfactant-assisted impregnation of SBA-15 with highly dispersed copper species for CO oxidation. *Materials Letters*, 335 (January): 133825. doi:10.1016/j.matlet.2023.133825.

Lin, J., Ma, C., Wang, Q., et al. (2019) Enhanced low-temperature performance of CO_2 methanation over mesoporous $Ni/Al_2O_3\text{-}ZrO_2$ catalysts. *Applied Catalysis B: Environmental*, 243: 262–272. doi:10.1016/j.apcatb.2018.10.059.

Lin, K., Yang, X., Ma, X., et al. (2021) Efficient bimetal loaded (Rh-Ni)/αβ-Mo_xC catalyst for CO_2 methanation. *Journal of Chemical Sciences*, 133 (4): 1–8. doi:10.1007/s12039-021-01972-9.

Lin, S., Hao, Z., Shen, J., et al. (2021) Enhancing the CO_2 methanation activity of Ni/CeO_2 via activation treatment-determined metal-support interaction. *Journal of Energy Chemistry*, 59: 334–342. doi:10.1016/j.jechem.2020.11.011.

Lindorfer, J., Reiter, G., Tichler, R., et al. (2019) "Hydrogen fuel, fuel cells, and methane." In *Managing Global Warming*. Academic Press. pp. 419–453. doi:10.1016/b978-0-12-814104-5.00014-4.

Lindsay, A.L. and Bromley, L.A. (1950) Thermal conductivity of gas mixtures. *Industrial & Engineering Chemistry*, 42 (8): 1508–1511. doi:10.1002/aic.690080219.

Lindsey, R. (2023) Climate change: Atmospheric carbon dioxide. Available at: https://www.climate.gov/news-features/understanding-climate/climate-change-atmospheric-carbon-dioxide (Accessed: 28 July 2023).

Liu, G., Li, H., Zheng, H., et al. (2022a) Mechanism of in-situ formation of spinel and its effect on the mechanical properties of Al_2O_3–C refractories. *Ceramics International*, 49 (6): 9231–9238. doi:10.1016/j.ceramint.2022.11.087.

Liu, H., Wang, H., Shen, J., et al. (2008) Promotion effect of cerium and lanthanum oxides on Ni/SBA-15 catalyst for ammonia decomposition. *Catalysis Today*, 131 (1–4): 444–449. doi:10.1016/j.cattod.2007.10.048.

Liu, H., Wierzbicki, D., Debek, R., et al. (2016) La-promoted Ni-hydrotalcite-derived catalysts for dry reforming of methane at low temperatures. *Fuel*, 182: 8–16. doi:10.1016/j.fuel.2016.05.073.

Liu, Q. and Tian, Y. (2017) One-pot synthesis of NiO/SBA-15 monolith catalyst with a three-dimensional framework for CO_2 methanation. *International Journal of Hydrogen Energy*, 42 (17): 12295–12300. doi:10.1016/J.IJHYDENE.2017.02.070.

Liu, Q., Yang, H., Dong, H., et al. (2018) Effects of preparation method and Sm_2O_3 promoter on CO methanation by a mesoporous NiO-Sm_2O_3/Al_2O_3 catalyst. *New Journal of Chemistry*, 42 (15): 13096–13106. doi:10.1039/c8nj02282h.

Liu, S., Yao, P., Lin, Q., et al. (2021) Optimizing acid promoters of Ce-based NH3-SCR catalysts for reducing NOx emissions. *Catalysis Today*, 382 (January): 34–41. doi:10.1016/j.cattod.2021.05.007.

Liu, Y., Wang, X., Meng, X., et al. (2019) A review on tube external heat transfer for passive residual heat removal heat exchanger in nuclear power plant. *Applied Thermal Engineering*, 149 (November 2018): 1476–1491. doi:10.1016/j.applthermaleng.2018.11.114.

Liu, Z., Ding, X., Zhu, R., et al. (2022b) Investigation on the effect of highly active Ni/ZrO_2 catalysts modified by MgO-Nd_2O_3 promoters in CO_2 methanation at low temperature condition. *ChemistrySelect*, 7 (3): 202103774. doi:10.1002/slct.202103774.

Loccufier, E., Watson, G., Zhao, Y., et al. (2023) CO_2 methanation with Ru@MIL-101 nanoparticles fixated on silica nanofibrous veils as stand-alone structured catalytic carrier. *Applied Catalysis B: Environmental*, 320. doi:10.1016/j.apcatb.2022.121972.

Lopera, A.A., Chavarriaga, E.A., Perez-Taborda, J.A., et al. (2022) Effect of the fuel in the synthesis of NiO–YSZ by solution combustion synthesis with potential application in catalysis of hydrogen. *International Journal of Self-Propagating High-Temperature Synthesis*, 31 (2): 74–79. doi:10.3103/S1061386222020042.

López-Rodríguez, S., Davó-Quiñonero, A., Bailón-García, E., et al. (2021) Effect of Ru loading on Ru/CeO_2 catalysts for CO_2 methanation. *Molecular Catalysis*, 515. doi:10.1016/j.mcat.2021.111911.

Lopez, E., Gepert, V., Gritsch, A., et al. (2012) Ethanol steam reforming thermally coupled with fuel combustion in a parallel plate reactor. *Industrial and Engineering Chemistry Research*, 51 (11): 4143–4151. doi:10.1021/ie202364y.

Lorenz, H., Rameshan, C., Bielz, T., et al. (2013) From oxide-supported palladium to intermetallic palladium phases: Consequences for methanol steam reforming. *ChemCatChem*, 5 (6): 1273–1285. doi:10.1002/cctc.201200712.

Lu, B., Ju, Y., Abe, T., et al. (2015) Grafting Ni particles onto SBA-15, and their enhanced performance for CO_2 methanation. *RSC Advances*, 5 (70): 56444–56454. doi:10.1039/c5ra07461d.

Lu, N. and Xie, D. (2016) Novel membrane reactor concepts for hydrogen production from hydrocarbons: A review. *International Journal of Chemical Reactor Engineering*, 14 (1): 1–31. doi:10.1515/ijcre-2015-0050.

Luan, C., Zhang, A., Huang, W., et al. (2015) Catalytic dehydration of methanol to dimethyl ether over mesoporous γ-Al_2O_3. *Energy Sources, Part A: Recovery, Utilization and Environmental Effects*, 37 (21): 2285–2292. doi:10.1080/15567036.2012.699161.

Luo, L., Wang, M., Cui, Y., et al. (2020) Surface iron species in palladium–iron intermetallic nanocrystals that promote and stabilize CO_2 methanation. *Angewandte Chemie*, 132 (34): 14542–14550. doi:10.1002/ange.201916032.

Lv, Z., Chen, S., Huang, X., et al. (2023) Recent progress and perspective on integrated CO_2 capture and utilization. Current Opinion in Green and Sustainable Chemistry, 40: 100771. doi:10.1016/j.cogsc.2023.100771.

Ma, X., Huang, J., Ma, L., et al. (2023) Bandgap and defects regulation of $La_{2-x}A_xNi_{1-y}B_yO_{4+\delta}$ (A = K, Sr, B = Co, Mn) Ruddlesden-Popper type perovskites for efficient photocatalytic hydrogen evolution. *Separation and Purification Technology*, 311 (January): 123310. doi:10.1016/j.seppur.2023.123310.

Ma, Y., Liu, J., Chu, M., et al. (2019) Cooperation between active metal and basic support in ni-based catalyst for low-temperature CO_2 methanation. *Catalysis Letters*, 150 (5): 1418–1426. doi:10.1007/s10562-019-03033-w.

Ma, Y., Liu, J., Chu, M., et al. (2022) Enhanced low-temperature activity of CO_2 methanation over Ni/CeO_2 catalyst. *Catalysis Letters*, 152 (3): 872–882. doi:10.1007/s10562-021-03677-7.

Ma, Z., Ghosh, A., Asthana, N., et al. (2018) Visualization of structural changes during deactivation and regeneration of FAU zeolite for catalytic fast pyrolysis of lignin using NMR and electron microscopy techniques. *ChemCatChem*, 10 (19): 4431–4437. doi:10.1002/cctc.201800670.

Marconi, E., Tuti, S. and Luisetto, I. (2019) Structure-sensitivity of CO_2 methanation over nanostructured Ni supported on CeO_2 nanorods. *Catalysts*, 9 (4): 1–13. doi:10.3390/catal9040375.

Marocco, P., Morosanu, E.A., Giglio, E., et al. (2018) CO_2 methanation over Ni/Al hydrotalcite-derived catalyst: Experimental characterization and kinetic study. *Fuel*, 225 (August 2017): 230–242. doi:10.1016/j.fuel.2018.03.137.

Market Research Future (2023) *Methane market research report*. Available at: https://www.marketresearchfuture.com/reports/methane-market-7373 (Accessed: 20 October 2023).

Martin-del-Campo, J. and Kopyscinski, J. (2020) Working diagrams to identify the operating range of a bubbling fluidized bed reactor for the CO_2 methanation. *Canadian Journal of Chemical Engineering*, (September 2019): 1–10. doi:10.1002/cjce.23868.

Martin, N.M., Hemmingsson, F., Schaefer, A., et al. (2019) Structure-function relationship for CO_2 methanation over ceria supported Rh and Ni catalysts under atmospheric pressure conditions. *Catalysis Science and Technology*, 9 (7): 1644–1653. doi:10.1039/c8cy02097c.

Martin, N.M., Velin, P., Skoglundh, M., et al. (2017) Catalytic hydrogenation of CO_2 to methane over supported Pd, Rh and Ni catalysts. *Catalysis Science and Technology*, 7 (5): 1086–1094. doi:10.1039/c6cy02536f.

Martins, J., Batail, N., Silva, S., et al. (2015) CO_2 hydrogenation with shape-controlled Pd nanoparticles embedded in mesoporous silica: Elucidating stability and selectivity issues. *Catalysis Communications*, 58: 11–15. doi:10.1016/j.catcom.2014.08.027.

Marwood, M., Doepper, R., Prairie, M., et al. (1994) Transient drift spectroscopy for the determination of the surface reaction kinetics of CO_2 methanation. *Chemical Engineering Science*, 49 (24 Part A): 4801–4809. doi:10.1016/S0009-2509(05)80060-0.

Marwood, M., Doepper, R. and Renken, A. (1997) In-situ surface and gas phase analysis for kinetic studies under transient conditions The catalytic hydrogenation of CO_2. *Applied Catalysis A: General*, 151 (1): 223–246. doi:10.1016/S0926-860X(96)00267-0.

Mary Isabella Sonali, J., Kavitha, R., Kumar, P.S., et al. (2022) Application of a novel nanocomposite containing micro-nutrient solubilizing bacterial strains and CeO_2 nanocomposite as bio-fertilizer. *Chemosphere*, 286: 131800. doi:10.1016/J.CHEMOSPHERE.2021.131800.

Masson-Delmotte, V., Zhai, P., Pörtner, H.-O., et al. (2018) *Global warming of 1.5 °C An IPCC Special Report*. Available at: https://report.ipcc.ch/sr15/pdf/sr15_spm_final.pdf (Accessed: 26 April 2019).

McClure, S.M., Lundwall, M.J. and Goodman, D.W. (2011) Planar oxide supported rhodium nanoparticles as model catalysts. *Proceedings of the National Academy of Sciences of the United States of America*. 108 (3) pp. 931–936. doi:10.1073/pnas.1006635107.

Mears, D.E. (1971) Tests for transport limitations in experimental catalytic reactors. *Industrial and Engineering Chemistry - Process Design and Development*, 10 (4): 541–547. doi:10.1021/i260040a020.

Mebrahtu, C., Krebs, F., Abate, S., et al. (2019) CO_2 methanation: Principles and challenges Albonetti, S., Perathoner, S. and Quadrelli, E.A.B.T.-S. in S.S. and C. (eds.). *Studies in Surface Science and Catalysis*, 178: 85–103. doi:10.1016/B978-0-444-64127-4.00005-

7.

Meerten, R.Z.C. van, Beaumont, A.H.G.M., Nisselrooij, P.F.M.T. va., et al. (1983) Structure sensitivity and crystallite size change of nickel during methanation of CO/H_2 on nicke-silica catalysts. *Surface Science*, 135: 565–579.

Mekhilef, S., Saidur, R. and Safari, A. (2011) A review on solar energy use in industries. *Renewable and Sustainable Energy Reviews*, 15 (4): 1777–1790. doi:10.1016/j.rser.2010.12.018.

Mendoza-Núñez, E.M., Fierro-Gonzalez, J.C., Zepeda, T.A., et al. (2022) Effect of platinum addition on the reaction mechanism of the CO_2 methanation catalyzed by ZrO_2-supported Rh. *Molecular Catalysis*, 533 (November). doi:10.1016/j.mcat.2022.112801.

Meng, F., Li, X., Li, M., et al. (2017) Catalytic performance of CO methanation over La-promoted Ni/Al_2O_3 catalyst in a slurry-bed reactor. *Chemical Engineering Journal*, 313: 1548–1555. doi:10.1016/J.CEJ.2016.11.038.

Mentus, S., Jelić, D. and Grudić, V. (2007) Lanthanum nitrate decomposition by both temperature programmed heating and citrate gel combustion: Comparative study. *Journal of Thermal Analysis and Calorimetry*, 90 (2): 393–397. doi:10.1007/s10973-006-7603-5.

Merkache, R., Fechete, I., Maamache, M., et al. (2015) 3D ordered mesoporous Fe-KIT-6 catalysts for methylcyclopentane (MCP) conversion and carbon dioxide (CO_2) hydrogenation for energy and environmental applications. *Applied Catalysis A: General*, 504: 672–681. doi:10.1016/j.apcata.2015.03.032.

Miao, B., Ma, S.S.K., Wang, X., et al. (2016) Catalysis mechanisms of CO_2 and CO methanation. *Catalysis Science and Technology*, 6 (12): 4048–4058. doi:10.1039/c6cy00478d.

Miao, C., Shang, K., Liang, L., et al. (2022) Efficient and stable Ni/ZSM-5@MCM-41 catalyst for CO_2 methanation. *ACS Sustainable Chemistry and Engineering*, 10 (38): 12771–12782. doi:10.1021/acssuschemeng.2c03693.

Michalska, K., Kowalik, P., Próchniak, W., et al. (2019) Methanation at very low CO_x/H_2 Ratio: Effect of Ce on Ni–Ce–Al catalyst properties and empirical kinetics. *Catalysis Letters*, 149 (1): 338–346. doi:10.1007/s10562-018-2607-x.

Mihet, M., Dan, M., Barbu-tudoran, L., et al. (2021) CO_2 methanation using multimodal Ni/SiO_2 catalysts: Effect of support modification by MgO, CeO_2, and La_2O_3. *Catalysts*,

11 (4): 443.

Mihet, M. and Lazar, M.D. (2018) Methanation of CO_2 on Ni/γ-Al_2O_3: Influence of Pt, Pd or Rh promotion. *Catalysis Today*, 306: 294–299. doi:10.1016/j.cattod.2016.12.001.

Moeini, T. and Meshkani, F. (2023) Facile synthesis of M-$CuFe_2O_4$ (M= Al_2O_3, CeO_2, La_2O_3, ZrO_2, Mn_2O_3) catalysts using a one-pot method and their applications in high-temperature water gas shift reaction. *International Journal of Hydrogen Energy*, 48 (16): 6370–6383. doi:10.1016/j.ijhydene.2022.07.045.

Moghaddam, S.V., Rezaei, M., Meshkani, F., et al. (2018) Synthesis of nanocrystalline mesoporous Ni/Al_2O_3–SiO_2 catalysts for CO_2 methanation reaction. *International Journal of Hydrogen Energy*, 43 (41): 19038–19046. doi:10.1016/j.ijhydene.2018.08.163.

Mohammadi Ziarani, G., Tahmasebi Ashtiani, S., Mohajer, F., et al. (2023) Architecture of a functionalized SBA-15 (SBA-Pr-N-BFE) chemosensor for the detection of Fe^{3+} ions in aqueous media. *Inorganic Chemistry Communications*, 150 (October 2022): 110483. doi:10.1016/j.inoche.2023.110483.

Montini, T., Melchionna, M., Monai, M., et al. (2016) Fundamentals and catalytic applications of CeO_2-based materials. *Chemical Reviews*, 116 (10): 5987–6041. doi:10.1021/acs.chemrev.5b00603.

Morales-Zapata, M.A., Larrea, A. and Laguna-Bercero, M.A. (2023) Lanthanide nickelates for their application on solid oxide cells. *Electrochimica Acta*, 444 (January): 141970. doi:10.1016/j.electacta.2023.141970.

Mota, F.M. and Kim, D.H. (2019) From CO_2 methanation to ambitious long-chain hydrocarbons: Alternative fuels paving the path to sustainability. *Chemical Society Reviews*, 48 (1): 205–259. doi:10.1039/c8cs00527c.

Muroyama, H., Tsuda, Y., Asakoshi, T., et al. (2016) Carbon dioxide methanation over Ni catalysts supported on various metal oxides. *Journal of Catalysis*, 343: 178–184. doi:10.1016/j.jcat.2016.07.018.

Mutschler, R., Moioli, E., Luo, W., et al. (2018) CO_2 hydrogenation reaction over pristine Fe, Co, Ni, Cu and Al_2O_3 supported Ru: Comparison and determination of the activation energies. *Journal of Catalysis*, 366: 139–149. doi:10.1016/j.jcat.2018.08.002.

Naderi, M. (2015) Surface Area: Brunauer-Emmett-Teller (BET). *Progress in Filtration and Separation*, pp. 585–608. doi:10.1016/B978-0-12-384746-1.00014-8.

Nadolny, K. (2014) State of the art in production, properties and applications of the microcrystalline sintered corundum abrasive grains. *International Journal of Advanced Manufacturing Technology*, 74 (9–12): 1445–1457. doi:10.1007/s00170-014-6090-2.

Naeem, M.A., Al-Fatesh, A.S., Fakeeha, A.H., et al. (2014) Hydrogen production from methane dry reforming over nickel-based nanocatalysts using surfactant-assisted or polyol method. *International Journal of Hydrogen Energy*, 39 (30): 17009–17023. doi:10.1016/j.ijhydene.2014.08.090.

Nagaraju, N. and Raja Annamalai, A. (2019) An investigation of phase stability, thermal conductivity and fracture toughness of 8YSZ-La_2O_3 ceramics. *Materials Research Express*, 6 (7): 0–7. doi:10.1088/2053-1591/ab1603.

Najafi, S., Soltanali, S. and Nazemi, A.H. (2021) Effect of synthesis parameters on zirconia phases: Tetragonal or monoclinic? *ECS Journal of Solid State Science and Technology*, 10 (4): 043003. doi:10.1149/2162-8777/abf0e8.

Nakamura, J. and Toyoshima, I. (1988) Formation of carbidic and graphitic carbon from co on polycrystalline cobalt. *Surface Science*, 201: 185–194.

Nam, H., Kim, J.H., Kim, H., et al. (2021) CO_2 methanation in a bench-scale bubbling fluidized bed reactor using Ni-based catalyst and its exothermic heat transfer analysis. *Energy*, 214: 118895. doi:10.1016/j.energy.2020.118895.

Narksri, P., Angnanon, S., Guntasub, J., et al. (2022) Production of alternative liquid fuels from catalytic hydrocracking of plastics over Ni/SBA-15 catalyst. *Materials Today: Proceedings*, 57: 1040–1047. doi:10.1016/j.matpr.2021.09.048.

Natesakhawat, S., Oktar, O. and Ozkan, U.S. (2005a) Effect of lanthanide promotion on catalytic performance of sol-gel Ni/Al_2O_3 catalysts in steam reforming of propane. *Journal of Molecular Catalysis A: Chemical*, 241 (1–2): 133–146. doi:10.1016/j.molcata.2005.07.017.

Natesakhawat, S., Watson, R.B., Wang, X., et al. (2005b) Deactivation characteristics of lanthanide-promoted sol-gel Ni/Al_2O_3 catalysts in propane steam reforming. *Journal of Catalysis*, 234 (2): 496–508. doi:10.1016/j.jcat.2005.07.014.

NBC News (2021) *Greenhouse gas levels hit a new record, cuts fall short, U.N. finds*. Available at: https://www.nbcnews.com/science/environment/greenhouse-gas-levels-hit-new-record-cuts-fall-short-un-finds-rcna3728 (Accessed: 3 November 2021).

Ngo, S.I., Lim, Y. Il, Lee, D., et al. (2020) Flow behaviors, reaction kinetics, and optimal

design of fixed- and fluidized-beds for CO_2 methanation. *Fuel*, 275 (February): 117886. doi:10.1016/j.fuel.2020.117886.

Nguyen, H.T.T., Kumabe, Y., Ueda, S., et al. (2019) Highly durable Ru catalysts supported on CeO_2 nanocomposites for CO_2 methanation. *Applied Catalysis A: General*, 577: 35–43. doi:10.1016/j.apcata.2019.03.011.

Nirmal Kumar, S., Appari, S. and Kuncharam, B.V.R. (2021) Techniques for overcoming sulfur poisoning of catalyst employed in hydrocarbon reforming. *Catalysis Surveys from Asia*, 25 (4): 362–388. doi:10.1007/s10563-021-09340-w.

Nizio, M., Albarazi, A., Cavadias, S., et al. (2016) Hybrid plasma-catalytic methanation of CO_2 at low temperature over ceria zirconia supported Ni catalysts. *International Journal of Hydrogen Energy*, 41 (27): 11584–11592. doi:10.1016/J.IJHYDENE.2016.02.020.

NOAA (2023) 2022 was world's 6th-warmest year on record. Available at: https://www.noaa.gov/news/2022-was-worlds-6th-warmest-year-on-record#:~:text=Climate by the numbers,in the 1880-2022 record. (Accessed: 29 July 2023).

Oemar, U., Kathiraser, Y., Mo, L., et al. (2016) CO_2 reforming of methane over highly active La-promoted Ni supported on SBA-15 catalysts: mechanism and kinetic modelling. *Catalysis Science & Technology*, 6: 1173–1186. doi:10.1039/C5CY00906E.

Olajire, A.A. (2010) CO_2 capture and separation technologies for end-of-pipe applications – A review. *Energy*, 35 (6): 2610–2628. doi:10.1016/J.ENERGY.2010.02.030.

Olajire, A.A. (2013) A review of mineral carbonation technology in sequestration of CO_2. *Journal of Petroleum Science and Engineering*, 109: 364–392. doi:10.1016/j.petrol.2013.03.013.

Omoregbe, O., Danh, H.T., Nguyen-Huy, C., et al. (2017) Syngas production from methane dry reforming over Ni/SBA-15 catalyst: Effect of operating parameters. *International Journal of Hydrogen Energy*, 42 (16): 11283–11294. doi:10.1016/j.ijhydene.2017.03.146.

Onrubia-Calvo, J.A., Bermejo-López, A., Pereda-Ayo, B., et al. (2023) Ca doping effect on the performance of $La_{1-x}Ca_xNiO_3/CeO_2$-derived dual function materials for CO_2 capture and hydrogenation to methane. *Applied Catalysis B: Environmental*, 321 (July 2022). doi:10.1016/j.apcatb.2022.122045.

Onsan, Z.I. and Avci, A.K. (2016) “Catalytic reactor types and their industrial significance.” In *Multiphase catalytic reactors*. John Wiley & Sons Incorporated. pp. 3–16.

Pan, Y., Han, X., Chang, X., et al. (2023) Enhanced low-temperature CO_2 methanation over bimetallic Ni−Ru catalysts. *Industrial & Engineering Chemistry Research*, 2023 (1). doi:10.1021/acs.iecr.2c04560.

Panagiotopoulou, P. (2018) Methanation of CO_2 over alkali-promoted Ru/TiO_2 catalysts: II. Effect of alkali additives on the reaction pathway. *Applied Catalysis B: Environmental*, 236 (May): 162–170. doi:10.1016/j.apcatb.2018.05.028.

Panagiotopoulou, P., Kondarides, D.I. and Verykios, X.E. (2009) Selective methanation of CO over supported Ru catalysts. *Applied Catalysis B: Environmental*, 88 (3–4): 470–478. doi:10.1016/j.apcatb.2008.10.012.

Pandey, D. and Deo, G. (2016) Effect of support on the catalytic activity of supported Ni–Fe catalysts for the CO_2 methanation reaction. *Journal of Industrial and Engineering Chemistry*, 33: 99–107. doi:10.1016/J.JIEC.2015.09.019.

Pansambal, S., Oza, R., Borgave, S., et al. (2022) Bioengineered cerium oxide (CeO_2) nanoparticles and their diverse applications: a review. *Applied Nanoscience*, (0123456789). doi:10.1007/s13204-022-02574-8.

Park, J.N. and McFarland, E.W. (2009) A highly dispersed $Pd-Mg/SiO_2$ catalyst active for methanation of CO_2. *Journal of Catalysis*, 266 (1): 92–97. doi:10.1016/j.jcat.2009.05.018.

Pastor-Pérez, L., Patel, V., Le Saché, E., et al. (2020) CO_2 methanation in the presence of methane: Catalysts design and effect of methane concentration in the reaction mixture. *Journal of the Energy Institute*, 93 (1): 415–424. doi:10.1016/j.joei.2019.01.015.

Patterson, A.L. (1939) The scherrer formula for X-ray particle size determination. *Physical Review*, 56 (10): 978–982. doi:10.1103/PhysRev.56.978.

Pechimuthu, N.A., Pant, K.K. and Dhingra, S.C. (2007) Deactivation studies over $Ni-K/CeO_2-Al_2O_3$ catalyst for dry reforming of methane. *Industrial and Engineering Chemistry Research*, 46 (6): 1731–1736. doi:10.1021/ie061389n.

Perego, C. and Villa, P. (1997) Catalyst preparation methods. *Catalysis Today*, 34: 281–305. doi:10.1016/S0920-5861(96)00055-7.

Pérez, S., Aragón, J.J., Peciña, I., et al. (2019) Enhanced CO_2 Methanation by New Microstructured Reactor Concept and Design. *Topics in Catalysis*, 62 (5–6): 518–523.

doi:10.1007/s11244-019-01139-4.

Perry, R.H. and Green, D.W. (2008) *Perry's Chemical Engineers' Handbook*. 8th ed. McGraw-Hill Professional.

Pizzolato, M., Da, G., Ghedini, E., et al. (2023) Vanadium doped Ni/Al_2O_3: Efficient and coke resistant catalysts for methane dry reforming. *Catalysis Today*, 418 (December 2022): 114041. doi:10.1016/j.cattod.2023.114041.

Pour, N.A., Housaindokht, M.R., Zarkesh, J., et al. (2010) Studies of carbonaceous species in alkali promoted iron catalysts during Fischer-Tropsch synthesis. *Journal of Industrial and Engineering Chemistry*, 16 (6): 1025–1032. doi:10.1016/j.jiec.2010.09.003.

Pourmadadi, M., Farokh, A., Rahmani, E., et al. (2022) Porous alumina as potential nanostructures for drug delivery applications, synthesis and characteristics. *Journal of Drug Delivery Science and Technology*, 77 (September): 103877. doi:10.1016/j.jddst.2022.103877.

Pradhan, P., Mahajani, S.M. and Arora, A. (2018) Production and utilization of fuel pellets from biomass: A review. *Fuel Processing Technology*, 181: 215–232. doi:10.1016/J.FUPROC.2018.09.021.

Previtali, D., Longhi, M., Galli, F., et al. (2020) Low pressure conversion of CO_2 to methanol over Cu/Zn/Al catalysts. The effect of Mg, Ca and Sr as basic promoters. *Fuel*, 274 (April): 117804. doi:10.1016/j.fuel.2020.117804.

Qi, Y.Y., Niu, Z.W., Cheng, C., et al. (2013) Structural and elastic properties of Ce_2O_3 under pressure from LDA+U method. *Frontiers of Physics*, 8 (4): 405–411. doi:10.1007/s11467-013-0331-y.

Qin, Z., Wang, X., Dong, L., et al. (2019) CO_2 methanation on Co/TiO_2 catalyst: Effects of Y on the support. *Chemical Engineering Science*, 210: 115245. doi:10.1016/j.ces.2019.115245.

Qiu, H., Ran, J., Huang, X., et al. (2022) Unrevealing the influence that preparation and reaction parameters have on Ni/Al_2O_3 catalysts for dry reforming of methane. *International Journal of Hydrogen Energy*, 47 (80): 34066–34074. doi:10.1016/j.ijhydene.2022.08.014.

Qiu, M., Tao, H., Li, Y., et al. (2019) Insight into the mechanism of CO_2 and CO methanation over Cu(100) and Co-modified Cu(100) surfaces: A DFT study. *Applied Surface Science*, 495: 143457. doi:10.1016/j.apsusc.2019.07.199.

Quindimil, A., Onrubia-Calvo, J.A., Davó-Quiñonero, A., et al. (2022) Intrinsic kinetics of CO_2 methanation on low-loaded Ni/Al_2O_3 catalyst: Mechanism, model discrimination and parameter estimation. *Journal of CO_2 Utilization*, 57. doi:10.1016/j.jcou.2022.101888.

Quintana-Solórzano, R., Che-Galicia, G., Trejo-Reyes, M.L., et al. (2018) On the influence of particle shape and process conditions in the pressure drop and hydrodynamics in a wall-effect fixed bed. *Chemical Engineering Communications*, 205 (10): 1323–1341. doi:10.1080/00986445.2018.1448274.

Rahmani, S., Rezaei, M. and Meshkani, F. (2014a) Preparation of highly active nickel catalysts supported on mesoporous nanocrystalline γ-Al_2O_3 for CO_2 methanation. *Journal of Industrial and Engineering Chemistry*, 20 (4): 1346–1352. doi:10.1016/j.jiec.2013.07.017.

Rahmani, S., Rezaei, M. and Meshkani, F. (2014b) Preparation of promoted nickel catalysts supported on mesoporous nanocrystalline gamma alumina for carbon dioxide methanation reaction. *Journal of Industrial and Engineering Chemistry*, 20 (6): 4176–4182. doi:10.1016/j.jiec.2014.01.017.

Rahmat, N., Abdullah, A.Z. and Mohamed, A.R. (2010) A review: Mesoporous Santa Barbara amorphous-15, types, synthesis and its applications towards biorefinery production. *American Journal of Applied Sciences*, 7 (12): 1579–1586. doi:10.3844/ajassp.2010.1579.1586.

Raza, A., Gholami, R., Rezaee, R., et al. (2019) Significant aspects of carbon capture and storage – A review. *Petroleum*. doi:10.1016/j.petlm.2018.12.007.

Razzaq, R., Zhu, H., Jiang, L., et al. (2013) Catalytic methanation of CO and CO_2 in coke oven gas over Ni-Co/ZrO_2-CeO_2. *Industrial and Engineering Chemistry Research*, 52 (6): 2247–2256. doi:10.1021/ie301399z.

Ribeiro, P.C., Kiminami, R.H.G.A. and Costa, A.C.F.M. (2014) Nanosilica synthesized by the Pechini method for potential application as a catalytic support. *Ceramics International*, 40 (1 PART B): 2035–2039. doi:10.1016/j.ceramint.2013.07.115.

Ricca, C., Ringuedé, A., Cassir, M., et al. (2015) A comprehensive DFT investigation of bulk and low-index surfaces of ZrO_2 polymorphs. *Journal of Computational Chemistry*, 36 (1): 9–21. doi:10.1002/jcc.23761.

Robertson, B.A.J.B. and Thnard, L.J. (1975) The early history of catalysis. *Platinum Metals*

Rev., 19: 64–69.

Rönsch, S., Schneider, J., Matthischke, S., et al. (2016) Review on methanation – From fundamentals to current projects. *Fuel*, 166: 276–296. doi:10.1016/J.FUEL.2015.10.111.

Rosales-Asensio, E., Borge-Diez, D., Blanes-Peiró, J.-J., et al. (2019) Review of wind energy technology and associated market and economic conditions in Spain. *Renewable and Sustainable Energy Reviews*, 101: 415–427. doi:10.1016/j.rser.2018.11.029.

Ruckenstein, E. and Pulvermacher, B. (1973) Growth kinetics and the size distributions of supported metal crystallites. *Journal of Catalysis*, 29 (2): 224–245. doi:10.1016/0021-9517(73)90226-1.

Rynkowski, J.M., Paryjczak, T., Lewicki, A., et al. (2000) Characterization of Ru/CeO_2-Al_2O_3 catalysts and their Performance in CO_2 Methanation. *Reaction Kinetics and Catalysis Letters*, 71 (1): 55–64. doi:10.1023/A:1010326031095.

Ryoo, R., Ko, C.H., Kruk, M., et al. (2000) Block-copolymer-templated ordered mesoporous silica: Array of uniform mesopores or mesopore−micropore network? *The Journal of Physical Chemistry B*, 104 (48): 11465–11471. doi:10.1021/jp002597a.

Sabatier, P. and Senderens, J.B. (1902) "New methane synthesis." In *Comptes Rendus Des Séances De L'Académie Des Sciences, Section VI–Chimie*. Paris, 1902. Imprimerie Gauthier-Villars.

Saha, B., Singha, D., Das, T., et al. (2023) Tris(4-formyl phenyl)amine functionalized mesoporous silica for selective sensing of Al^{3+} and its separation. *Inorganica Chimica Acta*, 550 (October 2022): 121455. doi:10.1016/j.ica.2023.121455.

Sakpal, T. and Lefferts, L. (2018) Structure-dependent activity of CeO_2 supported Ru catalysts for CO_2 methanation. *Journal of Catalysis*, 367: 171–180. doi:10.1016/j.jcat.2018.08.027.

Salomão, R., Kawamura, M.A., Souza, A.D.V., et al. (2017) Hydratable alumina-bonded suspensions: Evolution of microstructure and physical properties during first heating. *InterCeram: International Ceramic Review*, 66 (7): 28–37. doi:10.1007/BF03401226.

Sanders, M., Fuss, S. and Engelen, P.J. (2013) Mobilizing private funds for carbon capture and storage: An exploratory field study in the Netherlands. *International Journal of Greenhouse Gas Control*, 19: 595–605. doi:10.1016/j.ijggc.2013.09.015.

Santos, L.F.S., de Jesus, R.A., Costa, J.A.S., et al. (2019) Evaluation of MCM-41 and MCM-

48 mesoporous materials as sorbents in matrix solid phase dispersion method for the determination of pesticides in soursop fruit (Annona muricata). *Inorganic Chemistry Communications*, 101: 45–51. doi:10.1016/J.INOCHE.2019.01.013.

Sathyaseelan, B., Baskaran, I., Krishnmoorthy, S., et al. (2022) Synthesis of Er_2O_3 blended CeO_2 nanocomposites and investigation of their biomedical applications. *Chemical Physics Impact*, 6 (February): 100167. doi:10.2139/ssrn.4214036.

Schlereth, D., Donaubauer, P.J. and Hinrichsen, O. (2015) Metallic honeycombs as catalyst supports for methanation of carbon dioxide. *Chemical Engineering and Technology*, 38 (10): 1845–1852. doi:10.1002/ceat.201400717.

Schlögl, R. (2015) Heterogeneous catalysis. *Angewandte Chemie - International Edition*, 54 (11): 3465–3520. doi:10.1002/anie.201410738.

Schneider, S.H. (1988) The greenhouse effect: science and ecology. *Science*, 243 (4892): 771–782. Available at: http://science.sciencemag.org/ (Accessed: 25 April 2019).

Schwarz, J.A., Contescu, C. and Contescu, A. (1995) Methods for Preparation of Catalytic Materials. *Chemical Reviews*, 95 (3): 477–510. doi:10.1021/cr00035a002.

von Seckendorff, J. and Hinrichsen, O. (2021) Review on the structure of random packed-beds. *Canadian Journal of Chemical Engineering*, 99 (S1): S703–S733. doi:10.1002/cjce.23959.

Seddighi, S., Clough, P.T., Anthony, E.J., et al. (2018) Scale-up challenges and opportunities for carbon capture by oxy-fuel circulating fluidized beds. *Applied Energy*, 232: 527–542. doi:10.1016/J.APENERGY.2018.09.167.

Serrer, M.A., Stehle, M., Schulte, M.L., et al. (2021) Spatially-resolved insights into local activity and structure of Ni-based CO_2 methanation catalysts in fixed-bed reactors. ChemCatChem, 13 (13): 3010–3020. doi:10.1002/cctc.202100490.

Şen, Z. (2004) Solar energy in progress and future research trends. *Progress in Energy and Combustion Science*, 30 (4): 367–416. doi:10.1016/J.PECS.2004.02.004.

Shackelford, J.F. and Doremus, R.H. (2008) *Ceramic and glass materials: Structure, properties and processing*. New York: Springer. doi:10.1007/978-0-387-73362-3.

Shafiee, P., Alavi, S.M., Rezaei, M., et al. (2022) Promoted Ni–Co–Al_2O_3 nanostructured catalysts for CO_2 methanation. *International Journal of Hydrogen Energy*, 47 (4): 2399–2411. doi:10.1016/j.ijhydene.2021.10.197.

Shah, H.U.W., Yasmeen, R., Sarfraz, M., et al. (2023) The repercussions of economic

growth, industrialization, foreign direct investment, and technology on municipal solid waste: evidence from OECD economies. Sustainability, 15: 836.

Shahid, M., He, C., Sankarasubramanian, S., et al. (2020) Co_3O_4-Impregnated NiO-YSZ: An Efficient Catalyst for Direct Methane Electrooxidation. *ACS Applied Materials and Interfaces*, 12 (29): 32578–32590. doi:10.1021/acsami.0c06407.

Shakir, M.D., Sengupta, S., Sinhamahapatra, A., et al. (2022) B-Ni/$MgAl_2O_4$ catalyzed dry reforming of methane: The role of boron to resist the formation of graphitic carbon. *Fuel*, 320 (March): 123950. doi:10.1016/j.fuel.2022.123950.

Shao, X., Bu, W., Fan, Y., et al. (2020) High-precision cerium isotope analysis by thermal ionization mass spectrometry using the Ce^+ technique. *Journal of Analytical Atomic Spectrometry*, 35 (3): 467–477. doi:10.1039/c9ja00420c.

Sheikh, H.M., Ullah, A., Hong, K., et al. (2018) Thermo-economic analysis of integrated gasification combined cycle (IGCC) power plant with carbon capture. *Chemical Engineering and Processing - Process Intensification*, 128: 53–62. doi:10.1016/J.CEP.2018.04.007.

Shen, W., Zhang, Y., Zhao, L., et al. (2021) Micro-scale simulation and intensification of complex Sabatier reaction system in cylindrical catalyst bed. *Fuel*, 287: 119399. doi:10.1016/j.fuel.2020.119399.

Shi, Q. and Wu, J. (2021) Review on sulfur compounds in petroleum and its products: State-of-the-Art and perspectives. *Energy and Fuels*, 35 (18): 14445–14461. doi:10.1021/acs.energyfuels.1c02229.

Shi, Z., Wan, C., Huang, M., et al. (2020) Characterization and catalytic behavior of hydrotalcite-derived Ni-Al catalysts for methane decomposition. *International Journal of Hydrogen Energy*, 45 (35): 17299–17310. doi:10.1016/j.ijhydene.2020.04.141.

Shivakumar, R. and Maitra, S. (2023) “Micromorphology and pore size evaluation of biomass chars during pyrolysis.” In Chinthapudi, E., Basu, S. and Thorat, B.N. (eds.) *Sustainable Chemical, Mineral and Material Processing*. Lecture No. Springer, Singapore. pp. 226–234. doi:10.1007/978-981-19-7264-5_17.

Shoaib, M., Siddiqui, I., Rehman, S., et al. (2019) Assessment of wind energy potential using wind energy conversion system. *Journal of Cleaner Production*, 216: 346–360. doi:10.1016/j.jclepro.2019.01.128.

Siakavelas, G.I., Charisiou, N.D., AlKhoori, A., et al. (2021) Highly selective and stable

Ni/La-M (M=Sm, Pr, and Mg)-CeO_2 catalysts for CO_2 methanation. *Journal of CO_2 Utilization*, 51 (May): 101618. doi:10.1016/j.jcou.2021.101618.

Siakavelas, G.I., Charisiou, N.D., AlKhoori, A., et al. (2022) Cerium oxide catalysts for oxidative coupling of methane reaction: Effect of lithium, samarium and lanthanum dopants. *Journal of Environmental Chemical Engineering*, 10 (2): 107259. doi:10.1016/j.jece.2022.107259.

Siang, T.J., Jalil, A.A., Fatah, N.A.A., et al. (2021) Tailoring Rh content on dendritic fibrous silica alumina catalyst for enhanced CO_2 capture in catalytic CO_2 methanation. *Journal of Environmental Chemical Engineering*, 9 (1): 104616. doi:10.1016/j.jece.2020.104616.

Sietsma, J.R.A., Friedrich, H., Broersma, A., et al. (2008) How nitric oxide affects the decomposition of supported nickel nitrate to arrive at highly dispersed catalysts. *Journal of Catalysis*, 260 (2): 227–235. doi:10.1016/j.jcat.2008.10.007.

Sing, K.S.W., Everett, D.H., Haul, R.A.W., et al. (1985) Reporting physisorption data for gas/solid systems with special reference to the determination of surface area and porosity. Pure and Applied Chemistry, 57 (4): 603–619. doi:10.1351/pac198557040603.

Singh, P.S. (2008) High surface area nanoporous amorphous silica prepared by dodecanol assisted silica formate sol-gel approach. *Journal of Colloid and Interface Science*, 325 (1): 207–214. doi:10.1016/j.jcis.2008.05.037.

Skorodumova, N. V, Simak, S.I., Lundqvist, B.I., et al. (2002) Quantum origin of the oxygen storage capability of ceria. *Physical Review Letters*, 89 (16): 14–17. doi:10.1103/PhysRevLett.89.166601.

Solangi, K.H., Islam, M.R., Saidur, R., et al. (2011) A review on global solar energy policy. *Renewable and Sustainable Energy Reviews*, 15 (4): 2149–2163. doi:10.1016/J.RSER.2011.01.007.

Solano–Olivares, K., Romero, R.J., Santoyo, E., et al. (2019) Life cycle assessment of a solar absorption air-conditioning system. *Journal of Cleaner Production*, 240: 118206. doi:10.1016/j.jclepro.2019.118206.

Solis-Garcia, A. and Fierro-Gonzalez, J.C. (2019) Mechanistic insights into the CO_2 methanation catalyzed by supported metals: A Review. *Journal of Nanoscience and Nanotechnology*. 19 (6) pp. 3110–3123. Available at:

https://www.ingentaconnect.com/content/asp/jnn/2019/00000019/00000006/art00005.

Solymosi, F., Erdöhelyi, A. and Kocsis, M. (1981) Methanation of CO_2 on supported Ru catalysts. *Journal of the Chemical Society, Faraday Transactions 1: Physical Chemistry in Condensed Phases*, 77 (5): 1003–1012. doi:10.1039/F19817701003.

Song, Q., Ran, R., Wu, X., et al. (2023) Dry reforming of methane over Ni catalysts supported on micro- and mesoporous silica. *Journal of CO_2 Utilization*, 68 (September 2022): 102387. doi:10.1016/j.jcou.2022.102387.

de Souza, E.F. and Appel, L.G. (2021) Oxygen vacancy formation and their role in the CO_2 activation on Ca doped ZrO_2 surface: An ab-initio DFT study. *Applied Surface Science*, 553: 149589. doi:10.1016/j.apsusc.2021.149589.

Spigarelli, B.P. and Kawatra, S.K. (2013) Opportunities and challenges in carbon dioxide capture. *Journal of CO_2 Utilization*, 1: 69–87. doi:10.1016/j.jcou.2013.03.002.

Sreedhar, I., Varun, Y., Singh, S.A., et al. (2019) Developmental trends in CO_2 methanation using various catalysts. *Catalysis Science & Technology*, 9 (17): 4478–4504. doi:10.1039/c9cy01234f.

Stangeland, K., Kalai, D., Li, H., et al. (2017a) "CO_2 methanation: The effect of catalysts and reaction conditions." In *Energy Procedia*. 2017. The Author(s). pp. 2022–2027. doi:10.1016/j.egypro.2017.03.577.

Stangeland, K., Kalai, D., Li, H., et al. (2017b) The effect of temperature and initial methane concentration on carbon dioxide methanation on Ni based catalysts. *Energy Procedia*, 105 (1876): 2016–2021. doi:10.1016/j.egypro.2017.03.576.

Stanger, R., Wall, T., Spörl, R., et al. (2015) Oxyfuel combustion for CO_2 capture in power plants. *International Journal of Greenhouse Gas Control*, 40: 55–125. doi:10.1016/J.IJGGC.2015.06.010.

Stanke, A. and Kampars, V. (2022) Agglomeration of Fe/SBA-15 with clays for Fischer–Tropsch synthesis. *Energy Reports*, 8: 461–466. doi:10.1016/j.egyr.2022.10.251.

Stiegler, T., Meltzer, K., Tremel, A., et al. (2019) Development of a structured reactor system for CO_2 methanation under dynamic operating conditions. *Energy Technology*, 7 (6): 1–12. doi:10.1002/ente.201900047.

Su, X., Xu, J., Liang, B., et al. (2016) Catalytic carbon dioxide hydrogenation to methane: A review of recent studies. *Journal of Energy Chemistry*. 25 (4) pp. 553–565. doi:10.1016/j.jechem.2016.03.009.

Sugiawan, Y. and Managi, S. (2019) New evidence of energy-growth nexus from inclusive wealth. *Renewable and Sustainable Energy Reviews*. 103 pp. 40–48. doi:10.1016/j.rser.2018.12.044.

Sun, C., Li, H. and Chen, L. (2012) Nanostructured ceria-based materials: Synthesis, properties, and applications. *Energy and Environmental Science*, 5 (9): 8475–8505. doi:10.1039/c2ee22310d.

Sun, C., Świrk, K., Wang, Y., et al. (2022a) Unraveling catalytic properties by yttrium promotion on mesoporous SBA-16 supported nickel catalysts towards CO_2 methanation. *Fuel*, 317 (October 2021). doi:10.1016/j.fuel.2021.122829.

Sun, L., Xiao, W., Hao, X., et al. (2019) A first-principles study on the structural, thermal and electronic properties of cerium oxides by using different functional. *Electronic Structure*, 1 (1). doi:10.1088/2516-1075/aae6f2.

Sun, S., Sun, H., Guan, S., et al. (2022b) Integrated CO_2 capture and methanation on Ru/CeO_2-MgO combined materials: Morphology effect from CeO_2 support. *Fuel*, 317: 123420. doi:10.1016/J.FUEL.2022.123420.

Swaan, H.M., Kroll, V.C.H., Martin, G.A., et al. (1994) Deactivation of supported nickel catalysts during the reforming of methane by carbon dioxide. *Catalysis Today*, 21 (2–3): 571–578. doi:10.1016/0920-5861(94)80181-9.

Swart, J.C.W., Ciobîcă, I.M., Van Santen, R.A., et al. (2008) Intermediates in the formation of graphitic carbon on a flat FCC-Co(111) surface. *Journal of Physical Chemistry C*, 112 (33): 12899–12904. doi:10.1021/jp803305s.

Tada, S., Shimizu, T., Kameyama, H., et al. (2012) Ni/CeO_2 catalysts with high CO_2 methanation activity and high CH_4 selectivity at low temperatures. *International Journal of Hydrogen Energy*, 37 (7): 5527–5531. doi:10.1016/J.IJHYDENE.2011.12.122.

Tadepalli, S., Halder, R. and Lawal, A. (2007) Catalytic hydrogenation of o-nitroanisole in a microreactor: Reactor performance and kinetic studies. *Chemical Engineering Science*, 62 (10): 2663–2678. doi:10.1016/j.ces.2006.12.058.

Takahara, I., Murata, K., Sato, K., et al. (2013) Activity and deactivation nature of Ru/MnCO3 catalysts for Fischer-Tropsch reaction. *Applied Catalysis A: General*, 450: 80–87. doi:10.1016/j.apcata.2012.10.026.

Takenaka, S., Ogihara, H. and Otsuka, K. (2002) Structural change of Ni species in Ni/SiO_2

catalyst during decomposition of methane. *Journal of Catalysis*, 208 (1): 54–63. doi:10.1006/jcat.2002.3523.

Tang, R., Ullah, N., Hui, Y., et al. (2021a) Enhanced CO_2 methanation activity over Ni/CeO_2 catalyst by one-pot method. *Molecular Catalysis*, 508 (April): 111602. doi:10.1016/j.mcat.2021.111602.

Tang, R., Ullah, N. and Li, Z. (2023) Unveiling the promotion effect of Zr species on SBA-15 supported nickel catalysts for CO_2 methanation. *International Journal of Hydrogen Energy*, 48 (12): 4694–4707. doi:10.1016/j.ijhydene.2022.11.011.

Tang, Y., Men, Y., Liu, S., et al. (2021b) Morphology-dependent support effect of Ru/MnOx catalysts on CO_2 methanation. *Colloids and Surfaces A: Physicochemical and Engineering Aspects*, 630 (September): 127636. doi:10.1016/j.colsurfa.2021.127636.

The Business Research Company (2023) *Methane global market report*. Available at: https://www.thebusinessresearchcompany.com/report/methane-global-market-report (Accessed: 20 October 2023).

Thema, M., Bauer, F. and Sterner, M. (2019) Power-to-Gas: Electrolysis and methanation status review. *Renewable and Sustainable Energy Reviews*. 112 pp. 775–787. doi:10.1016/j.rser.2019.06.030.

Thommes, M., Kaneko, K., Neimark, A. V., et al. (2015) Physisorption of gases, with special reference to the evaluation of surface area and pore size distribution (IUPAC Technical Report). *Pure and Applied Chemistry*, 87 (9–10): 1051–1069. doi:10.1515/PAC-2014-1117/PDF.

Tibbetts, G.G. (1984) Why are carbon filaments tubular? *Journal of Crystal Growth*, 66 (3): 632–638. doi:10.1016/0022-0248(84)90163-5.

Tichler, R. and Bauer, S. (2016) "Power-to-Gas." In *Storing Energy: With Special Reference to Renewable Energy Sources*. Elsevier Inc. pp. 373–389. doi:10.1016/B978-0-12-803440-8.00018-X.

Tobias, G., Shao, L., Salzmann, C.G., et al. (2006) Purification and opening of carbon nanotubes using steam. *Journal of Physical Chemistry B*, 110 (45): 22318–22322. doi:10.1021/jp0631883.

Traitangwong, A., Guo, X., Meeyoo, V., et al. (2020) XNi/$Ni_{0.05}Ce_{0.20}Zr_{0.75}O_2$ Solid Solution over a CO_2 Methanation Reaction. *Industrial and Engineering Chemistry Research*, 59 (30): 13440–13449.

doi:10.1021/ACS.IECR.0C01526/ASSET/IMAGES/LARGE/IE0C01526_0008.JPEG.

Tsiotsias, A.I., Charisiou, N.D., AlKhoori, A., et al. (2022) Optimizing the oxide support composition in Pr-doped CeO_2 towards highly active and selective Ni-based CO_2 methanation catalysts. *Journal of Energy Chemistry*, 71: 547–561. doi:10.1016/j.jechem.2022.04.003.

Tu, B., Su, X., Yin, Y., et al. (2020) Methane conversion reactions over LaNi-YSZ and Ni-YSZ anodes of solid oxide fuel cell. *Fuel*, 278 (April): 118273. doi:10.1016/j.fuel.2020.118273.

Türks, D., Mena, H., Armbruster, U., et al. (2017) Methanation of CO_2 on Ni/Al_2O_3 in a structured fixed-bed reactor—A scale-up study. Catalysts, 7 (5): 152. doi:10.3390/catal7050152.

Ulagesan, S., Santhamoorthy, M., Tuong Vy Phan, T., et al. (2022) Mesoporous silica (SBA-15) with enriched amidoxime functionalities for pH-controlled anticancer drug delivery. *Inorganic Chemistry Communications*, 146 (October): 1–6. doi:10.1016/j.inoche.2022.110132.

UN News (2023) Hottest July ever signals 'era of global boiling has arrived' says UN chief. Available at: https://news.un.org/en/story/2023/07/1139162 (Accessed: 27 July 2023).

Valizadeh, S., Khani, Y., Yim, H., et al. (2023) H_2 generation from steam gasification of swine manure over nickel-loaded perovskite oxides catalysts. *Environmental Research*, 219 (December 2022): 115070. doi:10.1016/j.envres.2022.115070.

Vanzan, M., Marsili, M. and Corni, S. (2021) Study of the rate-determining step of Rh catalyzed CO_2 reduction: Insight on the hydrogen assisted molecular dissociation. *Catalysts*, 11 (5): 538. doi:10.3390/catal11050538.

Varvoutis, G., Lampropoulos, A., Oikonomou, P., et al. (2023) Fabrication of highly active and stable Ni CeO_2-nanorods wash-coated on ceramic NZP structured catalysts for scaled-up CO_2 methanation. *Journal of CO_2 Utilization*, 70 (February): 102425. doi:10.1016/j.jcou.2023.102425.

Villarba, M. and Jónsson, H. (1994) Diffusion mechanisms relevant to metal crystal growth: Pt/Pt(111). *Surface Science*, 317 (1–2): 15–36. doi:10.1016/0039-6028(94)90249-6.

Wachs, I.E., Phivilay, S.P. and Roberts, C.A. (2013) Reporting of reactivity for heterogeneous photocatalysis. *ACS Catalysis*, 3 (11): 2606–2611. doi:10.1021/cs4005979.

Wadell, H. (1935) Volume, shape, and roundness of quartz particles. *The Journal of Geology*, 43 (3): 250. doi:https://doi.org/10.1086/624298.

Wang, C., Lu, Y., Zhang, Y., et al. (2023a) Ru-based catalysts for efficient CO_2 methanation: Synergistic catalysis between oxygen vacancies and basic sites. *Nano Research*, pp. 1–12.

Wang, D., Xu, R., Wang, X., et al. (2006) NiO nanorings and their unexpected catalytic property for CO oxidation. *Nanotechnology*, 17 (4): 979–983. doi:10.1088/0957-4484/17/4/023.

Wang, F., Li, C., Zhang, X., et al. (2015) Catalytic behavior of supported Ru nanoparticles on the {100}, {110}, and {111} facet of CeO_2. *Journal of Catalysis*, 329 (1): 177–186. doi:10.1016/j.jcat.2015.05.014.

Wang, H., Pei, Y., Qiao, M., et al. (2017) Advances in methanation catalysis. *Catalysis*, 29: 1–28. doi:10.1039/9781788010634-00001.

Wang, L., Liu, H., Liu, Y., et al. (2013) Influence of preparation method on performance of Ni-CeO_2 catalysts for reverse water-gas shift reaction. *Journal of Rare Earths*, 31 (6): 559–564. doi:10.1016/S1002-0721(12)60320-2.

Wang, Q., Hisatomi, T., Ma, S.S.K., et al. (2014) Core/shell structured La- and Rh-Codoped $SrTiO_3$ as a hydrogen evolution photocatalyst in Z-scheme overall water splitting under visible light irradiation. *Chemistry of Materials*, 26 (14): 4144–4150. doi:10.1021/cm5011983.

Wang, S. and Lu, G.Q. (1998) Role of CeO_2 in Ni/CeO_2-Al_2O_3 catalysts for carbon dioxide reforming of methane. *Applied Catalysis B: Environmental*, 19 (3–4): 267–277. doi:10.1016/S0926-3373(98)00081-2.

Wang, S., Nabavi, S.A. and Clough, P.T. (2023b) A review on bi/polymetallic catalysts for steam methane reforming. *International Journal of Hydrogen Energy*, (xxxx): 1–15. doi:10.1016/j.ijhydene.2023.01.034.

Wang, W., Wang, H., Yang, Y., et al. (2012) Ni-SiO_2 and Ni-Fe-SiO_2 catalysts for methane decomposition to prepare hydrogen and carbon filaments. *International Journal of Hydrogen Energy*, 37 (11): 9058–9066. doi:10.1016/j.ijhydene.2012.03.003.

Wang, X., Hong, Y., Shi, H., et al. (2016) Kinetic modeling and transient DRIFTS–MS studies of CO_2 methanation over Ru/Al_2O_3 catalysts. *Journal of Catalysis*, 343: 185–195. doi:10.1016/j.jcat.2016.02.001.

Wang, X., Zhu, L., Liu, Y., et al. (2018) CO_2 methanation on the catalyst of Ni/MCM-41 promoted with CeO_2. *Science of The Total Environment*, 625: 686–695. doi:10.1016/J.SCITOTENV.2017.12.308.

Wang, Y., Ma, B., Ulbricht, M., et al. (2022) Progress in alumina ceramic membranes for water purification: Status and prospects. *Water Research*, 226 (May): 119173. doi:10.1016/j.watres.2022.119173.

Wang, Y., Zhang, P., Li, M., et al. (2020) Alleviation of nitrogen stress in rice (Oryza sativa) by ceria nanoparticles. *Environmental Science: Nano*, 7 (10): 2930–2940. doi:10.1039/d0en00757a.

Weatherbee, G.D. and Bartholomew, C.H. (1982) Hydrogenation of CO_2 on group VIII metals. II. Kinetics and mechanism of CO_2 hydrogenation on nickel. *Journal of Catalysis*, 77 (2): 460–472. doi:10.1016/0021-9517(82)90186-5.

Weber, S., Zimmermann, R.T., Bremer, J., et al. (2022) Digitization in catalysis research: towards a holistic description of a Ni/Al_2O_3 reference catalyst for CO_2 methanation. *ChemCatChem*, 14 (8). doi:10.1002/cctc.202101878.

Wefers, K. and Misra, C. (1987) Oxides and hydroxides of aluminum. *Alcoa Technical Paper*, 19: 1–100.

Weissberg, H.L. (1963) Effective diffusion coefficient in porous media. *Journal of Applied Physics*, 34 (9): 2636–2639. doi:10.1063/1.1729783.

Weisz, P.B. and Prater, C.D. (1954) Interpretation of measurements in experimental catalysis. *Advances in Catalysis*, 6 (C): 143–196. doi:10.1016/S0360-0564(08)60390-9.

Willauer, H.D., Ananth, R., Olsen, M.T., et al. (2013) Modeling and kinetic analysis of CO_2 hydrogenation using a Mn and K-promoted Fe catalyst in a fixed-bed reactor. *Journal of CO2 Utilization*, 3–4: 56–64. doi:10.1016/j.jcou.2013.10.003.

Wolf, M., Schüler, C. and Hinrichsen, O. (2019) Sulfur poisoning of co-precipitated Ni-Al catalysts for the methanation of CO_2. *Journal of CO2 Utilization*, 32 (March): 80–91. doi:10.1016/j.jcou.2019.03.003.

Wong-Ng, W., Holomany, M. and McClune, W.F. (1982) "The JCPDS Data Base-Present and Future." In *Advances in X-Ray Analysis*. Cambridge, United Kingdom and New York, NY, USA, 6 March 1982. Cambridge University Press. pp. 87–88. doi:10.1154/s0376030800012313.

World Meteorological Organization WMO (2018) *WMO provisional Statement on the Status*

of the Global Climate in 2018. Available at: https://library.wmo.int/doc_num.php?explnum_id=5789 (Accessed: 26 April 2019).

Worldometers (2023) *World Population Clock: 7.7 Billion People*. Available at: https://www.worldometers.info/world-population/ (Accessed: 10 April 2023).

Worstell, J. (2014) *Adiabatic Fixed-Bed Reactors*. Elsevier Science.

WPR (2019) *2019 World Population by Country*. Available at: http://worldpopulationreview.com/ (Accessed: 19 June 2019).

Wu, H., Yuan, M., Huang, J., et al. (2020) CO_2 methanation over Ru/12CaO·7Al_2O_3 catalysts: Effect of encaged anions on catalytic mechanism. *Applied Catalysis A: General*, 595 (December 2019). doi:10.1016/j.apcata.2020.117474.

Wu, H.C., Chang, Y.C., Wu, J.H., et al. (2015) Methanation of CO_2 and reverse water gas shift reactions on Ni/SiO_2 catalysts: the influence of particle size on selectivity and reaction pathway. *Catalysis Science and Technology*, 5 (8): 4154–4163. doi:10.1039/c5cy00667h.

Wu, H.C., Chen, T.C., Wu, J.H., et al. (2021) Influence of sodium-modified Ni/SiO_2 catalysts on the tunable selectivity of CO_2 hydrogenation: Effect of the CH_4 selectivity, reaction pathway and mechanism on the catalytic reaction. *Journal of Colloid and Interface Science*, 586: 514–527. doi:10.1016/j.jcis.2020.10.117.

Wu, Y., Pei, C., Tian, H., et al. (2021) Role of Fe Species of Ni-Based Catalysts for Efficient Low-Temperature Ethanol Steam Reforming. *JACS Au*, 1 (9): 1459–1470. doi:10.1021/jacsau.1c00217.

Xiao, W., Guo, Q. and Wang, E.G. (2003) Transformation of CeO_2 (1 1 1) to Ce_2O_3 (0 0 0 1) films. *Chemical Physics Letters*, 368 (5–6): 527–531. doi:10.1016/S0009-2614(02)01889-4.

Xiao, Y., Feng, Z., Huang, X., et al. (2014) Synthesis of lanthanum oxide nanosheets by a green carbonation process. *Chinese Science Bulletin*, 59 (16): 1864–1867. doi:10.1007/s11434-014-0233-6.

Xiao, Z., Li, P., Zhang, S., et al. (2023) Effects of Metal-Support Interactions and Interfaces on Catalytic Performance over M_2O_3 - (M = La , Al-) Supported Ni Catalysts. *International Journal of Energy Research*, 2023: 1–13.

Xie, C., Chen, Y., Engelhard, M.H., et al. (2012) Comparative study on the sulfur tolerance and carbon resistance of supported noble metal catalysts in steam reforming of liquid

hydrocarbon fuel. *ACS Catalysis*, 2 (6): 1127–1137. doi:10.1021/cs200695t.

Xie, C., Chen, Y., Li, Y., et al. (2011) Influence of sulfur on the carbon deposition in steam reforming of liquid hydrocarbons over CeO_2-Al_2O_3 supported Ni and Rh catalysts. *Applied Catalysis A: General*, 394 (1–2): 32–40. doi:10.1016/j.apcata.2010.12.019.

Xin, H., Li, M., Chen, L., et al. (2023) Lanthanide oxides supported Ni nanoparticles for the selective hydrogenation of cinnamaldehyde. *Catalysis Science & Technology*. doi:10.1039/d2cy01868c.

Xu, J. and Bartholomew, C.H. (2005) Temperature-programmed hydrogenation (TPH) and in situ Mossbauer spectroscopy studies of carbonaceous species on silica-supported iron Fischer-Tropsch Catalysts. *Journal of Physical Chemistry B*, 109 (6): 2392–2403. doi:10.1021/jp048808j.

Xu, L., Cui, Y., Chen, M., et al. (2021a) Screening transition metals (Mn, Fe, Co, and Cu) promoted Ni-based CO_2 methanation bimetal catalysts with advanced low-temperature activities. *Industrial and Engineering Chemistry Research*, 60 (22): 8056–8072. doi:10.1021/acs.iecr.1c00656.

Xu, L., Wang, F., Chen, M., et al. (2017a) Alkaline-promoted Ni based ordered mesoporous catalysts with enhanced low-temperature catalytic activity toward CO_2 methanation. *RSC Advances*, 7 (30): 18199–18210. doi:10.1039/C7RA01673E.

Xu, L., Xu, C., Chen, B., et al. (2023) One-pot synthesis of hexagonal mesoporous silica confined Ni based catalysts with advanced CO_2 methanation performance. *Fuel*, 333 (P1): 126411. doi:10.1016/j.fuel.2022.126411.

Xu, W., Dong, M., Di, L., et al. (2019) A facile method for preparing uio-66 encapsulated Ru catalyst and its application in plasma-assisted CO_2 methanation. *Nanomaterials*, 9 (10): 10–13. doi:10.3390/nano9101432.

Xu, X., Liu, L., Tong, Y., et al. (2021b) Facile Cr^{3+}-doping strategy dramatically promoting Ru/CeO_2 for low-temperature CO_2 methanation: Unraveling the roles of surface oxygen vacancies and hydroxyl groups. *ACS Catalysis*, 11 (9): 5762–5775. doi:10.1021/acscatal.0c05468.

Xu, X., Shuai, K. and Xu, B. (2017b) Review on copper and palladium based catalysts for methanol steam reforming to produce hydrogen. *Catalysts*, 7 (6): 1–15. doi:10.3390/catal7060183.

Yan, C., Wang, C.H., Lin, M., et al. (2020) Local synergetic collaboration between Pd and

local tetrahedral symmetric Ni oxide enables ultra-high-performance CO_2 thermal methanation. *Journal of Materials Chemistry A*, 8 (25): 12744–12756. doi:10.1039/d0ta02957b.

Yan, X., Liu, Y., Zhao, B., et al. (2013) Methanation over Ni/SiO_2: Effect of the catalyst preparation methodologies. *International Journal of Hydrogen Energy*, 38 (5): 2283–2291. doi:10.1016/J.IJHYDENE.2012.12.024.

Yang, C., Lu, Y., Zhang, L., et al. (2021) Defect engineering on CeO_2-based catalysts for heterogeneous catalytic applications. *Small Structures*, 2 (12): 2100058. doi:10.1002/sstr.202100058.

Yang, H., Xu, L., Chen, M., et al. (2020a) Facilely fabricating highly dispersed Ni-based catalysts supported on mesoporous MFI nanosponge for CO_2 methanation. *Microporous and Mesoporous Materials*, 302 (April): 110250. doi:10.1016/j.micromeso.2020.110250.

Yang, J., Bu, S., Dong, Q., et al. (2015) Experimental study of flow transitions in random packed beds with low tube to particle diameter ratios. *Experimental Thermal and Fluid Science*, 66: 117–126. doi:10.1016/j.expthermflusci.2015.03.018.

Yang, Y., Liu, J., Liu, F., et al. (2020b) Reaction mechanism of CO_2 methanation over Rh/TiO2 catalyst. *Fuel*, 276 (March): 118093. doi:10.1016/j.fuel.2020.118093.

Ye, J., Liu, C., Mei, D., et al. (2013) Active oxygen vacancy site for methanol synthesis from CO2 hydrogenation on In2O3(110): A DFT study. *ACS Catalysis*, 3 (6): 1296–1306. doi:10.1021/cs400132a.

Ye, R.P., Li, Q., Gong, W., et al. (2020) High-performance of nanostructured Ni/CeO_2 catalyst on CO_2 methanation. *Applied Catalysis B: Environmental*, 268 (November 2019): 118474. doi:10.1016/j.apcatb.2019.118474.

Yeo, T.Y., Ashok, J. and Kawi, S. (2019) Recent developments in sulphur-resilient catalytic systems for syngas production. *Renewable and Sustainable Energy Reviews*, 100 (July 2018): 52–70. doi:10.1016/j.rser.2018.10.016.

Yi, H., Xue, Q., Lu, S., et al. (2022) Effect of pore structure on Ni/Al_2O_3 microsphere catalysts for enhanced CO_2 methanation. *Fuel*, 315 (December 2021): 123262. doi:10.1016/j.fuel.2022.123262.

Yoshitake, H., Sugihara, T. and Tatsumi, T. (2003) XAFS study on the local structure of Ti in amorphous mesoporous titania. *Physical Chemistry Chemical Physics*, 5 (4): 767–772.

doi:10.1039/b210209a.

Younas, M., Loong Kong, L., Bashir, M.J.K., et al. (2016) Recent advancements, fundamental challenges, and opportunities in catalytic methanation of CO_2. *Energy and Fuels*. 30 (11) pp. 8815–8831. doi:10.1021/acs.energyfuels.6b01723.

Younis, A., Gennequin, C., Aad, E.A., et al. (2022) "Dry reforming of polypropylene over Ni and Ru-Ni catalysts supported on mesoporous alumina : Effect of calcination temperature." In *The 13th International Renewable Energy Congress*. 2022. IEEE. pp. 1–5.

Yuan, S., Duan, Y., Yu, C., et al. (2023) Construction of defects-rich TiO_2-supported Pd catalyst for phenol hydrogenation with ball-milling process. *Molecular Catalysis*, 535 (November 2022): 112830. doi:10.1016/j.mcat.2022.112830.

Yu, Y., Chan, Y.M., Bian, Z., et al. (2018) Enhanced performance and selectivity of CO_2 methanation over g-C_3N_4 assisted synthesis of Ni–CeO_2 catalyst: Kinetics and DRIFTS studies. *International Journal of Hydrogen Energy*, 43 (32): 15191–15204. doi:10.1016/j.ijhydene.2018.06.090.

Yue, L., Li, J., Chen, C., et al. (2018) Thermal-stable Pd@mesoporous silica core-shell nanocatalysts for dry reforming of methane with good coke-resistant performance. *Fuel*, 218: 335–341. doi:10.1016/j.fuel.2018.01.052.

Zamani, A.H., Ali, R. and Abu Bakar, W.A.W. (2015) Optimization of CO_2 methanation reaction over M*/Mn/Cu-Al_2O_3 (M*: Pd, Rh and Ru) catalysts. *Journal of Industrial and Engineering Chemistry*, 29: 238–248. doi:10.1016/j.jiec.2015.02.028.

Zamani, A.H., Shohaimi, N.A.M., Rosid, S.J.M., et al. (2019) Enhanced low temperature reaction for the CO_2 methanation over Ru promoted Cu/Mn on alumina support catalyst using double reactor system. *Journal of the Taiwan Institute of Chemical Engineers*, 96: 400–408. doi:10.1016/j.jtice.2018.12.009.

Zandalinas, S.I., Fritschi, F.B. and Mittler, R. (2021) Global warming, climate change, and environmental pollution: Recipe for a multifactorial stress combination disaster. *Trends in Plant Science*, 26 (6): 588–599. doi:10.1016/J.TPLANTS.2021.02.011.

Zare, M. and Hashemabadi, S.H. (2020) Particle-fluid heat transfer close to the bed wall: CFD simulation and experimental study of particle shape influence on the formation of hot zones. *International Journal of Thermal Sciences*, 150 (December 2019): 106223. doi:10.1016/j.ijthermalsci.2019.106223.

Zhang, C., Gao, Y., Zhang, J., et al. (2023a) Optimizing Ni dispersion and stability over SiO_2 supported Ni – La_2O_3 catalysts by preparation method for enhancing H_2 selectivity and durability on steam reforming of methylcyclohexane. *Journal of Power Sources*, 555 (August 2022): 232340. doi:10.1016/j.jpowsour.2022.232340.

Zhang, H., Zhu, Y., Wang, S., et al. (2015) Activity and thermal stability of $Pt/Ce_{0.64}Mn_{0.16}R_{0.2}O_x$ (R = Al, Zr, La, or Y) for soot and NO oxidation. *Fuel Processing Technology*, 137 (2): 38–47. doi:10.1016/j.fuproc.2015.03.027.

Zhang, L., Millet, J.M. and Ozkan, U.S. (2009) Deactivation characteristics of Fe – Al – Cu water-gas shift catalysts in the presence of H_2S. *Journal of Molecular Catalysis A: Chemical*, 309 (1–2): 63–70. doi:10.1016/j.molcata.2009.04.016.

Zhang, T., Ai, H. and Liu, Q. (2019) La_2O_3-promoted Ni/Al_2O_3 Catalyst for CO methanation: Enhanced catalytic activity and stability. *Energy Technology*, 7 (10). doi:10.1002/ente.201900531.

Zhang, T., Zheng, P., Gu, F., et al. (2023b) The dual-active-site tandem catalyst containing Ru single atoms and Ni nanoparticles boosts CO_2 methanation. *Applied Catalysis B: Environmental*, 323 (September 2022): 122190. doi:10.1016/j.apcatb.2022.122190.

Zhang, Y., Yu, L., Cui, K., et al. (2023c) Carbon capture and storage technology by steel-making slags: Recent progress and future challenges. *Chemical Engineering Journal*, 455 (September 2022): 140552. doi:10.1016/j.cej.2022.140552.

Zhang, Z., Deng, S., Fang, X., et al. (2023d) CrO_x-promoted Ru/Al_2O_3 for CO_2 methanation: Formation of surface Cr-doped RuO_2 solid solution plays key roles. *Fuel*, 339 (October 2022): 127414. doi:10.1016/j.fuel.2023.127414.

Zhang, Z., Yu, Z., Feng, K., et al. (2022) Eu^{3+} doping-promoted Ni-CeO_2 interaction for efficient low-temperature CO_2 methanation. *Applied Catalysis B: Environmental*, 317 (May): 121800. doi:10.1016/j.apcatb.2022.121800.

Zhao, D., Feng, J., Huo, Q., et al. (1998a) Triblock copolymer syntheses of mesoporous silica with periodic 50 to 300 Angstrom pores. *Science*, 279 (5350): 548–552. doi:10.1126/science.279.5350.548.

Zhao, D., Huo, Q., Feng, J., et al. (1998b) Nonionic triblock and star diblock copolymer and oligomeric surfactant syntheses of highly ordered, hydrothermally stable, mesoporous silica structures. *J. Am. Chem. Soc.*, 120 (24): 6024–6036.

Zhao, K., Li, Z. and Bian, L. (2016) CO_2 methanation and co-methanation of CO and CO_2

over Mn-promoted Ni/Al_2O_3 catalysts. *Frontiers of Chemical Science and Engineering*, 10 (2): 273–280. doi:10.1007/s11705-016-1563-5.

Zhao, Y., Girelli, V., Ersen, O., et al. (2023) CO_2 methanation with high-loading mesoporous Ni/SiO_2 catalysts: Toward high specific activity and new mechanistic insights. *Journal of Catalysis*, 426 (April): 283–293. doi:10.1016/j.jcat.2023.07.021.

Zheng, C., Liu, Z., Xiang, J., et al. (2015a) Fundamental and technical challenges for a compatible design scheme of oxyfuel combustion technology. *Engineering*, 1 (1): 139–149. doi:10.15302/j-eng-2015008.

Zheng, Q., Farrauto, R., Deeba, M., et al. (2015b) Part I: A comparative thermal aging study on the regenerability of Rh/Al_2O_3 and Rh/CexOy-ZrO_2 as model catalysts for automotive three way catalysts. *Catalysts*, 5 (4): 1770–1796. doi:10.3390/catal5041770.

Zhou, G., Jin, P., Wang, Y., et al. (2020) X-ray diffraction analysis of the yttria stabilized zirconia powder by mechanical alloying and sintering. *Ceramics International*, 46 (7): 9691–9697. doi:10.1016/J.CERAMINT.2019.12.236.

Zhou, G., Liu, H., Cui, K., et al. (2017) Methanation of carbon dioxide over Ni/CeO_2 catalysts: Effects of support CeO_2 structure. *International Journal of Hydrogen Energy*, 42 (25): 16108–16117. doi:10.1016/j.ijhydene.2017.05.154.

Zhou, G., Xu, S., Li, Y., et al. (2022) Preparation of porous NiCe composite catalyst and its performance for CO_2 hydrogenation. *ChemNanoMat*, 8 (4). doi:10.1002/cnma.202100533.

Zhou, L., Wang, Q., Ma, L., et al. (2015) CeO_2 promoted mesoporous $Ni/\gamma\text{-}Al_2O_3$ catalyst and its reaction conditions for CO_2 methanation. *Catalysis Letters*, 145 (2): 612–619. doi:10.1007/s10562-014-1426-y.

Zhou, Z., Wang, X., Yu, R., et al. (2023) Synthesis of b-axis oriented ZSM-5 zeolite by mechanochemical-assisted quasi-solvent-free method and its MTO catalytic performance. *Advanced Powder Technology*, 34 (1): 103930. doi:10.1016/j.apt.2022.103930.

Zhu, J., Araya, S.S., Cui, X., et al. (2020) Modeling and design of a multi-tubular packed-bed reactor for methanol steam reforming over a $Cu/ZnO/Al_2O_3$ catalyst. *Energies*, 13 (3). doi:10.3390/en13030610.

Zuliani, A., Ivars, F. and Luque, R. (2018) Advances in nanocatalyst design for biofuel production. *ChemCatChem*, 10 (9): 1968–1981. doi:10.1002/cctc.201701712.

Appendix A

Calculations for catalyst preparation

Before synthesising a catalyst, the following components need to be determined:

The total mass of catalyst to be prepared.

The percentage of the support and the metal component.

Mass of metal salt required to achieve the desired percentage of the metal component.

For example, let us prepare 20 g of 15%Ni/YSZ:

Total mass of catalyst = 20g

Percentage of support (YSZ) = 100% - 15% = 85%

Mass of support = 85% × 20g = 17g

Therefore, mass of 15%Ni = 20g (total mass) - 17g (mass of support)

= 3g

$$\text{Mass of Ni salt} = \frac{m_{Ni} \times M_{Ni,salt}}{M_{Ni}}$$

Where m_{Ni} = mass of Ni contained in the total mass of catalyst to be prepared

$M_{Ni,salt}$ = Molecular weight of Ni salt

M_{Ni} =Molecular weight of Ni

Assuming that the Ni salt is $Ni(NO_3)_2.6H_2O$, then $M_{Ni,salt} = 290.79 g\ mol^{-1}$

$$M_{Ni} = 58.70 g\ mol^{-1}$$

Therefore, Mass of Ni salt containing 3g of Ni $= \frac{3g \times 290.79g\ mol^{-1}}{58.70g\ mol^{-1}}$

$= 14.8615g$

This means that to prepare 20g of 15%Ni/YSZ catalyst, 14.8615g of Ni salt and 17g of YSZ are required to be mixed using deionised water.

Similarly, to prepare 10g of 3%La-10%Ni/YSZ,

Total mass = 10g

Percentage of YSZ (support) = 100% - 10%Ni - 3%La = 87%

Mass of YSZ = 87% × 10g = 8.7g

Mass of 10%Ni = 10% × 10g = 1g

Mass of 3%La = 3% × 10g = 0.3g

Mass of Ni salt required $= \frac{1g \times 290.79g\ mol^{-1}}{58.70g\ mol^{-1}}$

$\approx 4.954g$

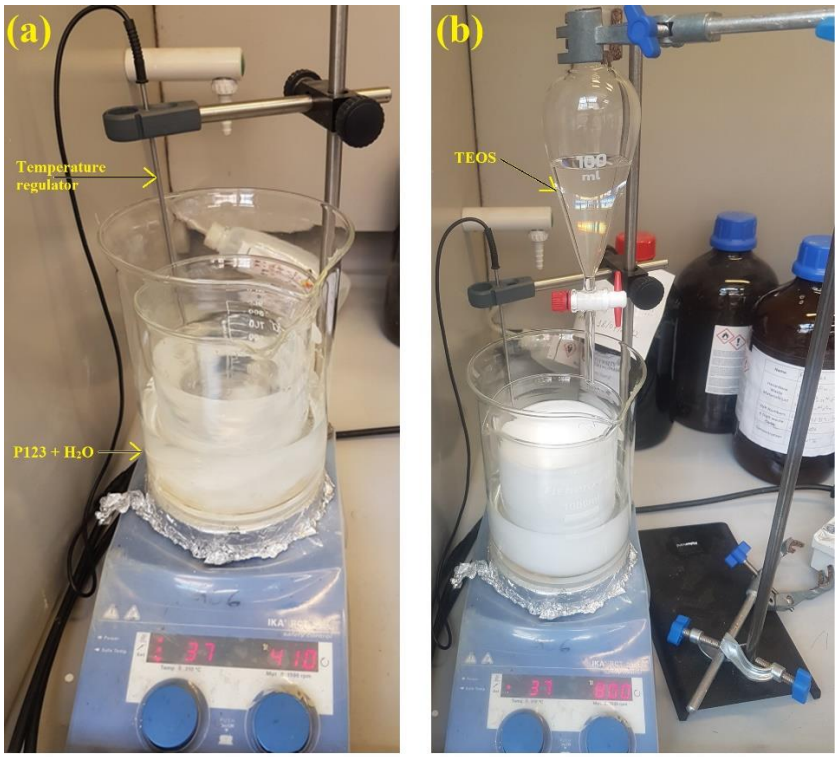
Assuming that the La salt is $La(NO_3)_3.6H_2O$,

ass of La salt containing 0.3g of La $= \frac{0.3g \times 433.01g\ mol^{-1}}{138.905g\ mol^{-1}}$

$\approx 0.935g$

Therefore, 0.935g of $La(NO_3)_3.6H_2O$, 4.954g of $Ni(NO_3)_2.6H_2O$ and 8.7g of YSZ are required to synthesise 10g of 3%L-10%Ni/YSZ catalyst. This procedure is the same for other types of supports.

Figure A.1 represents some of the stages involved in the preparation of SBA-15. Figure A.1 (a) and (b) show the mixture of the P123 copolymer and the TEOS silica precursor while Figure A.1 (c) shows the washing step of the as-synthesised SBA-15. Vacuum pump is connected to the filter funnel to enable fast washing while employing enough water to bring the pH of the material to 7 (neutral). Figure A.2 (a) and (b) reveal the importance of thoroughly washing the as-synthesised SBA-15 before calcination. As mentioned in chapter three, the P123 copolymer and the TEOS silica precursor are hydrolysed in HCl acidic medium. The calcination of the unwashed SBA-15 as seen in Figure A.2 (b) caused the residual reactants such as HCl and unreacted P123 to react with the silica material, thereby, altering the composition of the SBA-15 which gave a black product instead of white.



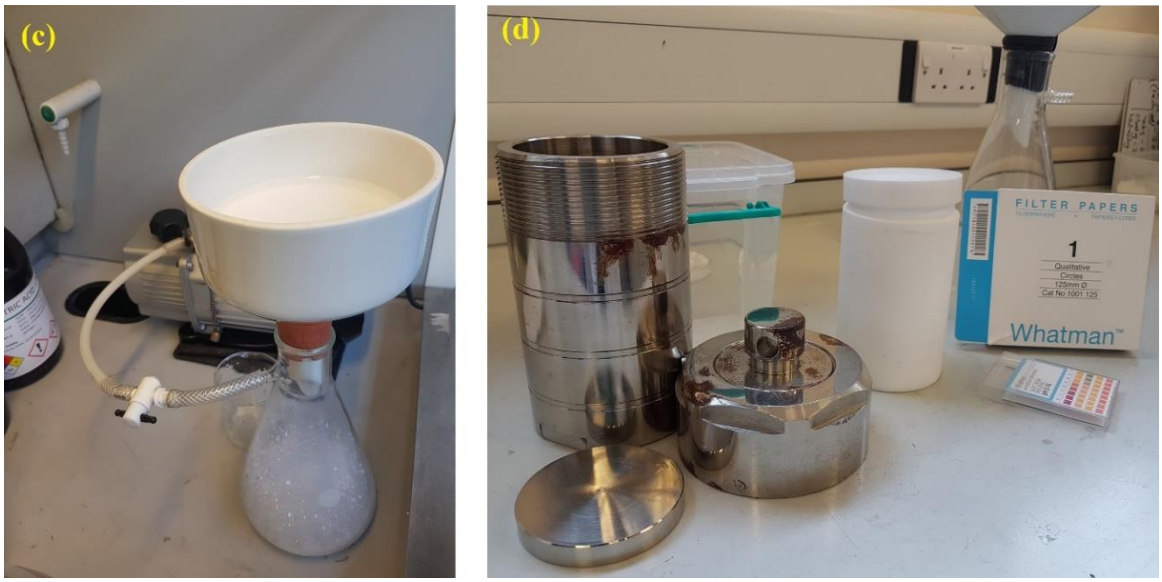


Figure A.1 Pictorial view of the synthesis stages for SBA-15 (a) dissolution of P123, (b) introduction of TEOS into the dissolved P123, (c) washing and filtration and (d) Teflon-lined autoclave for hydrothermal treatment of as-synthesised SBA-15.

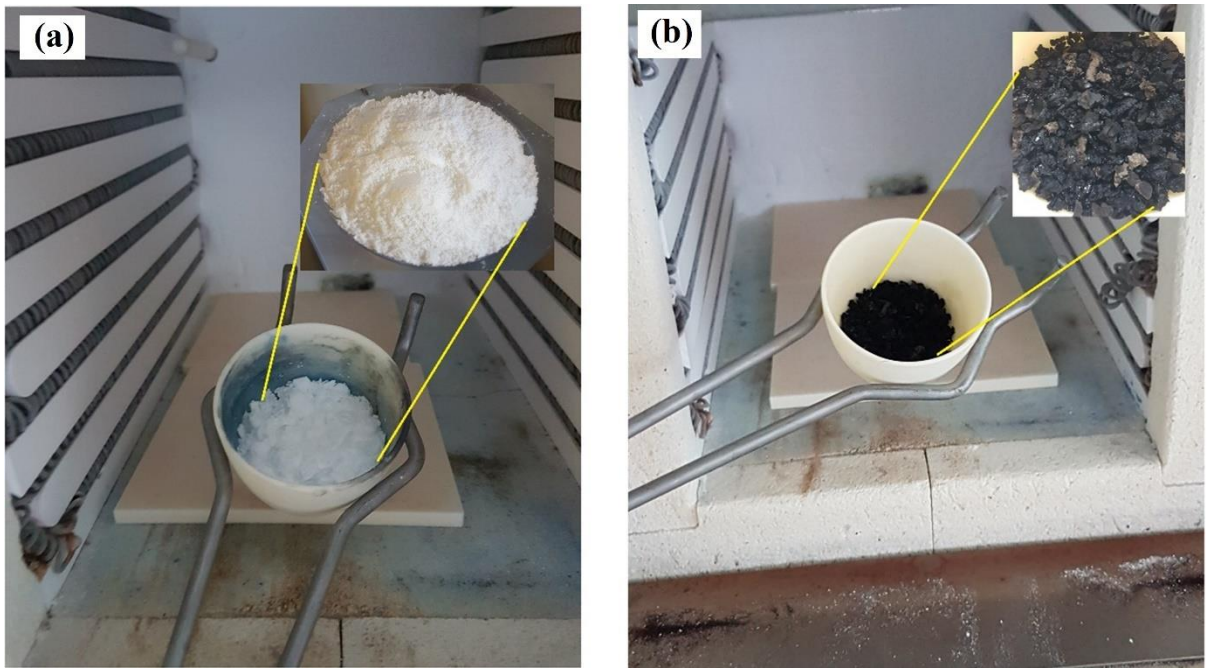


Figure A.2 Pictorial view showing the effect of washing the as-synthesised SBA-15 before calcination (a) calcined washed SBA-15 and (d) calcined unwashed SBA-15.

Appendix B

Crystallite size calculation from XRD data

The average crystallite sizes of the crystals for each sample were calculated from XRD data by the Scherrer equation using Eq. **(**3.6**)**. The FWHM for each Ni peaks was obtained using OriginPro software and an example is shown in Figure B.1.

$$d_p \text{ (nm)} = \frac{K\lambda}{\beta \cos \theta}$$

Where d_p = Particle size in nm,

K = Shape factor with the value of 0.9 (assuming a spherical particle),

λ = X-ray wavelength of the X-ray source Cu Kα (1.5406 Å),

β = Line broadening at half the maximum intensity (FWHM) of Ni diffraction peak.

Note that both FWHM and 2θ must be converted to radian before applying the Scherrer equation.

From Figure B.1, first Ni peak is at 2θ = 44.8° or 0.782 rad θ = (0.782/2)°

β or FWHM = 0.216° or 0.00377 rad

Therefore, crystallite size =

$$\frac{0.9 \times 1.5406}{0.00377 \times \cos(0.782/2)}$$

= 397.8 Å or 39.78 nm

Second Ni peak is at 2θ = 52.15° or 0.91 rad

FWHM = 0.262° or 0.00457 rad

Therefore, crystallite size = $\frac{0.9 \times 1.5406}{0.00457 \times \cos(0.91/2)}$

= 337.8 Å or 33.78 nm

Average crystallite size =

$$\frac{33.78 + 39.78}{2}$$

= 36.78 nm

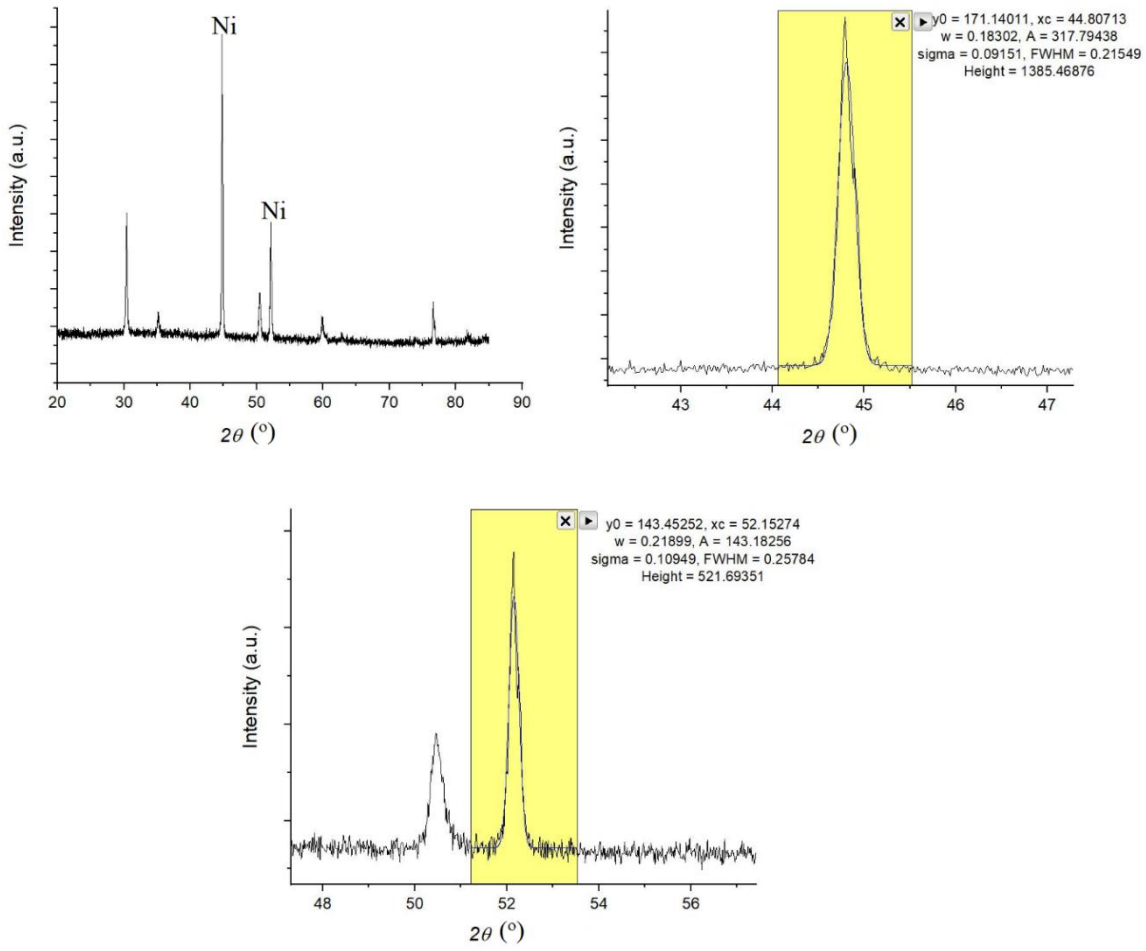


Figure B.1 XRD pattern of reduced Ni-based catalyst showing the FWHM as obtained from OriginPro software.

Appendix C

TPO calculations for mass of carbon deposited

The amount of carbon deposited on the spent catalysts during TPO experiments was determined by first calibrating the mass spectrometer using carbon black. 10, 25 and 100 mg of carbon black were subjected to a TPO condition: O_2 and N_2 flows of 5 mL min^{-1} and 20 mL min^{-1}, respectively; maximum temperature of 1073 K at heating rate of 5 K min^{-1}. The CO_2 signals for each of the masses of carbon employed, and the resulting calibration curve for carbon deposited are shown in Figure C.1.

From the calibration curve, slope = 4×10^{-6}

Equation of the straight line, $m_c = 4 \times 10^{-6} \times A_{CO2}$

$m_c =$ mass of carbon deposited (mg)

A_{CO2} = =Total area under each of the curves of CO_2 signal

For example, if a spent catalyst is subjected to TPO conditions and total area under the CO_2 signal is 265000, the amount of carbon deposited = $4\times10^{-6}\times265000$

= 1.06 mg

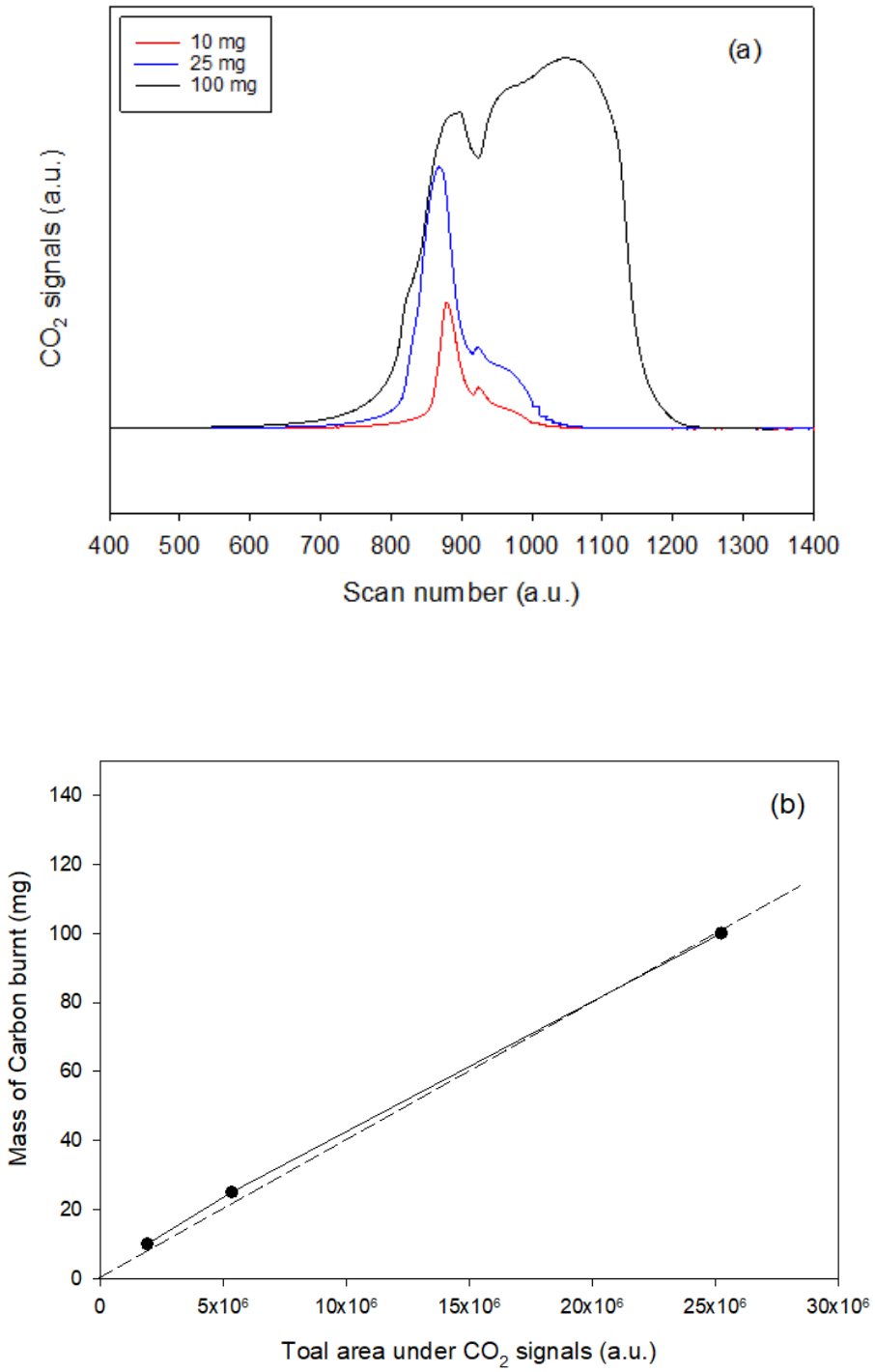


Figure C.1 Profile of (a) CO_2 signals for each mass of carbon black burnt, and (b) calibration curve showing the relationship between the mass of carbon and the total area under the curve of the CO_2 signals during TPO.

Appendix D

Activation energy calculation

The activation energies of the catalysts were estimated using the Arrhenius equation given in Eq. (D.1).

$$k = Ae^{-\frac{E_A}{RT}} \quad \text{(D.1)}$$

k = rate constant

A = frequency or collision factor

T = reaction temperature in Kelvin

E_A = activation energy or minimum energy required for reaction to take place (J mol^{-1})

R = gas constant (8.314 J mol^{-1} K^{-1})

Meanwhile, the rate of reaction between reactants A and B can be related to the rate constant using Eq. (D.2).

$$-r_A = kC_A^n C_B^m \quad \text{(D.2)}$$

$-r_A$ = rate of consumption of reactant A (mol kg^{-1} s^{-1})

m and n = order of reaction

C_A and C_B = concentrations of reactants A and B (mol m^{-3})

k = rate constant

By substituting the rate constant of Eq. (D.1) into Eq. (D.2), Eq. (D.3) is obtained.

$$-r_A = Ae^{-\frac{E_A}{RT}} \times C_A^n C_B^m \quad \textbf{(D.3)}$$

$$Or \ -r_A = e^{-\frac{E_A}{RT}} \times AC_A^n C_B^m$$

By taking the log of both sides of Eq. (D.3), Eq. (D.4) was derived.

$$\ln(-r_A) = \ln(e^{-\frac{E_A}{RT}} \times (AC_A^n C_B^m)) \quad \textbf{(D.4)}$$

$$\ln(-r_A) = \ln e^{-\frac{E_A}{RT}} + ln(AC_A^n C_B^m)$$

$$\ln(-r_A) = -\frac{E_A}{RT} + \ln(AC_A^n C_B^m) \quad \textbf{(D.5)}$$

By comparing Eq. (D.5) with the typical straight line $y = mx + C$ the activation energy can be obtained as follows:

$\ln(-r_A)$ = the dependent variable (Y-axis)

1/T = the independent variable (X-axis)

$\ln(AC_A^n C_B^m)$ = the Y-intercept

$-\frac{E_A}{R}$ = slope of the straight line (m) which is determined from the plot like the one shown in Figure D.1.

Therefore, E_A = -R × m

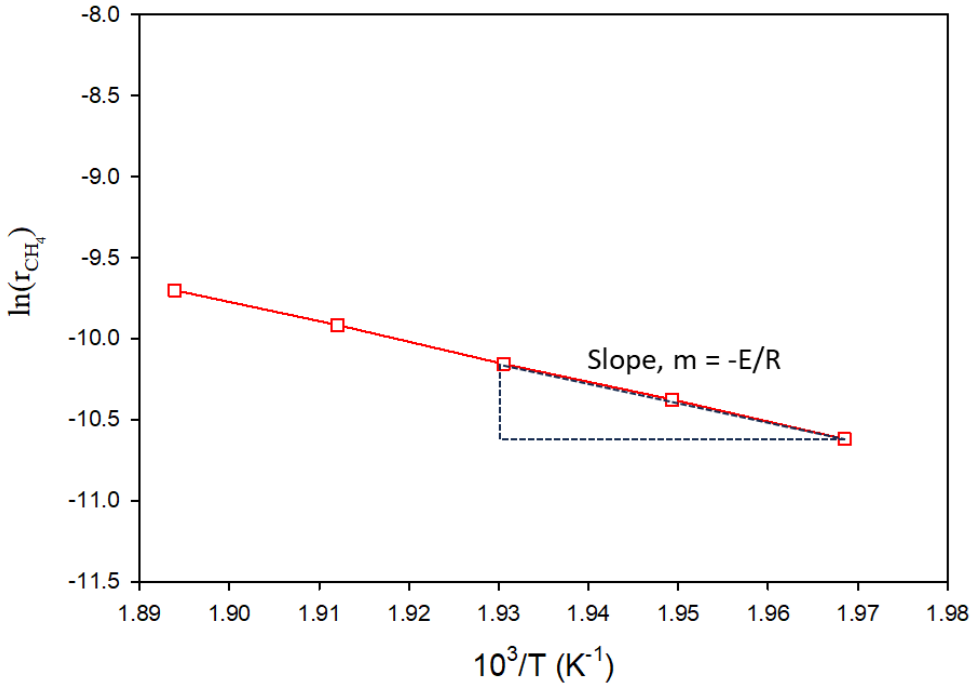


Figure D.1 Arrhenius plot demonstrating the relationship between activation energy and the slope.

Appendix E

Determination of transport resistances

The various calculations that were carried out before deriving the outcomes of transport resistances discussed in chapter 5 are presented here.

E.1 External Mass Transfer Resistance

As mentioned earlier, resistance to external mass transfer may be ignored the Mears criterion given by Eq. (E.1) is satisfied.

$$\frac{(-r_{\exp})\rho_b R_p n}{k_c C_{Ab}} < 0.15 \qquad \text{(E.1)}$$

Where

$(-r_{\exp})$ = reaction rate (5.41×10^{-2} mol kg_{cat}^{-1} s^{-1})

ρ_b = catalyst bulk density (2260.38 kg m^{-3})

R_p = catalyst pellet radius (7.50×10^{-5} m)

n = order of reaction

C_{Ab} = Concentration of reactant A (CO_2) in the bulk gas phase (4.54 mol m^{-3})

k_c = mass transfer coefficient

E.1.1 Calculation of mass transfer coefficient

The mass transfer coefficient (k_c) was estimated using Eq. (E.2).

$$k_c = \frac{j_D U}{Sc^{\frac{2}{3}}} \qquad \text{(E.2)}$$

Where

U = superficial gas velocity (m s^{-1})

j_D = Colburn's J-factor for mass transfer

Sc = Schmidt number

Superficial gas velocity

The Superficial gas velocity (U) was estimated by Eq. (E.3).

$$U = \frac{\dot{v}}{A_t} \qquad \text{(E.3)}$$

A_t = Area of the tubular reactor

$A_t = \pi d_t^2/4$

$$= \pi \times 0.0055^2/4$$

$= 2.38 \times 10^{-5}$ m^2

$\dot{v}$ = Volumetric gas flow rate at 298 K = 135 mL min^{-1} or 2.25×10^{-6} m^3 s^{-1}

At 523 K, $\dot{v}$ was estimated using Charles's law as follows:

$$\frac{\dot{v}_1}{T_1} = \frac{\dot{v}_2}{T_2}$$

$$\dot{v}_2 = \frac{\dot{v}_1 \times T_2}{T_1} = \frac{2.25 \times 10^{-6} \times 523}{298} = 3.95 \times 10^{-6}\ m^3 s^{-1}$$

From Eq. (E.3), $U = \frac{3.95\times10^{-6} m^3 s^{-1}}{2.38\times10^{-5}\ \mathrm{m}^2} = 0.166$ m s^{-1}

Colburn's J-factor for mass transfer

The Colburn's J-factor is a dimensionless parameter which can be used to show the effectiveness of the mass transfer in a system or of an equipment. In this study, the Reynolds number was first evaluated before the Colburn's J-factor since it is dependent on the Reynolds number.

The Reynold number, *Re* was estimated using Eq. (E.4).

$$\mathrm{Re} = \frac{\rho_g U d_p}{\mu_g} \tag{E.4}$$

where

U = superficial gas velocity estimated as 0.166 m s^{-1}

d_p = average particle diameter (1.50×10^{-4} m)

ρ_g = density of the gas mixture (CO_2, H_2, and N_2) in kg m^{-3}

μ_g = viscosity of the gas mixture, kg m^{-1} s^{-1}

The density of the gas mixture was estimated by Eq. (E.5).

$$\rho_g = \frac{M_g P}{RT} \tag{E.5}$$

P = standard pressure (101325 Pa)

R = gas constant (8.314 m^3 Pa K^{-1} mol^{-1})

T = reaction temperature (523 K)

M_g = molar mass of gas mixture, and was estimated by $M_g = \sum_i M_i y_i$

Table E. 1 Composition of feed gas and their molecular weights.

Species	M_i (× 10^{-3} kg mol^{-1})	y_i	$M_i y_i$ (kg mol^{-1})
CO_2	44.01	0.111	0.00489
H_2	2.016	0.444	0.000896
N_2	28.01	0.444	0.01245

From Table E.1, $M_g = \sum_i M_i y_i$

= 0.01824 kg mol^{-1}

After substitution into Eq. (E.5), the density of the feed gas was estimated as follows:

$$\rho_g = \frac{0.01824 \text{ kg mol}^{-1} \times 101325 \text{ Pa}}{8.314 \text{ m}^3 \text{ Pa K}^{-1} \text{ mol}^{-1} \times 523 \text{ K}} = 0.425 \text{ kg m}^{-3}$$

Next is the viscosity of the feed gas (μ_g) which was estimated by Eq. (E.6).

$$\mu_g = \sum_i \frac{y_i \mu_i}{\sum_{j \neq i} y_j \phi_{ij}} \quad \text{(E.6)}$$

Where

y_i = mole fraction of component gases (see Table E.1).

μ_i = viscosity of each species in the feed gas H_2, CO_2 and N_2 in kg m^{-1} s^{-1}.

ϕ_{ij} = dimensionless constant which is a function of the molecular weight and viscosity of binary component (*ij*).

The viscosity of each species (μ_i) was estimated by Eq. (E.7), and the values of C1, C2, C3 and T4 constants are given in Table E.2 as adapted from Perry's Chemical Engineers' Handbook between page 2-421 and 2-426 (Perry and Green, 2008).

$$\mu_i = \frac{C1T^{C2}}{1+\frac{C3}{T}+C4/T^2} \tag{E.7}$$

Table E. 2 Vapor viscosity of the components of the feed gas (kg m^{-1} s^{-1}). Adapted from ref (Perry and Green, 2008).

Species	C1	C2	C3	C4
CO_2	21.48×10^{-7}	0.46	290	0
N_2	6.5592×10^{-7}	0.6081	54.714	0
H_2	1.80×10^{-7}	0.685	-0.59	140

After substitution into Eq. (E.7), the viscosity of each species at 523 K was obtained as follows:

μ_{CO2}= 2.46012×10^{-5} kg m^{-1} s^{-1}

μ_{N2} = 2.67153×10^{-5} kg m^{-1} s^{-1}

μ_{H2} = 1.31×10^{-5} kg m^{-1} s^{-1}

The dimensionless constant (ϕ_{ij}) of binary component was estimated by Eq. (E.8) as provided in the literature (Cheung et al., 1962). Note that the binary component *ij* could be CO_2-H_2 and CO_2-N_2, H_2-CO_2 and H_2-N_2 or N_2-CO_2 and N_2-H_2

$$\phi_{ij} = \frac{\left[1+\left(\frac{\mu_i}{\mu_j}\right)^{\frac{1}{2}}\left(\frac{M_j}{M_i}\right)^{\frac{1}{4}}\right]^2}{\left[8\left(1+\left(\frac{M_i}{M_j}\right)\right)\right]^{\frac{1}{2}}} \quad \text{(E.8)}$$

where

M = molecular weight of component gases as given in Table E.1.

μ = viscosity of the component gases as estimated from Eq. (E.7).

After substitution into Eq. (E.8), the dimensionless parameters ϕ_{ij} for each of the binary components is given as follows:

$\phi_{CO2\text{-}H2} = 0.1976$

$\phi_{CO2\text{-}N2} = 0.7605$

$\phi_{N2\text{-}CO2} = 1.2972$

$\phi_{N2\text{-}H2} = 0.2773$

$\phi_{H2\text{-}CO2} = 2.2956$

$\phi_{H2\text{-}N2} = 1.8883$

From Eq. (E.6), $\mu_g = 5.61 \times 10^{-5}$ kg m^{-1} s^{-1}

From Eq. (E.4), the Reynolds number was estimated as follows:

$$Re = \frac{0.425 \text{ kg m}^{-3} \times 0.166 \text{ m s}^{-1} \times 1.50 \times 10^{-4} \text{ m}}{5.61 \times 10^{-5} \text{ kg m}^{-1}s^{-1}} = 0.1886$$

Since the calculated Reynolds number is less than 10 or is within the range of 0.01 to 15000, the Colburn's mass-transfer factor j_D was estimated using Eq. (E.9) as provided in the literature (Dwivedi and Upadhyay, 1977).

$$j_D = \frac{1}{\varepsilon}\left[\left(\frac{0.765}{Re^{0.82}}\right) + \left(\frac{0.365}{Re^{0.386}}\right)\right] \quad \text{(E.9)}$$

Where

ε = void fraction = 0.6022 (determined by a Helium pycnometer AccuPyc II 1340).

$$j_D = \frac{1}{0.6022}\left[\left(\frac{0.765}{0.1886^{0.82}}\right) + \left(\frac{0.365}{0.1886^{0.386}}\right)\right]$$

$$j_D = 6.14$$

Schmidt number (S_c)

The Schmidt number, *Sc* was estimated by Eq. (E.10).

$$S_c = \frac{\mu_g}{\rho_g D_g} \quad \text{(E.10)}$$

Where

ρ_g = density of the gaseous mixture H_2, CO_2 and N_2 which was evaluated as 0.425 kg m^{-3} from Eq. (E.5).

μ_g= viscosity of the gaseous mixture H_2, CO_2 and N_2 which was evaluated as 5.61×10^{-5} kg m^{-1} s^{-1} from Eq. (E.6)

D_g = diffusivity of CO_2 in the gas mixture which was estimated by Eq. (E.11).

$$D_g = \frac{1 - y_i}{\sum_j \frac{y_j}{D_{ij}}} \tag{E.11}$$

where

i = CO_2

j = H_2, N_2

y = mole fraction of component gases (CO_2 = 0.111, H_2 = 0.444, N_2 = 0.444).

D_{ij} = binary diffusion coefficient between components ij ($m^2\ s^{-1}$) and was estimated by Eq. (E.12).

$$Dij = \frac{1 \times 10^{-3} T^{1.75} \sqrt{\frac{\left(M_i + M_j\right)}{M_i M_j}}}{P\left[\left(\sum v\right)_i^{\frac{1}{3}} + \left(\sum v\right)_j^{\frac{1}{3}}\right]^2} \tag{E.12}$$

P = standard pressure (1 atm)

T = reaction temperature (523 K)

M = molecular weight of component gases in g mol^{-1} (see Table E.1).

v = atomic diffusion volumes which were obtained from the literature (Fuller et al., 1966) as CO_2 = 26.9 $cm^3\ mol^{-1}$, H_2 = 7.707 $cm^3\ mol^{-1}$, N_2 = 17.9 $cm^3\ mol^{-1}$.

After substitution into Eq. (E.12), the binary diffusion coefficients were obtained as follows:

$D_{CO_2-H_2}$ = 1.705 × 10^{-4} $m^2\ s^{-1}$,

$D_{CO_2-N_2}$ = 4.389 × 10^{-5} $m^2\ s^{-1}$

Fom Eq. (E.11),

$$D_g = \frac{1 - 0.111}{\sum\left(\frac{0.444}{1.705 \times 10^{-4}\ \mathrm{m^2 s^{-1}}} + \frac{0.444}{4.389 \times 10^{-5}\ \mathrm{m^2 s^{-1}}}\right)}$$

$$= 6.98 \times 10^{-5}\ \mathrm{m^2 s^{-1}}$$

From Eq. (E.10), Schmidt number, $Sc = \frac{\mu_g}{\rho_g D_g}$

$$S_c = \frac{5.61 \times 10^{-5}\ \mathrm{kg\ m^{-1}\ s^{-1}}}{0.425\ \mathrm{kg\ m^3} \times 6.98 \times 10^{-5}\ \mathrm{m^2 s^{-1}}}$$

$$= 1.892$$

From Eq. (E.2), mass transfer coefficient, $k_c = \frac{j_D U}{Sc^{\frac{2}{3}}}$

$$k_c = \frac{6.1414 \times 0.166\ \mathrm{m\ s^{-1}}}{1.892^{\frac{2}{3}}} = 0.667\ \mathrm{m\ s^{-1}}$$

Thus from Eq. (E.1), Mears's criterion is calculated as:

$$\frac{5.41 \times 10^{-2}\ \mathrm{mol\ kg_{cat}^{-1}\ s^{-1}} \times 0.425\ k\mathrm{g\ m^{-3}} \times 7.50 \times 10^{-5}\ \mathrm{m^3} \times 1}{0.667\ \mathrm{m\ s^{-1}} \times 4.544\ \mathrm{mol\ m^{-3}}}$$

$$= 0.00303$$

Since the value from the expression is less than 0.15, the external mass transfer effect can be neglected.

E.2 Internal (intraparticle) mass transfer resistance

The resistance to intraparticle mass transfer may be determined using Weisz-Prater criterion given in Eq. (E.13).

$$\frac{(-r_{\exp})\rho_c R_p^2}{D_{eff} C_{As}} < 1 \qquad \text{(E.13)}$$

Where

$(-r_{exp})$ = 5.41 × 10^{-2} mol kg_{cat}^{-1} s^{-1} (as stated in section E.1).

ρ_c = density of the 10%Ni/YSZ catalyst. The value obtained by pycnometer was 5682.2 kg m^{-3}

R_p = 7.50 × 10^{-5} m (as stated in section E.1).

C_{As} = concentration of reactant A (CO_2) at the catalyst external surface.
= concentration of reactant A or CO_2 in the gas bulk phase (C_{Ab}) since the external mass transfer effects was negligible as determined in section E.1.
= 4.544 mol m^{-3}.

D_{eff} = effective diffusivity of CO_2 in a mixture N_2 and H_2 (m^2 s^{-1}) and was estimated using Eq. (14).

$$D_{eff} = \frac{D_g \varepsilon}{\tau} \qquad \text{(E.14)}$$

Where

D_g = diffusivity of CO_2 in a mixture N_2 and H_2 (estimated in section E.1 as 6.98 × 10^{-5} m^2 s^{-1})

ε = catalyst pellet porosity (0.6022)

τ = tortuosity parameter estimated as 1.254 by the Weissberg correlation (Delgado, 2006; Weissberg, 1963) given in Eq. 15.

$$\tau = 1 - 0.5\ln(\varepsilon) \tag{E.15}$$

$$D_{eff} = \frac{6.98 \times 10^{-5}\ \mathrm{m^2 s^{-1}} \times 0.6022}{1.254}$$

$$= 2.68 \times 10^{-5}\ \mathrm{m^2 s^{-1}}$$

By substitution into Eq. (E.13), Weisz-Prater criterion was evaluated as follows:

$$\frac{5.41 \times 10^{-2}\ \mathrm{mol\ kg_{cat}^{-1}\ s^{-1}} \times 5682.2\ \mathrm{kg\ m^{-3}} \times (7.50 \times 10^{-5}\ \mathrm{m})^2}{2.68\ \times 10^{-5}\ \mathrm{m^2\ s^{-1}} \times 4.54\ \mathrm{mol\ m^{-3}}}$$

$$= 0.014183$$

The effect of intraparticle mass transfer resistance is considered negligible since the value from the expression in Eq. 13 is less than 1.

E.3 External heat transfer resistance

The resistance to external heat transfer was determined by the Mears criterion given in Eq. (E.16).

$$\frac{|(\Delta H_r)|\left(|(-r_{exp})|\rho_b R_p E_A\right)}{hRT_b^2} < 0.15 \tag{E.16}$$

Where

E_A = 49909.48 J mol^{-1}

R = ideal gas constant (8.314 J mol^{-1} K^{-1})

T_b = reactant gas bulk temperature (523 K)

ΔH_r = heat of reaction at 523 K.

h = heat transfer coefficient between gas mixture and catalyst (J m^{-2} s^{-1} K^{-1}).

The heat of reaction (ΔH_r) and the heat transfer coefficient (h) were estimated as follows:

E.3.1 Estimation of the heat of reaction (ΔH_r)

The heat of reaction at temperature T, is given by Eq. (E.17).

$$\Delta H_r = \Delta H^0_{r,298K} + Q \tag{E.17}$$

For CO_2 methanation, $\Delta H^0_{r,298K} = -164.6\ kJ\ mol^{-1}$

$$Q = \int_{T_1}^{T_2} \Delta C_P dT \tag{E.18}$$

The specific heat capacity for each component gas (C_P) was estimated by the correlation given in Eq. (E.19).

$$C_P = a + bT + cT^2 + dT^3 \tag{E.19}$$

The temperature T is in °C while the constants a, b, c and d are provided in page 635 to 637 of "Elementary principles of chemical processes" (Felder and Rousseau, 2005). The difference between the specific heat capacities of the product (CH_4 and $2H_2O$) and the reactants (CO_2 and $4H_2$) is represented by Eq. (E.20).

$$\Delta C_P = \Delta a + \Delta bT + \Delta cT^2 + \Delta dT^3 \tag{E.20}$$

After substitution of ΔC_P from Eq. (E.19) into Eq. (E.18),

$$Q = \int_{25}^{250} ((-5 \times 10^{-2}) + (2.58 \times 10^{-5})T + (3.46 \times 10^{-8})T^2 + (-2.22 \times 10^{-11})T^3)dT$$

$$Q = -10.35\ kJ\ mol^{-1}$$

From Eq. (E.17),

$$\Delta H_r = -164.6 + (-10.35)$$

$$\Delta H_r = -174.95\ kJ\ mol^{-1}\ or\ -174947.068\ J\ mol^{-1}$$

E.3.2 Estimation of the heat transfer coefficient, h

The heat transfer coefficient, *h*, was evaluated by Eq. (E.21).

$$j_D = j_H = \frac{h\,\mathrm{Pr}^{2/3}}{C_{pg}\rho_g U} \tag{E.21}$$

where

j_H = Colburn's *j*-factor for heat transfer ($j_H = j_D$)

ρ_g = density of the gas mixture (3.43×10^{-1} kg m^{-3})

U = superficial gas velocity (8.92×10^{-2} m s^{-1})

C_{pg} = specific heat capacity of feed gas mixture at constant pressure (J kg^{-1} K^{-1}) was estimated by Eq. (E.22).

Pr = Prandtl number

$$C_{pg} = \sum_i y_i C_p^i \tag{E.22}$$

The C_P and y_i of each gas have been determined in subsection E.2.1 as follows:

C_{CO2} = 1022.60 J kg^{-1} K^{-1}, 0.111

C_{N2} = 1066.03 J kg^{-1} K^{-1}, 0.444

C_{H2} = 14410.23531 J kg^{-1} K^{-1}, 0.444

Therefore, C_{pg} = 6991.96 J kg^{-1} K^{-1}

Next parameter to be evaluated is the Prandtl number (Pr).

Estimation of Prandtl number

The Prandtl number (*Pr*) was estimated using Eq. (E.23).

$$\mathrm{Pr} = \frac{C_{pg}\mu_g}{\lambda_g} \tag{E.23}$$

where

λ_g = thermal conductivity of the gas mixture estimated using Eq. (E.24).

$$\lambda_g = \sum_i \frac{y_i \lambda_i}{\sum_{j \neq i} y_j \psi_{ij}} \tag{E.24}$$

where

i,j = CO_2, H_2, N_2

y = mole fraction of component gases (N_2 = 0.444, CO_2 = 0.111, H_2 = 0.444)

λ = thermal conductivity of component gases estimated by Eq. (E.25).

$$\lambda_i = \frac{C1T^{C2}}{1+\frac{C3}{T}+C4/T^2} \tag{E.25}$$

The values of constants C1, C2, C3 and C4 can be found in page 2-433 to 2-438 of Perry's Chemical Engineers' Handbook (Perry and Green, 2008).

After substitution into Eq. (E.25), the viscosity of each species at 523 K was obtained as follows:

λ_{CO2}= 0.0346 W m^{-1} K^{-1}

λ_{N2} = 0.0403 W m^{-1} K^{-1}

λ_{H2} = 0.2752 W m^{-1} K^{-1}

ψ_{ij} = thermal conductivity's correction factor, and was estimated by Eq. (E.26) as provided in the literature (Lindsay and Bromley, 1950).

$$\psi_{ij} = \frac{1}{4}\left\{1+\left[\left(\frac{\mu_i}{\mu_j}\right)\left(\frac{M_j}{M_i}\right)^{3/4}\left(\frac{T+S_i}{T+S_j}\right)\right]^{1/2}\right\}^2\left(\frac{T+S_{ij}}{T+S_i}\right) \quad \text{(E.26)}$$

μ = viscosity of component gases which have been determined from Eq. (E.7) as μ_{CO2}= 2.46012 × 10^{-5} kg m^{-1} s^{-1}; μ_{N2} = 2.67153 × 10^{-5} kg m^{-1} s^{-1} μ_{H2} = 1.31 × 10^{-5} kg m^{-1} s^{-1}.

M = molecular weight of component gases (see Table E.1)

T = gas mixture temperature (523 K)

S = Sutherland's constant. Except for H_2 with Sutherland constant of 79 K, the Sutherland constants of CO_2 and N_2 were estimated by 1.5 × T_i (Lindsay and Bromley, 1950). T_i is the boiling point of the pure gases in K, (T_{N_2} = 77.2 K, T_{CO_2} = 194.5 K). The Sutherland's constants employed are S_{H2} = 79 K, S_{CO2} = 291.75 K, S_{N2} = 115.8 K.

S_{ij} = Sutherland's constant for a binary gas mixture *ij* was estimated by Eq. (E.27). The constant C is 1 for nonpolar pure gases and 0.733 for strongly polar gases (Lindsay and Bromley, 1950). Since the feed gas components in this study (CO_2, N_2 and H_2) are nonpolar, C = 1.

$$S_{ij} = S_{ji} = C(S_i S_j)^{1/2} \quad \text{(E.27)}$$

After substitution into Eq. (E.24), the thermal conductivity of gas mixture λ_g = 0.08524 J m^{-1} s^{-1} K^{-1} or 0.08524 W m^{-1} K^{-1}.

From Eq. (E.23) the Prandtl number was estimated as follows: $\Pr = \frac{C_{pg}\mu_g}{\lambda_g}$

$$Pr = \frac{6991.98 \text{ J kg}^{-1} \text{ K}^{-1} \times 5.61 \times 10^{-5} \text{ kg m}^{-1} \text{ s}^{-1}}{0.08524 \text{ J m}^{-1} \text{ s}^{-1} \text{ K}^{-1}} = 4.605$$

From Eq. (E.21), the heat transfer coefficient (h) was evaluated as follows:

$$h = \frac{j_D C_{pg} \rho_g U}{\Pr^{2/3}}$$

$$h = \frac{6.14 \times 6991.98 \text{ J kg}^{-1} \text{ K}^{-1} \times 0.425 \text{ kg m}^{-3} \times 0.166 \text{ m s}^{-1}}{4.605^{2/3}}$$

$$= 1095.30 \text{ J m}^{-2} \text{ s}^{-1} \text{ K}^{-1}$$

External heat transfer resistances = $\frac{\left|(-\Delta H_r)\right|\left(-r_{\exp}\right)\rho_b R_p E_A}{hRT_b^2}$

$$= (|-174947.068| \text{ J mol}^{-1} \times 5.41 \times 10^{-2} \text{ mol kg}_{\text{cat}}^{-1} \text{ s}^{-1})$$

$$\times \frac{2260.38 \text{ kg m}^{-3} \times 7.50 \times 10^{-5} \text{ m} \times 49909.48 \text{ J mol}^{-1}}{1095.30 \text{ J m}^{-2} \text{ s}^{-1} \text{ K}^{-1} \times 8.314 \text{ J mol}^{-1} \text{ K}^{-1} \times (523)^2 \text{ K}^2}$$

$$= 0.03215$$

Since the value from the criterion is less than 0.15, the effect of external heat transfer resistance was neglected.

E.4 Internal Heat Transfer Resistance

The internal heat transfer resistance was determined using Anderson criterion (Anderson, 1963; Italiano et al., 2018) expressed in Eq. (E.28).

$$\frac{\left|\left(-\Delta H_r\right)\right|\left(-r_{\exp}\right)\rho_b R_p^2 E_A}{\lambda_p R T_s^2} < 0.75 \tag{E.28}$$

where

$(-r_{\exp})$ = 5.41 x10^{-2} mol kg_{cat}^{-1} s^{-1}

ρ_b = 2260.38 kg m^{-3}

R_p = 7.50 x10^{-5} m

$-\Delta H_r$ = -174947.068 J mol^{-1}

E_A = 49909.48 J mol^{-1}

R = ideal gas constant (8.314 J mol^{-1} K^{-1})

T_s = reactant gas temperature at the catalyst's surface

= 523 K (since resistance to external heat transport is negligible)

λ_p = thermal conductivity of the catalyst pellet (J m^{-2} s^{-1} K^{-1}). This parameter was taken as 2.12 J m^{-2} s^{-1} K^{-1} which is within the range of values for 8YSZ based porous materials (Aziz et al., 2022; Nagaraju and Raja Annamalai, 2019).

From Eq. (E.28), resistance to internal heat transfer = $\frac{\left|\left(-\Delta H_r\right)\right|\left(-r_{\exp}\right)\rho_b R_p^2 E_A}{\lambda_p R T_s^2}$

$$= \frac{|-174947.068| \text{ J mol}^{-1} \times 5.41\times10^{-2} \text{ mol kg}_{\text{cat}}^{-1} \text{ s}^{-1} \times 2260.38 \text{ kg m}^{-3} \times (7.50\times10^{-5})^2 \text{ m}^2 \times 49909.48 \text{ J mol}^{-1}}{2.12 \text{ J m}^{-2} \text{ s}^{-1} \text{ K}^{-1} \times 8.314 \text{ J mol}^{-1} \text{ K}^{-1} \times (523)^2 \text{ K}^2}$$

$$= 0.001246$$

The internal heat transfer resistance effect was ignored since the value from the Anderson criterion is less than 0.001246. Take note that this situation was still the same when the thermal conductivity of the catalyst pellet (λ_p) was varied between 0.5 and 10.

E.5 Wall and radial heat dispersion effects

The impact of tube diameter to particle diameter ratio on wall heat transfer was determined by Eq. (E.29). Typically, when this ratio exceeds 4, the wall heat transfer effect is considered insignificant.

$$\frac{d_t}{d_p} > 4 \tag{E.29}$$

Where

d_p = catalyst particle diameter (1.5×10^{-4} m)

d_t = reactor tube diameter (5.5×10^{-3} m)

The value of $d_p/d_t = 36.67$

> 4

The radial heat dispersion effect may be calculated using the Mears criterion in Eq. (E.30).

$$\left(\frac{E_a}{RT_w}\right)\left(\frac{|(-\Delta H_r)|\left((-r_{exp})\rho_b R_p^2\left[\frac{(1-\varepsilon)}{(1-b)}\right]\right)}{4\lambda_p T_w}\left(\frac{1}{8}+\frac{R_p}{Bi_w R_t}\right)\right) < 0.05 \tag{E.30}$$

Where

T_w = the reactor's wall temperature 523 K (assuming an isothermal condition).

ε = void fraction in the catalyst bed (0.6022).

b = inert solids fraction of the catalyst bed (0).

R_t = radius of reactor tube (2.75×10^{-3} m).

R_p = radius of catalyst particle (7.50×10^{-5} m).

Bi_w = Biot number of the tube wall, and may be calculated using Eq. (E.31)

$$Bi_w = \frac{h_w d_p}{\lambda_p} \tag{E.31}$$

Where

h_w = heat transfer coefficient of reactor tube wall (for quartz material, h_w = 30 J m^{-2} s^{-1} K^{-1})

d_p = catalyst particle diameter ($1.5\ x10^{-4}$ m)

λ_p = thermal conductivity of catalyst pellet (2.12 J m^{-1} s^{-1} K^{-1})

$$Bi_w = \frac{30\ \text{J m}^{-2}\ \text{s}^{-1}\ \text{K}^{-1} \times 1.5 \times 10^{-4}\ \text{m}}{2.12\ \text{J m}^{-2}\ \text{s}^{-1}\ \text{K}^{-1}} = 2.12 \times 10^{-3}$$

From Eq. (E.31), radial heat dispersion

$$= \left(\frac{49909.48 \text{ J mol}^{-1}}{8.314 \text{ J mol}^{-1} \text{ K}^{-1} \times 523 \text{ K}}\right) \times$$

$$\left(\frac{-174947.068 \text{ J mol}^{-1} \times 5.41 \times 10^{-2} \text{ mol kg}_{\text{cat}}^{-1} \text{ s}^{-1} \times 2260.38 \text{ kg m}^{-3} \times (7.50 \times 10^{-5})^2 \text{ m}^2 \times \left[\frac{(1-0.667)}{(1-0)}\right]}{4 \times 2.12 \text{ J m}^{-2} \text{ s}^{-1} \text{ K}^{-1} \times 523 \text{ K}}\right)$$

$$\times \left(\frac{1}{8} + \frac{7.50 \times 10^{-5} \text{ m}}{2.12 \times 10^{-3} \times 2.75 \times 10^{-3} \text{ m}}\right) = 3.827 \times 10^{-6}$$

$$0.00161 < 0.05$$

Therefore, the radial heat dispersion effect is negligible.